รายงานวิจัยฉบับสมบูรณ์

โครงการผลิตเชื้อเพลิงทางเลือกใหม่อันประกอบด้วย Gas-to-Liquid (GTL), Biomass-to-Liquid (BTL), ก๊าซสังเคราะห์ (Synthesis gas) และ Dimethyl Ether (DME) จากวัตถุดิบประเภทต่าง ๆ ในประเทศไทย

จัดทำโดย

รศ.ดร. นวดล เหล่าศิริพจน์

บัณฑิตวิทยาลัยร่วมด้านพลังงานและสิ่งแวดล้อม
มหาวิทยาลัยเทคโนโลยีพระจอมเกล้าธนบุรี

กรกฎาคม 2552

สัญญาเลขที่ RMU4980020

รายงานวิจัยฉบับสมบูรณ์

โครงการผลิตเชื้อเพลิงทางเลือกใหม่อันประกอบด้วย Gas-to-Liquid (GTL), Biomass-to-Liquid (BTL), ก๊าซสังเคราะห์ (Synthesis gas) และ Dimethyl Ether (DME) จากวัตถุดิบประเภทต่าง ๆ ในประเทศไทย

รศ.ดร. นวดล เหล่าศิริพจน์

บัณฑิตวิทยาลัยร่วมด้านพลังงานและสิ่งแวดล้อม
มหาวิทยาลัยเทคโนโลยีพระจอมเกล้าธนบุรี

สนับสนุนโดยสำนักงานกองทุนสนับสนุนการวิจัย
และสำนักงานคณะกรรมการการอุดมศึกษา

กิตติกรรมประกาศ

ข้าพเจ้าขอขอบพระคุณ ฝ่ายวิชาการ สำนักงานกองทุนสนับสนุนการวิจัย (สกว.) ที่ให้การสนับสนุนเงินทุนเพื่อทำวิจัยแก่ข้าพเจ้ามาโดยตลอดตั้งแต่เริ่มทำงาน คือให้ทุนเพิ่มขีดความสามารถด้านการวิจัยของอาจารย์รุ่นใหม่ ในปี พ.ศ. 2547-2549 และให้ทุนเพิ่มขีดความสามารถด้านการวิจัยของอาจารย์รุ่นกลาง ในปี พ.ศ. 2549-2552 อีกทั้งยังให้การสนับสนุนการทำวิจัยแก่ข้าพเจ้าอย่างต่อเนื่องผ่านทุนองค์ความรู้ใหม่ที่เป็นพื้นฐานต่อการพัฒนา ในปี พ.ศ. 2552-2555 โดย สกว. จัดได้ว่าเป็นองค์กรแห่งเดียวในประเทศไทย ที่ให้การสนับสนุนการทำวิจัยพื้นฐาน หรืองานวิจัยเชิงวิชาการอย่างจริงจัง ซึ่งหากปราศจากการสนับสนุนเงินวิจัยจาก สกว. การที่ข้าพเจ้าจะเริ่มต้นทำงานวิจัยดังกล่าวอย่างจริงจังและต่อเนื่องดังที่เป็นอยู่ในปัจจุบันคงเป็นเรื่องยาก และคงจะไม่สามารถผลิตผลงานวิชาการออกมาได้ดังเช่นทุกวันนี้

Abstract

Hydrocarbons (i.e. CH_4, C_2H_4, C_2H_6, and C_3H_8) and oxyhydrocarbon (i.e. CH_3OH and C_2H_5OH) conversions with and without H_2O and CO_2 were studied over ceria-based materials prepared by precipitation and cationic surfactant-assisted methods with/without Zr doping with an aim to understand the relation between material specific surface area, oxygen storage capacity (OSC), hydrocarbon turnover rate, resistance toward carbon deposition, and rigorous kinetic dependencies.

High surface area CeO_2 and Ce-ZrO_2 prepared by cationic surfactant-assisted method provided significantly higher degree of OSC and turnover rates and greater resistance toward carbon deposition than Ce-ZrO_2 and CeO_2 from the conventional precipitation method. Importantly, the turnover rates (mol g_{cat}^{-1} s^{-1}) per degree of OSC (mol_{Oxygen} g_{cat}^{-1}) were identical for all materials indicating the linear influence of OSC on the turnover rates. Nevertheless, the kinetic dependencies of all hydrocarbon conversions were unaffected by specific surface area, doping element, degree of OSC and reactions (i.e. H_2O reforming, CO_2 reforming and cracking). The turnover rates for all ceria-based materials, measured under the conditions undetectable carbon formation and corrected the net rates for approach to equilibrium, were proportional to all hydrocarbon partial pressures with the reaction order in the range of 0.50 ±0.05. The rate was found independent of co-reactant partial pressures, whereas the presences of CO and H_2 inhibited the rate with the reaction orders in CO of -0.15 ±0.03 and in H_2 of -0.30 ±0.03. The activation energies for these reactions were in the same range of 145-155 kJ mol^{-1}. These kinetic dependencies were explained by a set of unifying redox mechanistic proposal, in which the sole kinetically relevant elementary step is the reaction of intermediate surface hydrocarbon species with the lattice oxygen (O_O^x), and that lattice oxygen is efficiently replenished by rapid surface reactions with oxygen source from either CO_2, H_2O, or even CH_3OH (in case of CH_3OH reaction); this fast step maintains the lattice oxygen (O_O^x) essentially unreduced during reactions.

Keywords: reforming, hydrogen, CeO_2, ethanol, methanol

บทคัดย่อ

งานวิจัยนี้เกี่ยวข้องกับการศึกษากระบวนการแปรสภาพสารประกอบไฮโดรคาร์บอน เช่น มีเทน เอทีลีน อีเทน และโพรเพน รวมถึงสารจำพวกแอลกอฮอล์ เช่น เมทานอล และเอทานอล ไปเป็นก๊าซสังเคราะห์ ผ่านกระบวนการรีฟอร์มมิ่งด้วยน้ำและคาร์บอนไดออกไซด์ รวมถึงกระบวนการสลายตัวทางความร้อน บนตัวเร่งปฏิกิริยาจำพวกซีเรียมออกไซด์ ซึ่งเตรียมขึ้นโดยกระบวนการ precipitation และ cationic surfactant-assisted method โดยมีวัตถุประสงค์เพื่อศึกษาความสัมพันธ์ระหว่างอัตราการเกิดปฏิกิริยา พื้นที่ผิวของตัวเร่งปฏิกิริยา ความสามารถในการกักเก็บออกซิเจน ความต้านทานต่อการเสื่อมสภาพเนื่องจากการเกิดคาร์บอนที่ผิวของตัวเร่งปฏิกิริยา และคุณสมบัติเชิงจลศาสตร์

จากผลการศึกษาพบว่าตัวเร่งปฏิกิริยาจำพวกซีเรียมออกไซด์ ซึ่งเตรียมขึ้นโดยกระบวนการ cationic surfactant-assisted method จะให้พื้นที่ผิว และความสามารถในการกักเก็บออกซิเจนที่สูงกว่าตัวเร่งปฏิกิริยาจำพวกซีเรียมออกไซด์ ซึ่งเตรียมขึ้นโดยกระบวนการ precipitation มาก และส่งผลให้มีอัตราการเกิดปฏิกิริยาและความต้านทานต่อการเสื่อมสภาพดีกว่าอย่างชัดเจน อย่างไรก็ดีจากการศึกษาคุณสมบัติเชิงจลศาสตร์ของตัวเร่งปฏิกิริยาจำพวกซีเรียมออกไซด์พบว่าคุณสมบัติดังกล่าวไม่ขึ้นกับวิธีการเตรียม พื้นที่ผิวของตัวเร่งปฏิกิริยา และความสามารถในการกักเก็บออกซิเจน นอกจากนั้นยังพบว่าคุณสมบัติเชิงจลศาสตร์ของกระบวนการรีฟอร์มมิ่งด้วยน้ำ และกระบวนการรีฟอร์มมิ่งด้วยคาร์บอนไดออกไซด์บนตัวเร่งปฏิกิริยาจำพวกซีเรียมออกไซด์มีลักษณะที่ใกล้เคียงกัน โดยค่าตัวแปรสำคัญที่ค้นพบคือ ค่า Reaction order ของสารประกอบไฮโดรคาร์บอนทุกชนิดจะมีค่าอยู่ระหว่าง 0.50 ±0.05 ส่วนความเข้มข้นของน้ำและคาร์บอนไดออกไซด์ไม่ส่งผลต่อการเกิดปฏิกิริยา (Reaction orders เท่ากับ 0) ส่วนการเติมคาร์บอนมอนออกไซด์ และไฮโดรเจน จะทำให้อัตราการเกิดปฏิกิริยามีค่าลดลง (Reaction order ของคาร์บอนมอนออกไซด์เท่ากับ -0.15 ±0.03 ส่วน Reaction order ของไฮโดรเจนเท่ากับ -0.30 ±0.03) และพลังงานก่อกัมมันต์ของทั้งสองปฏิกิริยามีค่าอยู่ระหว่าง 145-155 kJ mol^{-1} จากผลทั้งหมดดังที่ได้กล่าวมาทำให้สามารถอธิบายกลไกการเกิดปฏิกิริยารีฟอร์มมิ่งของตัวเร่งปฏิกิริยาจำพวกซีเรียมออกไซด์ได้ว่า ปฏิกิริยาที่เกิดขึ้นคือปฏิกิริยารีด๊อกซ์ โดยมี Rate determining step คือการการเกิดปฏิกิริยาระหว่างธาตุคาร์บอนที่ถูกดูดซับบนพื้นผิวกับออกซิเจนที่อยู่บนผิวของตัวเร่งปฏิกิริยาจำพวกซีเรียมออกไซด์ โดยออกซิเจนเหล่านี้จะถูกใช้ไปและเติมใหม่โดยใช้ออกซิเจนอะตอมของน้ำ หรือคาร์บอนไดออกไซด์ได้อย่างรวดเร็วและมีประสิทธิภาพ

คำสำคัญ รีฟอร์มมิง ไฮโดรเจน ซีเรียมออกไซด์ เอทานอล เมทานอล

(ความเห็นในรายงานนี้เป็นของผู้วิจัย สกว.ไม่จำเป็นต้องเห็นด้วยเสมอไป)

หน้าสรุปโครงการ (Executive Summary)
ทุนเพิ่มขีดความสามารถด้านการวิจัยของอาจารย์รุ่นกลางในสถาบันอุดมศึกษา
(RMU4980020)

ชื่อโครงการ (ภาษาไทย)	การผลิตเชื้อเพลิงทางเลือกใหม่อันประกอบด้วย Gas-to-Liquid (GTL), Biomass-to-Liquid (BTL), ก๊าซสังเคราะห์ (Synthesis gas) และ Dimethyl Ether (DME) จากวัตถุดิบประเภทต่างๆ ในประเทศไทย
(ภาษาอังกฤษ)	Productions of alternative fuels including Gas-to-Liquid (GTL), Biomass-to-Liquid (BTL), Synthesis gas, and Dimethyl Ether (DME) from available feedstock in Thailand

ชื่อหัวหน้าโครงการ	นายนวดล เหล่าศิริพจน์ Mr. Navadol Laosiripojana
ตำแหน่ง	อาจารย์ (Ph.D.)
หน่วยงานที่สังกัด	บัณฑิตวิทยาลัยร่วมด้านพลังงานและสิ่งแวดล้อม
สถาบัน	มหาวิทยาลัยเทคโนโลยีพระจอมเกล้าธนบุรี 91 ถนนประชาอุทิศ บางมด ทุ่งครุ กรุงเทพฯ 10140
โทรศัพท์	(02)-8729014 (4146)
โทรสาร	(02)-8726736
โทรศัพท์มือถือ	(01)-9240461
E-mail address	navadol_l@jgsee.kmutt.ac.th

ระยะเวลาโครงการ	20 กรกฎาคม 2549 ถึง 19 กรกฎาคม 2552

1. ความสำคัญและที่มาของปัญหา

ปัจจุบันภาวการณ์ขาดแคลนน้ำมันเป็นปัญหาที่สำคัญมากอย่างหนึ่งของโลก ซึ่งปัญหาดังกล่าวสืบเนื่องมาจากความต้องการพลังงานของมนุษย์ที่เพิ่มสูงขึ้นอย่างมากมายและต่อเนื่องในปัจจุบันโดยเฉพาะอย่างยิ่งในภาคอุตสาหกรรมและภาคการขนส่ง จากรายงานประจำปีของแต่ละ

ประเทศทั่วโลกพบว่าผลิตภัณฑ์มวลรวม (GDP) ของแต่ละประเทศโดยเฉพาะอย่างยิ่งในประเทศขนาดใหญ่ เช่น ประเทศจีนและอินเดีย มีอัตราการเพิ่มของ GDP สูงถึงปีละกว่า 10% ซึ่งส่งผลให้ความต้องการพลังงาน (Energy Demand) ของโลกมีค่าสูงขึ้นมาก ในทางตรงกันข้าม การค้นพบแหล่งพลังงานใหม่รวมถึงกำลังการผลิตพลังงานจากแหล่งพลังงานทั้งหมด (Energy Supply) กลับเพิ่มขึ้นในอัตราที่ต่ำกว่า ปัจจัยดังกล่าวส่งผลให้ราคาน้ำมันดิบ ซึ่งเป็นแหล่งพลังงานหลักของโลกในปัจจุบันมีแนวโน้มปรับตัวสูงขึ้นอย่างรวดเร็วและต่อเนื่อง สำหรับประเทศไทยซึ่งเป็นประเทศที่พึ่งพาแหล่งพลังงานก๊าซธรรมชาติและน้ำมันดิบเป็นหลักก็ประสบปัญหาเช่นเดียวกับหลายประเทศในโลก โดยในแต่ละปีประเทศไทยจำเป็นต้องนำเข้าเชื้อเพลิงจำนวนมากโดยเฉพาะอย่างยิ่งน้ำมันเชื้อเพลิงเนื่องจากอัตราการใช้พลังงานที่สูงขึ้นซึ่งเป็นสาเหตุหนึ่งที่ทำให้เกิดปัญหาการขาดดุลการค้าระหว่างประเทศและความผันผวนทางด้านเศรษฐกิจจากการเปลี่ยนแปลงราคาเชื้อเพลิง

จากรายงานในปี 2546 ประเทศไทยใช้พลังงานขั้นต้น (Primary Energy) ทั้งที่ผลิตจากแหล่งภายในประเทศและการนำเข้าจากต่างประเทศรวม 99,465 พันตันเทียบเท่าน้ำมันดิบ (ktoe) ในจำนวนนี้ ร้อยละ 98 อยู่ในรูปของเชื้อเพลิงซึ่งน้ำมันปิโตรเลียมมีสัดส่วนเกือบครึ่งหนึ่ง (ร้อยละ 47.5) และในการผลิตกระแสไฟฟ้าจำนวน 116,983 ล้านกิโลวัตต์ชั่วโมง (GWh) เชื้อเพลิงก็มีสัดส่วนสูงถึงร้อยละ 93.8 โดยก๊าซธรรมชาติมีสัดส่วนสูงสุดคือ ร้อยละ 76.3 [1,2]

ตารางที่ 1 พลังงานขั้นต้น และที่มาของพลังงานไฟฟ้าที่ผลิตในประเทศไทย

การจัดหาพลังงานขั้นต้น (รวม 99,465 ktoe)		การผลิตพลังงานไฟฟ้า (รวม 116,983 GWh)	
น้ำมัน	47.5%	● เชื้อเพลิง	93.8%
ก๊าซธรรมชาติ	25.9%	- ก๊าซธรรมชาติ	76.3%
ถ่านหิน	9.8%	- ถ่านหินและลิกไนต์	17.2%
ชีวมวล	15.0%	- น้ำมันเตา	2.6%
พลังงานน้ำ	1.6%	- น้ำมันดีเซล	0.2%
ไฟฟ้านำเข้า	0.2%	- ชีวมวลและขยะ	2.8%
		- อื่นๆ	0.9%
		● พลังงานน้ำ	6.2%

นอกจากนั้นพบว่าจากปริมาณพลังงานทั้งหมด 99,465 พันตันเทียบเท่าน้ำมันดิบ (ktoe) ที่ใช้นั้น ประเทศไทยนำเข้าพลังงานรวมทั้งสิ้น 51,316 พันตันเทียบเท่าน้ำมันดิบ หรือร้อยละ 51.6 ของพลังงานที่จัดหาทั้งหมด เพิ่มขึ้นจากปี 2545 ร้อยละ 8.1 และเป็นการเพิ่มขึ้นอย่างต่อเนื่องเป็นที่ 5 การนำเข้าดังกล่าวคิดเป็นมูลค่ารวม 407,477 ล้านบาท (หรือประมาณร้อยละ 40 ของงบประมาณรายจ่ายของประเทศ) ซึ่งสูงกว่าปีก่อนร้อยละ 21.2 [1] และคาดว่ามูลค่าดังกล่าวจะสูงขึ้นมากในอนาคตเนื่องจากการเพิ่มขึ้นของราคาน้ำมันอย่างต่อเนื่อง โดยร้อยละ 75 ของพลังงาน

ที่นำเข้าคือ น้ำมันดิบ ซึ่งมีแหล่งนำเข้าจากลุ่มประเทศตะวันออกกลางเป็นหลัก คือร้อยละ 74.3 ดังแสดงในตารางที่ 2

ตารางที่ 2 การนำเข้าเชื้อเพลิงที่ใช้ในการผลิตพลังงานของประเทศไทย

ภาพรวมการนำเข้าพลังงานในปี 2546	
■ ปริมาณ 51,316 ktoe (51.6% ของพลังงานที่จัดหา) มูลค่า 407,477 ล้านบาท	
■ น้ำมันดิบ 75% ของพลังงานที่นำเข้าทั้งหมด	
■ แหล่งนำเข้าน้ำมันดิบ	
- ตะวันออกกลาง	74.3%
- อาเซียน	19.2%
- แอฟริกา	5.0%
- เอเชียแปซิฟิค	1.3%
- ยุโรป	1.2%
สัดส่วนการนำเข้าพลังงานประเภทต่างๆ (เทียบกับปริมาณที่จัดหาของแต่ละประเภท)	
■ น้ำมันดิบ	89.0%
■ ก๊าซธรรมชาติ	27.0%
■ ถ่านหิน	37.0%

นอกจากปัญหาการใช้พลังงานที่สูงขึ้นอย่างต่อเนื่องของประเทศไทยแล้ว อีกปัญหาหนึ่งที่ประเทศไทยกำลังประสบอยู่คือ ประสิทธิภาพการใช้พลังงานในประเทศนั้นต่ำมากเมื่อเทียบกับประเทศพัฒนาแล้วทั้งหลายโดยในปี 2545 มูลค่าการใช้พลังงานในประเทศสูงถึงร้อยละ 14.3 ของ GDP [3] และปริมาณพลังงานที่ใช้ ยังมีแนวโน้มสูงขึ้นเรื่อยๆ ตามการขยายตัวของเศรษฐกิจ โดยในรอบ 10 ปีที่ผ่านมา ค่า Energy elasticity (หรืออัตราส่วนการเพิ่มขึ้นของการใช้พลังงาน เทียบกับการขยายตัวของ GDP) อยู่ที่ 1.4 : 1 โดยเฉลี่ย ในขณะที่ประเทศที่พัฒนาแล้วอย่างประเทศญี่ปุ่น อัตราส่วนดังกล่าวอยู่ที่ 0.95 : 1 ซึ่งแสดงว่า การใช้พลังงานยังขาดประสิทธิภาพ ทำให้ต้นทุนการผลิตสินค้าและบริการสูงกว่าที่ควรจะเป็น โดยเฉพาะอย่างยิ่ง การผลิตไฟฟ้านั้นมีอัตราการสูญเสียสูงถึงร้อยละ 63-64 [1] ประเทศไทยจำเป็นต้องเพิ่มประสิทธิภาพการผลิตและการใช้พลังงานอย่างมาก ซึ่งเทคโนโลยีเชื้อเพลิงจะมีบทบาทอย่างมาก

ในปัจจุบันการพัฒนาเชื้อเพลิงทางเลือกใหม่ (Alternative fuels) ขึ้นมาใช้งานแทนที่น้ำมันดิบจึงเป็นสิ่งที่ประเทศพัฒนาแล้วต่างๆ ทั่วโลก อาทิเช่น สหรัฐอเมริกา เยอรมัน อังกฤษ และญี่ปุ่นกำลังให้ความสนใจ และดำเนินงานวิจัยเพื่อสังเคราะห์เชื้อเพลิงประเภทใหม่จากวัตถุดิบต่างๆ ออกมากันอย่างแพร่หลาย ตัวอย่างของเชื้อเพลิงชนิดสำคัญที่ทั่วโลกกำลังให้ความสนใจศึกษาและวิจัยอยู่ได้แก่ GTL (Gas to Liquid) และ BTL (Biomass to Liquid) รวมถึง Dimethyl Ether (DME) และไฮโดรเจน ซึ่งถูกนำไปใช้งานควบคู่กับเซลล์เชื้อเพลิง (Fuel Cells) ในการผลิตไฟฟ้า (Power generation) และใช้แทนที่น้ำมันเชื้อเพลิงในรถยนต์ (Vehicle applications) ซึ่งเชื้อเพลิงเหล่านี้

สามารถสังเคราะห์ขึ้นได้จากวัตถุดิบตามธรรมชาติมากมาย อาทิเช่น วัสดุชีวมวล (Biomass) ก๊าซชีวภาพ (Biogas) ก๊าซธรรมชาติ (Natural gas) และถ่านหิน (Coal) โดยกระบวนการแปรรูปวัตถุดิบตามธรรมชาติเหล่านี้ไปเป็นเชื้อเพลิงทางเลือกใหม่ดังกล่าวสามารถดำเนินการได้หลายกระบวนการ แต่กระบวนการที่สำคัญ และมีความเป็นไปได้ที่จะใช้ในเชิงพาณิชย์มากที่สุดกระบวนการหนึ่งคือ กระบวนการความร้อนเคมี (Thermo-Chemical Processes) ซึ่งใช้ความร้อนในการแปรสภาพวัตถุดิบต่างๆ ไปเป็นเชื้อเพลิงไฮโดรเจน, GTL, BTL, CTL และ DME ดังกล่าวได้ โดยมากแล้วกระบวนการความร้อนเคมีจำต้องใช้สารตัวเร่งปฏิกิริยา (Catalyst) เข้าช่วยเพื่อลดพลังงาน หรือความร้อนที่ใช้ในการแปรสภาพวัตถุดิบต่างๆ ซึ่งตัวเร่งปฏิกิริยาจะช่วยลดพลังงานก่อกัมมันต์ (Activation energy) ลงได้ ซึ่งกระบวนการความร้อนเคมีแต่ละกระบวนการก็จะมีชื่อและชนิดของตัวเร่งปฏิกิริยาที่เหมาะสมแตกต่างกันไป อาทิเช่น กระบวนการผลิตไฮโดรเจนจากวัตถุดิบที่เป็นก๊าซ หรือของเหลว เช่น ก๊าซชีวภาพ และก๊าซธรรมชาติ ได้แก่ กระบวนการรีฟอร์มมิ่ง (Reforming Process) [4] กระบวนการผลิตไฮโดรเจนจากวัตถุดิบที่เป็นของแข็ง เช่น วัสดุชีวมวลและถ่านหิน ได้แก่กระบวนการก๊าซซิฟิเคชัน (Gasification) [5,6] กระบวนการในการผลิต GTL, BTL, และ CTL ได้แก่กระบวนการ Fischer–Tropsch (FT) Process [7] กระบวนการผลิต DME ได้แก่ กระบวนการ Dehydration [8] ส่วนชนิดของตัวเร่งปฏิกิริยาที่ใช้ในกระบวนการต่างๆ จะแต่ต่างกันไป แต่โดยมากจะอยู่ในรูปสารประกอบของแข็งประเภทเมทิลออกไซด์ (Metal Oxide) อาทิเช่น Ni/Al_2O_3, $Rh/Ce\text{-}ZrO_2$, Co/SiO_2, หรือ $Cu/Zn/Al_2O_3$

กระบวนการแปลงสภาพเชื้อเพลิงที่สำคัญและมีการทำการวิจัยมาเป็นระยะเวลายาวนาน ได้แก่ กระบวนการรีฟอร์มมิ่ง และกระบวนการก๊าซซิฟิเคชัน (ซึ่งใช้ในการผลิตแก๊สไฮโดรเจน หรือแก๊สสังเคราะห์) กระบวนการ Fischer–Tropsch (ซึ่งใช้ในการสังเคราะห์ GTL, BTL และ CTL) กระบวนการ Dehydration (ซึ่งใช้ในการผลิต DME) กระบวนการ Water gas shift และ CO oxidation (ซึ่งใช้เพื่อเพิ่มความบริสุทธิ์ให้ไฮโดรเจน) ส่วนกระบวนการอื่นซึ่งเพิ่งมีการค้นพบเมื่อไม่นานมานี้ และมีรายงานว่ามีโอกาสในการนำไปใช้งานจริงในเชิงพาณิชย์มากกว่ากระบวนการดั้งเดิม ได้แก่ กระบวนการ Dehydration/Hydrogenation/Aldol condensation [9] (ซึ่งใช้ในการผลิต BTL) และกระบวนการ Cracking/Hydrogenation/Oligimerazation [10] (ซึ่งใช้ในการผลิต GTL) ในส่วนของส่วนเทคโนโลยีที่ใช้เปลี่ยนเชื้อเพลิงไปเป็นพลังงานไฟฟ้าที่สำคัญในอนาคตได้แก่ เทคโนโลยีเซลล์เชื้อเพลิง (Fuel Cells) ซึ่งอาจแบ่งได้เป็น 2 ประเภทใหญ่ๆ คือ เซลล์เชื้อเพลิงแบบอุณหภูมิต่ำ (ตัวอย่างสำคัญคือ เซลล์เชื้อเพลิงชนิด Proton Exchanged Membrane Fuel Cells (PEMFCs)) ซึ่งเซลล์เชื้อเพลิงประเภทนี้จะถูกใช้เป็นเครื่องกำเนิดไฟฟ้าสำหรับเครื่องมือขนาดเล็ก (Portable applications) เช่น โทรศัพท์มือถือ หรือ คอมพิวเตอร์ และใช้ในรถยนต์ (Vehicle applications) [11] ส่วนเซลล์เชื้อเพลิงอีกประเภทหนึ่งคือ เซลล์เชื้อเพลิงแบบอุณหภูมิสูง (ตัวอย่างสำคัญคือ เซลล์เชื้อเพลิงชนิด Solid Oxide Fuel Cells (SOFCs)) ซึ่งเซลล์เชื้อเพลิงประเภทนี้จะถูกใช้เพื่อเป็นเครื่องกำเนิดไฟฟ้าขนาดใหญ่ในโรงไฟฟ้า (Stationary applications) [12,13] เซลล์เชื้อเพลิงเป็น

หนึ่งในเทคโนโลยีที่แต่ละประเทศทั่วโลกกำลังศึกษาวิจัยกันอย่างแพร่หลายเพื่อให้สามารถใช้งานได้จริงในเชิงพาณิชย์ เนื่องจากข้อดีในแง่ของประสิทธิภาพ ความหลากหลายของเชื้อเพลิงที่สามารถเลือกใช้ได้ รวมถึงการเป็นมิตรต่อสิ่งแวดล้อม

เอกสารอ้างอิง

[1] รายงานพลังงานของประเทศไทย 2546, กรมพัฒนาพลังงานทดแทนและอนุรักษ์พลังงาน

[2] รายงานไฟฟ้าของประเทศไทย 2546, กรมพัฒนาพลังงานทดแทนและอนุรักษ์พลังงาน

[3] “ยุทธศาตร์พลังงานเพื่อการแข่งขันของประเทศไทย” กระทรวงพลังงาน, 4 พฤศจิกายน 2546

[4] Thomas Rostrup-Nielsen, Manufacture of hydrogen, Catalysis Today, 106(1-4), (2005), 293-296

[5] E. Shoko, B. McLellan, A.L. Dicks and J.C. Diniz da Costa, Hydrogen from coal: Production and utilisation technologies, International Journal of Coal Geology, In Press

[6] Mohammad Asadullah, Shin-ichi Ito, Kimio Kunimori, Muneyoshi Yamada and Keiichi Tomis, Biomass Gasification to Hydrogen and Syngas at Low Temperature: Novel Catalytic System Using Fluidized-Bed Reactor, Journal of Catalysis, 208(2), (2002), 255-259

[7] Burtron H. Davis, Overview of reactors for liquid phase Fischer–Tropsch synthesis, Catalysis Today 71 (2002) 249–300

[8] K.L. Ng, D. Chadwick, B.A. Toseland, Kinetics and modelling of dimethyl ether synthesis from synthesis gas, Chemical Engineering Science 54 (1999) 3587}3592

[9] George W. Huber, Juben N. Chheda, Christopher J. Barrett, and James A. Dumesic, Production of Liquid Alkanes by Aqueous-Phase Processing of Biomass-Derived Carbohydrates, Science, Vol 308, Pages 1446-1450

[10] Kenneth R. Hall, A new gas to liquids (GTL) or gas to ethylene (GTE) technology, Catalysis Today, 106(1-4), (2005), 243-246

[11] The online fuel cell information center, www.fuelcells.org

[12] W.L. Lundberg, S.E. Veyo, Conceptual design and performance analysis of a 300 MW_{el} LNG-fuelled pressurised SOFC/Gas turbine power plant, in: Yokohawa, S.C. Singhal (Eds.), Proceeding of the 7^{th} International Symposium Solid Oxide Fuel Cells VII, 2001, 78-87

[13] R.A. George, J. Power Sources, 86, (2000), 134-139

RESEARCH I

Kinetic dependencies and reaction pathways in hydrocarbon and oxyhydrocarbon conversions catalyzed by ceria-based materials

Hydrocarbons (i.e. CH_4, C_2H_4, C_2H_6, and C_3H_8) and oxyhydrocarbon (i.e. CH_3OH) conversions with and without H_2O and CO_2 were studied over ceria-based materials prepared by precipitation and cationic surfactant-assisted methods with/without Zr doping with an aim to understand the relation between material specific surface area, oxygen storage capacity (OSC), hydrocarbon turnover rate, resistance toward carbon deposition, and rigorous kinetic dependencies.

High surface area CeO_2 and Ce-ZrO_2 prepared by cationic surfactant-assisted method provided significantly higher degree of OSC and turnover rates and greater resistance toward carbon deposition than Ce-ZrO_2 and CeO_2 from the conventional precipitation method. Importantly, the turnover rates (mol g_{cat}^{-1} s^{-1}) per degree of OSC (mol_{Oxygen} g_{cat}^{-1}) were identical for all materials indicating the linear influence of OSC on the turnover rates. Nevertheless, the kinetic dependencies of all hydrocarbon conversions were unaffected by specific surface area, doping element, degree of OSC and reactions (i.e. H_2O reforming, CO_2 reforming and cracking). The turnover rates for all ceria-based materials, measured under the conditions undetectable carbon formation and corrected the net rates for approach to equilibrium, were proportional to all hydrocarbon partial pressures with the reaction order in the range of 0.50 ±0.05. The rate was found independent of co-reactant partial pressures, whereas the presences of CO and H_2 inhibited the rate with the reaction orders in CO of -0.15 ±0.03 and in H_2 of -0.30 ±0.03. The activation energies for these reactions were in the same range of 145-155 kJ mol^{-1}. These kinetic dependencies were explained by a set of unifying redox mechanistic proposal, in which the sole kinetically relevant elementary step is the reaction of intermediate surface hydrocarbon species with the lattice oxygen (O_O^x), and that lattice oxygen is efficiently replenished by rapid surface reactions with oxygen source from

either CO_2, H_2O, or even CH_3OH (in case of CH_3OH reaction); this fast step maintains the lattice oxygen (O_O^x) essentially unreduced during reactions. The unchanged state of lattice oxygen was confirmed by the calculation of oxygen balance during reactions.

1.1 Introduction

Cerium oxide (or ceria) based material is an important catalyst for a variety of reactions involving oxidation of hydrocarbons. It is also being used as a promoter or support in several industrial processes and as a key component in the formulation of catalysts for controlling noxious emissions from transportation section [1]. This material contains a high concentration of highly mobile oxygen vacancies, which act as local sources or sinks for oxygen involved in reactions taking place on its surface. That high oxygen mobility, high oxygen storage capacity, and its modifiable ability render the ceria-based material very interesting for a wide range of catalytic applications [2-8]. Recently, one of the great potential applications of ceria-based materials is in an Indirect Internal Reforming-Solid Oxide Fuel Cell (IIR-SOFC) as an in-stack reforming catalyst [9, 10]. It is also successfully applied in a direct internal reforming (DIR-SOFC), in which the hydrocarbons can be reformed internally at the anode side of SOFC, using ceria-based anodes (i.e. Cu-CeO_2, and Cu-CeO_2-YSZ) fueled by several hydrocarbon and oxyhydrocarbon compounds (i.e. C_4H_{10} and CH_3OH) [11-16].

It has been well established that the gas–solid reaction between CeO_2 and CH_4 produces synthesis gas with H_2/CO ratio of two, according to the following reaction [17]:

$$CH_4 + O_O^x = 2\,H_2 + CO + V_O^{\bullet\bullet} + 2\,e' \qquad (1)$$

O_O^x is the lattice oxygen on ceria surface, $V_O^{\bullet\bullet}$ denotes as an oxygen vacancy with an effective charge 2^+, and e' is an electron which can either be more or less localized on a cerium ion or delocalized in a conduction band. It was also demonstrated that the reactions of the reduced ceria with co-reactants i.e. CO_2 and H_2O produced CO and H_2 and regenerated the CeO_2 surface [18, 19]:

$$V_O^{\bullet\bullet} + 2\,e' + CO_2 = O_O^x + CO \quad (2)$$

$$V_O^{\bullet\bullet} + 2\,e' + H_2O = O_O^x + H_2 \quad (3)$$

The great benefit of ceria-based catalysts for the cracking and reforming reactions is their high resistance toward carbon deposition compared to the conventional metal catalysts i.e. Ni [9, 10]; however, the main weaknesses of the materials are their low specific surface area and high deactivation due to the thermal sintering particularly when operated at such a high temperature [20]. The preparation and use of high surface area ceria (CeO_2 (HSA)) with high resistance toward the sintering would be a good alternative method to improve the catalytic reactivity [20]. Several methods have recently been described for the preparation of CeO_2 (HSA) solid solution. Most interest has focused on the homogeneous precipitation techniques with different precipitating agents and additives [21-24], hydrothermal synthesis [25], spray pyrolysis methods [26], inert gas condensation of Ce followed by oxidation [27], thermal decomposition of carbonates [28], microemulsion [29], and electrochemical methods [30]. However, a few of these composites showed a regular pore structure after calcination at moderate temperatures (973-1073 K) and a severe loss of surface area occurs during the thermal treatment [31]. Recently, Terribile et al. [32] synthesized CeO_2 (HSA) with improved textural, structural and chemical properties for environmental applications by using a novel cationic surfactant-assisted approach. They reported that the reaction of cerium salts under basic conditions with ammonia in the presence of a cationic surfactant results in the precipitation of a gelatinous hydrous cerium oxide/surfactant mixture, which after calcination gives high surface area, fluorite-structured CeO_2 with good homogeneity and stability. They suggested that the cationic surfactant acts as a surface area enhancer by incorporation into the hydrous oxide and lowering of the surface tension of water in the pores during drying. Surface area excess of 200 $m^2\ g^{-1}$ after calcination at 723 K, which drops to 40 $m^2\ g^{-1}$ after calcination at the temperature higher than 1173 K, was reported. Compared to conventional CeO_2 (CeO_2 (LSA)) prepared by precipitation method with a

surface area less than 10 m^2 g^{-1} after calcination at 1173 K [10], this highlights the better potential of CeO_2 (HSA) to operate as a redox catalyst under high reaction temperature.

In addition to the investigation on preparation method, the addition of zirconium oxide (ZrO_2) has also been reported to improve the specific surface area, oxygen storage capacity, redox property, thermal stability and catalytic activity of ceria [33-38]. These benefits were associated with enhanced reducibility of cerium (IV) in Ce-ZrO_2, which is a consequence of high O^{2-} mobility inside the fluorite lattice. The reason for the increasing mobility might be related to the lattice strain, which is generated by the introduction of a smaller isovalent Zr cation into the CeO_2 lattice (Zr^{4+} has a crystal ionic radius of 0.84 Å, which is smaller than 0.97 Å for Ce^{4+} in the same co-ordination environment) [39].

Focusing on the reforming reactions (with H_2O and CO_2), until now, only a few studies have reported the role of ceria-based materials as catalysts for reforming and cracking of hydrocarbons (i.e. CH_4, and C_nH_m where n, m >1), furthermore, the reaction pathways and kinetic dependencies in hydrocarbon activation and conversion remains unclear. Here, we thereby probe the kinetic dependence of CH_4 reforming with H_2O and CO_2 and also CH_4 cracking over ceria-based materials prepared by precipitation and cationic surfactant-assisted methods and with/without Zr doping. The relation between the material specific surface area, doping element, oxygen storage capacity (OSC), reforming reactivity, resistance toward carbon deposition, and kinetic dependence were identified. A rigorous kinetic, mechanism, and rate expressions for the reforming and cracking of ceria-based materials were then established. In addition, the reactivity and kinetic dependence toward the reforming of high hydrocarbon (i.e. C_2H_4, C_2H_6, and C_3H_8) and toward the decomposition of oxyhydrocarbon (i.e. CH_3OH) with and without co-reactant elements were also carried out in order to verify our proposed kinetic and mechanism over ceria-based materials. Lastly, the kinetics of CH_4 reforming with H_2O and CO_2 over Rh supported by high surface area ceria-based material was performed and compared to those over conventional Rh/ZrO_2 in order to identify the effect of ceria-based support on the kinetics of CH_4 reforming over Rh metal.

1.2 Experimental methods

1.2.1 Material synthesis and characterization

CeO_2 was synthesized by 2 different methods i.e. precipitation (CeO_2 (LSA)) and cationic surfactant-assisted (CeO_2 (HSA)) methods. For CeO_2 (LSA), the starting solution was prepared by mixing 0.1 M of cerium nitrate ($Ce(NO_3)_3 \cdot H_2O$ from Aldrich) solution with 0.4 M of ammonia at a volumetric ratio of 2:1. This solution was stirred by magnetic stirring (100 rpm) for 3 h, then sealed and placed in a thermostatic bath maintained at 263 K. The precipitate was filtered and washed with deionised water and acetone to remove the free surfactant. It was dried overnight in ambient air at 383 K, and then calcined in flowing dry air by increasing the temperature to 1173 K with the rate of 0.167 K s^{-1} and holding at 1173 K for 6 h.

Following to the work from Terribile et al. [32], CeO_2 (HSA) was prepared by adding a solution of appropriate cationic surfactant, 0.1 M cetyltrimethylammonium bromide from Aldrich, to a 0.1 M cerium chloride. The ([Ce])/[cetyltrimethylammonium bromide] molar ratio was kept constant at 0.8. The mixture was stirred and then aqueous ammonia was slowly added until the pH was 11.5. Similarly, the mixture was continually stirred, sealed and placed in the thermostatic bath maintained at 263 K. After that, the mixture was cooled and the resulting precipitate was filtered and washed repeatedly with solvents. The filtered powder was then treated under the same procedures as CeO_2 (LSA). After calcination, the fluorite-structured CeO_2 with good homogeneity was obtained.

$Ce_{1-x}Zr_xO_2$ (or Ce-ZrO_2) with different Ce/Zr molar ratios were prepared by either co-precipitation or surfactant-assisted method of cerium nitrate ($Ce(NO_3)_3 \cdot H_2O$), and zirconium oxychloride ($ZrOCl_2 \cdot H_2O$) (from Aldrich). The ratio between each metal salt was altered to achieve nominal Ce/Zr molar ratios: $Ce_{1-x}Zr_xO_2$, where x = 0.25, 0.50, and 0.75 respectively. After treatment, the specific surface areas of all CeO_2 and Ce-ZrO_2 were achieved from BET measurement. As presented in Table 1, after drying in the oven, surface areas of 105 and 55 m^2 g^{-1} were observed for CeO_2 (HSA) and CeO_2 (LSA), respectively and, as expected, the surface area decreased at high calcination temperatures. However, the value for CeO_2 (HSA) is still appreciable after calcination at 1173 K. It can

also be seen that the introduction of ZrO_2 stabilizes the surface area of ceria, which is in good agreement with several previous reports. After treatment, the degree of OSC and redox reversibilities of all CeO_2 and Ce-ZrO_2 were determined by the temperature programmed reduction (TPR-1) at 1173 K and temperature programmed oxidation (TPO) following with second time temperature programmed reduction (TPR-2), respectively, at the same conditions. Details of these measurements are given in Section 3.1.

Rh/Ce-ZrO_2 and Rh/ZrO_2 catalysts (1.0 wt%) were prepared by wet impregnation of synthesized Ce-ZrO_2 (HSA) and ZrO_2 with an aqueous solution of $RhCl_3$ (from Aldrich). The solution was dried in ambient air at 383 K for 6 h and calcined in flowing dry air at 1073 K for 6 h. Both catalysts were ultimately treated in H_2 by increasing the temperature to 973 K with the rate of 0.167 K s^{-1} and holding at that temperature for 6 h and evacuated at 973 K for 1 h before undergone the characterization.

The weight contents of Rh loadings were determined by X-ray fluorescence (XRF) analysis. The dispersion percentages of Rh were measured by the volumetric H_2 chemisorption measurement after reduced and evacuated at 973 K by assuming 1:1 stoichiometry of adsorbed H and Rh surface atoms [40]. It is noted that the possible changing in Rh dispersion after exposure in reforming reactions, which might occurs by the sintering or blockage of Rh surface sites by carbon species, was tested by the oxidation of CO at 363 K, following the testing conditions of Wei and Iglesia [41].

1.2.2 Catalytic H_2O and CO_2 reforming and cracking of hydrocarbons

To undergo the catalytic testing, an experimental reactor system was constructed as shown elsewhere [42]. The feed gases including the components of interest i.e. CH_4, C_2H_4, C_2H_6, C_3H_8, CH_3OH, deionized H_2O (introduced by a syringe pump pass through an evaporator), CO_2, CO, and H_2 were introduced to the reaction section, in which a 10-mm diameter quartz reactor was mounted vertically inside tubular furnace. The catalysts (50 mg of ceria-based catalysts and 5 mg for Rh catalysts) were diluted with SiC (to obtain the total weight of 500 mg) in order to avoid temperature gradients and loaded in the quartz reactor, which was packed with quartz wool to prevent the catalyst moving. Preliminary experiments were also carried out to find suitable conditions in which

internal and external mass transfer effects are not predominant. Considering the effect of external mass transfer, the total gas flow rate was varied under a constant residence time of 5 x 10^{-4} g min cm^{-3}. The CH_4 reaction rate was found to be independent of the gas velocity when the gas flow rate was higher than 60 cm^3 min^{-1}, indicating the absence of external mass transfer effects at this high velocity. The reactions on different average sizes of catalysts were carried out in order to confirm that the experiments were carried out within the region of intrinsic kinetics. It was observed that the catalysts with the particle size less than 400 μm showed no intraparticle diffusion limitation in the range of conditions studied. Therefore, in the following studies, the total flow rate was kept constant at 100 cm^3 min^{-1} whereas the catalyst diameters were kept within the above-mentioned range in all experiments.

In our system, a Type-K thermocouple was placed into the annular space between the reactor and furnace. This thermocouple was mounted in close contact with the catalyst bed to minimize the temperature difference. Another Type-K thermocouple, covering by closed-end quartz tube, was inserted in the middle of the quartz reactor in order to re-check the possible temperature gradient. The record showed that the maximum temperature fluctuation during the reaction was always ±0.75 K or less from the temperature specified for the reaction.

Kinetic effects were studied over wide ranges of temperature and reactant partial pressures. After the reactions, the exit gas mixture was transferred via trace-heated lines (373 K) to the analysis section, which consists of a Porapak Q column Shimadzu 14B gas chromatograph (GC) and a mass spectrometer (MS). The gas chromatography was applied for the steady state kinetic studies, whereas the mass spectrometer in which the sampling of the exit gas was done by a quartz capillery and differential pumping was used for the transient experiments. In the present work, the outlet of the GC column was directly connected to a thermal conductivity detector (TCD) and a frame ionization detector (FID). In order to satisfactorily separate all elements, the temperature setting inside the GC column was programmed varying with time. In the first 3 min, the column temperature was constant at 333 K, it was then increased steadily by the rate of 15 K min^{-1} until 393 K and lastly decreased to 333 K.

1.2.3 Measurement of carbon formation

The temperature programmed oxidation (TPO) was applied to investigate the amount of carbon formed on catalyst surface by introducing 10% O_2 in He into the system, after purging with helium. The operating temperature increased from room temperature to 1273 K by a rate of 10 K min^{-1}. The amount of carbon formation on the surface of catalysts was determined by measuring the CO and CO_2 yields from the TPO results (using Microcal Origin Software). It is noted that the calibrations of CO and CO_2 were performed by injecting a known amount of these calibration gases from a loop, in an injection valve in the bypass line. The response factors were obtained by dividing the number of moles for each component over the respective areas under peaks. In addition to the TPO method, the amount of carbon deposition was confirmed by the calculation of carbon balance in the system, in which theoretically equal to the difference between the inlet carbon containing components and the outlet carbon containing components.

1.3. Results and discussion

1.3.1 Redox properties and redox reversibility

The oxygen storage capacities (OSC) and the degree of redox properties for fresh CeO_2 (both LSA and HSA) after calcinations were investigated using TPR-1, which was performed by heating the catalysts up to 1173 K in 5%H_2 in helium. The amount of hydrogen uptake is correlated to the amount of oxygen stored in the catalysts. As presented in Table 2, the amount of hydrogen uptakes over Ce-ZrO_2 and CeO_2 (HSA) are significantly higher than that observed over the low surface area cerias, suggesting the improvement of OSC and redox properties by the doping of Zr and the increasing of catalyst specific surface area. The benefit of OSC on the reforming reaction will be later presented in Section 3.3. After purged with helium, the redox reversibilities were then determined by applying TPO following with TPR-2. The TPO was carried out by heating the catalyst up to 1173 K in 10%O_2 in helium; the amounts of oxygen chemisorbed were then measured, Table 2. Regarding the TPR-2 results as also shown in Table 2, the amount of hydrogen uptakes for all catalysts were approximately similar to those from

the first time reduction reaction, indicating the redox reversibility for the synthesized ceria-based materials.

1.3.2 Reactivity toward the (H_2O and CO_2) reforming and cracking of CH_4

The H_2O reforming, CO_2 reforming and cracking of CH_4 were tested at 1123 K by introducing CH_4 along with co-reactant (for H_2O and CO_2 reforming). It should be noted that the reactions over Ce-ZrO_2 catalysts with different Ce/Zr ratios (1/3, 1/1, and 3/1) were firstly tested. The results revealed that Ce-ZrO_2 with Ce/Zr ratio of 3/1 shows the best performance in terms of stability and activity. Therefore, we report here detailed reactivity and kinetic data of Ce-ZrO_2 only with Ce/Zr ratio of 3/1.

Fig. 1 shows the variations in CH_4 reforming rate ($mol_{CH4}\ g_{cat}^{-1}\ s^{-1}$) with time at the initial state (10 min; using MS) over Ce-ZrO_2 (HSA) by varying inlet co-reactant/CH_4 ratios from 0.0 (cracking reaction) to 0.3, 0.5, 0.7, 1.0, and 2.0, while Fig. 2 shows the stability and activity (under the period of 10 h; using GC-TCD) of H_2O and CO_2 reforming of CH_4 over several catalysts. The reforming rate expressed in the figures is obtained from the relation between the measured net reaction rate (r_m; $mol_{CH4}\ g_{cat}^{-1}\ s^{-1}$) and the approach to equilibrium condition (η) using the following equation, [41]:

$$r_t = r_m (1-\eta)^{-1} \quad (5)$$

where η is either the approach to equilibrium for H_2O reforming (η_s) or the approach to equilibrium for CO_2 reforming (η_d). Both parameters are determined from following equation:

$$\eta_s = \frac{[P_{CO}][P_{H_2}]^3}{[P_{CH_4}][P_{H_2O}]}\frac{1}{K_s} \quad (6)$$

$$\eta_d = \frac{[P_{CO}]^2[P_{H_2}]^2}{[P_{CH_4}][P_{CO_2}]}\frac{1}{K_d} \quad (7)$$

where P_i is partial pressure of component i (atm); K_s and K_d are the equilibrium constants for H_2O and CO_2 reforming of CH_4 at a given temperature. It should be noted that, in the present work, the values of η were always kept below 0.2 in all experiments.

The main products from the reactions over these catalysts were H_2 and CO with some CO_2, indicating a contribution from the water-gas shift at this high temperature. Based on the measured concentrations of reactants and products during CH_4 reforming, the approach to water-gas shift equilibrium condition (η_{WGS}) in the range of temperature studied (1023 -1123 K) are always closed to 1.0 in all type of catalysts indicated that water-gas shift (WGS) reaction is at equilibrium. Fig. 1 indicates that the initial CH_4 reforming rate is unaffected by the concentration and type of co-reactants. Nevertheless, significant deactivation was observed for the cracking of CH_4 due to the loss of lattice oxygen (O_O^x) on the surface of ceria-based materials without the replacement by external oxygen containing sources (i.e. H_2O and CO_2). The rate of deactivation rapidly reduced when small content of H_2O or CO_2 was added.

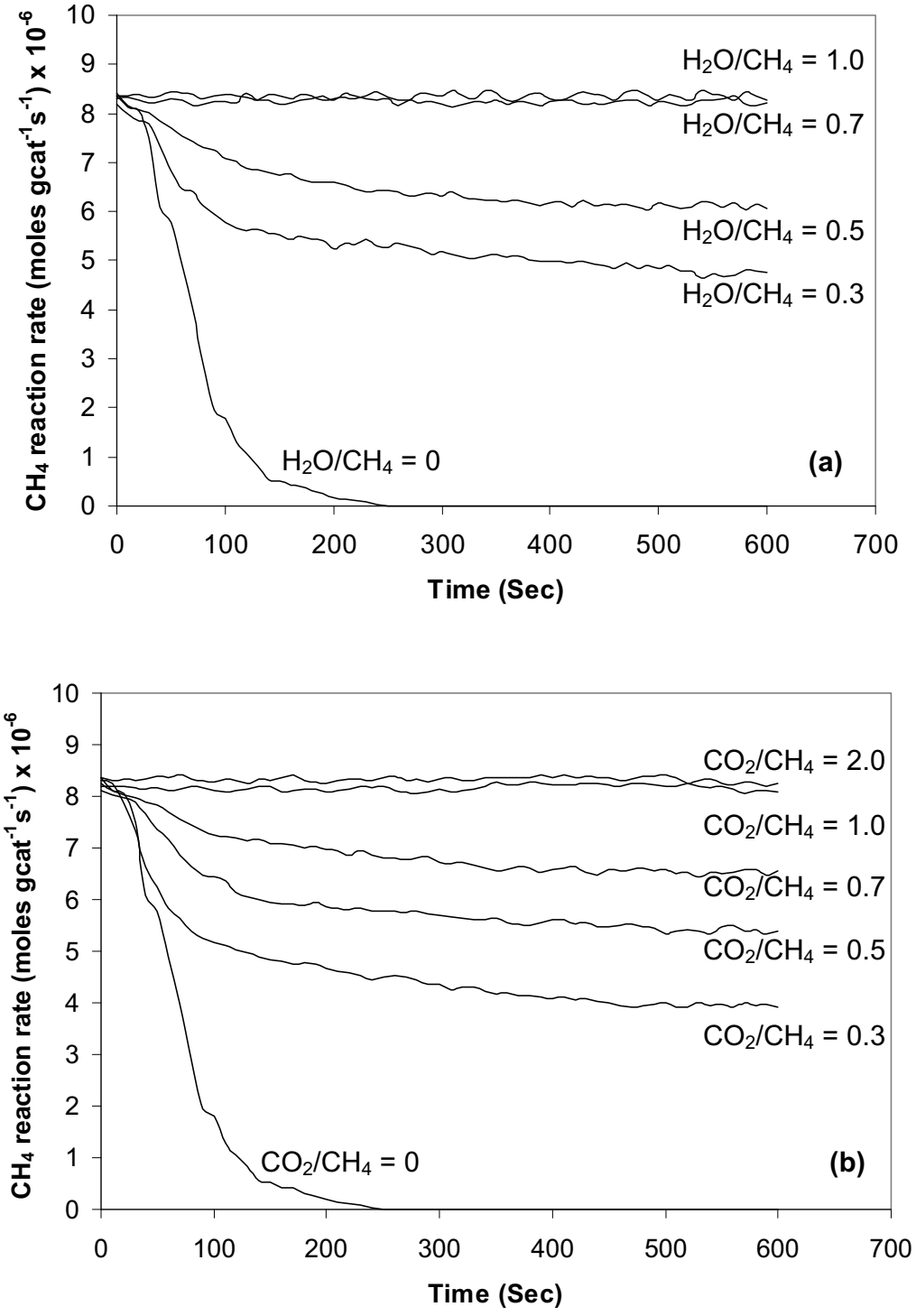

Fig. 1 CH4 reaction rate at initial state (10 min) for H_2O reforming of CH_4 (a) and CO_2 reforming of CH_4 (b) over Ce-ZrO_2 (HSA) (at 1123 K with 3 kPa CH_4, balance in He).

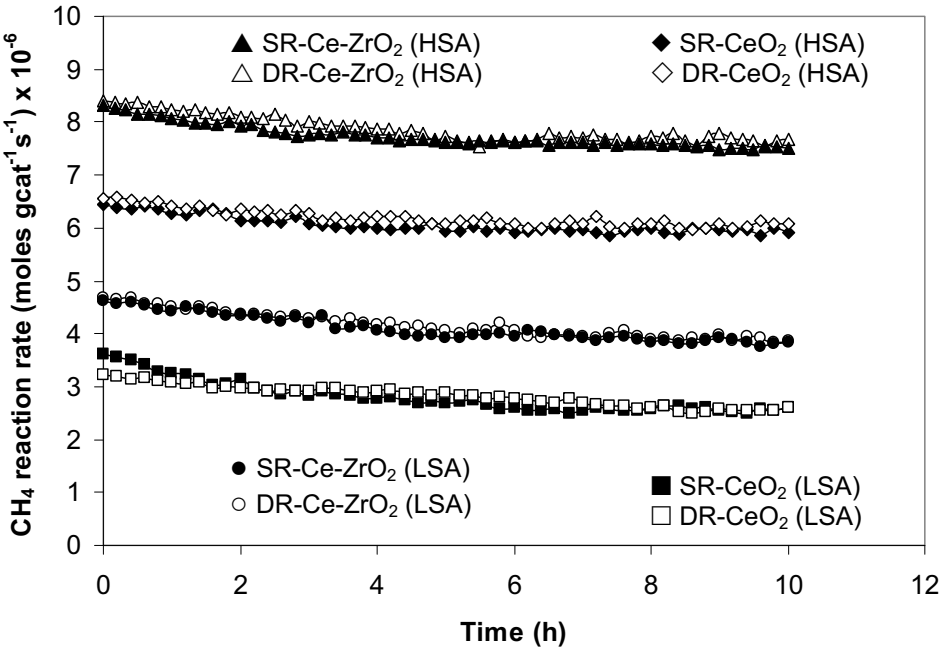

Fig. 2 Stability and activity testing of H_2O reforming (SR) and CO_2 reforming (DR) of CH_4 over several catalysts (at 1123 K with 3 kPa CH_4).

Fig. 2 indicated that, at steady state, CeO_2 (HSA) and Ce-ZrO_2 (HSA) presented much higher reactivity toward the CH_4 reforming than Ce-ZrO_2 (LSA), and CeO_2 (LSA). Importantly, at the same reaction conditions, the CH_4 reaction rates (mol_{CH4} g_{cat}^{-1} s^{-1}) per degree of OSC (mol_{Oxygen} g_{cat}^{-1}) (in Table 2) for each catalyst are approximately identical (2.8×10^{-3} mol_{CH4} mol_{oxygen}^{-1} s^{-1} for the inlet CH_4 of 3 kPa at 1123 K) indicating the linear influence of OSC on the reforming reactivity.

After purging in helium, the TPO detected small amount of carbon on the surface of materials from CH_4 cracking reaction (between 0.09-0.15 mmol g_{cat}^{-1} for high surface area materials and between 0.18-0.21 mmol g_{cat}^{-1} for low surface area one). These amounts of carbon deposited were ensured by the calculation of carbon balance. Regarding the calculation, the moles of carbon remain in the system were 0.07-0.14 mmol g_{cat}^{-1} for high surface area materials and were 0.20±0.01 mmol g_{cat}^{-1} for low surface

area materials, which are in good agreement with the values observed from the TPO. No carbon formation was observed on high surface area materials when the inlet H_2O/CH_4 and CO_2/CH_4 ratios were higher than 0.7 and 1.0, whereas low surface area materials required inlet H_2O/CH_4 and CO_2/CH_4 ratios higher than 1.0 and 2.0 to operate without detectable carbon. The good resistance toward carbon deposition for ceria-based materials, which has been widely reported by previous researchers [9-10], is mainly due to their sufficient oxygen storage capacity (OSC). It should be noted that we observed high amount of carbon formation on the surface of Ni catalysts after exposure in the same reforming conditions as ceria-based materials. Regarding the possible carbon formation during the reforming processes, the following reactions are theoretically the most probable reactions that could lead to carbon formation:

$$2CO \Leftrightarrow CO_2 + C \quad (8)$$

$$CH_4 \Leftrightarrow 2H_2 + C \quad (9)$$

$$CO + H_2 \Leftrightarrow H_2O + C \quad (10)$$

$$CO_2 + 2H_2 \Leftrightarrow 2H_2O + C \quad (11)$$

At low temperature, reactions (10)–(11) are favorable, while reaction (8) is thermodynamically unflavored [43]. The Boudouard reaction (Eq. 8) and the decomposition of CH_4 (Eq. 9) are the major pathways for carbon formation at such a high temperature as they show the largest change in Gibbs energy [44]. According to the range of temperature in this study, carbon formation would be formed via the decomposition of CH_4 and Boudouard reactions especially at high inlet CH_4/co-reactant ratio. By applying CeO_2, both reactions (Eqs. 8 and 9) could be inhibited by the redox reaction between the surface carbon (C) forming via the adsorptions of CH_4 and CO (produced during the reforming process) with the lattice oxygen (O_O^x) at CeO_2 surface (Eq. 12).

$$C + O_O^x \rightarrow CO + V_O^{\bullet\bullet} + 2e' \quad (12)$$

The greater resistance toward carbon deposition for high surface area ceria-based catalyst particularly Ce-ZrO_2 (HSA) is due to the significant higher amount of lattice oxygen (O_O^x) on their surfaces, according to the results in Section 1.3.1.

1.3.3 Kinetic dependencies of forward CH_4 reforming rate on partial pressures of reactants (i.e. CH_4 and H_2O or CO_2) and products (CO and H_2)

The kinetic dependencies of CH_4 reforming rates on the partial pressures of CH_4, H_2O, CO_2, CO, and H_2 for all ceria-based materials were studied in the temperature range of 1023-1123 K. All measurements were carried out under the operating conditions without detectable carbon formation by controlling H_2O/CH_4 and CO_2/CH_4 inlet ratio according to the results from Section 1.3.2.

Fig. 3 shows the effect of CH_4 partial pressure on the turnover rate (mol_{CH4} mol_{oxygen}^{-1} s^{-1}) over Ce-ZrO_2 (HSA) at several reaction temperatures, while Fig. 4 shows the effect of CH_4 partial pressure on the rate (per degree of OSC) over different catalysts (Fig. 4a) and different reactions (i.e. H_2O reforming, CO_2 reforming and cracking (initial rates) of CH_4) (Fig. 4b). The turnover rate increased linearly with increasing CH_4 partial pressures and operating temperature for all catalysts and reactions. The reaction order in CH_4 was determined by plotting $\ln(r_t)$ versus $\ln P_{CH_4}$ (the effects of product concentrations are taken into account via the term equilibrium condition (η)). The reaction orders in other components (CO_2, H_2O, H_2, and CO) were achieved using the same approach by varying the inlet partial pressure of the component of interest while keeping other inlet component partial pressures constant. The reaction order in CH_4 was observed to be positive fraction values approximately 0.52 ($\pm$0.03) for all catalysts and reactions, and seemed to be essentially independent of the operating temperature and co-reactant (CO_2 and H_2O) partial pressures for the range of conditions studied.

Several inlet CO_2 or H_2O partial pressures were then introduced to the feed with constant CH_4 partial pressure in order to investigate the influence of these co-reactant partial pressures on the turnover rate. Fig. 5 shows the effects of co-reactant on CH_4 reaction rate with several inlet CH_4 partial pressures over different reactions (Fig. 5a) and over different catalysts (Fig. 5b). It is clear that the turnover rates were not influenced by

H_2O and CO_2 partial pressures; thus, the reaction orders in both components would be zero. The reforming in the presences of CO and H_2 were also investigated by adding either CO or H_2 to the feed gas at several operating temperatures. The results in Figs. 6 and 7 showed that the turnover rates are dependent on both CO and H_2 concentrations. Unlike CH_4, both components inhibited the turnover rate. The reaction order in CO was in the range of -0.15 to -0.12, while the reaction order in H_2 was between -0.31 to -0.28 for all catalysts. Similar reaction orders and kinetic constants for all ceria-based materials indicate that the kinetic dependencies are not affected by the specific surface area (or degree of OSC) and the doping of Zr.

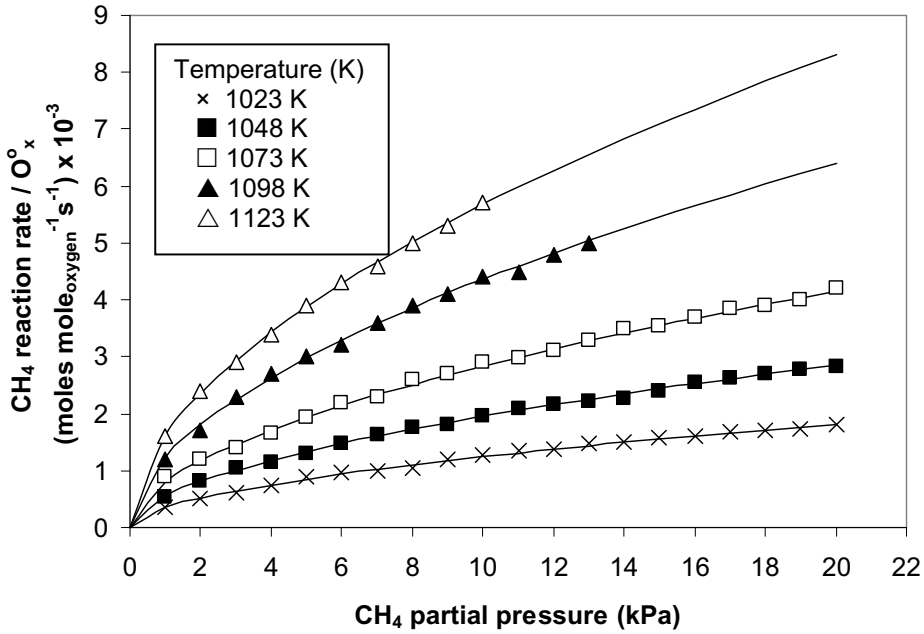

Fig. 3 Effect of temperature on CH_4 steam reforming over Ce-ZrO_2 (HSA) (with inlet CH_4/H_2O of 1.0).

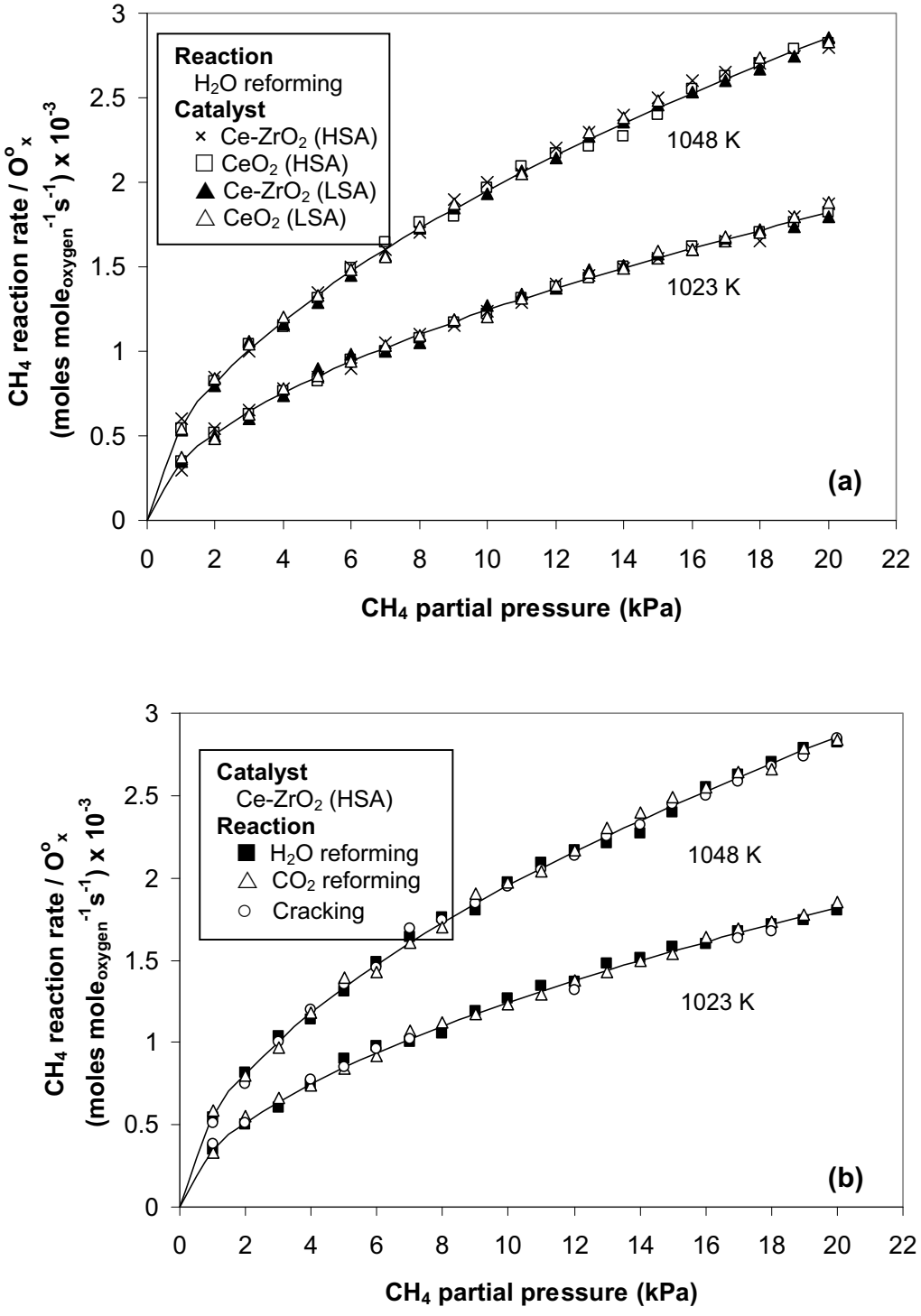

Fig. 4 Effect of CH_4 partial pressure on CH_4 reaction rate (per moles of oxygen stored) over different catalysts (a) and different reactions (b).

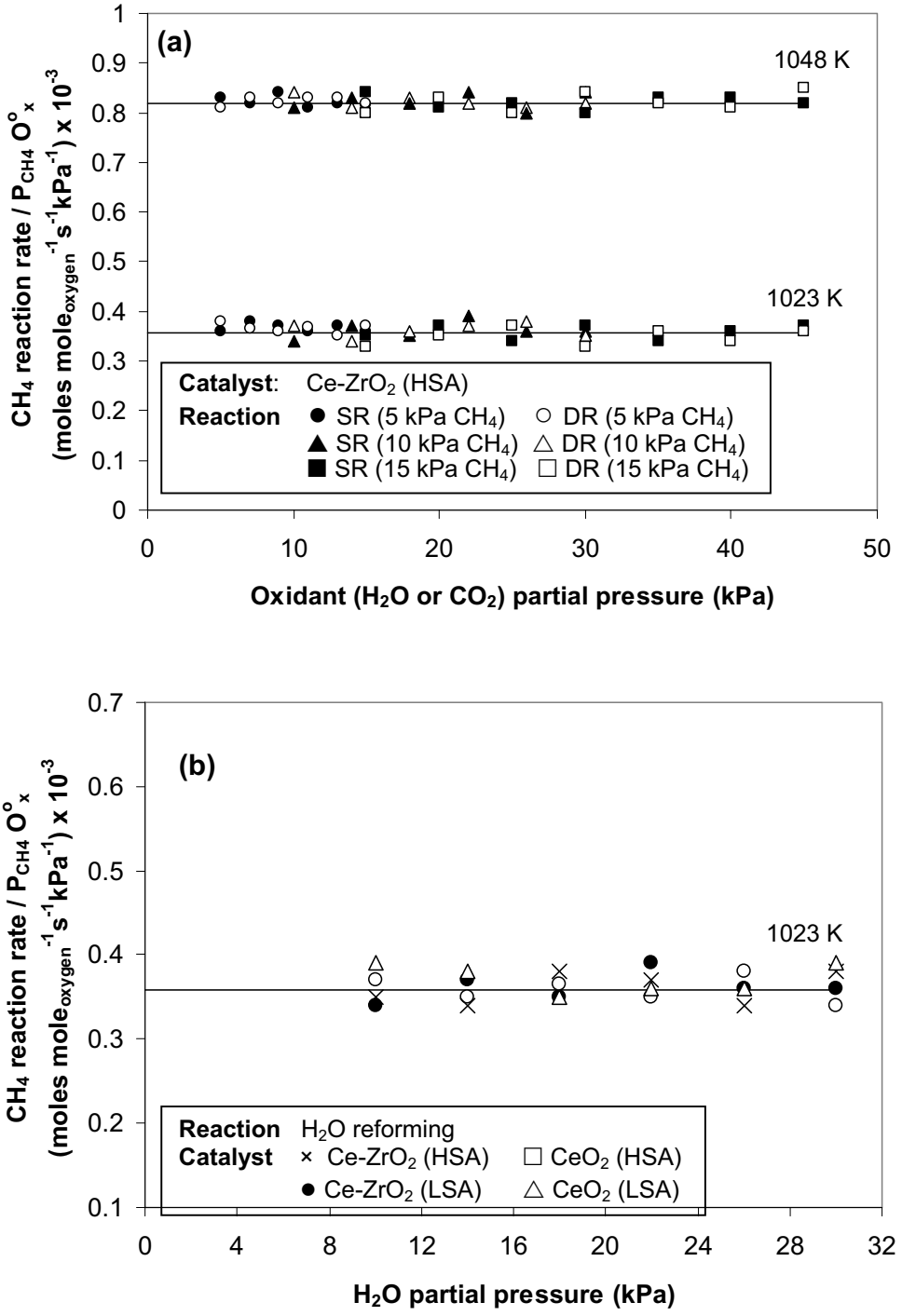

Fig. 5 Effect of co-reactant on CH_4 reaction rate (per moles of oxygen stored and inlet CH_4 partial pressure) over different reactions (with several inlet CH_4 partial pressures) (a) and different catalysts (b).

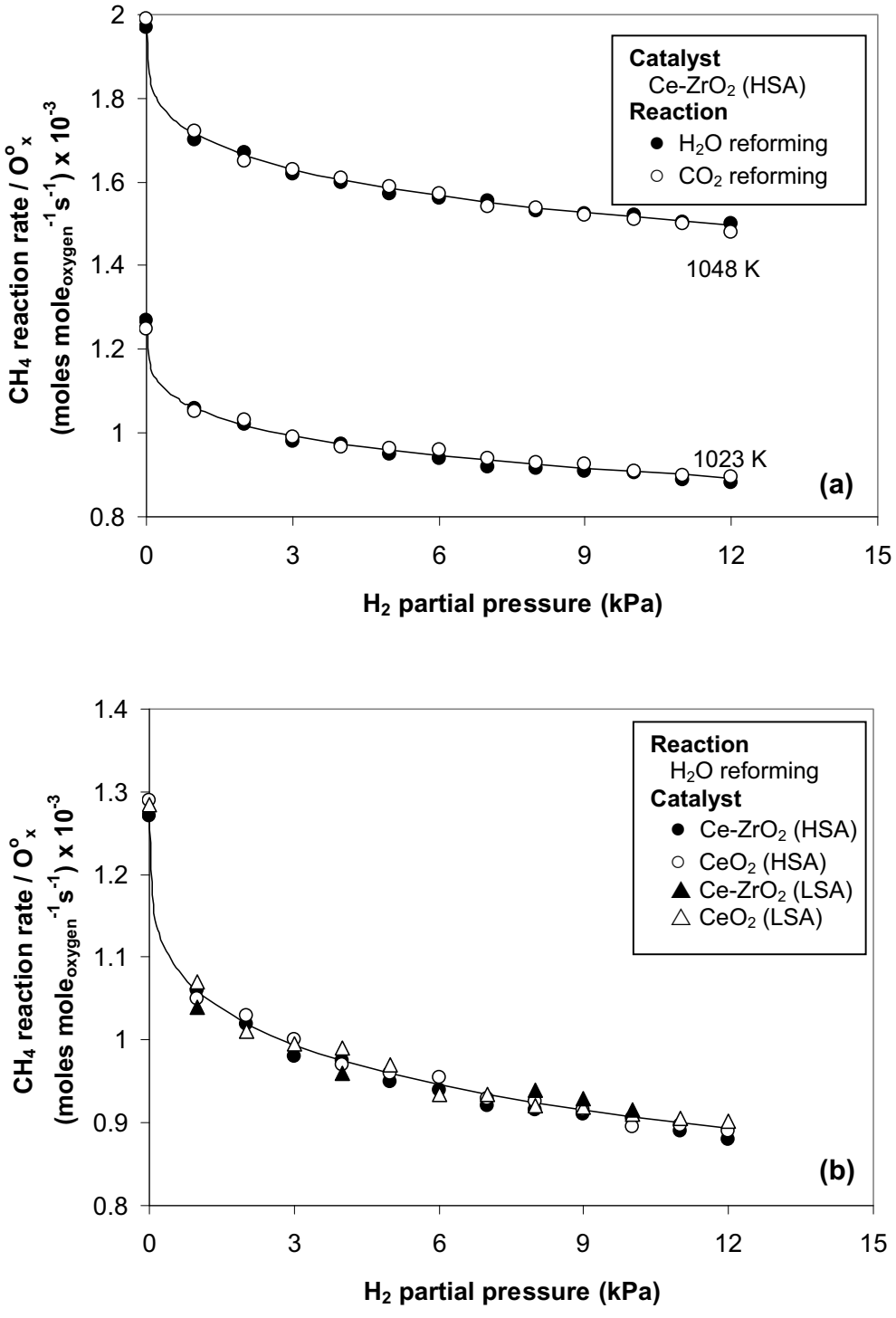

Fig. 6 Effect of H_2 on CH_4 reaction rate (per moles of oxygen stored) over different reactions (a) and different catalysts (b).

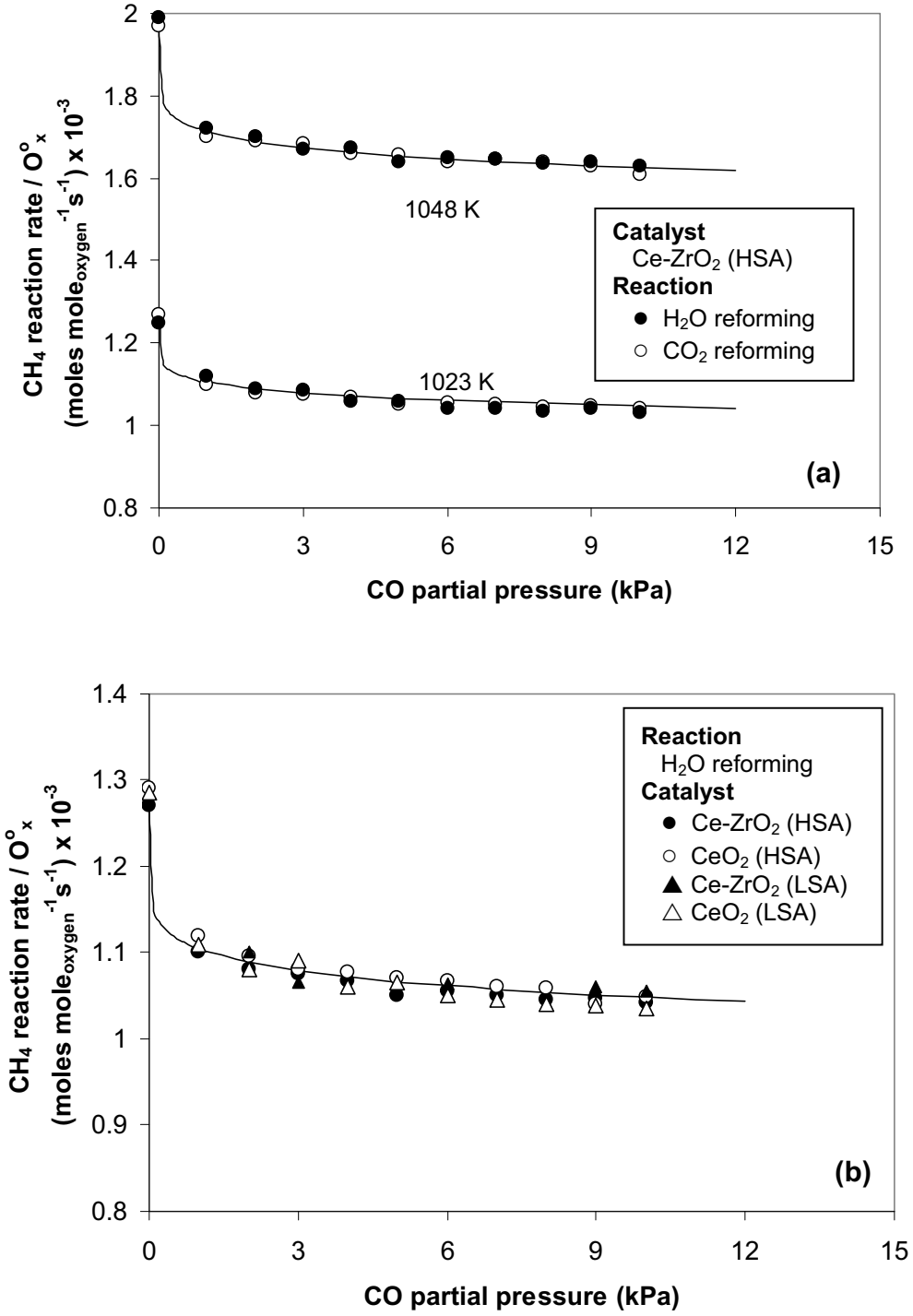

Fig. 7 Effect of CO on CH_4 reaction rate (per moles of oxygen stored) over different reactions (a) and different catalysts (b).

Some previous researchers have proposed the redox mechanism to explain the reforming behavior of ceria-based catalysts [9-10]. Here, we indicated that the CH_4 reaction pathway for ceria-based materials involves the reaction between absorbed CH_4 (forming intermediate surface hydrocarbon species) with the lattice oxygen (O_O^x) at CeO_2 surface, as illustrated schematically below.

CH_4 adsorption

$$CH_4 + 2* \rightarrow CH_3* + H* \quad (13)$$

$$CH_3* + * \rightarrow CH_2* + H* \quad (14)$$

$$CH_2* + * \rightarrow CH* + H* \quad (15)$$

$$CH* + * \rightarrow C* + H* \quad (16)$$

Co-reactant (H_2O and CO_2) adsorption

$$H_2O + 2* \Leftrightarrow OH* + H* \quad (17)$$

$$OH* + * \Leftrightarrow H* + O* \quad (18)$$

$$CO_2 + 2* \Leftrightarrow CO* + O* \quad (19)$$

Redox reactions of lattice oxygen (O_O^x) with C* and O*

$$C* + O_O^x \rightarrow CO* + V_O^{\bullet\bullet} + 2\,e' \quad (20)$$

$$V_O^{\bullet\bullet} + 2\,e' + O* \Leftrightarrow O_O^x + * \quad (21)$$

Inhibitory effects of CO and H_2

$$H_2 + 2* \Leftrightarrow H* + H* \quad (22)$$

$$H* + O_O^x \Leftrightarrow OH* + V_O^{\bullet\bullet} + 2\,e' \quad (23)$$

$$CO + * \Leftrightarrow CO* \quad (24)$$

$$CO* + O_O^x \Leftrightarrow CO_2* + V_O^{\bullet\bullet} + 2\,e' \quad (25)$$

where * is the surface active site of ceria-based materials. During the reactions, CH_4 adsorbed on * forming intermediate surface hydrocarbon species (CH_x*) (Eqs. 13-16) and later reacted with the lattice oxygen (O_O^x) (Eq. 20). The steady state reforming rate is due to the continuous supply of the oxygen source by either CO_2 or H_2O (Eqs. 17-19) that

reacted with the reduced-state catalyst to recover lattice oxygen (O_O^x) (Eq. 21). The identical rate for the H_2O and CO_2 reforming at similar CH_4 partial pressures, as well as the stronger linear dependence of the reforming rate on CH_4 partial pressure with the positive fraction value of reaction order in this component, and the independent effects of CO_2 and H_2O provide the evidence that the sole kinetically relevant elementary step is the reaction of intermediate surface hydrocarbon species with the lattice oxygen (O_O^x), and that oxygen is replenished by a significantly rapid surface reaction of the reduced state with the oxygen source from either CO_2 or H_2O; this fast step maintains the lattice oxygen (O_O^x) essentially unreduced by adsorbed intermediate surface hydrocarbon. The unchanged state of lattice oxygen was confirmed by the calculation of oxygen balance during reactions and TPO after reactions. We have used these methods to probe the state of lattice oxygen, because characterizations of used catalysts are not practical due to the low catalyst amounts used and its mixing with SiC. According to the oxygen balance calculation, the mole of oxygen (from co-reactant) fed into the system was almost similar to that in the products for all reactions and testing times indicating the unchanged state of CeO_2 (to CeO_{2-x}) during the experiments. Furthermore, the TPO results after reactions also proved the unchanged state of material, as no oxygen uptakes were detected.

The negative effects of CO and H_2 are due with the reactions between these adsorbed components (CO* and H*) with the lattice oxygen (O_O^x) (Eq. 22-25), which consequently results in the inhibition of CH_4 conversion. From all observation, the CH_4 reaction rate expression for H_2O reforming, CO_2 reforming and cracking (initial rate) can be written as following:

$$\text{Rate} = \frac{k[P_{CH_4}]^{0.5}}{1 + K_H[P_{H_2}]^{0.3} + K_{CO}[P_{CO}]^{0.15}} \qquad (26)$$

The rate constants (k) and the activation energies measured from the H_2O reforming, CO_2 reforming and cracking (initial rate) of CH_4 are identical at each reaction temperature, Table 3. The activation energies for these three reactions, achieved by the Arrhenius plots as shown in Fig. 8, were between 150-155 kJ mol^{-1}, which are in good agreement with the values previously reported [9-10]. Due to the identical CH_4 turnover rates, the reaction order in CH_4, the rate constants, and the activation energies for all H_2O

reforming, CO_2 reforming and cracking of CH_4, it could be concluded that all three reactions over ceria-based materials have similar reaction pathways in CH_4 activity.

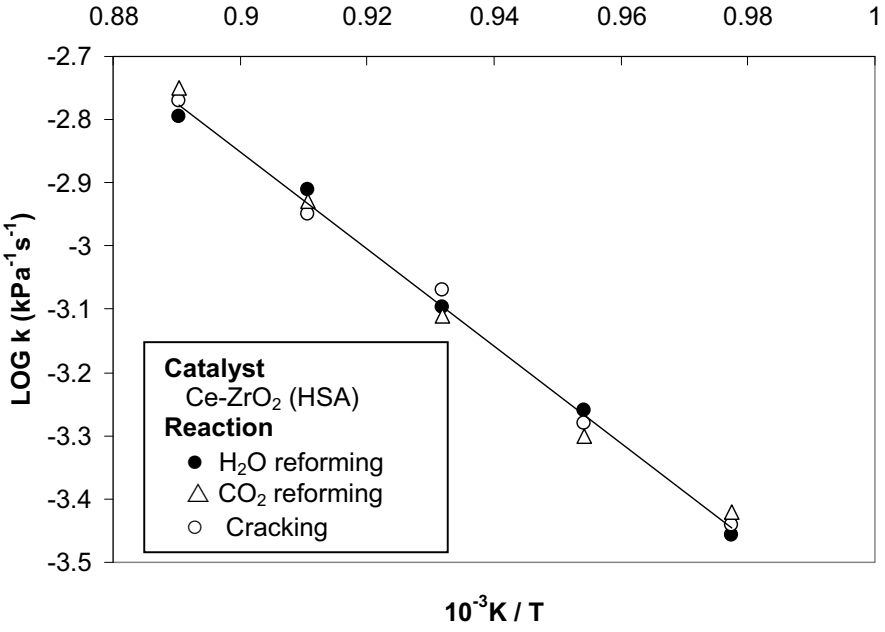

Fig. 8 Arrhenius plots for H_2O reforming, CO_2 reforming and cracking of CH_4 over Ce-ZrO_2 (HSA).

1.3.4 Reactivity toward reforming and decomposition of oxyhydrocarbon

The decompositions of CH_3OH with and without co-reactant elements (i.e. H_2O and CO_2) were studied to confirm the above redox mechanism. The feed condition was co-reactant/CH_3OH in helium with the several molar ratios in the temperature range of 873-1073 K (to prevent the influence of homogeneous non-catalytic reaction). It should be noted according to our experiments that, similar to CH_4 reforming, the turnover rate (per degree of OSC) and the kinetic dependencies of CH_3OH reaction rates were identical for all ceria-based materials, except the requirement of inlet co-reactant partial pressure to operate without detectable carbon formation. We thereby report here detailed reactivity and kinetic data only on Ce-ZrO_2 (HSA) sample.

After operated for 10 h, the main products from this reaction were H_2, CO, and CO_2, with small amount of CH_4 depending on the operating conditions, Table 4. According to the TPO measurements, no carbon formation was observed on the surface of Ce-ZrO_2 (HSA) in all studies. The effects of CH_3OH, H_2O, CO_2, CO and H_2 partial pressures on the turnover rate was then studied by varying inlet CH_3OH partial pressure from 1 to 10 kPa (Fig. 9a) and changing the inlet co-reactant (H_2O or CO_2) partial pressure from 0 to 10 kPa (while keeping CH_3OH partial pressure constant at 4 kPa) (Fig. 9b). The results show that the reaction rate was proportional to CH_3OH concentration with the reaction order of 0.50 (±0.04). The turnover rate was unaffected by H_2O and CO_2 partial pressures, in contrast, it was inhibited by the presence of H_2 and CO in the feed. The reaction orders in H_2 and CO were between -0.29 to -0.27 and -0.11 to -0.15, respectively, in the range of conditions studied. The activation energies for H_2O reforming, CO_2 reforming and cracking of CH_3OH, achieved by the Arrhenius plots as shown in Fig. 10, were between 150-155 kJ/mol, which are closed to those observed from the CH_4 reactions. Therefore, based on the redox mechanistic proposal for CH_4 reaction, the CH_3OH reaction mechanism over ceria-based materials can be written below:

$$CH_3OH + 2* \rightarrow CH_3* + OH* \quad (27)$$

$$CH_3* + 3* \rightarrow C* + 3H* \quad (28)$$

$$C* + O_O^x \rightarrow CO* + V_O^{\bullet\bullet} + 2\,e' \quad (29)$$

$$OH* + * \Leftrightarrow H* + O* \quad (30)$$

$$V_O^{\bullet\bullet} + 2\,e' + O* \Leftrightarrow O_O^x + * \quad (31)$$

CH_3OH first adsorbed on * forming intermediate surface hydrocarbon species (CH_x*) and OH* (Eq. 27). Similar to CH_4 reforming, the intermediate surface hydrocarbons then adsorbed on the active surface site and reacted with the lattice oxygen (O_O^x) (Eqs. 28-29). The steady state reforming rate is due to the continuous supply of the oxygen containing compounds present in the system (i.e. H_2O, CO_2 and also CH_3OH) to regenerate the lattice oxygen (O_O^x). The strong linear dependence of the CH_3OH decomposition rate on CH_3OH partial pressure without the co-reactant requirement and its independence of the co-reactant partial pressures indicate that the lattice oxygen (O_O^x) is replenished by a sufficiently rapid reaction of the partially reduced state with the

oxygen containing molecules in CH_3OH. The unchanged state of material was also confirmed by the calculation of oxygen balance during reactions and TPO after reactions.

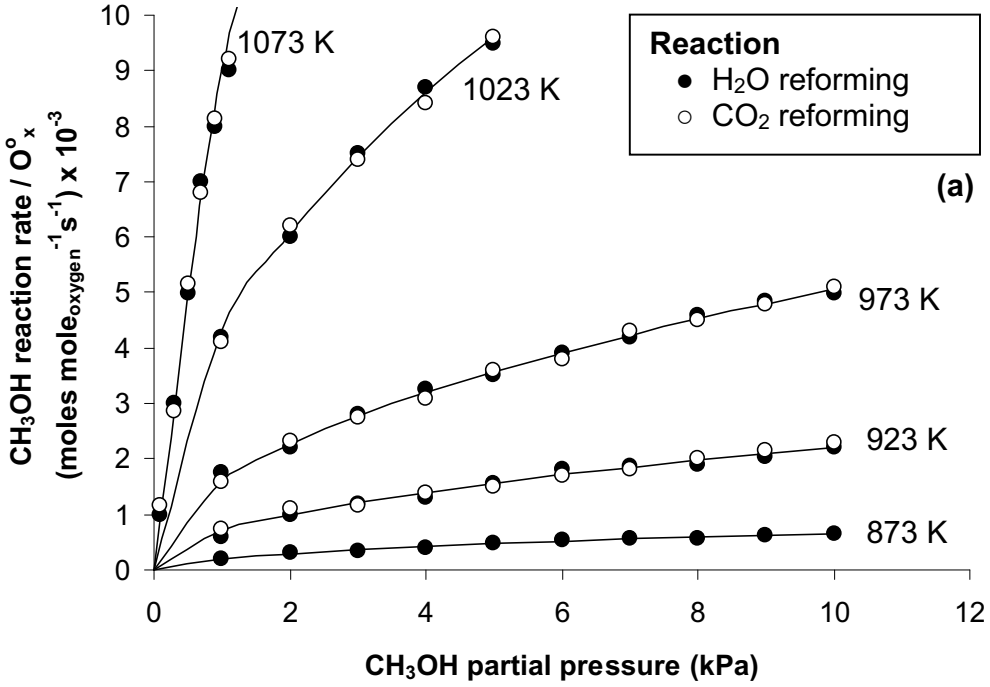

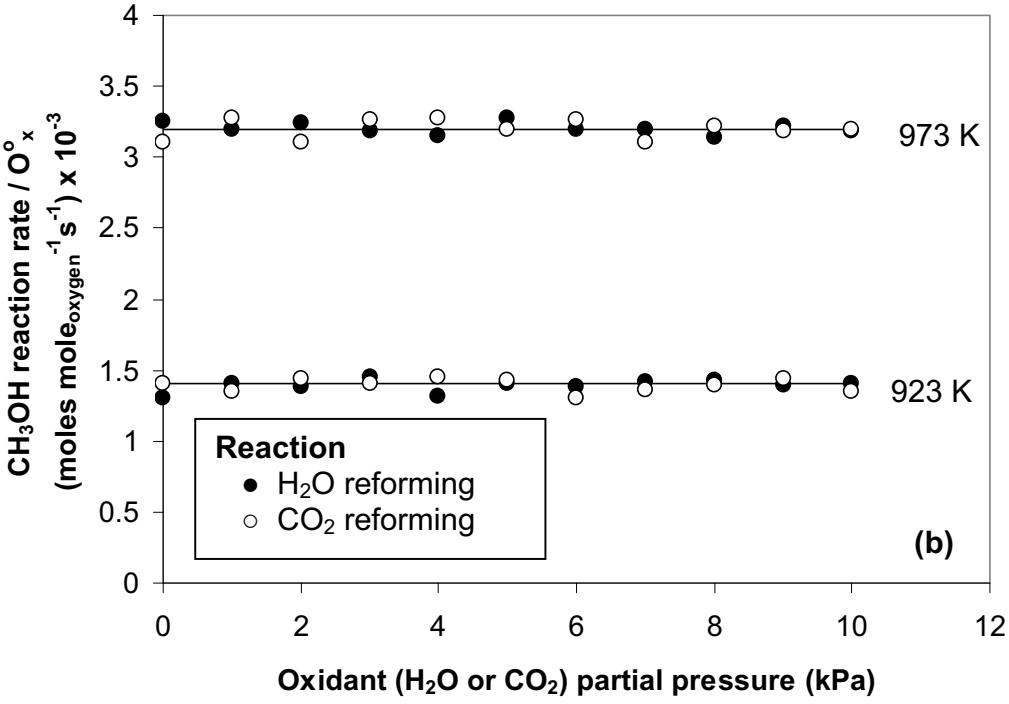

Fig. 9 Effects of CH_3OH partial pressure (a) and co-reactant partial pressure (b) on CH_3OH reaction rate (per moles of oxygen stored) over Ce-ZrO_2 (HSA).

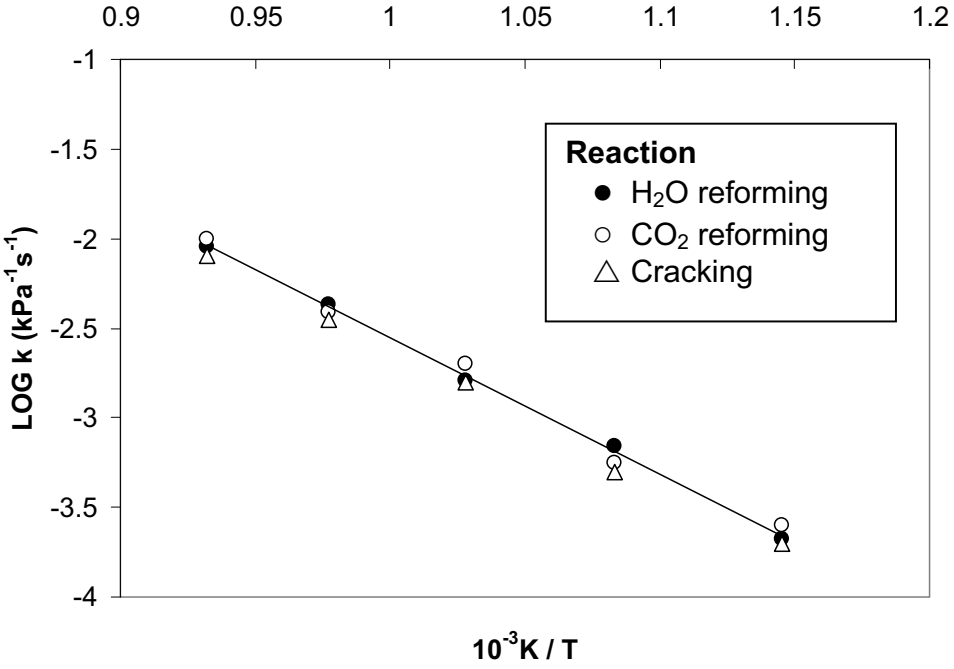

Fig. 10 Arrhenius plots for H_2O reforming, CO_2 reforming and cracking of CH_3OH over Ce-ZrO_2 (HSA).

The capability to decompose CH_3OH without the requirement of steam is the great advantage of ceria-based materials for applying in SOFC system. Without the presence of steam being required, the consideration of water management in SOFC system is negligible and it is expected to simplify the overall SOFC system design, making SOFC more attractive to be used commercially. It should also be noted according to our previous report that high surface area ceria-based catalysts also have the capability to reform C_2H_5OH with and without the presence of steam [42]. However, the operating conditions i.e. temperature, inlet C_2H_5OH partial pressure, and the space velocity are important parameters that must be carefully controlled, as C_2H_5OH have higher potential to form carbon species during the reforming reaction than CH_3OH and CH_4.

1.3.5 Reactivity toward the high hydrocarbons (C_2H_4, C_2H_6, and C_3H_8) reforming

We again report here details only on Ce-ZrO_2 (HSA) sample, as the kinetic dependencies for these hydrocarbons were identical for all ceria-based materials. The feed was hydrocarbon (either C_2H_4, C_2H_6, or C_3H_8) and co-reactant (either H_2O or CO_2) in He. Catalyst reactivity and the product selectivities are given in Table 5. At 923 K, the main products from the reforming reactions were CH_4, H_2 CO, and CO_2. The formation of C_2H_4 was also observed toward the reforming of C_3H_8 and C_2H_6. From the studies, H_2 and CO selectivities increased with increasing temperature, whereas CO_2 and C_2H_4 selectivities decreased. The dependence of CH_4 selectivity on the operating temperature was non-monotonic; maximum CH_4 production occurred at approximately 1073 K. The decreasing in CH_4 and C_2H_4 selectivities at higher temperature could be due to the further reforming to generate more CO and H_2. From the TPO testing, the amount of carbon deposited decreased with increasing inlet co-reactant concentration. At H_2O/hydrocarbons molar ratio higher than 3.0 and CO_2/hydrocarbons molar ratio higher than 5.0, no carbon formation was detected on the surface of Ce-ZrO_2 (HSA).

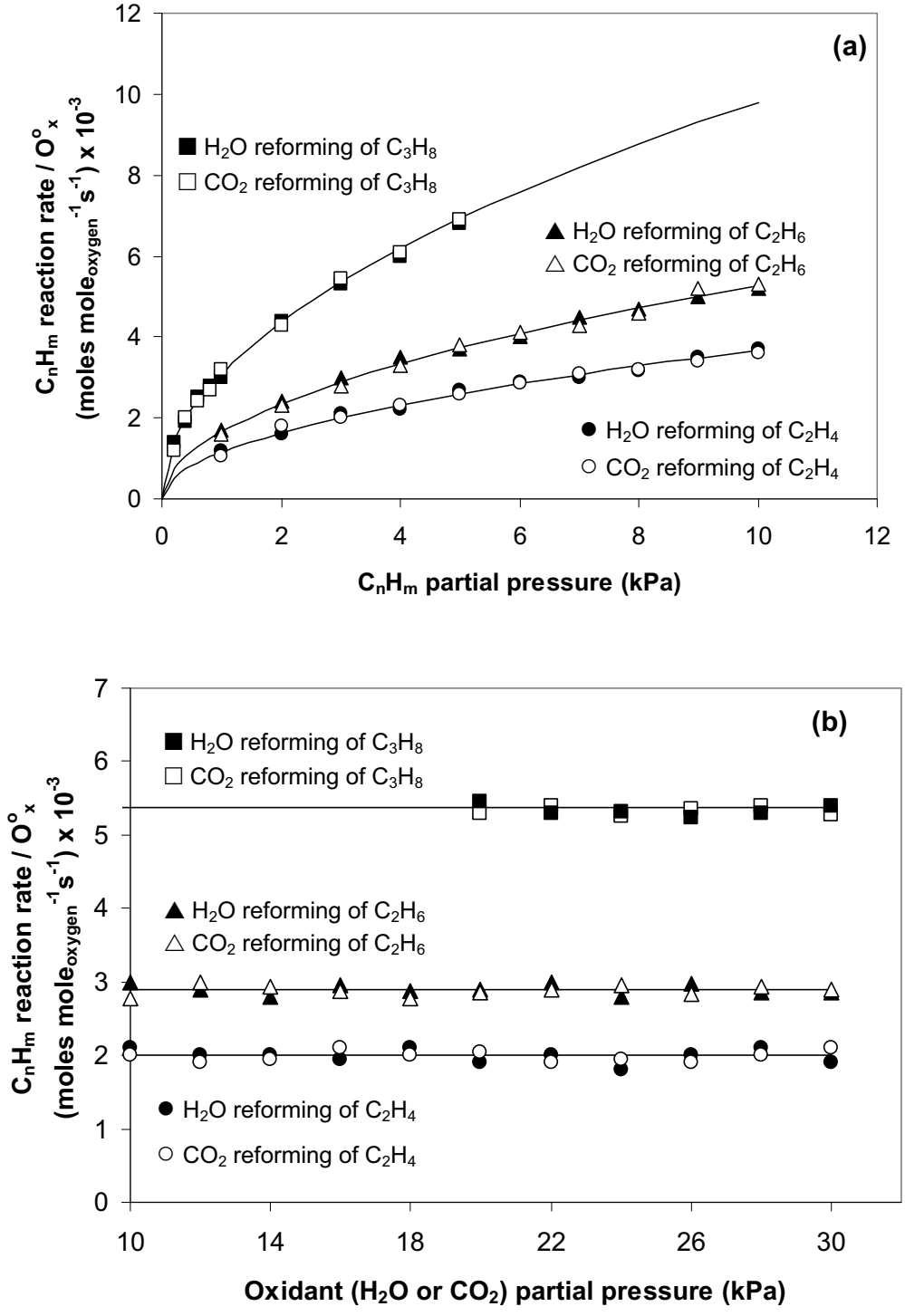

Fig. 11 Effects of C_nH_m partial pressures (a) and co-reactant partial pressure (b) on C_nH_m reaction rate (per moles of oxygen stored) over Ce-ZrO_2 (HSA) at 923 K.

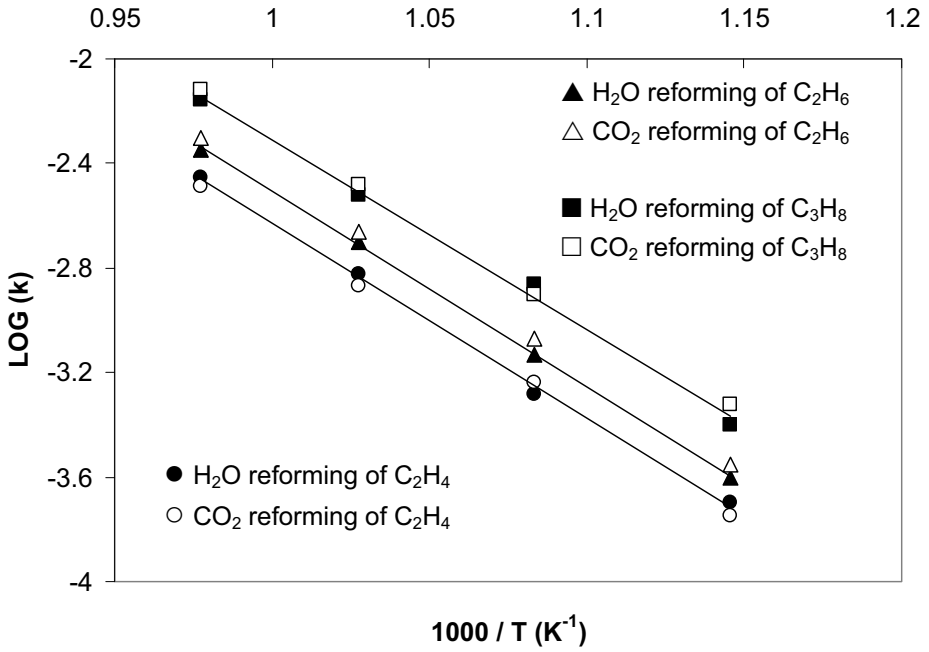

Fig. 12 Arrhenius plots for H_2O and CO_2 reforming of C_nH_m over Ce-ZrO_2 (HSA).

The influences of inlet component partial pressures on the turnover rate were then studied under the operating conditions without detectable carbon formation by changing the inlet hydrocarbon and co-reactant partial pressures as represented in Fig. 11a and 11b. Similar trends as CH_4 and CH_3OH reforming were observed. The reforming rate was proportional to the hydrocarbons concentration with the reaction orders in all hydrocarbons between 0.53-0.55. The turnover rate was independent of inlet H_2O and CO_2 partial pressures, but it was inhibited by the presence of H_2 and CO in the feed. Fig. 12 shows the Arrhenius plots for both H_2O and CO_2 reforming of C_nH_m over Ce-ZrO_2 (HSA). The observed activation energies for these C_nH_m reactions were in the same range as achieved from the CH_4 and CH_3OH reactions (145-152 kJ mol^{-1}). Therefore, it can also be summarized that the mechanisms for H_2O and CO_2 reforming of high hydrocarbon are almost similar to those of CH_4 except that the adsorptions of these hydrocarbon elements (Eqs. 32-34) are applied instead of the CH_4 adsorption. In addition, the reforming of high

hydrocarbons requires considerably higher content of co-reactant at the feed in order to operate properly without the problem of carbon deposition.

$$C_3H_8 + 2* \rightarrow 2(CH_3*) + CH_2* \quad (32)$$

$$C_2H_6 + 2* \rightarrow 2CH_3* \quad (33)$$

$$C_2H_4 + 2* \rightarrow 2CH_2* \quad (34)$$

The capability to reform high hydrocarbon compounds with excellent resistance toward carbon deposition is another great benefit of ceria-based catalysts. Currently, natural gas and liquid petroleum gas (LPG) are the most promising primary fuels for the production of H_2 via reforming process. In order to reform these fuels, either an external pre-reforming unit or expensive noble metal catalysts (i.e. Rh) is normally required. By applying high surface area ceria-based materials as the reforming catalyst, all hydrocarbon elements can be reformed properly without the problem of carbon deposition eliminating the requirements of these costly processes.

1.3.6 Kinetic dependencies of CH_4 reaction rate on partial pressures of reactants and products over Rh supported on ZrO_2 and Ce-ZrO_2 (HSA)

The kinetic dependencies of CH_4 reforming with H_2O and CO_2 over Rh supported on Ce-ZrO_2 (HSA) were studied and compared to Rh supported on conventional ZrO_2 at 973-1073 K. All measurements were carried out under the operating conditions without detectable carbon formation. It should be noted according to the XRF and volumetric H_2 chemisorption measurements that the % Rh loading for both catalysts were approximately 1.0 and the % Rh dispersion for Rh/Ce-ZrO_2 (HSA) was 32.4% whereas that for Rh/ZrO_2 was 29.2%. In addition, according to the CO oxidation testing, the CO turnover rates on fresh catalysts were similar to those measured after exposure in H_2O and CO_2 reforming of CH_4 (4.38 ±0.11 moles $mole_{Rh}^{-1}s^{-1}$ for Rh/ZrO_2 and 5.01 ±0.09 moles $mole_{Rh}^{-1}s^{-1}$ for Rh/Ce-ZrO_2), indicating that Rh surface sites were not changed by sintering or carbon species blockage.

The turnover rate increased linearly with increasing CH_4 partial pressures and operating temperature for both catalysts. The first-reaction order in CH_4 for Rh/ZrO_2, independent of the operating temperature and other component partial pressures (H_2O, CO_2, H_2, and CO), was always observed, Fig. 13. By varying H_2O and CO_2 partial pressures and by adding either H_2 or CO at the feed, it was found that the rates were not affected by these components (Fig. 14); thus, the reaction orders in H_2O, CO_2, H_2, and CO were zero. These results are in good agreement with the work from J. Wei and E. Iglesia [41], who studied the kinetics of CH_4 reforming over Rh/Al_2O_3 and Rh/ZrO_2.

According to the kinetic dependencies for $Rh/Ce\text{-}ZrO_2$ (HSA), the first-order in CH_4 and zero-orders in H_2O, CO_2, H_2, and CO were also observed at 973 K. Nevertheless, with increasing the reaction temperature, significant deviation from the above results occurred. At 1073 K, the observed reaction order in CH_4 for this catalyst shifted to 0.90, whereas the reaction orders in H_2 and CO altered to negative fraction values between -0.15 to -0.08 (Figs. 13 and 14). Apparently, these deviations are due to the reforming reactivity of $Ce\text{-}ZrO_2$ support at high temperature, which affects on the actual inlet component concentrations that adsorbed and reacted on the Rh active sites.

We eliminated the influence of $Ce\text{-}ZrO_2$ on the net CH_4 turnover rate by applying the rate expression in Eq. 26 and also the approach to equilibrium for WGS reaction (η_{WGS}) in the turnover rate calculations and estimated the actual reactant concentrations adsorbed and reacted on the active surface sites of Rh metal. By eliminated the effect of ceria-based support reactivity, the approximate first-order in CH_4 and zero-orders in H_2O, CO_2, H_2, and CO were achieved. We therefore concluded here from the kinetic studies of methane reforming over supported catalysts that the reforming reactivity of the support must be carefully concerned.

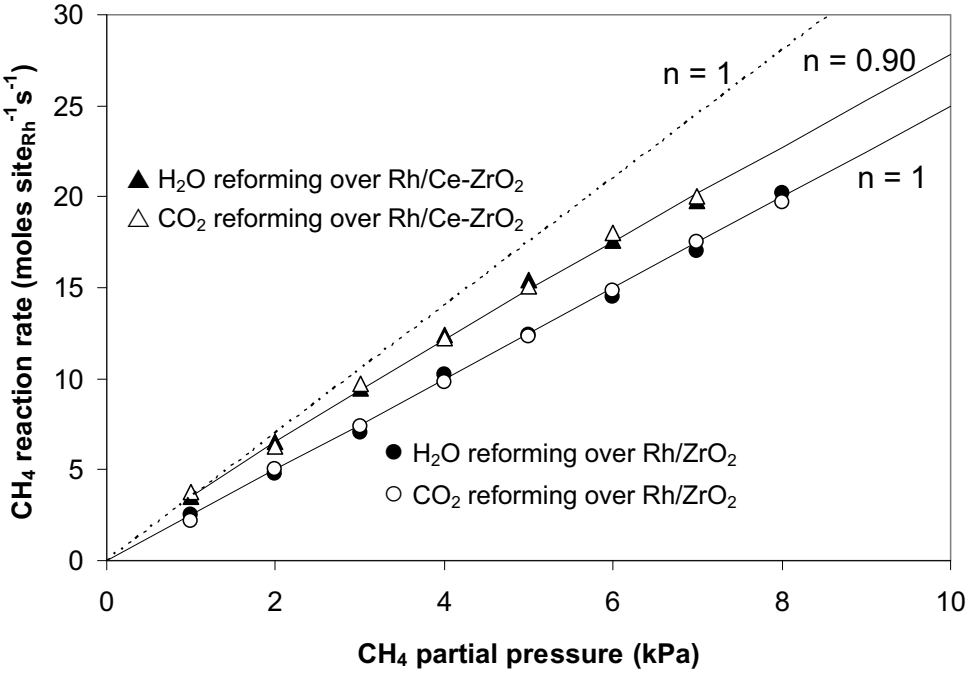

Fig. 13 Effect of CH_4 partial pressure on CH_4 reaction rate over different catalysts and different reactions at 1073 K.

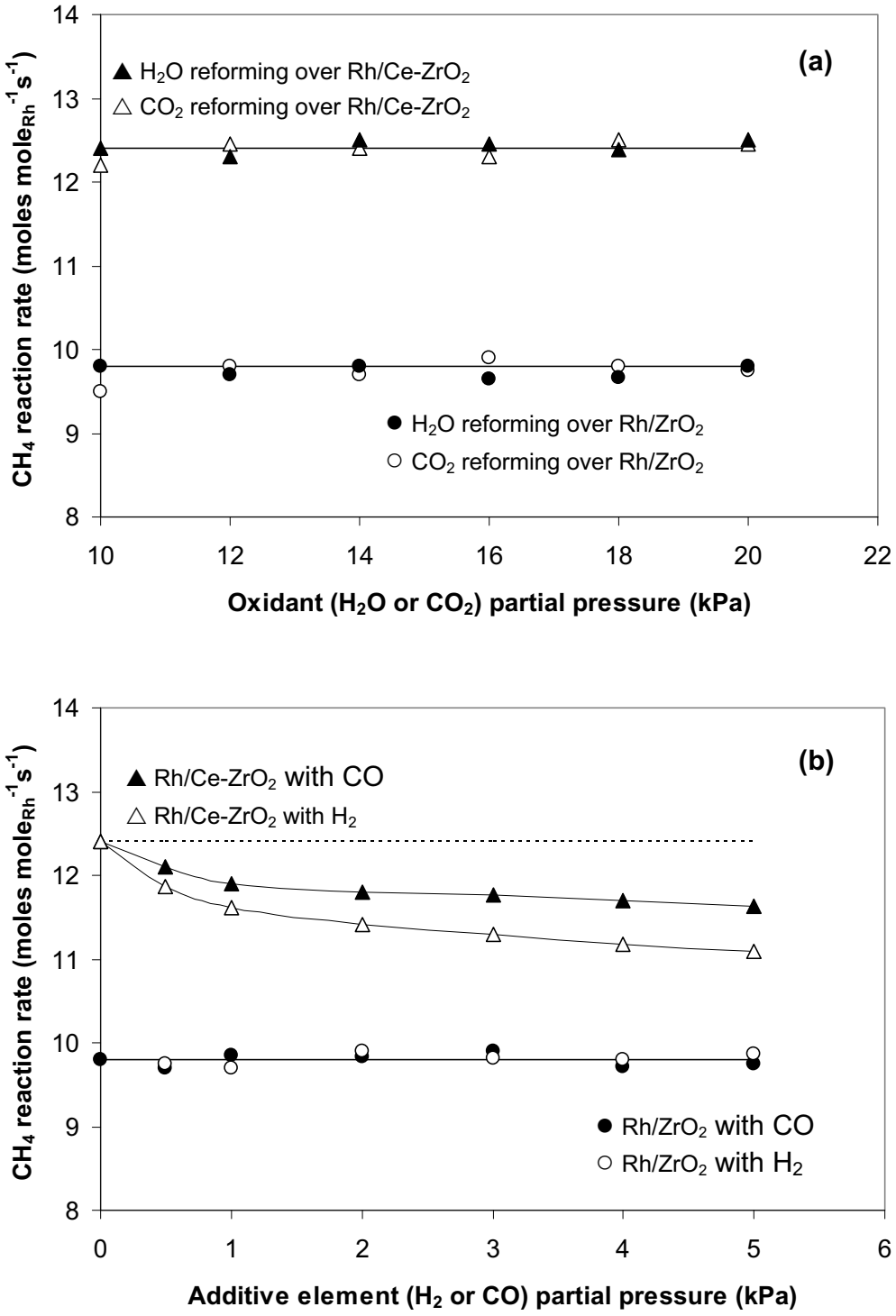

Fig. 14 Effects of co-reactant (a) and additive element (b) on CH_4 reaction rate over different catalysts and different reactions (at 1073 K with 4 kPa CH_4 balance in He).

Table 1 Specific surface areas of ceria-based materials before and after calcination at 1173 K.

Catalysts	Surface area after drying ($m^2\ g^{-1}$)	Surface area after calcination ($m^2\ g^{-1}$)
CeO_2 (HSA)	105	29
Ce-ZrO_2 (HSA) (Ce/Zr=1/3)	135	49
Ce-ZrO_2 (HSA) (Ce/Zr=1/1)	120	47
Ce-ZrO_2 (HSA) (Ce/Zr=3/1)	115	46.5
CeO_2 (LSA)	55	11
Ce-ZrO_2 (LSA) (Ce/Zr=1/3)	82	22
Ce-ZrO_2 (LSA) (Ce/Zr=1/1)	74	20.5
Ce-ZrO_2 (LSA) (Ce/Zr=3/1)	70	20

Table 2 Results of TPR-1, TPO, TPR-2 analyses of ceria-based materials after calcination.

Catalyst	Total H_2 Uptake from TPR-1 ($\mu mol/g_{cat}$)	Total O_2 Uptake from TPO ($\mu mol/g_{cat}$)	Total H_2 Uptake from TPR-2 ($\mu mol/g_{cat}$)
CeO_2 (HSA)	4105	2067	4109
Ce-ZrO_2 (HSA) (Ce/Zr=1/3)	2899	1475	2876
Ce-ZrO_2 (HSA) (Ce/Zr=1/1)	3701	1862	3694
Ce-ZrO_2 (HSA) (Ce/Zr=3/1)	5247	2640	5250
CeO_2 (LSA)	1794	898	1788
Ce-ZrO_2 (LSA) (Ce/Zr=1/3)	1097	553	1085
Ce-ZrO_2 (LSA) (Ce/Zr=1/1)	1745	744	1746
Ce-ZrO_2 (LSA) (Ce/Zr=3/1)	2649	1328	2643

Table 3 CH_4 reaction rate, rate constant and activation energies for CH_4 reactions on ceria-based materials (1048 K, 10 kPa CH_4 balance in He).

Catalysts	Reaction	CH_4 reaction rate / O^o_x (moles $mole_{oxygen}^{-1}s^{-1}$) x 10^{-3}	Rate constant ($s^{-1}kPa^{-1}$) x 10^{-3}	Activation energy (kJ mol^{-1})
CeO_2 (HSA)	H_2O reforming	1.96	0.53	154.2
	CO_2 reforming	1.98	0.55	155.0
	Cracking	1.95[a]	0.53	151.8
Ce-ZrO_2 (HSA)	H_2O reforming	1.97	0.54	154.2
	CO_2 reforming	1.95	0.52	153.4
	Cracking	1.94	0.55	150.9
CeO_2 (LSA)	H_2O reforming	1.96	0.56	154.9
	CO_2 reforming	1.95	0.54	152.1
	Cracking	1.96	0.57	154.3
Ce-ZrO_2 (LSA)	H_2O reforming	1.95	0.56	155.2
	CO_2 reforming	1.94	0.55	154.4
	Cracking	1.97	0.55	153.2

[a] Initial CH_4 reaction rate

Table 4

Reaction rate and fraction of by-products from the H_2O reforming of CH_3OH on Ce-ZrO_2 (HSA) at several temperature and various inlet H_2O/CH_3OH ratios (3 kPa CH_3OH balance in He).

Temperature (K)	H_2O/CH_3OH ratio	CH_3OH reaction rate / O^o_x (moles $mole_{oxygen}^{-1}s^{-1}$) x 10^{-3}	Yield of H_2 production (%)	Fraction of by-products (%)		
				CO	CO_2	CH_4
923	0.0	1.21	24.5	46.6	17.5	35.9
973	0.0	2.77	34.9	68.1	16.7	15.2
1023	0.0	7.45	42.8	85.1	14.9	0
1023	1.0	7.44	44.1	77.2	22.8	0
1023	2.0	7.46	45.9	70.3	29.7	0
1023	3.0	7.42	47.7	64.2	35.8	0

Table 5

Reaction rate and fraction of by-products from the H_2O and CO_2 reforming of C_nH_m on Ce-ZrO_2 (HSA) (923 K, 3 kPa C_nH_m and 15 kPa co-reactant, balance in He).

Reactant	Co-reactant	C_nH_m Reaction rate / O^o_x	Yield of H_2 production (%)	Fraction of by-products (%)				Activation energy (kJ mol^{-1})
				C_2H_4	CH_4	CO	CO_2	
C_2H_4	H_2O	2.04[a]	26.7	-	40	48.2	11.8	150.4
	CO_2	2.10	15.5					151.9
C_2H_6	H_2O	2.85	29.9	9.3	28.6	49.2	12.9	148.6
	CO_2	2.78	18.4					147.5
C_3H_8	H_2O	5.39	34.3	18.6	20.3	48.5	12.6	145.0
	CO_2	5.44	22.1					149.7

[a] (moles $mole_{oxygen}^{-1} s^{-1}$) x 10^{-3}

1.4. Conclusion

High surface area CeO_2 and Ce-ZrO_2 provided higher CH_4, C_2H_4, C_2H_6, C_3H_8 and CH_3OH reforming rates with greater resistance toward carbon deposition than conventional Ce-ZrO_2 and CeO_2. The turnover rates per amount of oxygen stored (moles mol_{Oxygen}^{-1} s^{-1}) on the surface of all ceria sample were in the same range indicating the linear influence of OSC on the turnover rates. The kinetic dependencies of hydrocarbon conversions and the activation energies over these ceria-based materials were unaffected by the material specific surface area, doping element, degree of OSC and reactions (i.e. H_2O reforming and CO_2 reforming). The turnover rates were proportional to these hydrocarbon partial pressures (with positive fraction reaction order); independent of co-reactant partial pressures; but inhibited by the presences of CO and H_2. A set of unifying redox mechanistic proposal, in which the sole relevant elementary step is the reaction of intermediate surface hydrocarbon species with the lattice oxygen (O^o_x) and that oxygen is

efficiently replenished by a rapid surface reaction with oxygen source in the system, was applied to explain these observed kinetic dependencies.

The capabilities to decompose oxyhydrocarbons without the requirement of steam and reform high hydrocarbon compounds with excellent resistance toward carbon deposition are the great benefit of ceria-based catalysts particularly for applying in SOFC system. Without the presence of steam being required, the consideration of water management in SOFC system is negligible, while the capability to reform high hydrocarbon compounds with excellent resistance toward carbon deposition eliminates the requirement of expensive noble metal catalysts or the installation of external pre-reformer. These benefits simplify the overall SOFC system design, making SOFC more attractive to be used commercially.

Lastly, we indicated that the kinetic dependencies of CH_4 reforming over metal catalysts on ceria-based supports at such a high temperature must be carefully studied, as the reforming reactivity of ceria supports can result in the deviation of the actual component concentrations absorbed and reacted on the surface sites of metal catalyst.

1.5 References

[1] A. Trovarelli., Catal. Rev.-Sci. Eng., 38 (1996), 439.

[2] P. Fornasiero, G. Balducci, R.D. Monte, J. Kaspar, V. Sergo, G. Gubitosa, A. Ferrero and M. Graziani., J. Catal., 164 (1996), 173.

[3] T. Miki, T. Ogawa, M. Haneda, N. Kakuta, A. Ueno, S. Tateishi, S. Matsuura and M. Sato, J. Phys. Chem., 94 (1990), 339.

[4] C. Padeste, N.W. Cant and D.L. Trimm, Catal. Lett., 18 (1993), 305.

[5] S. Kacimi, J. Barbier Jr., R. Taha and D. Duperz, Catal. Lett., 22 (1993), 343.

[6] G.S. Zafiris and R.J. Gorte, J. Catal., 143 (1993), 86.

[7] G.S. Zafiris and R.J. Gorte, J. Catal., 139 (1993), 561.

[8] S. Imamura, M. Shono, N. Okamoto, R. Hamada and S. Ishida, Appl. Catal. A, 142 (1996), 279.

[9] E. Ramírez-Cabrera, A. Atkinson and D. Chadwick, Appl. Catal. B, 36 (2002), 193.

[10] E. Ramírez-Cabrera, N. Laosiripojana, A. Atkinson and D. Chadwick, Catal. Today, 78 (2003), 433.

[11] R.J. Gorte, J.M. Vohs and S. McIntosh, Solid State Ionics, 175(1-4) (2004), 1.

[12] S. Jung, C. Lu, H. He, K. Ahn, R.J. Gorte and J.M. Vohs, Journal of Power Sources, (2005), In Press

[13] T. Kim, G. Liu, M. Boaro, S.-I. Lee, J.M. Vohs, R.J. Gorte, O.H. Al-Madhi and B.O. Dabbousi, Journal of Power Sources, (2005), In Press

[14] O. Costa-Nunes, R.J. Gorte and J.M. Vohs, Journal of Power Sources, 141(2), (2005), 241.

[15] S. An, Lu C., W.L. Worrell, R.J. Gorte and J.M. Vohs, Solid State Ionics, 175(1-4), (2004), 135.

[16] D.J.L. Brett, A. Atkinson, D. Cumming, E. Ramírez-Cabrera, R. Rudkin and N.P. Brandon, Chem. Eng. Sci., 60 (21), (2005), 5649.

[17] K. Otsuka, M. Hatano and A. Morikawa, J. Catal. 79 (1983), 493.

[18] K. Otsuka, M. Hatano and A. Morikawa, Inorganica Chimica Acta, (1985) 109, 193.

[19] P.J. Gellings and H.J.M. Bouwmeester, Catal. Today 58 (2000), 1.

[20] D. Terribile, A. Trovarelli, J. Llorca, C. Leitenburg and G. Dolcetti, J. Catal., 178 (1998), 299.

[21] E. Abi-aad, R. Bechara, J. Grimblot and A. Aboukaïs, Chem. Mater., 5 (1993), 793.

[22] L. A. Bruce, M. Hoang, A. E. Hughes and T. W. Turney., Appl. Catal. A, 134 (1996), 351.

[23] P.L. Chen and I.W. Chen., J. Amer. Ceram. Soc., 76 (1993), 1577.

[24] H. K. Varma, P. Mukundam, K. G. K. Warrier and A. D. Damodaran., J. Mater. Sci. Lett., 10 (1991), 666.

[25] M. Hirano and E. Kato., J. Amer. Ceram. Soc., 79 (1996), 777.

[26] M. Vallet-Regi, F. Conde, S. Nicolopoulos, C. V. Ragel and J. M. Gonzales-Calbet., Material Science Forum, 235–238 (1997), 291.

[27] A. Tschöpe and J. Y. Ying. NanoStruct. Mater., 4 (1994), 617.

[28] M. Pijolat, J. P. Viricelle and M. Soustelle., Stud. Surf. Sci. Catal., 91 (1995), 885.

[29] T. Masui, K. Fujiwara, K. Machida, G. Adachi, T. Sakata and H. Mori., Chem. Mater., 9 (1997), 2197.

[30] Y. Zhou, R. J. Phillips and J. A. Switzer., J. Amer. Ceram. Soc., 78 (1995), 981.

[31] V. Perrichon, A. Laachir, S. Abouarnadasse, O. Touret and G. Blanchard., Appl. Catal. A, 129 (1995), 69.

[32] D. Terribile, A. Trovarelli, J. Llorca, C. Leitenburg and G. Dolcetti, Catal. Today, 43 (1998), 79-88.

[33] M. Ozawa, M. Kimura, A. Isogai, J. Alloys Comp., 193 (1993) 73.

[34] G. Balducci, J. Kaspar, P. Fornasiero, M. Graziani, M.S. Islam, J. Phys. Chem. B, 102 (1998) 557.

[35] G. Vlaic, P. Fornasiero, S. Geremia, J. Kaspar, M. Graziani, J. Catal., 168 (1997) 386.

[36] G.R. Rao, J. Kaspar, S. Meriani, R. Dimonte, M. Graziani, Catal. Lett., 24 (1994) 107.

[37] P. Fornasiero, R. Dimonte, G.R. Rao, J. Kaspar, S. Meriani, A. Trovarelli, M. Graziani, J. Catal., 151 (1995) 168.

[38] M.H. Yao, T.E. Hoost, R.J. Baird, F.W. Kunz, J. Catal., 166 (1997) 67.

[39] D. Kim, J. Am. Ceram. Soc., 72 (1989) 1415.

[40] C. Force, A. Ruiz Paniego, J.M. Guil, J.M. Gatica, C. Lopez-Cartes, S. Bernal, J. Sanz, Langmuir, 17 (2001), 2720.

[41] J. Wei and E. Iglesia, J. Catal, 225 (2004), 116.

[42] N. Laosiripojana, W. Sutthisripok, S. Assabumrungrat, Chem. Eng. J., (2006), In Press

[43] Y. Lwin, W.R.W. Daud, A.B. Mohamad and Z. Yaakob, Int. J. Hydrogen Energy, 25(1) (2000), 47.

[44] J.N. Amor, Appl. Catal. A, 176 (1999), 159.

RESEARCH II

Catalytic steam reforming of methane, methanol, and ethanol over Ni/YSZ: the possible use of these fuels in internal reforming SOFC

This study investigated the possible use of methane, methanol, and ethanol with steam as a direct feed to Ni/YSZ anode of a direct internal reforming Solid Oxide Fuel Cell (DIR-SOFC). It was found that methane with appropriate steam content can be directly fed to Ni/YSZ anode without the problem of carbon formation, while methanol can also be introduced at a temperature as high as 1000°C. In contrast, ethanol can not be used as the direct fuel for DIR-SOFC operation even at high steam content and high operating temperature due to the easy degradation of Ni/YSZ by carbon deposition. From the steam reforming of ethanol over Ni/YSZ, significant amounts of ethane and ethylene were present in the product gas due to the incomplete reforming of ethanol. These formations are the major reason for the high rate of carbon formation as these components act as very strong promoters for carbon formation.

It was further observed that ethanol with steam can be used for an indirect internal reforming operation (IIR-SOFC) instead. When ethanol was first reformed by Ni/Ce-ZrO_2 at the temperature above 850°C, the product gas can be fed to Ni/YSZ without the problem of carbon formation. Finally, it was also proposed from the present work that methanol with steam can be efficiently fed to Ni/YSZ anode (as DIR operation) at the temperature between 900-975°C without the problem of carbon formation when SOFC system has sufficient space volume at the entrance of the anode chamber, where methanol can homogeneously convert to CH_4, CO, CO_2, and H_2 before reaching SOFC anode.

2.1. Introduction

Solid Oxide Fuel cell (SOFC) is an electrochemical energy conversion unit that converts chemical energy to electrical energy and heat with greater energy efficiency and lower pollutant emission than combustion process [1]. This type of

fuel cell is expected to apply in power applications i.e. for power plant (300 MWel) or as combined heat and power generation [1, 2]. SOFC is also being investigated for using as an auxiliary power unit (APU) in mobile applications and as a portable system [1].

It is well established that hydrogen and carbon monoxide can be typically used as the fuels for SOFC. Furthermore, as SOFC is generally operated at such a high temperature (700-1100°C), it is known that some hydrocarbons (i.e. methane) can also be directly used as fuels instead of hydrogen and carbon monoxide by feeding straight to the anode side of SOFC; this operation is called a direct internal reforming SOFC (DIR-SOFC). According to this operation, the hydrocarbon fuels are reformed at the anode producing hydrogen and carbon monoxide, which are electrochemically consumed for generating electricity simultaneously. The advantage of DIR-SOFC is that the hydrogen consumption by the electrochemical reaction could directly promote the reforming or conversion of hydrocarbons at the anode side. Therefore, DIR-SOFC results in high conversion and high efficiency [3].

DIR-SOFC operation requires an anode material that has good catalytic reforming and electrochemical reactivities. Ni/YSZ is the most common SOFC anode material due to its cost effective compared with other supported metals (e.g. Co, Pt, Ru, and Rh) and also well fitting with fuel cell design requirements. In addition, this material also provides catalytic reforming activity, which is beneficial for the DIR-SOFC operation. The nickel content for Ni/YSZ anode is usually 40 to 60% in order to match the thermal expansion of YSZ [4]. Some previous researchers have investigated the performance of DIR-SOFC operation fueled by methane. Yentekakis et al. [5] investigated the effect of steam on methane steam reforming rate over nickel-yttria stabilized zirconia cermets (Ni/YSZ) in the temperature range from 800 to 930ºC by varying the ratio of H_2O/CH_4 from 0.15 to 2.0. The experiment indicated the strong influence of steam on the reforming rate, which could be due to the steam deficiency. In contrast, Achenbach and Riensche [6] reported no influence of inlet steam partial pressure on the methane steam reforming rate over nickel cermet (20 wt% Ni and 80 wt% ZrO_2) at 700-940ºC with the inlet H_2O/CH_4 ratio from 2.6 to 8.0. Dicks et al. [7] observed that the dependence of methane steam reforming rate over Ni/ZrO_2 anode was a function of both temperature and gas compositions. They also reported that the steam reforming of methane over nickel/zirconia exhibited non-

Arrhenius behavior in the temperature range of 700-1000ºC. It should be noted that most of the previous works on DIR-SOFC have concluded that the major difficulty of DIR-SOFC operation over Ni/YSZ is the possible formation of carbon species on the surface of Ni due to cracking of hydrocarbons. This formation could obstruct gas access and degrade anode performance by blocking the catalyst active sites resulting in the loss of cell performance and poor durability.

Another alternative internal reforming operation is an indirect internal reforming (IIR-SOFC). By this operation, the reforming reaction takes place at the reformer, which is in close thermal contact with the anode side of SOFC. IIR-SOFC gives the advantage of good heat transfer between the reformer and the fuel cell and is expected to provide an autothermal operation. In addition, unlike DIR-SOFC, the reformer part and the anode side for IIR-SOFC operation are operated separately. Therefore, the catalyst for reforming reaction at the reformer part and the material for electrochemical reactions at the anode side of fuel cell can be optimized individually preventing the possible degradation of anode from the carbon deposition.

Focusing on the fuel selection, currently, methane is the major fuel for SOFC due to its well-developed and cost effective. Nevertheless, the use of alcohols (i.e. methanol and ethanol) should be also possible when operated as an internal or in-stack reforming. Methanol is favorable due to its ready availability, high-specific energy and storage transportation convenience [8, 9], while ethanol is also a promising candidate, since it is readily produced from renewable resources (e.g., fermentation of biomasses) and has reasonably high hydrogen content [10, 11]. Douvartzides et al. [12] applied a thermodynamic analysis to evaluate the feasibility of different fuels, i.e., methane, methanol, and ethanol for SOFC. The results obtained in terms of electromotive force output and efficiency show that ethanol and methanol are very promising alternatives to hydrogen.

In the present work, the first approach was to study the possible uses of alcohols (i.e. methanol and ethanol) as the fuels for DIR-SOFC by feeding these fuels as well as steam over Ni/YSZ. The reforming activity as well as the effects of fuel type, the fuel/steam ratio, and operating temperature on the degradation of Ni/YSZ by carbon deposition were determined. It should be noted that methane was also used as the feed in the present work for comparison. Secondly, in order to study the possible use of these fuels for IIR-SOFC operation, an annular ceramic reactor was designed

and constructed. Details of this reactor configuration will be described in Section 2.1. Each fuel (i.e. methane, methanol, and ethanol) was fed into this annular reactor together with steam at several operating conditions, and the degradation of Ni/YSZ by carbon deposition was then investigated. Finally, the suitable operation (DIR or IIR) and conditions (the fuel/steam ratio, and operating temperature) of each fuel for SOFC were then determined.

2.2. Experimental

2.2.1 Annular reactor configuration

An annular ceramic reactor was constructed in order to study the use of hydrocarbon fuels for IIR operation, Fig. 1. According to the design, the reforming catalyst (Ni/Ce-ZrO_2) was packed at the inner side of the annular reactor, where the inlet gas was firstly introduced. At the end of the inner tube, all gas components flowed backward through the outer side of this annular reactor, where 300 mg of Ni/YSZ (with SiC) was packed. Therefore, both Ni/Ce-ZrO_2 and Ni/YSZ are operated at the same operating temperature. The main obligation of Ni/Ce-ZrO_2 is to reform all hydrocarbons before reaching the surface of Ni/YSZ preventing the degradation of Ni/YSZ by the carbon formation. It should be noted that Ni/Ce-ZrO_2 was selected as the reforming catalyst because the excellent reforming reactivity of this catalyst was reported recently [13].

2.2.2. Material preparation and characterization

$Ce_{0.75}Zr_{0.25}O_2$ support was prepared by co-precipitation of cerium nitrate ($Ce(NO_3)_3 \cdot H_2O$), and zirconium oxychloride ($ZrOCl_2 \cdot H_2O$) (from Aldrich). The molar ratio of ([Ce])/[cetyltrimethylammonium bromide] was kept constant at 0.8. It should be noted that aqueous solution of 0.1 M cetyltrimethylammonium bromide solution (from Aldrich), was also added in the cerium nitrate and zirconium oxychloride solution as a cationic surfactant. Our previous work reported that the preparation of ceria-based material by this surfactant-assisted method can achieve the high surface area and high thermal stability material due to the incorporation of surfactants during preparation, which reduces the interfacial energy and eventually decreases the surface tension of water contained in the pores [14-16]. The starting solution was prepared by

mixing 0.1 M of metal salt solution with 0.4 M of urea at a 2 to 1 volumetric ratio. This solution was stirred by magnetic stirring (100 rpm) for 3 h, and the precipitate was filtered and washed with deionised water and ethanol to prevent an agglomeration of the particles. It was dried overnight in an oven at 110°C, and then calcined in air at 1000°C for 6 h. Ni/Ce-ZrO_2 was prepared by impregnating above Ce-ZrO_2 with $Ni(NO_3)_2$ solution (from Aldrich), whereas Ni/YSZ was prepared by mixing NiO (42.86 vol%) with YSZ (57.14 vol%) with a ball milling for 18 h at room temperature. These catalysts were calcined in air at 1000°C for 6 h and then reduced with 10%H_2/Ar for 6 h before use.

After reduction, the catalysts were characterized with several physicochemical methods. The weight content of Ni in Ni/Ce-ZrO_2 and Ni/YSZ was determined by X-ray fluorescence (XRF) analysis. The reducibility and dispersion percentages of nickel were measured from temperature-programmed reduction (TPR) with 5% H_2 in Ar and temperature-programmed desorption (TPD), respectively. All physicochemical properties of the synthesized catalysts are presented in Table 1.

2.2.3. Apparatus and Procedures

An experimental reactor system was constructed as shown elsewhere [13-16]. The feed gases including the components of interest (ethanol, methanol, methane, and steam) and the carrier gas (helium) were introduced to the reaction section, in which either a quartz reactor (for DIR studying) or the annular ceramic reactor (for IIR studying) was mounted vertically inside a furnace. Ni/YSZ (with SiC) was loaded in the quartz reactor, which was packed with a small amount of quartz wool to prevent the catalyst from moving. In the case of the annular reactor, Ni/Ce-ZrO_2 and Ni/YSZ were packed inside the reactor as described in section 2.1. Regarding the results in our previous publications [13-16], to avoid any limitations by intraparticle diffusion, the constant residence time of 5×10^{-4} g min cm^{-3} was applied in all experiments. A Type-K thermocouple was placed into the annular space between the reactor and the furnace. This thermocouple was mounted on the tubular reactor in close contact with the catalyst bed to minimize the temperature difference between the catalyst bed and the thermocouple. Another Type-K thermocouple was inserted in the middle of the quartz tube in order to re-check the possible temperature gradient. The record showed that the maximum temperature fluctuation during the reaction was always ± 0.75°C or

less from the temperature specified for the reaction. After the reactions, the exit gas mixture was transferred via trace-heated lines to the analysis section, which consisted of a Porapak Q column Shimadzu 14B gas chromatograph (GC) and a mass spectrometer (MS).

The effects of temperature, type of fuel, and inlet fuel/steam molar ratios on the amount of carbon formation over catalysts and the product distribution from the steam reforming reaction were studied. In order to study the formation of carbon species on catalyst surface, Temperature programmed Oxidation (TPO) was applied by introducing 10% oxygen in helium, after the catalyst was purged with helium. The operating temperature was increased from 100ºC to 1000ºC at a rate of 20ºC/min. The amount of carbon formations on the surface of catalysts were determined by measuring the CO and CO_2 yields from the TPO results (using Microcal Origin Software) assuming a value of 0.026 nm^2 for the area occupied by a carbon atom in a surface monolayer of the basal plane in graphite [17].

In order to study the steam reforming reactivity, the rate of hydrocarbon reforming was defined in terms of conversion and product distribution. The yield of hydrogen production was calculated by the hydrogen balance, defined as the molar fraction of hydrogen produced to the total hydrogen in the products. Distributions of other by-products (i.e. carbon monoxide, carbon dioxide, methane, ethane, ethylene, and acetaldehyde for ethanol steam reforming) were calculated by the carbon balance, defined as the ratios of the product moles to the consumed moles of hydrocarbon, accounting for stoichiometry. This information was presented in term of (relative) fraction of all by-product components (i.e. carbon monoxide, carbon dioxide, methane, ethane, and ethylene), which are summed to 100%.

2.3. Results and Discussion

2.3.1 Steam reforming over Ni/YSZ

Ni/YSZ was tested for the steam reforming of methane, methanol, and ethanol at 900°C with the inlet fuel/steam molar ratio of 1.0/3.0 (partial pressure of inlet feed of 4 kPa). The reforming rate was measured as a function of time in order to indicate the stability and the deactivation rate. The variations in the yield of hydrogen production with time at 900°C are shown in Fig. 2. Significant deactivations were

detected from the steam reforming of ethanol and methanol, whereas much lower deactivation was observed from the steam reforming of methane. Catalyst stabilities expressed as deactivation percentages as well as the product distributions from the steam reforming over these fuels are given in Table 2. It is clear that hydrogen, carbon monoxide, and carbon dioxide are the main products from the methane steam reforming. In the cases of methanol and ethanol, methane is also produced along with hydrogen, carbon monoxide, and carbon dioxide. In addition, significant amount of ethane and ethylene are also observed from the steam reforming of ethanol. It should be noted that the thermodynamic analysis of these reactions at 900°C were also performed using MATLAB program. At equilibrium condition, the main products from these three reactions are only hydrogen, carbon monoxide, and carbon dioxide. Very few amount of methane (2.8×10^{-4} kPa) was detected from the steam reforming of ethanol, whereas no formation of ethane and ethylene was observed from the calculation. These calculated values are also presented in Table 2 (in the blanket). The deviation of the experimental results from the thermodynamic values particularly for the steam reforming of ethanol (i.e. significant formations of methane, ethane, and ethylene), which have also been observed by several researchers [11, 18-20], are due to several side reactions. For instance, ethane and ethylene can be formed by the dehydration of ethanol (Eq. 1) following with the production of ethane by ethylene hydrogenation (Eq. 2). Simultaneously, methane can be formed by the decomposition and reforming of these ethane and ethylene, methanation [11], and decomposition of ethanol [18].

$$C_2H_5OH \rightarrow C_2H_4 + H_2O \quad (1)$$

$$C_2H_4 + H_2 \rightarrow C_2H_6 \quad (2)$$

According to the catalytic reforming of methanol with steam, the well known reactions involved in this process can be represented by the decomposition-shift mechanism, Eqs. (3)-(5).

$$CH_3OH = 2H_2 + CO \quad \text{(methanol decomposition)} \quad (3)$$

$$CO + H_2O = H_2 + CO_2 \quad \text{(water gas shift reaction)} \quad (4)$$

$$CO + 3H_2 = CH_4 + H_2O \quad \text{(methanation)} \quad (5)$$

Firstly, methanol can be directly converted to hydrogen and carbon monoxide by the decomposition process (Eq. 3). In the presence of steam, the water-gas shift reaction (Eq. 4) takes place to produce carbon dioxide and more hydrogen. Methane can be formed by the methanation reaction (Eq. 5). It should be noted that the formations of higher molecular weight compounds such as formaldehyde, methyl formate and formic acid were not observed from the reaction. This observation is in good agreement with the previous work from Lwin et al. [21].

In order to determine the reason of the deactivation in Fig. 2, the post-reaction temperature-programmed oxidation (TPO) experiments were carried out to investigate the amount of carbon formation on the surface of Ni/YSZ. From the TPO results as shown in Fig. 3, the huge amounts of carbon deposition were observed from the steam reforming of ethanol, whereas much lower carbon formations were detected from the steam reforming of methane. The values of carbon formations (monolayer) on the surface of catalysts were determined by measuring these CO and CO_2 yields (using Microcal Origin Software). Using a value of 0.026 nm^2 for the area occupied by a carbon atom in a surface monolayer of the basal plane in graphite [17], the quantities of carbon deposited for each inlet fuel (i.e. methane, methanol, and ethanol) were observed to be 0.21, 0.37, and 4.29 monolayer respectively.

The formations of ethylene and ethane are the major reason for the high rate of carbon formation from the ethanol steam reforming as these components act as very strong promoters for carbon formation [15]. Eqs. 6-11 below present the most probable reactions that could lead to carbon deposition from the system of the steam reforming of ethanol [15]:

$$C_2H_6 \Leftrightarrow 3H_2 + 2C \quad (6)$$

$$C_2H_4 \Leftrightarrow 2H_2 + 2C \quad (7)$$

$$CH_4 \Leftrightarrow 2H_2 + C \quad (8)$$

$$2CO \Leftrightarrow CO_2 + C \quad (9)$$

$$CO + H_2 \Leftrightarrow H_2O + C \quad (10)$$

$$CO_2 + 2H_2 \Leftrightarrow 2H_2O + C \quad (11)$$

C is the carbonaceous deposits. At low temperature, Eqs. (10-11) are favorable, while Eqs. (6-9) are thermodynamically unflavored [21]. The Boudouard reaction (Eq. 9) and the decomposition of hydrocarbons (Eqs. 6-8) are the major pathways for carbon formation at such a high temperature as they show the largest change in Gibbs energy [22]. According to the range of temperature in this study, carbon formation would be formed via the decomposition of hydrocarbons and Boudouard reactions.

For the steam reforming of methanol and methane, ethane and ethylene do not appear in the reaction products, the potential formation of carbon species on the surface of catalyst arises from the decomposition and Boudouard reactions. Apart from the carbon formation problem, another major cause for the deactivation from methanol steam reforming is due to the oxidation of Ni, as the reducibility of Ni reduced to 82.9% after exposure in the steam reforming conditions for 10 h, regarding to the TPR experiments, Table 3. It should be noted that the oxidation of Ni/YSZ also occurred after exposure in the ethanol steam reforming conditions.

2.3.2 Effects of temperature and fuel/steam ratio on the steam reforming over Ni/YSZ

The influences of operating temperature and the inlet steam content on the amount of carbon formation and product distribution from the steam reforming of these hydrocarbons were studied by varying temperature from 900°C to 1000°C for three different inlet fuel/steam molar ratios (1.0/3.0, 1.0/4.0, and 1.0/5.0). Fig. 4 shows the effect of temperature on the yield of hydrogen production from methanol steam reforming over Ni/YSZ anode, while Tables 4 and 5 summarize the influences of the inlet steam content and temperature on all product distribution and amount of carbon formation.

Clearly, the amount of carbon formation from the steam reforming of methanol and methane significantly decreased with increasing temperature and inlet steam concentration. These are due to the higher reforming reactivity of methane and methanol at high temperature and inlet steam concentration. In addition, it was also observed that the oxidized state of Ni/YSZ from the steam reforming of methanol and ethanol decreased with increasing temperature. In contrast, the amount of carbon formation from the steam reforming of ethanol slightly changed with increasing

temperature and inlet steam concentration. Although the formations of ethane, and ethylene from the steam reforming of ethanol decreased with increasing temperature and inlet steam concentration, significant amount of these hydrocarbons remain observed even at the temperature as high as 1000°C, Table 5.

Considering product distribution from the steam reforming, the yield of hydrogen production and carbon monoxide fraction increased with increasing temperature, whereas carbon dioxide and methane production fraction decreased. Regarding the effect of steam, hydrogen and carbon dioxide fraction increased with increasing inlet steam concentration, whereas carbon monoxide fraction decreased. The yield of methane production reduced at higher temperature. It should be noted that the changes of hydrogen, carbon monoxide, and carbon dioxide are mainly due to the influence of mildly exothermic water-gas shift reaction ($CO + H_2O \rightarrow CO_2 + H_2$), whereas the decrease of methane production is due to the further reforming to carbon monoxide and hydrogen.

2.3.3 Steam reforming with IIR-SOFC configuration

It is clear from the above observation that ethanol can not be used as the inlet fuel for DIR-SOFC operation due to the easy degradation of Ni/YSZ anode. In contrast, methane with high steam content can be directly fed to Ni/YSZ anode, while methanol could also be used as the direct feed at a temperature as high as 1000°C. The next approach is to investigate the possible uses of ethanol and methanol at lower operating temperature in IIR-SOFC operation by performing the reaction in the annular ceramic reactor as described above.

With the same feeding conditions, Fig. 5 shows the variations in the yield of hydrogen production with time at 900°C over this configuration compared to those from the system with only Ni/YSZ. The yields of hydrogen production from the steam reforming of all hydrocarbon feeds over this configuration were considerably higher than those of single Ni/YSZ. In addition, according to the TPO after reaction, the amounts of carbon formation on the surface of Ni/YSZ were significantly reduced, Table 6. These improvements are due to the conversion of all alcohol and high hydrocarbon components from the decomposition of ethanol (i.e. ethylene and ethane) to methane, carbon monoxide, and hydrogen by Ni/Ce-ZrO_2 before these components reach the surface of Ni/YSZ at the outer side of the annular reactor.

Therefore, the main reaction on the surface of Ni/YSZ is the steam reforming of methane, which is thermodynamically unflavored to form carbon deposition, instead of the steam reforming of alcohol or high hydrocarbon.

The effect of temperature on the degree of carbon formation over Ni/YSZ was then studied by varying the operating temperature from 700°C to 900°C. As also seen in Table 6, methanol can be used as the feed in all range of this temperature with only small amount of carbon deposition detected on the surface of Ni/YSZ at low temperature. In contrast, at the temperature of 700-800°C, the amount of carbon deposition on the surface of Ni/YSZ when ethanol was used as the feed is considerably high, but it decreases significantly when the temperature is higher than 900°C. The high carbon formation could be due to the incomplete reforming of ethanol, ethane, and ethylene at the temperature lower than 900°C. Fig. 6 shows the effect of temperature on the ethanol conversion and product distribution from the ethanol steam reforming over Ni/Ce-ZrO_2. It is clear from the figure that all ethanol, ethane, and ethylene are reformed at the temperature above 850°C.

2.3.4 Steam reforming of methanol over Ni/YSZ with preliminary homogeneous reforming

From the above observation, methanol with steam can be directly fed to the anode side of fuel cell (DIR) at such a high temperature, 1000°C, without the problem of carbon formation. In contrast, when fuel cell is operated at lower temperature (700-975°C), methanol must be firstly converted to methane and other small molecular-weight products in the catalytic reformer (IIR).

Nevertheless, it has been reported in the previous publication [23] that methanol can homogeneously decompose to CH_4, CO, CO_2, and H_2 at high temperature. Therefore, this benefit was also considered in this work. Firstly, the homogeneous (non-catalytic) decomposition of methanol was investigated by feeding CH_3OH/H_2O in helium to the blank reactor and the temperature was increased from 200ºC to 1000ºC. It was observed that methanol was converted to methane, carbon monoxide, carbon dioxide, and hydrogen at the temperature above 800°C, Table 7. These components were formed via the decomposition of methanol, water gas shift and methanation reactions.

The annular ceramic reactor was then applied without the filling of Ni/Ce-ZrO_2 at the inner side of the tube; only Ni/YSZ was packed at the outer side. Methanol and steam were fed through the inner side of the annular reactor before flowing backward through the outer side where catalytic steam reforming took place. Fig. 7 and Table 8 present the stability, product distribution, and degree of carbon deposition (from TPO testing) from this system. Surprisingly, the amount of carbon formation on the surface of Ni/YSZ decreases considerably when the operating temperature is higher than 900°C. In addition, the catalyst stability and hydrogen yield increase significantly.

The improvements are due to the homogeneous cracking of methanol to CH_4, CO, CO_2, and H_2 before reaching the surface of Ni/YSZ. At the temperature higher than 900°C, the conversion of methanol is closed to 100%, therefore, the main reaction at the surface of Ni/YSZ is the steam reforming of methane, which is thermodynamically unflavored to form carbon deposition compared to the steam reforming of methanol.

For comparison, the steam reforming of ethanol over Ni/YSZ with preliminary homogeneous reforming was also studied. Similar to the methanol case, the homogeneous (non-catalytic) steam reforming of ethanol was primarily investigated. The inlet C_2H_5OH/H_2O in helium with the molar ratio of 1.0/3.0 (inlet C_2H_5OH of 4 kPa) was introduced to the blank reactor, while the temperature increased from 200ºC to 1000ºC. As presented in Table 9, it was observed that ethanol was converted to acetaldehyde, and hydrogen at the temperature above 200°C. Methane and carbon monoxide productions were then observed from the decomposition of acetaldehyde at the temperature of 250-300°C. When the temperature increased up to 550°C, the selectivity of acetaldehyde significantly decreased, while hydrogen, carbon monoxide, and carbon dioxide remained increasing. At the temperature above 550°C, the formations of ethane and ethylene were also observed due to the dehydration of ethanol following with the production of ethane by ethylene hydrogenation.

The annular ceramic reactor was then applied by feeding ethanol and steam through the blank inner side of the annular reactor before flowing backward through the outer side where Ni/YSZ was filled. Significant deactivation was detected from this system, Fig. 8. In addition, high amount of carbon formation was observed on the

surface of Ni/YSZ in all ranges of temperature, according to the TPO testing (Table 10). This is due to the presents of ethylene and ethane, which are very strong promoters for carbon formation. Therefore, it is clear that ethanol can not be fed directly to Ni/YSZ even with the preliminary homogeneous reforming.

2.4. Conclusion

Methane with high steam content can be directly fed to Ni/YSZ anode without the problem of carbon formation, while methanol can be used as the direct feed at the temperature as high as 1000°C. In contrast, ethanol can not be used as the direct fuel for DIR-SOFC operation (with Ni/YSZ anode) even at high steam content and high operating temperature due to the easy degradation of anode material; it must be first converted to methane by the catalytic reformer (IIR-SOFC operation). Ni/Ce-ZrO_2 was found to be a good internal reforming catalyst in the present work.

It was then found from the study that methanol can be efficiently fed to Ni/YSZ anode (as DIR operation) at lower temperature (900-975°C) without the problem of carbon formation if SOFC system has sufficient space volume at the entrance of the anode chamber where methanol is homogeneously converted to CH_4, CO, CO_2, and H_2 before reaching SOFC anode.

2.5 References

[1] George, R. Fuel Cell Handbook, Sixth Edition, by EG&G Technical Services,Inc. Science Applications International Corp., Under Contract No. DE-AM-26-99FT40575, U.S. Dept. of Energy, Office of Fossil Energy, National Energy Technology Laboratory, Morgantown, W. Virginia.

[2] Lundberg, W.L., Veyo, S.E., Conceptual design and performance analysis of a 300 MWel LNG-fuelled pressurised SOFC/Gas turbine power plant, in: Yokohawa, S.C. Singhal (Eds.), Proceeding of the 7th International Symposium Solid Oxide Fuel Cells VII, (2001), 78

[3] Stephen H. Clarke, Andrew L. Dicks, Kevin Pointon, Thomas A. Smith and Angie Swann, Catalysis Today, 38(4), (1997), 411

[4] Wincewicz, K.C., and Cooper, J.S., J. Power Sources, 140, (2005), 280

[5] I.V. Yentekakis, S.G. Neophytides, A.C. Kaloyiannis, and C.G. Vayenas, Proceeding of the 3rd International Symposium on Solid Oxide Fuel Cells, Honolulu, HI, USA, 4, (1993), 904

[6] E. Achenbach and E. Riensche, J. Power Sources, 52, (1994), 283

[7] A.L. Dick, K.D. Pointon, A. Siddle, J. Power Sources, 86, (2000), 523

[8] Emonts B., Hansen J.B., Jorgensen S.L., Hohlein B. and Peters R., J. Power Sources, 71, (1998), 288

[9] Ledjeff-Hey K., Formanski V., Kalk T. and Roes J., J. Power Sources, 71(1-2), (1998), 199

[10] S. Cavallaro, S. Freni, Int. J. Hydrogen Energy, 21 (6), (1996), 465

[11] A.N. Fatsikostas, X.E. Verykios, J. Catal., 225 (4), (2004), 439

[12] Douvartzides S.L., Coutelieris F.A., Demin K. and Tsiakaras P.E., AIChE, 49, (2003), 248

[13] N. Laosiripojana and S. Assabumrungrat, Appl. Catal. A, 290, (2005), 200

[14] N. Laosiripojana and S. Assabumrungrat, J. Power Sources, 158(2), (2006), 1348

[15] N. Laosiripojana and S. Assabumrungrat, Appl. Catal. B, 66(1-2), (2006), 29

[16] N. Laosiripojana and S. Assabumrungrat, Appl. Catal. B, 60 (2005) 107

[17] E. Ramirez, A. Atkinson and D. Chadwick, Appl. Catal. B, 36 (2002) 193

[18] F. Aupretre, C. Descorme, D. Duprez, D. Casanave and D. Uzio, J. Catal., 233 (2), (2005), 464

[19] J. Comas , F. Mariño , M. Laborde and N. Amadeo, Chem. Eng. Jour., 98 (1-2), (2004), 61

[20] M.A. Goula, S.K. Kontou and P.E. Tsiakaras, Appl. Catal. B, 49 (2), (2004), 135

[21] Lwin Y., Daud W.R.W., Mohamad A.B. and Yaakob Z. Int. J. Hydrogen Energy, 25(1), (2000), 47

[22] J.N. Armor, Appl. Catal. A: General, 176 (1999) 159

[23] N. Laosiripojana and S. Assabumrungrat, Chem. Eng. Sci., 61(8), (2006), 2540

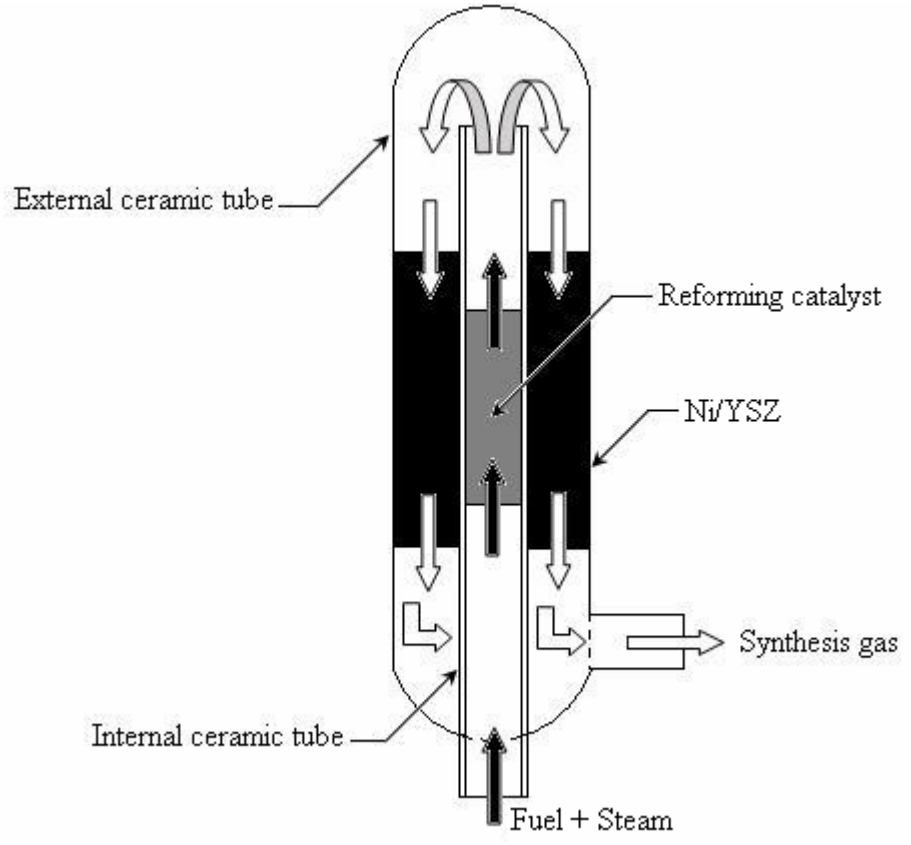

Fig. 1 Configuration of annular ceramic reactor for experiments under IIR operation.

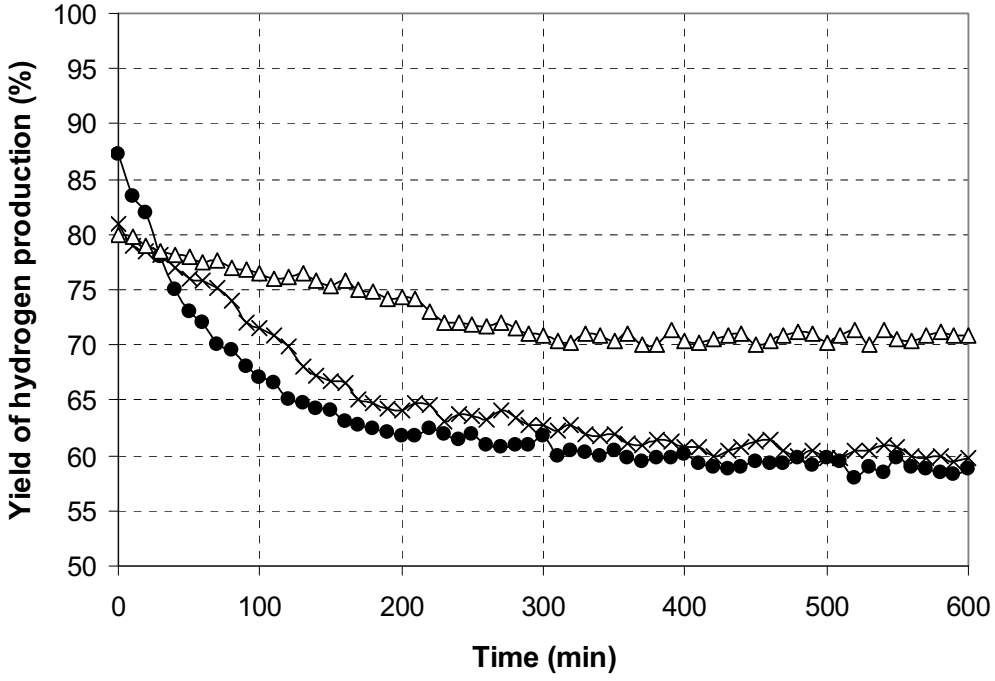

Fig. 2 Yield of H_2 production from the steam reforming of ethanol (●), methanol (×), and methane (△) over Ni/YSZ at 900^{o}C

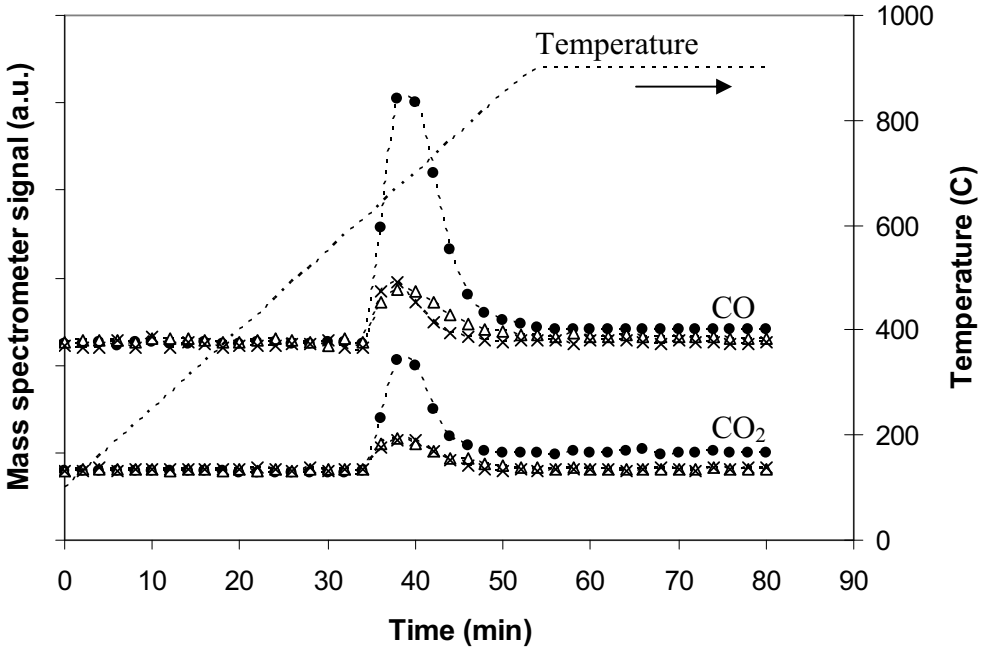

Fig. 3 Temperature Programmed Oxidation (TPO) of Ni/YSZ after exposure in steam reforming of ethanol (●), methanol (×), and methane (△) for 10 h

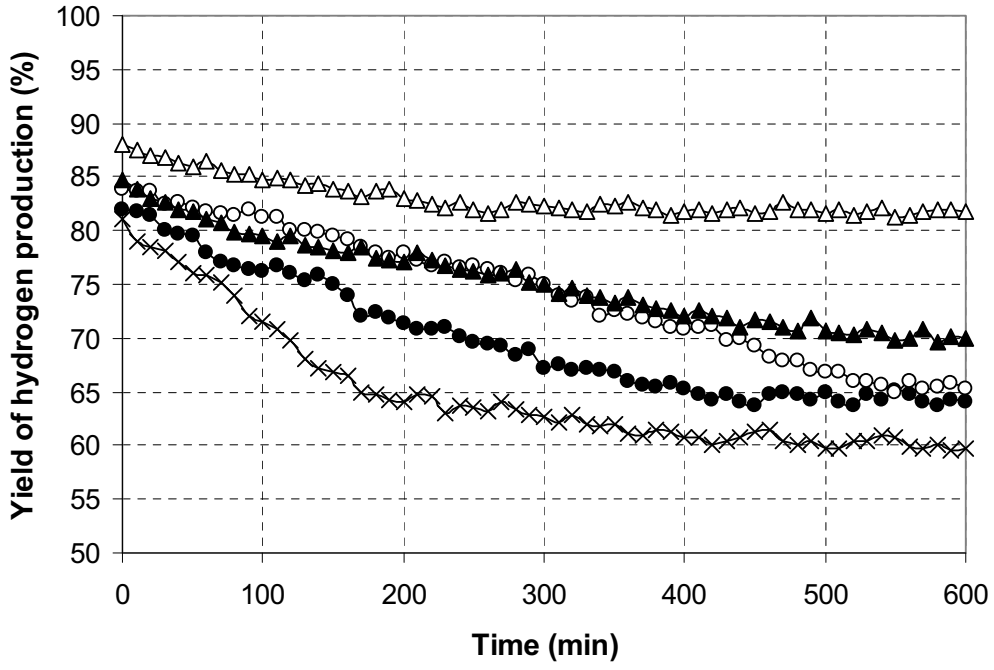

Fig. 4 Yield of hydrogen production from the steam reforming of methanol over Ni/YSZ at 900°C (×), 925°C (●), 950°C (○), 975°C (▲), and 1000°C (△)

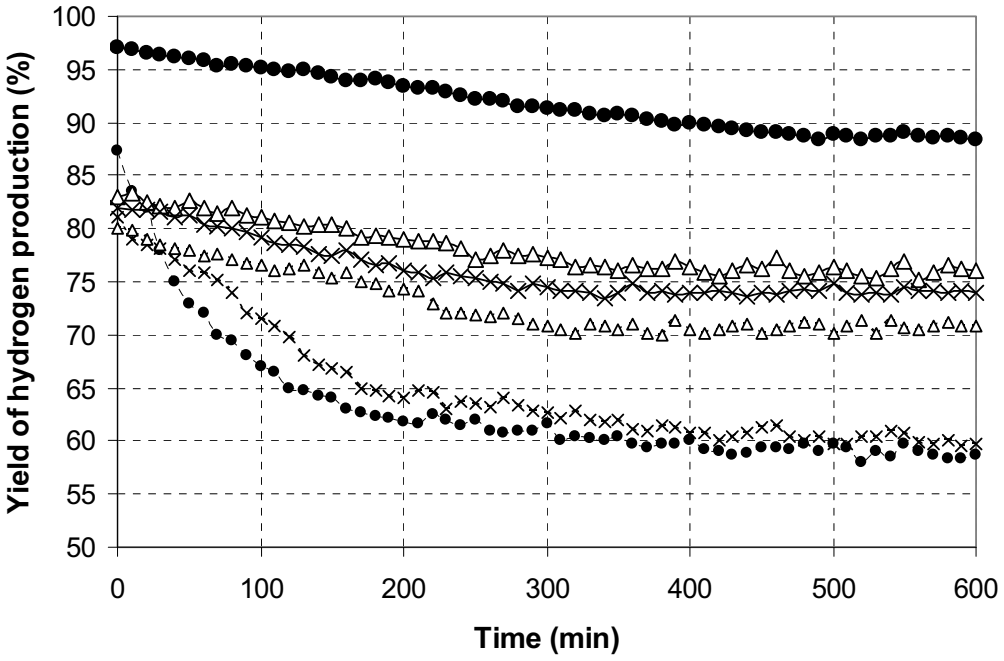

Fig. 5 Yield of H_2 production from the steam reforming of ethanol (●), methanol (×), and methane (△) over Ni/Ce-ZrO_2 + Ni/YSZ at 900°C compared to those over Ni/YSZ in Fig. 2 (dot line with small symbols)

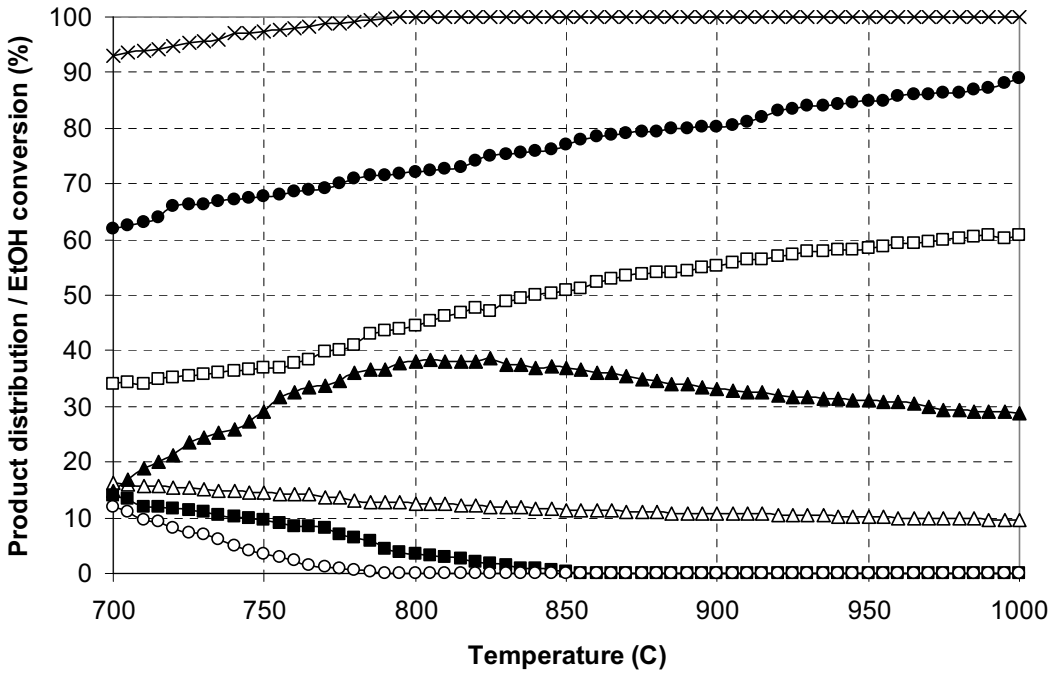

Fig. 6 Effect of temperature on the conversion of EtOH (×), the fractions of CO (□), CO_2 (△), CH_4 (▲), C_2H_6 (○), and C_2H_4 (■), and the yield of H_2 production (●) from ethanol steam reforming over Ni/Ce-ZrO_2 (4 kPa EtOH, and 12 kPa H_2O)

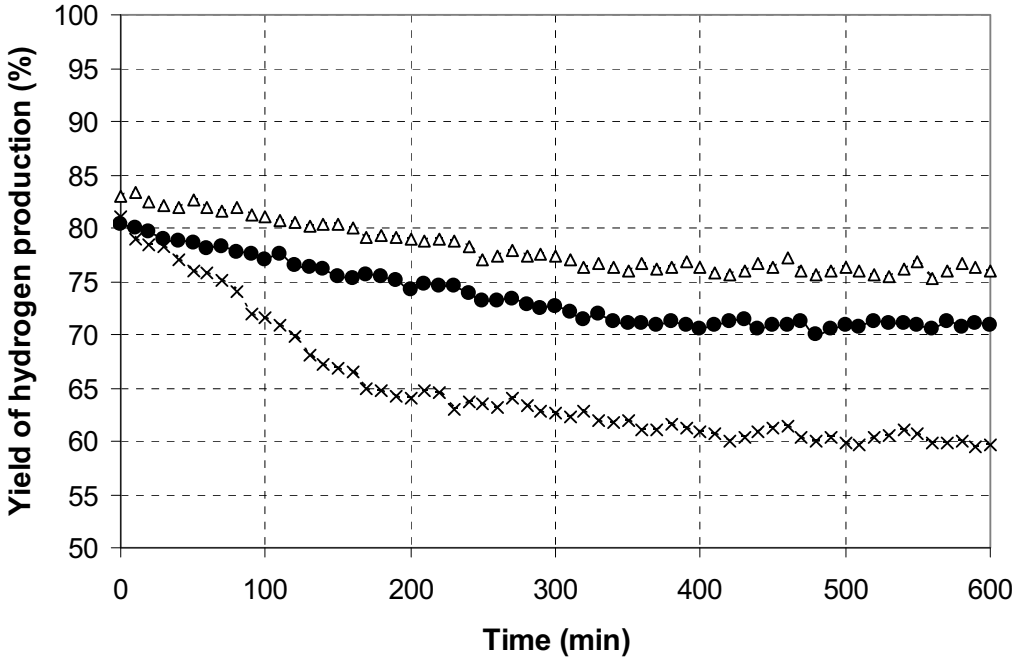

Fig. 7 Yield of H_2 production from methanol steam reforming over Ni/YSZ with preliminary homogeneous reforming at 900°C (●) compared to that without homogeneous reforming in Fig. 2 (×) and over Ni/Ce-ZrO_2 + Ni/YSZ in Fig. 5 (△)

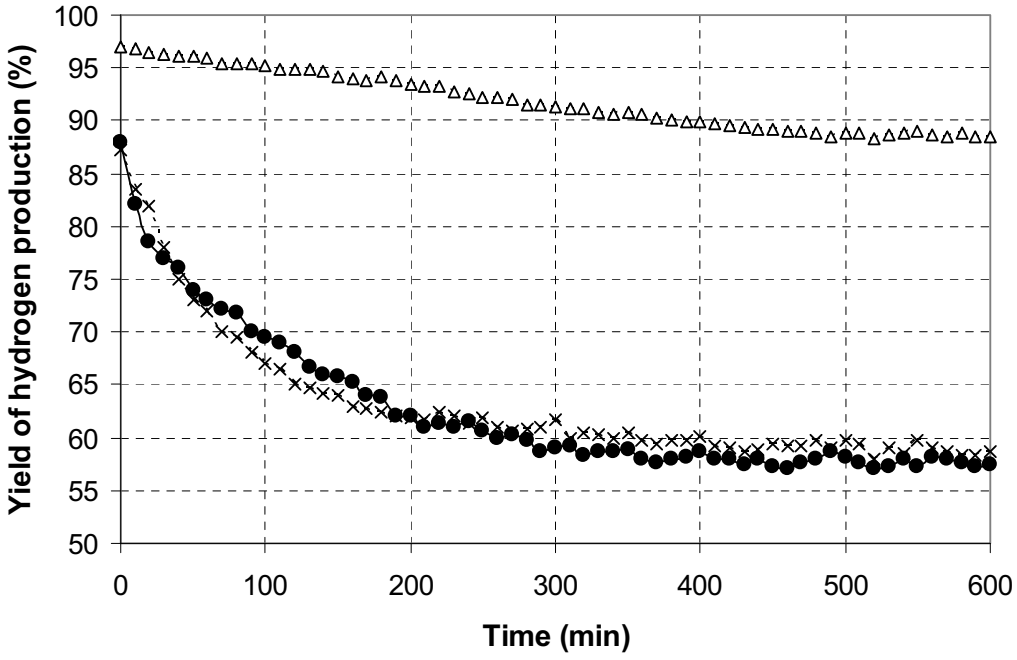

Fig. 8 Yield of H_2 production from ethanol steam reforming over Ni/YSZ with preliminary homogeneous reforming at 900°C (●) compared to that without homogeneous reforming in Fig. 2 (×) and over Ni/Ce-ZrO_2 + Ni/YSZ in Fig. 5 (△)

Table 1
Physicochemical properties of the catalysts after reduction

Catalyst	Ni-load[a] (wt%)	Ni-reducibility[b] (Ni%)	Ni-dispersion[c] (Ni%)
Ni/Ce-ZrO_2	4.8	92.4	4.74
Ni/YSZ	39	95.9	

[a] Measured from X-ray fluorescence analysis.
[b] Measured from temperature-programmed reduction (TPR) with 5% hydrogen.
[c] Measured from temperature-programmed desorption (TPD) of hydrogen after TPR measurement.

Table 2
Product analysis after exposure in the steam reforming conditions at 900ºC for 10 h

Type of fuel	Deactivation (%)	Yield of H_2 production (%)	Fraction of the by-products (%)				
			CO	CO_2	CH_4	C_2H_6	C_2H_4
Methane	11.3	70.9	68.1[a] (71.7)[b]	31.9 (28.3)	-	-	-
Methanol	26.2	59.7	62.9 (55.0)	27.7 (45.0)	9.4 (~0)	-	-
Ethanol	32.7	58.3	44.5 (78.2)	11.8 (21.7)	30.2 (~0)	4.7 (0)	8.8 (0)

[a] Observed from the Experiments
[b] Calculated from the thermodynamic analysis (at equilibrium)

Table 3
Physicochemical properties of the catalysts after reactions

Condition	Ni-load (wt%)	Ni-reducibility (Ni%)
Fresh catalyst	39	95.9
Spent catalyst after exposure in		
- Methane steam reforming	38.8	95.5
- Methanol steam reforming	39	82.9
- Ethanol steam reforming	38.6	92.7

Table 4
Products and amount of carbon deposition after exposure in the steam reforming at different inlet fuel/H_2O ratios at 900ºC

Type of fuel	Fuel/H_2O ratio	Yield of H_2 production (%)	Fraction of the by-products (%)					C formation (monolayers)
			CO	CO_2	CH_4	C_2H_6	C_2H_4	
Methane	1.0/3.0	70.9	68.1	31.9	-	-	-	0.21
	1.0/4.0	73.7	65.2	34.8	-	-	-	0.15
	1.0/5.0	77.5	59.3	40.7	-	-	-	0.09
Methanol	1.0/3.0	59.7	62.9	27.7	9.4	-	-	0.37
	1.0/4.0	64.2	60.4	30.5	9.1	-	-	0.32
	1.0/5.0	66.3	57.5	33.8	8.7	-	-	0.26
Ethanol	1.0/3.0	58.3	44.5	11.8	30.2	4.7	8.8	4.29
	1.0/4.0	60.0	42.9	14.9	29.8	4.3	8.1	4.18
	1.0/5.0	61.4	41.2	18.3	29.1	3.9	7.5	4.12

Table 5
Products and amount of carbon deposition after exposure in the steam reforming at different temperatures (inlet fuel/H_2O ratio of 1.0/3.0)

Type of fuel	Temperature (ºC)	Yield of H_2 production (%)	Fraction of the by-products (%)					C formation (monolayers)
			CO	CO_2	CH_4	C_2H_6	C_2H_4	
Methane	900	70.9	68.1	31.9	-	-	-	0.21
	925	75.7	71.2	28.8	-	-	-	0.14
	950	78.3	74.0	26.0	-	-	-	0.08
	975	81.6	76.5	23.5	-	-	-	~0
	1000	84.9	79.7	20.3	-	-	-	~0
Methanol	900	59.7	62.9	27.7	9.4	-	-	0.37
	925	64.0	66.7	26.0	7.3	-	-	0.19
	950	65.3	70.3	25.0	4.7	-	-	0.12
	975	70.1	73.4	24.5	2.1	-	-	0.05
	1000	81.8	77.0	22.7	0.3	-	-	~0
Ethanol	900	58.3	44.5	11.8	30.2	4.7	8.8	4.29
	925	60.7	48.9	5.9	32.4	3.5	9.3	4.17
	950	62.9	51.2	5.1	31.7	2.9	9.1	3.94
	975	65.0	53.7	5.0	30.8	1.8	8.7	3.91
	1000	67.2	55.1	6.0	29.5	1.1	8.3	3.82

Table 6
Products and amount of carbon deposition from the steam reforming over Ni/Ce-ZrO_2 + Ni/YSZ at different temperatures (inlet Fuel/H_2O ratio of 1.0/3.0)

Type of fuel	Temperature (^oC)	Yield of H_2 production (%)	Fraction of the by-products (%)					C formation (monolayers)
			CO	CO_2	CH_4	C_2H_6	C_2H_4	
Methane	700	55.3	58.2	41.8	-	-	-	0.09
	750	60.0	60.7	39.3	-	-	-	~0
	800	67.6	64.4	35.6	-	-	-	~0
	850	72.9	69.0	31.0	-	-	-	~0
	900	76.1	72.1	27.9	-	-	-	~0
Methanol	700	51.0	51.0	45.2	3.8	-	-	0.13
	750	58.6	53.8	44.1	2.1	-	-	0.05
	800	64.1	57.9	40.6	1.5	-	-	~0
	850	69.9	60.5	38.8	0.7	-	-	~0
	900	73.9	64.1	35.9	-	-	-	~0
Ethanol	700	67.9	37.1	18.8	22.0	12.6	9.5	3.97
	750	71.6	40.2	16.5	34.7	6.7	1.9	2.83
	800	75.9	47.9	15.0	34.2	2.9	~0	2.39
	850	81.2	55.6	12.7	31.7	~0	~0	0.66
	900	88.4	61.3	11.9	26.8	~0	~0	0.42

Table 7
Effect of temperature on the homogeneous (in the absence of catalyst) reactivity of methanol steam reforming (1 kPa MeOH and 3 kPa steam)

Temperature (^oC)	Methanol conversion (%)	Yield of H_2 production (%)	Fraction of the by-products (%)		
			CO	CO_2	CH_4
800	0.8	0.2	0.5	0.1	0.2
825	4.1	0.8	2.1	1.0	1.3
850	16.5	6.1	10.0	2.4	4.0
875	52.1	12.3	27.6	3.7	20.8
900	93.2	20.9	46.3	7.3	39.5
925	~100	23.3	50.2	8.6	41.2
950	~100	23.7	50.1	8.3	41.6
975	~100	23.4	50.1	8.4	41.5
1000	~100	23.5	50.1	8.0	41.8

Table 8
Products and amount of carbon deposition after exposure in methanol steam reforming over Ni/YSZ with preliminary homogeneous reforming

Temperature (^oC)	Deactivation (%)	Yield of H_2 production (%)	Fraction of the by-products (%)			C formation (monolayers)
			CO	CO_2	CH_4	
900	11.9	70.8	65.7	31.6	2.7	0.18
925	21.8	72.3	68.2	29.9	1.9	0.11
950	22.1	74.9	74.3	25.7	~0	~0
975	17.3	79.6	75.1	24.9	~0	~0
1000	7.1	83.9	79.9	20.1	~0	~0

Table 9
Effect of temperature on the homogeneous (in the absence of catalyst) reactivity of ethanol steam reforming (1 kPa EtOH and 3 kPa steam)

Temperature (^oC)	Yield of H_2 production (%)	Fraction of the by-products (%)					
		CH_3CHO	CO	CO_2	CH_4	C_2H_6	C_2H_4
200	~0	1.3	0	0	0	0	0
300	11.9	21.1	5.1	0	0.5	0	0
400	23.2	31.9	10.9	3.2	3.1	0	0
500	31.4	37.4	16.2	7.8	5.3	0	0
600	37.8	24.8	21.5	9.4	5.5	16.1	8.1
700	43.0	0	29.2	9.7	5.9	23.9	19.2
800	46.2	0	29.1	9.6	5.8	23.4	19.8
900	48.5	0	29.3	9.4	6.0	22.2	20.0
1000	49.8	0	28.9	9.6	5.9	22.3	19.8

Table 10
Products and amount of carbon deposition after exposure in ethanol steam reforming over Ni/YSZ with preliminary homogeneous reforming

Temperature (^oC)	Deactivation (%)	Yield of H_2 production (%)	Fraction of the by-products (%)					C formation (monolayers)
			CO	CO_2	CH_4	C_2H_6	C_2H_4	
900	34.7	57.4	46.7	10.5	31.6	5.1	6.1	4.38
950	31.9	61.9	54.7	5.3	31.9	3.2	4.9	3.86
1000	28.4	68.6	59.2	5.8	30.2	1.4	3.4	3.84

RESEARCH III

Steam reforming of ethanol with co-fed oxygen and hydrogen over Ni on high surface area ceria support

Ethanol steam reforming with/without co-fed oxygen and hydrogen over Ni on high surface area CeO_2 support, synthesized via a surfactant-assisted method, (Ni/CeO_2 (High surface area; HSA)) was studied under solid oxide fuel cell (SOFC) operating conditions for later application as an in-stack reforming catalyst. The catalyst provides considerably higher reforming reactivity and excellent resistance towards carbon deposition in comparison with Ni/Al_2O_3 and Ni on conventional ceria (Ni/CeO_2 (Low surface area; LSA)). At the temperature above 800°C, the main products from the reforming processes over Ni/CeO_2 (HSA) were H_2, CO, and CO_2 with some amount of CH_4 depending on the inlet steam/ethanol and co-fed reactant (i.e. O_2 and H_2)/ethanol ratios, whereas high hydrocarbon compound i.e. C_2H_4 was also observed from the reforming of ethanol over Ni/CeO_2 (LSA) and Ni/Al_2O_3.

An addition of O_2 (as oxidative steam reforming) and H_2 significantly reduced the degree of carbon deposition. The presence of both reactants also promoted the conversions of hydrocarbon presented in the system (i.e. CH_4 and C_2H_4) to CO and H_2. The major consideration of these addition is the suitable co-fed reactant/C_2H_5OH ratio. The presence of too high oxygen concentration could oxidize Ni particles to NiO, which resulted in a lower reforming reactivity, and also combusts H_2 to H_2O. The suitable O_2/C_2H_5OH molar ratio for the oxidative steam reforming of Ni/CeO_2 was 0.4, which is less than that of Ni/Al_2O_3. An addition of too high hydrogen content slightly decreased the catalyst activity, which could be due to the active site competition of nickel particle and the inhibition of gas-solid redox reactions between the gaseous hydrocarbon components with the lattice oxygen (O_O^x) on the surface of CeO_2 support in the case of Ni/CeO_2.

3.1. Introduction

A mixture of hydrogen and carbon monoxide (so-called synthesis gas) is a major fuel for Solid Oxide Fuel Cell (SOFC). Nevertheless, the use of other hydrocarbon fuel such as

methane, methanol, ethanol, gasoline and other oil derivatives is also possible when operated as an internal or in-stack reforming (IR-SOFC) [1]. According to the global environmental problems and current fossil fuel crisis, the development of IR-SOFC fed by biomass or renewable based fuels attracts more attention to be an alternative method for power generation in the near future. Among renewable sources, bio-ethanol is a promising candidate since it is readily produced by fermentation of biomasses and has reasonably high hydrogen content. In addition, ethanol is also safe and simple to handle, transport and store [2,3]. The major difficulty for a reforming of ethanol is the deactivation of the reforming catalyst due to a possible carbon deposition during ethanol decomposition, particularly at high temperature.

Previously, a steam reforming of ethanol has been studied by several researchers [4-12]. Most of them have investigated the reforming of ethanol over noble metal catalysts on several oxide supports [4-7]. Verykios and coworkers [8-10] reported that Rh based catalyst provides significantly higher activity and stability towards the steam reforming of ethanol comparing with Ru, Pt, Pd, and also Ni. Similarly, Freni et al. [4, 6, 7] presented that Rh/Al_2O_3 provides the highest reforming reactivity among noble metal catalysts (e.g. Rh, Ru, Pt, Pd) on several oxide supports (e.g. Al_2O_3, MgO, SiO_2, TiO_2). Sobyanin and coworkers [11] studied the decomposition of ethanol in the presence of steam over Pd supported on a porous carbonaceous material. They presented that the catalyst exhibits a high activity and long-term stability. Burch and coworkers [12] found that the order of ethanol steam reforming reactivity over metals was Rh > Pd > Ni = Pt, and also reported the important role of the catalyst support. Verykios and coworkers [8-10] also investigated the steam reforming of ethanol over Ni based catalyst on several oxide supports (e.g. La_2O_3, Al_2O_3, YSZ, and MgO). They revealed that Ni/La_2O_3 and $Ni/La_2O_3/Al_2O_3$ exhibit high activity and stability.

According to these previous publications, an extensive formation of encapsulated carbon was always observed from the steam reforming of ethanol even if the noble metal catalysts were applied. This carbon formation was mainly due to the decomposition of ethanol forming high hydrocarbons (e.g. acetaldehyde, ethylene, and ethane), which easily formed the carbonaceous deposits. An addition of oxygen to perform an oxidative steam reforming (or autothermal reforming) was proven to provide great benefits in terms of catalyst stability and coke suppression [13]. However, the yield of hydrogen production could be minimized due to the oxidation of hydrogen from added oxygen. The attractive characteristic of the autothermal reforming operation is that the exothermic heat from the partial oxidation can

directly supply the energy required for the endothermic steam reforming reaction, and it is considered to be a thermally self-sustaining process.

In this work, it is aimed at developing an alternative catalyst, which can reform ethanol with high stability and activity at such a high temperature (700-1000°C) for later application in IR-SOFC. According to the economical point of view, Ni was selected as a catalyst rather than other precious metals such as Pt, Rh and Ru. Although the precious metals have been reported to be active for the reforming reactions and resistant to the carbon formation than Ni [14-15], the current prices of these metals are very high for commercial uses, and the availability of some precious metals such as ruthenium was too low to have a major impact on the total reforming catalyst market [16]. A selection of the support material is a major consideration of this work. It has been widely reported that metal catalysts are not very active for the steam reforming when supported on inert oxides [17]. Various supports have been investigated, e.g. α-Al_2O_3 [18], γ-Al_2O_3 and γ-Al_2O_3 with alkali metal oxide and rare earth metal oxide [19], $CaAl_2O_4$ [20] and CeO_2 based supports [21]. A promising catalyst system for the reforming reactions appeared to be a metal on CeO_2 based supports, where metals can be Ni, Pt or Pd [22-24]. Therefore, CeO_2 was chosen as a catalyst support over Ni in this work.

CeO_2 (or called ceria) is an important material for a variety of catalytic reactions involving oxidation of hydrocarbons (e.g. automobile exhaust catalysts). It contains a high concentration of highly mobile oxygen vacancies, which act as local sources or sinks for oxygen involved in reactions taking place on its surface. Recently, the high resistance toward carbon deposition over ceria has been reported [25-27]. However, the major considerations of applying CeO_2 in the high temperature steam reforming reaction are their low specific surface and their percentage of high surface area reduction due to the high surface sintering. The use of high surface area (HSA) ceria-based materials as the catalyst support would be a good alternative procedure to improve the reforming performance. Several methods have recently been described for the preparation of high surface area CeO_2. Among these methods, the surfactant-assisted approach was reported to provide CeO_2 (HSA) with improved textural, structural, and chemical properties [28]. Our previous publication [25] also presented the achievement of CeO_2 with high surface area and good stability after thermal treatment by this preparation method.

In the present work, the stability and activity toward the steam reforming of ethanol over Ni on high surface area CeO_2 support (Ni/CeO_2 (HSA)) was firstly studied and compared

with Ni on conventional low surface area CeO_2 support (Ni/CeO_2 (LSA)), and Ni/Al_2O_3. The resistance toward carbon formation and the influences of inlet C_2H_5OH/H_2O molar ratio and temperature on the product selectivities over these catalysts were also studied. As the next step, the addition of co-fed reactant (i.e. O_2 and H_2) was then investigated. An improvement of the resistance toward carbon deposition by the presence of these components and the suitable inlet co-fed reactant/C_2H_5OH molar ratio were eventually determined.

3.2. Experimental

3.2.1. Catalyst preparation and characterization

Conventional CeO_2 support (CeO_2 (LSA)) was prepared by a precipitation method. The mixture of 0.1 M cerium nitrate ($Ce(NO_3)_3 \cdot H_2O$) (from Aldrich) and 0.4 M of urea at a 2 to 1 volumetric ratio was prepared and stirred using a magnetic stirrer (100 rpm) for 3 h. The precipitate was filtered and washed with deionised water and ethanol to prevent an agglomeration of particles. It was dried overnight in an oven at 110°C, and then calcined in air at 1000°C for 6 h.

High surface area CeO_2 support (CeO_2 (HSA)) was prepared by adding an aqueous solution of an appropriate cationic surfactant, 0.1 M cetyltrimethylammonium bromide solution from Aldrich, to a 0.1 M cerium nitrate. The molar ratio of ([Ce])/[cetyltrimethylammonium bromide] was kept constant at 0.8. The mixture was stirred and then aqueous ammonia was slowly added with vigorous stirring until the pH was 11.5. The mixture was continually stirred for 3 h, then sealed and placed in a thermostatic bath maintained at 90°C for 3 days. Next, the mixture was cooled and the resulting precipitate was filtered and washed repeatedly with water and acetone. The filtered powder was then treated under the same procedures as CeO_2 (LSA). BET measurements of CeO_2 (both LSA and HSA) were carried out at different calcination temperatures to determine the decrease in specific surface area due to the thermal sintering. As presented in Table 1, after drying, surface areas of 105 and 55 $m^2\ g^{-1}$ were observed for CeO_2 (HSA) and conventional CeO_2, respectively. As expected, the surface area dramatically decreased at high calcination temperatures. However, the value for CeO_2 (HSA) is still appreciable after calcination at 1000°C and it is almost 3 times of that for the conventional CeO_2.

Ni/CeO_2 (5 wt% Ni) was then prepared by impregnating CeO_2 (both LSA and HSA) with a $Ni(NO_3)_2$ solution (from Aldrich). The catalyst was reduced with 10%H_2 at 500ºC for 6 h before use. For comparison, a conventional Ni/Al_2O_3 (5 wt% Ni) was also prepared by impregnating α-Al_2O_3 (from Aldrich) with $Ni(NO_3)_2$. After reduction, the catalyst was characterized by several physicochemical methods. The weight contents of Ni in Ni/Al_2O_3 and Ni/CeO_2 were determined by X-ray fluorescence (XRF) analysis. The reducibility percentage of nickel was measured and calculated from the degree of H_2 uptakes from the temperature-programmed reduction (TPR) test using 5% H_2 with the total flow rate of 100 cm^3 min^{-1} and temperature from room temperature to 500ºC, while the dispersion percentage of nickel was identified from the volumetric H_2 chemisorption measurement using chemisorption analyzer. According to this measurement, the H_2 chemisorption and backsorption isotherms were measured and their difference was used to calculate strongly chemisorbed H_2 uptakes, from which Ni dispersions were obtained by assuming 1:1 stoichiometry of adsorbed H and metal surface atoms [29, 30]. The catalyst specific surface areas were obtained from BET measurement. All physicochemical properties of the synthesized catalysts are presented in Table 2.

As described in the introduction section, the advantage of CeO_2 as the support is mainly due to its high redox properties. In addition to the above characterizations, the redox properties and redox reversibilities of synthesized Ni/CeO_2 (both LSA and HSA) and Ni/Al_2O_3 were also determined by the temperature programmed reduction (TPR) and the temperature programmed oxidation (TPO). Regarding these experiments, 5% H_2 and 10% O_2 were used for the TPR and TPO, respectively, while the temperature of the system increased from room temperature to 900ºC for both experiments.

3.2.2. Apparatus and Procedures

An experimental reactor system was constructed as presented elsewhere [25-27]. The feed gases including the components of interest (ethanol and steam from the evaporator, oxygen and hydrogen as the additive gas) and the carrier gas (helium) were introduced to the reaction section, in which a 10-mm diameter quartz reactor was mounted vertically inside a furnace. The catalyst was loaded in the quartz reactor, which was packed with a small amount of quartz wool to prevent the catalyst from moving. Regarding the results in our previous publications [25-27], in order to avoid any limitations by intraparticle diffusion, the weight of catalyst loading was kept constant at 50 mg, while the total gas flow rate was 100

$cm^3\ min^{-1}$ under a constant residence time of 3×10^{-2} g sec cm^{-3} in all experiments. A Type-K thermocouple was placed into an annular space between the reactor and the furnace. This thermocouple was mounted on the tubular reactor in close contact with the catalyst bed to minimize the temperature difference between the catalyst bed and the thermocouple. Another Type-K thermocouple was inserted in the middle of the quartz tube to re-check the possible temperature gradient.

After the reactions, the exit gas mixture was transferred via trace-heated lines to the analysis section, which consists of a Porapak Q column Shimadzu 14B gas chromatograph (GC) and a mass spectrometer (MS). The gas chromatography was applied to investigate the steady state condition experiments, whereas the mass spectrometer in which the sampling of the exit gas was done by a quartz capillery and differential pumping was used for the transient carbon formation experiment. To study the formation of carbon species on catalyst surface, Temperature programmed Oxidation (TPO) was applied by introducing 10% O_2 in He (with the flow rate of 100 $cm^3\ min^{-1}$) into the system, after being purged with He. The operating temperature increased from room temperature to 900ºC with a rate of 10ºC min^{-1}. The amount of carbon formation on the surface of catalysts were determined by measuring the CO and CO_2 yields from the TPO results (using Microcal Origin Software) assuming a value of 0.026 nm^2 for the area occupied by a carbon atom in a surface monolayer of the basal plane in graphite [31]. In addition to the TPO method, the amount of carbon deposition was confirmed by the calculation of carbon balance in the system. The amount of carbon deposited on the surface of catalyst is theoretically equal to the difference between the inlet carbon containing components (C_2H_5OH) and the outlet carbon containing components (CO, CO_2, CH_4, C_2H_6, C_2H_4, and C_2H_4O). The amount of carbon deposited per gram of catalyst is given by the following equation:

$$C_{deposition} = \frac{mole_{carbon(in)} - mole_{carbon(out)}}{m_{catalyst}} \qquad (1)$$

To study the steam reforming reactivity, the rate of ethanol steam reforming was defined in terms of conversion and product distribution. The yield of hydrogen production was calculated by the hydrogen balance, defined as the molar fraction of hydrogen produced to the total hydrogen in the products. Distributions of other by-products (i.e. CO, CO_2, CH_4, C_2H_6, C_2H_4, and C_2H_4O) were calculated by the carbon balance, defined as the ratios of the

product moles to the consumed moles of hydrocarbon, accounting for stoichiometry. This information was presented in term of (relative) fraction of all by-product components (i.e. CO, CO_2, CH_4, C_2H_6, C_2H_4, and C_2H_4O), which are summed to 100%.

3.3. Results

3.3.1 Redox properties and redox reversibility of the synthesized catalysts

After reducing, the oxygen storage capacities (OSC) and the degree of redox properties for Ni/CeO_2 (both LSA and HSA) and Ni/Al_2O_3 were investigated using a temperature programmed reduction (TPR-1), which was performed by heating the catalysts up to 900°C in 5% H_2-He. The amount of hydrogen uptake is correlated to the amount of oxygen stored and enabled to consume in the ceria-based supports. The solid lines in Fig. 1 represent the results of TPR-1 for these three catalysts. It is apparent that the greater amount of hydrogen uptake is detected from Ni/CeO_2 (HSA) compared to Ni/CeO_2 (LSA), suggesting that the OSC strongly depends on the specific surface area of CeO_2. In contrast, hydrogen consumption was not observed from the TPR over Ni/Al_2O_3, indicating no occurrence of redox properties for this catalyst. After being purged with He, the redox reversibilities for Ni/CeO_2 (both LSA and HSA) were then determined by applying a temperature programmed oxidation (TPO) following with the second time temperature programmed reduction (TPR-2). Regarding the TPO and TPR-2 results as shown in Figs. 1 (dotted lines), 2 and Table 3, the amount of hydrogen uptakes for Ni/CeO_2 (both LSA and HSA) were approximately similar to those from TPR-1, indicating their redox reversibilities. It should be noted that the TPO over Ni/Al_2O_3 was also carried out to clarify the effect of Ni oxidation on the TPO spectra. As seen in Fig. 2, insignificant amount of oxygen uptake was observed over Ni/Al_2O_3, indicating that the observed oxygen uptakes for Ni/CeO_2 (both LSA and HSA) were mostly related to the redox property of CeO_2. The insignificant oxygen uptake for Ni/Al_2O_3 during TPO could be due to the presence of only small amount of Ni in the catalyst (5 wt%).

3.3.2 Homogenous (non catalytic) reaction

Before studying performances of the catalysts, homogeneous (non-catalytic) reaction was investigated. Previously, we reported the product distribution at different temperatures (150-1000°C) from the homogeneous steam reforming of ethanol [27]. Here, the homogeneous

steam reforming of ethanol in the presence of oxygen (as oxidative steam reforming) was further investigated. Similar trend as the steam reforming was observed. Firstly, ethanol was converted to acetaldehyde, and hydrogen at the temperature above 200°C via the dehydrogenation of ethanol (Eq. 2). Simultaneously, methane and carbon monoxide productions were initially observed at the temperature around 250-300°C via the fast decomposition of acetaldehyde (Eq. 3).

$$C_2H_5OH \rightarrow C_2H_4O + H_2 \quad (2)$$

$$C_2H_4O \rightarrow CH_4 + CO \quad (3)$$

The concentration of acetaldehyde significantly dropped at the temperature of 550°C and approached zero at the temperature of 650^{o}C. In this range of temperature, the formations of ethane and ethylene were observed. Ethane is formed by the dehydration of ethanol (Eq. 4) whereas the production of ethane is from ethylene hydrogenation (Eq. 5). This phenomenon is confirmed by the observation of lower H_2 selectivity compared to CO selectivity.

$$C_2H_5OH \rightarrow C_2H_4 + H_2O \quad (4)$$

$$C_2H_4 + H_2 \rightarrow C_2H_6 \quad (5)$$

The concentration of carbon monoxide, carbon dioxide, methane, ethane and ethylene remained almost constant at temperatures higher than 650^{o}C. It should be noted that, when compared to the homogeneous (non-catalytic) ethanol steam reforming at the same operating temperatures in our previous report [27], the addition oxygen along with ethanol and steam as autothermal reforming increased the conversion of ethanol and reduced the formations of ethane and ethylene. These are due to the possible oxidation of ethanol in the presence of oxygen forming more acetaldehyde (Eq. 6), which is eventually converted to methane and carbon monoxide. This oxidation reduces the degree of ethanol dehydration and consequently, less ethylene and ethane were generated.

$$C_2H_5OH + 1/2\ O_2 \rightarrow C_2H_4O + H_2O \quad (6)$$

Nevertheless, significant amount of ethylene and ethane (12-18%) remains observed from the homogeneous autothermal reforming of ethanol.

3.3.3 Reactivity towards ethanol steam reforming

The steam reforming of ethanol over Ni/CeO_2 (both LSA and HSA) and conventional Ni/Al_2O_3 without co-fed reactant were firstly tested at 900°C by introducing C_2H_5OH/H_2O in helium with the molar ratios of 1.0/1.0, 1.0/2.0, and 1.0/3.0 to the catalyst-bed. After 10 h operation, the catalyst reactivity expressed as yield of hydrogen production and the post reaction characterizations were measured, as presented in Table 4. The post-reaction temperature-programmed oxidation (TPO) experiments were also carried out after a helium purge by introducing 10% O_2 in He in order to determine the degree of carbon formation. From the TPO results shown in Fig. 3, small peaks of carbon dioxide and carbon monoxide were observed for Ni/CeO_2 (HSA) and Ni/CeO_2 (LSA), whereas huge amount of carbon dioxide and carbon monoxide formations were detected for Ni/Al_2O_3. The amount of carbon formations were then determined by measuring the CO and CO_2 yields from these TPO results. Using a value of 0.026 nm^2 for the area occupied by a carbon atom in a surface monolayer of the basal plane in graphite [31], the quantities of carbon deposited over Ni/CeO_2 (HSA), Ni/CeO_2 (LSA), and Ni/Al_2O_3 were observed to be approximately 1.08, 2.17, and 4.52 monolayers, respectively, for the inlet C_2H_5OH/H_2O ratio of 1.0/3.0. It should be noted that these values were found to decrease with increasing inlet H_2O concentration as shown in Table 5. In addition to the TPO method, the total amounts of carbon deposited were ensured by the calculations of carbon balance of the system. Regarding the calculations, the moles of carbon deposited per gram of Ni/CeO_2 (HSA), Ni/CeO_2 (LSA), and Ni/Al_2O_3 were 1.12, 2.19, and 4.55 mmol g^{-1}, respectively. Using the same assumption for the area occupied by a carbon atom [31], these values are equal to 1.08, 2.15, and 4.54 monolayers respectively, which is in good agreement with the values observed from the TPO method described above. These results clearly indicated the highest resistance towards carbon formation for Ni/CeO_2 (HSA).

The influence of operating temperature on the product distribution over Ni/CeO_2 (HSA), Ni/CeO_2 (LSA), and Ni/Al_2O_3 were further studied by varying temperature from 700°C to 1000°C. All product distributions over these catalysts at different temperature are presented in Table 6. It was found that the main products from the ethanol steam reforming over Ni/CeO_2 (HSA) were H_2, CO, CO_2, and CH_4, with small amounts of C_2H_4 and C_2H_6 depending on the operating temperature. In contrast, significant amounts of C_2H_4 and C_2H_6 were also observed as well as other chemical components from the ethanol steam reforming over Ni/CeO_2 (LSA) and Ni/Al_2O_3 in the range of conditions studied.

3.3.4 Reactivity towards reforming of ethanol with co-fed oxygen

Ni/CeO_2 (HSA) and Ni/Al_2O_3 were selected for further studied by adding oxygen together with ethanol and steam as autothermal reforming operation. The inlet C_2H_5OH/H_2O molar ratio was kept constant at 1.0/3.0, while the inlet O_2/C_2H_5OH molar ratios were varied from 0.2, 0.4, 0.6, 0.8, to 1.0. The effect of oxygen concentration on the variations in hydrogen yield (%) with time at 900°C for Ni/CeO_2 (HSA) and Ni/Al_2O_3 are shown in Figs. 4 and 5. The dependences of oxygen on the yield of hydrogen production are non-monotonic. The yield of hydrogen production increased with increasing O_2/C_2H_5OH molar ratio until the ratio reached 0.4 for Ni/CeO_2 (HSA) and 0.6 for Ni/Al_2O_3. Then, oxygen presented a negative effect on the hydrogen yield at higher inlet O_2/C_2H_5OH molar ratio values.

Fig. 6 (a and b) presents the comparison between the product distribution from the autothermal reforming of ethanol (with the suitable O_2/C_2H_5OH molar ratio for each catalyst) and those from the steam reforming over Ni/CeO_2 (HSA) and Ni/Al_2O_3 at different temperatures (700°C to 1000°C). It was found that the main products from the autothermal reforming of ethanol over both catalysts are similar to the steam reforming (e.g., H_2, CO, CO_2, and CH_4). Nevertheless, higher H_2, CO, and CO_2 were observed from the autothermal reforming, whereas less CH_4, C_2H_6, and C_2H_4 were found compared to the steam reforming at the same operating conditions.

The post-reaction temperature-programmed oxidations were then carried out to determine the degree of carbon formation on catalyst surface. From the TPO results shown in Table 7, significantly less quantities of carbon deposited were observed for both Ni/CeO_2 (HSA) and Ni/Al_2O_3. No carbon formation was detected on Ni/CeO_2 (HSA) when the inlet O_2/C_2H_5OH molar ratio reached 0.4.

Regarding the temperature-programmed reduction (TPR) experiments over the spent catalysts after exposure in autothermal reforming condition, the addition of too high oxygen content (higher than 0.4 for Ni/CeO_2 and 0.6 for Ni/Al_2O_3) results in the oxidation of Ni to NiO as shown in the last column of Table 7 and it consequently reduces the reforming reactivity of the catalysts. Therefore, in order to produce hydrogen from the autothermal reforming of ethanol, the inlet O_2/C_2H_5OH molar ratios of 0.4 for Ni/CeO_2 (HSA) and 0.6 for Ni/Al_2O_3 are the optimum ratio, which provide the highest resistance towards carbon deposition and are able to operate without the oxidation of Ni.

3.3.5 Reactivity towards reforming of ethanol with co-fed hydrogen

As a next step, hydrogen was added as co-feeding along with ethanol and steam at the feed. The inlet C_2H_5OH/H_2O molar ratio was kept constant at 1.0/3.0, while the inlet H_2/C_2H_5OH molar ratios were varied from 0.5-5.0. As hydrogen is a feed, the effect of this component on the catalyst performance was investigated in term of hydrocarbon (i.e. CH_4, C_2H_4, and C_2H_6) distribution instead of the yield of hydrogen production. Table 8 presents all product distribution from the steam reforming of ethanol in the presence of hydrogen for Ni/CeO_2 (HSA) and Ni/Al_2O_3. Apparently, the production of CH_4, C_2H_4, and C_2H_6 decreases with increasing H_2/C_2H_5OH molar ratio, which means the higher CH_4, C_2H_4, and C_2H_6 conversions occurred, until the ratio reached 3.0. Then, the effect of hydrogen becomes less pronounced at higher inlet H_2/C_2H_5OH ratio and eventually the CH_4 concentration slightly grows up. The post-reaction TPO were also carried out to determine the degree of carbon formation. From the TPO results as also shown in Table 8, with the presence of hydrogen, less amount of carbon deposited were observed for both Ni/CeO_2 (HSA) and Ni/Al_2O_3.

3.4. Discussion

According to the homogeneous (non-catalytic) oxidative steam reforming test, significant amount of ethylene and ethane were observed at the temperatures above 650°C. These formations are the major difficulties for the catalytic reforming of ethanol, as it has been widely established that at such a high temperature ethane and ethylene can easily decompose and form carbon species on the surface of catalyst ($C_nH_m \rightarrow 0.5mH_2 + nC$). Furthermore, in this range of temperature, in addition to the decomposition of ethane and ethylene, carbon formation can also be formed via the Boudouard reaction ($2CO \Leftrightarrow CO_2 + C$) during the catalytic steam reforming of ethanol. By increasing an inlet steam to ethanol molar ratio, the degree of carbon formation from the steam reforming of ethanol decreases, as the equilibrium of water-gas shift reaction moves forward producing more CO_2 rather than CO and eventually avoids carbon deposition via the Boudouard reaction. However, significant amount of carbon remains detected due to the decomposition of ethane, ethylene, and methane.

Ni/CeO_2 (HSA) was found in this study to have excellent resistance towards carbon deposition compared to conventional Ni/CeO_2 (LSA) and Ni/Al_2O_3. At the temperature above 800ºC, the main products from the reforming of ethanol over Ni/CeO_2 (HSA) were H_2,

CO, CO_2, and small amount of methane; neither ethylene nor ethane was observed from the system over this catalyst. The high resistance towards carbon deposition for Ni/CeO_2 (HSA) is mainly due to the high oxygen storage capacity (OSC) of ceria support. We previously reported the excellent resistance towards carbon deposition for CeO_2 especially for high surface area CeO_2 [25]. CeO_2 contains a high concentration of highly mobile oxygen vacancies and thus acts as a local source or sink for oxygen on its surface. It has been reported that at high temperature the lattice oxygen (O_O^x) at the CeO_2 surface can oxidize gaseous hydrocarbons (methane [25], ethane [27] and propane [27]). Although conventional CeO_2 (CeO_2 (LSA)) has also been reported to provide high resistance towards carbon formation, the major weaknesses of CeO_2 (LSA) are its low specific surface area and also high size reduction due to the thermal sintering impact, resulting in its significant lower redox properties than CeO_2 (HSA) and its lower Ni dispersion percentage on the surface compared to Ni/CeO_2 (HSA) and Ni/Al_2O_3. These disadvantages result in the low ethanol steam reforming reactivity for Ni/CeO_2 (LSA). By using Ni/CeO_2 (HSA) as a catalyst, in addition to the reaction on Ni surface, ethane and ethylene formations and the possible carbon depositions from these hydrocarbons could be inhibited by the gas-solid reactions between these hydrocarbons and the lattice oxygen (O_O^x) at CeO_2 surface forming hydrogen and carbon dioxide, which are thermodynamically unflavored to form carbon species. The lattice oxygen can then be regenerated by reaction with oxygen containing compounds (steam) present in the system.

It was also observed from the study that the addition of either oxygen or hydrogen together with ethanol and steam reduced the degree of carbon deposition. As described, the oxidation of oxygen with ethanol can prevent the formation of ethylene and ethane via the dehydration of ethanol. In addition, oxygen can prevent the formation of carbon species via the hydrocarbon depositions by oxidizing these hydrocarbons producing the elements that are unflavored to form carbon species. In the case of Ni/CeO_2, the presence of oxygen also helps steam to regenerate the lattice oxygen (O_O^x) on CeO_2 surface ($0.5O_2 + V_O^{\bullet\bullet} + 2\ e' \rightarrow O_O^x$). The major consideration of the autothermal reforming operation is the O_2/C_2H_5OH ratio. The presence of too high oxygen concentration could oxidize Ni particles to NiO, which has low reforming reactivity. The suitable oxygen concentration for the autothermal reforming of Ni/CeO_2 (O_2/C_2H_5OH molar ratio of 0.4) is lower than that of Ni/Al_2O_3 (O_2/C_2H_5OH molar ratio of 0.6) due to the high oxygen storage capacity (OSC) of CeO_2.

By adding hydrogen at the feed, the degree of carbon formation can be reduced by the hydrogenation reaction. The positive effect of hydrogen appearance on CH_4, C_2H_4, and C_2H_6 conversions could be due to the reduction of oxidized state on the surface active site of nickel (*) by hydrogen (H_2 + O-* $\Leftrightarrow$ H_2O + *), whereas the increase in CH_4 selectivity at high hydrogen partial pressure could be due to the promotion of the methanation, the reverse water-gas shift reactions and the reverse methane steam reforming [32, 33]. In addition, the occupying of hydrogen atom on some active sites of nickel particle (H_2 + 2* $\Leftrightarrow$ 2H-*) could also lead to the decrease in methane conversion, as explained by Xu and Froment [32, 33]. It should be noted, in addition, that the increase in CH_4 selectivity at high hydrogen partial pressure for Ni/CeO_2 could also be due to the reduction of lattice oxygen by hydrogen via the reverse of Eq. (21) and consequently inhibits the reaction of the lattice oxygen with the surface hydrocarbon species. This explanation is in good agreement with the previous studies [25, 31] which studied kinetics parameters for the methane steam reforming on ceria-based materials and reported the negative effect of hydrogen on methane conversion over these materials.

3.5. Conclusions

Ni on high surface area CeO_2 support (Ni/CeO_2 (HSA)) provides excellent reactivity towards the steam reforming of ethanol with high resistance toward carbon deposition and better product selectivities compared to Ni/Al_2O_3 and Ni on conventional low surface area ceria (Ni/CeO_2 (LSA)). The great benefits of Ni/CeO_2 (HSA) in terms of stability and reactivity toward ethanol reforming, high resistance towards carbon deposition, and good product selectivities are due to the high redox property of CeO_2 (HSA). An addition of oxygen (as autothermal reforming) and hydrogen can reduce the degree of carbon deposition and promote the conversions of hydrocarbons (i.e. CH_4 and C_2H_4) presented in the system to CO and H_2. The major consideration in adding these co-fed reactants is the suitable co-fed reactant/C_2H_5OH ratio. The presence of too high oxygen could reduce the yield of H_2 production, while too high hydrogen content could slightly decrease the catalyst activity.

3.6 References

[1] P. Aguiar, D. Chadwick and L. Kershenbaum, Chem. Eng. Sci. 57 (2002), p. 1665

[2] S. Cavallaro, S. Freni, Int. J. Hydrogen Energy 21 (6) (1996), p. 465.

[3] N.F. Athanasio, X.E. Verykios, J. Catal. 225 (4) (2004), p. 39.

[4] S. Cavallaro and S. Freni. Int. J. Hydrogen Energy 21 (1996), p. 465.

[5] S. Cavallaro. Energy and Fuels 14 (2000), p. 1195.

[6] S. Freni. J. Power Sour. 94 (2001), p. 14.

[7] S. Freni, S. Cavallaro, N. Mondello, L. Spadaro and F. Frusteri. J. Power Sour. 108 (2002), p. 53.

[8] A. Fatsikostas, D. Kondarides and X. Verykios. Catal. Today 75 (2002), p. 145.

[9] A. Fatsikostas, D. Kondarides and X. Verykios. Catal. Today 75 (2002), p. 145.

[10] D. Liguras, D. Kondarides and X. Verykios. Appl. Catal. B 43 (2003), p. 345.

[11] V.V. Galvita, V.D. Balyaer, V.A. Semikolenov, P. Tsiakaras, A. Frumin and V.A. Sobyanin. React. Kinet. Catal. Lett. 76 (2002), p. 343.

[12] J.P. Breen, R. Burch and H.M. Coleman. Appl. Catal. B 39 (2002), p. 65.

[13] N. Laosiripojana and S. Assabumrungrat, Appl. Catal. A 290 (2005), p. 200.

[14] L.V. Mattos, E. Rodino, D.E. Resasco, F.B. Possos and F.B. Noronha, Fuel Proc. Technol. 83 (2003), p. 147.

[15] H.S. Roh, K.W. Jun and S.E. Park, Appl. Catal. A 251 (2003), p. 275.

[16] J.R. Rostrup-Nielsen and J.-H. Bak-Hansen, J. Catal. 144 (1993), p. 38.

[17] X. Wang and R.J. Gorte, Appl. Catal. A 224 (2002), p. 209.

[22] A.A. Lemonidou, M.A. Goula and I.A. Vasalos, Catal. Today 46 (1987), p. 175.

[23] T. Takeguchi, S.N. Furukawa and M. Inoue, J. Catal. 202 (2001), p. 14.

[24] J. Sfeir, P.A. Philippe, P. Moseki, N. Xanthopoulos, R. Vasquez, J.M. Hans, V.H. Jan and K.R. Thampi, J. Catal. 202 (2001), p. 229.

[25] N. Laosiripojana and S. Assabumrungrat, Appl. Catal. B 60 (2005), p. 107.

[26] N. Laosiripojana, W. Sutthisripok, and S. Assabumrungrat, Chem. Eng. J. 112 (2005) p. 13.

[27] N. Laosiripojana, and S. Assabumrungrat, Appl. Catal. B 66/1-2 (2006) p. 29.

[28] D. Terribile, A. Trovarelli, J. Llorca, C. de Leitenburg and G. Dolcetti, Catal. Today 43 (1998), p. 79.

[29] C. Force, A. Ruiz Paniego, J.M. Guil, J.M. Gatica, C. Lopez-Cartes, S. Bernal, J. Sanz, Langmuir, 17 (2001), 2720.

[30] J. Wei and E. Iglesia, J. Catal, 225 (2004), 116.

[31] E. Ramirez, A. Atkinson and D. Chadwick, Appl. Catal. B 36 (2002), p. 193.

[32] J. Xu, G.F. Froment, AIChE., 35 (1989) 88.

[33] J. Xu, G.F. Froment, AIChE., 35 (1989) 97.

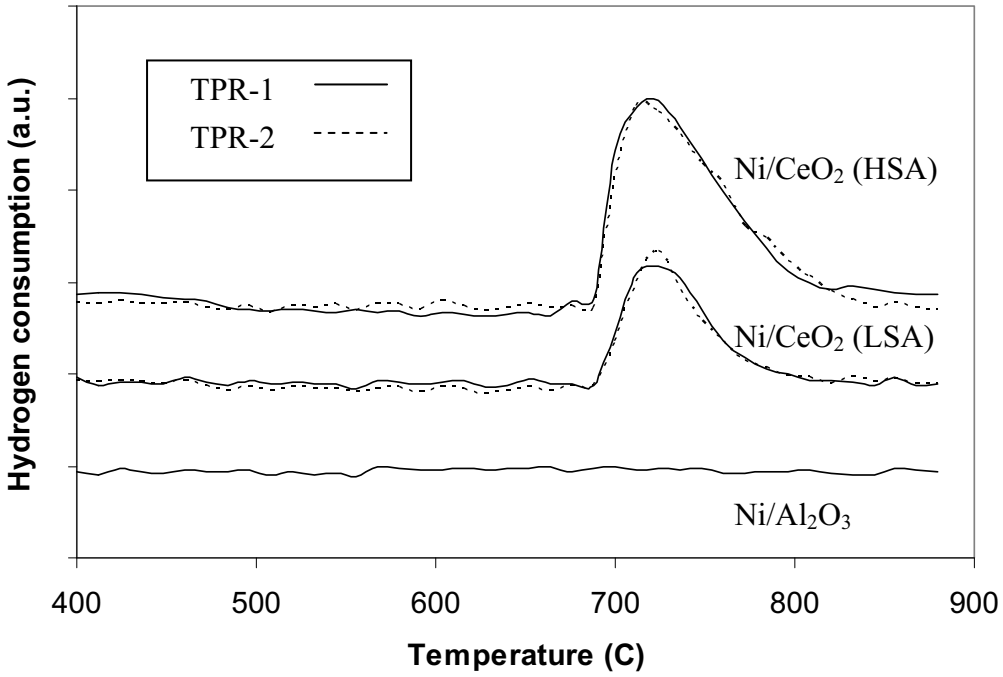

Fig. 1 Temperature Programmed Reduction (TPR-1) of fresh catalysts after reduction and second time Temperature Programmed Reduction (TPR-2) of Ni/CeO_2 (HSA and LSA).

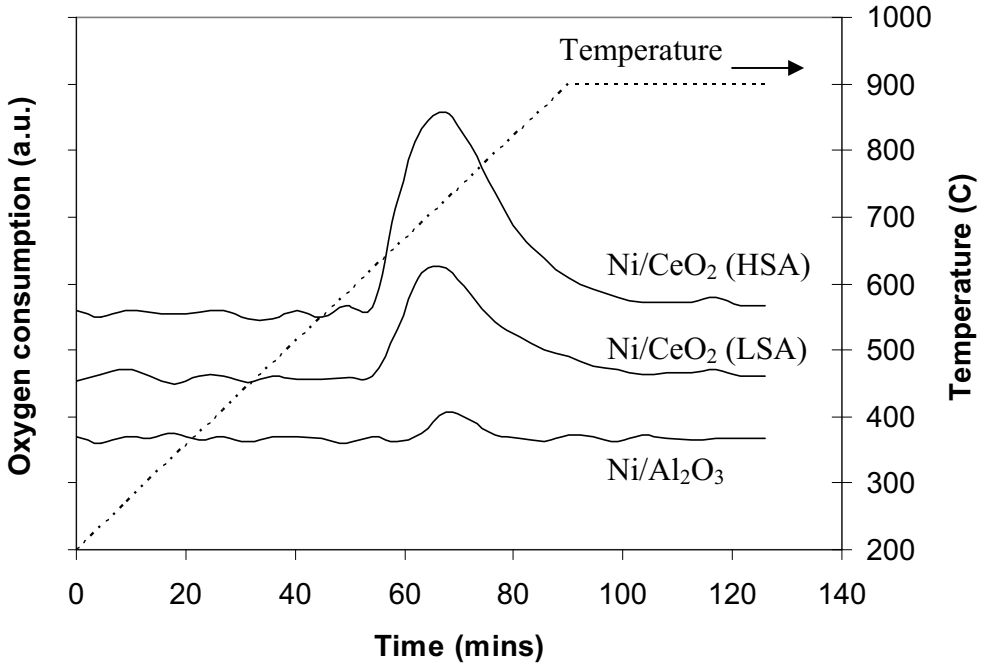

Fig. 2 Temperature Programmed Oxidation (TPO) of Ni/CeO_2 (HSA and LSA) and Ni/Al_2O_3 after TPR-1.

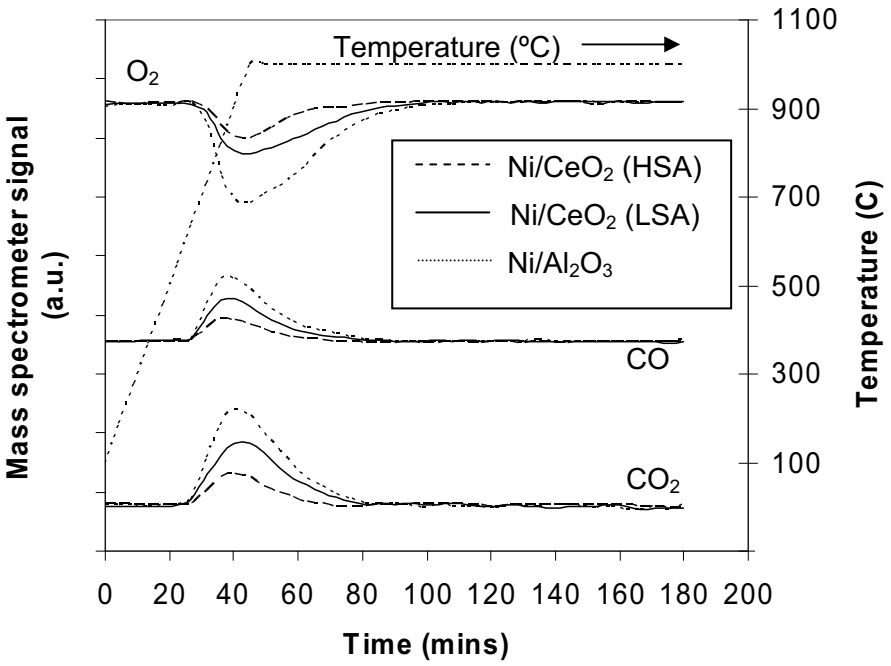

Fig. 3 Temperature Programmed Oxidation (TPO) of Ni/CeO_2 (HSA), Ni/CeO_2 (LSA), and Ni/Al_2O_3 after exposure in steam reforming of ethanol (4 kPa C_2H_5OH, and 12 kPa H_2O) for 10 h.

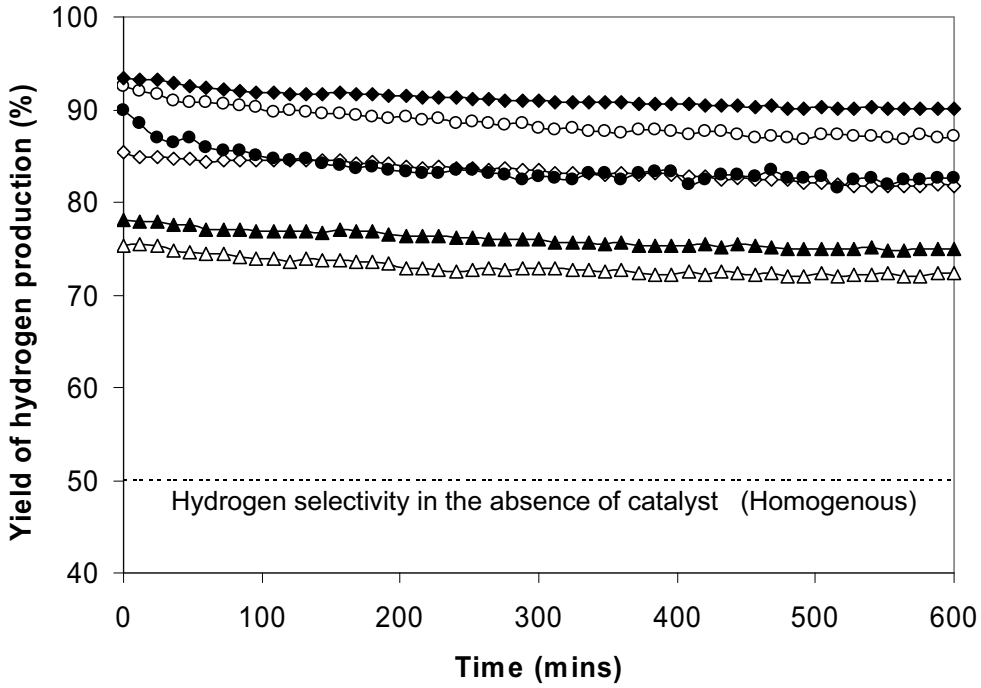

Fig. 4 Autothermal reforming of ethanol at 900ºC for Ni/CeO_2 (HSA) with the inlet O_2/C_2H_5OH ratios of 0 (●), 0.2 (○), 0.4 (◆), 0.6 (◇), 0.8 (▲), and 1.0 (△)) (4 kPa C_2H_5OH, and 12 kPa H_2O).

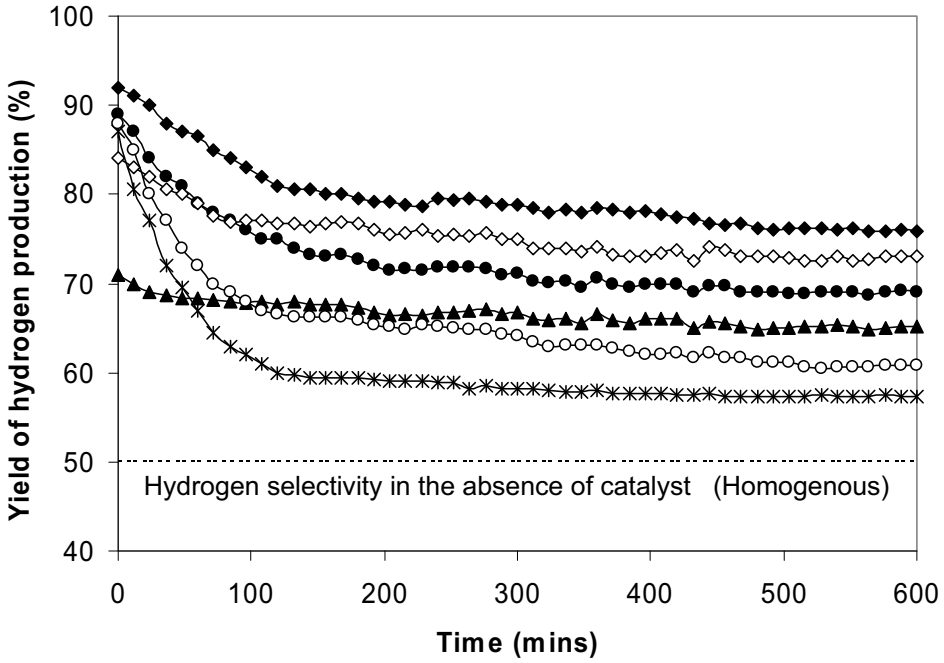

Fig. 5 Autothermal reforming of ethanol at 900°C for Ni/Al_2O_3 with the inlet O_2/C_2H_5OH ratios of 0 (×), 0.2 (○), 0.4 (●), 0.6 (◆), 0.8 (◇), and 1.0 (▲)) (4 kPa C_2H_5OH, and 12 kPa H_2O).

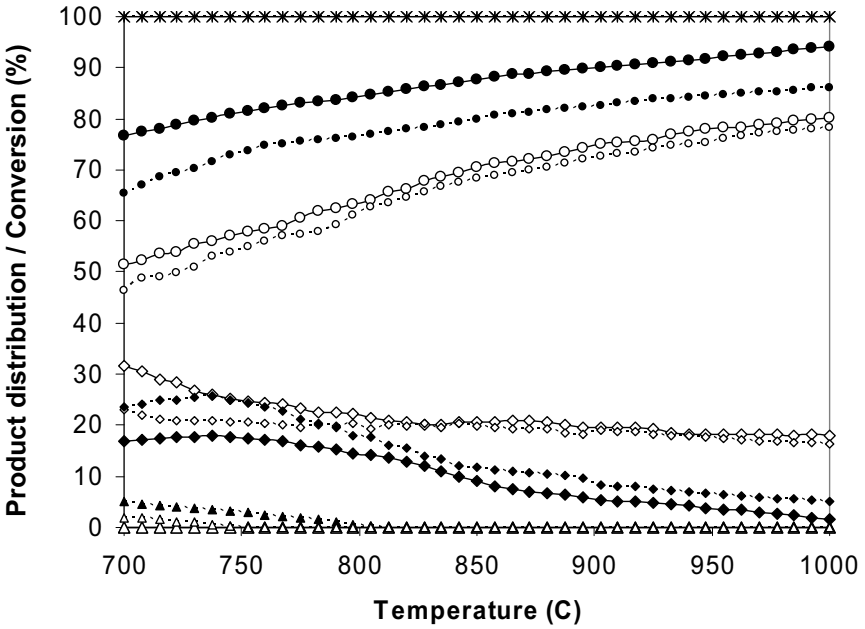

Fig. 6a

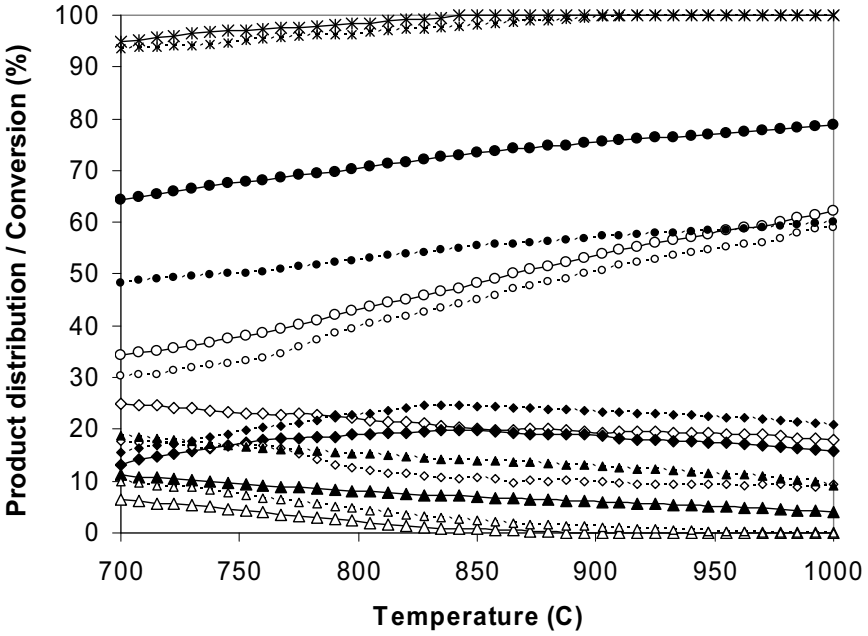

Fig. 6b

Fig. 6 Comparison of the conversion and product distributions (EtOH (×), H_2 (●), CO (○), CO_2 (◇), CH_4 (◆), C_2H_6 (△), and C_2H_4 (▲)) from steam reforming (small symbols with dot lines) (4 kPa C_2H_5OH, and 12 kPa H_2O) and autothermal reforming (large symbols with solid lines) (4 kPa C_2H_5OH, 12 kPa H_2O, and 1.6 kPa O_2) of ethanol over Ni/CeO_2 (HSA) (Fig. 8a) and Ni/Al_2O_3 (Fig. 8b).

Table 1
Specific surface area of CeO_2 (HSA and LSA) after drying and calcinations for 6 h at different temperatures

Catalyst	BET surface area (m^2 g^{-1}) after drying or calcination at						
	100ºC	200ºC	400ºC	600ºC	800ºC	900ºC	1000ºC
CeO_2 (LSA)[a]	55	49	36	21	15	11	8.5
CeO_2 (HSA)[b]	105	97	69	48	35	29	24

[a] conventional low surface area CeO_2 prepared by the precipitation method
[b] high surface area CeO_2 prepared by the surfactant-assisted approach

Table 2
Physicochemical properties of the catalysts after reduction

Catalyst	Ni-load (wt.%)	BET surface area (m^2 g^{-1})	Ni-reducibility (Ni%)	Ni-dispersion (Ni%)
Ni/CeO_2 (HSA)	5.0	24	92.2	6.41
Ni/CeO_2 (LSA)	4.8	8.5	91.3	3.12
Ni/Al_2O_3	5.0	40	94.5	4.85

Table 3
Results of TPR(1), TPO, TPR(2) analyses of Ni/CeO_2 (both CeO_2(HSA), CeO_2(LSA))

Catalyst	Total H_2 uptake from TPR(1)[a] (μmol/g_{cat})	Total O_2 uptake from TPO[b] (μmol/g_{cat})	Total H_2 uptake from TPR(2)[c] (μmol/g_{cat})
Ni/CeO_2 (HSA)	2104	1031	2100
Ni/CeO_2 (LSA)	1018	506	1015

[a] Temperature Programmed Reduction of the reduced catalysts
[b] Temperature Programmed Oxidation after TPR (1)
[c] Re-Temperature Programmed Reduction after TPO

Table 4
Yield of H_2 production and the physicochemical properties of catalysts after exposure in the steam reforming of ethanol at 900°C with different inlet C_2H_5OH/H_2O ratios

Catalyst	C_2H_5OH/H_2O ratio	Yield of H_2 production (%)	BET surface ($m^2\ g^{-1}$)	Ni-load (wt.%)	Ni-red. (Ni%)	Ni-disp. (Ni%)
Ni/CeO_2 (HSA)	1.0/3.0	82.5	23.2	4.9	90.2	6.39
	1.0/2.0	76.4	23.1	4.8	90.5	6.41
	1.0/1.0	65.5	23.2	4.8	90.4	6.37
Ni/CeO_2 (LSA)	1.0/3.0	61.1	9.8	4.8	89.2	3.11
	1.0/2.0	57.3	9.8	4.8	89.6	3.10
	1.0/1.0	54.6	9.5	4.7	89.7	3.12
Ni/Al_2O_3	1.0/3.0	57.2	40.0	4.9	92.0	4.85
	1.0/2.0	54.2	39.5	4.9	91.7	4.81
	1.0/1.0	53.1	40.0	4.8	91.8	4.83

Table 5
Dependence of inlet C_2H_5OH/H_2O ratio on the amount of carbon formation remaining on the catalyst surface

C_2H_5OH/H_2O ratio	Total carbon formation (monolayers)		
	Ni/CeO_2 (HSA)	Ni/CeO_2 (LSA)	Ni/Al_2O_3
1.0/3.0	1.08[a] (1.08)[b]	2.17 (2.15)	4.52 (4.54)
1.0/2.0	1.19 (1.17)	2.23 (2.21)	4.76 (4.78)
1.0/1.0	1.24 (1.26)	2.31 (2.34)	4.81 (4.79)

[a] Calculated using CO and CO_2 yields from temperature-programmed oxidation (TPO) with 10% oxygen.
[b] Calculated from the balance of carbon in the system.

Table 6
Products and amount of carbon deposition after exposure in the steam reforming of ethanol at different temperatures (with inlet C_2H_5OH/H_2O ratio of 1.0/3.0)

Catalyst	Temperature	Yield of H_2	Fraction of the by-products (%)					C formation
	(^oC)	production (%)	CO	CO_2	CH_4	C_2H_6	C_2H_4	(monolayers)
Ni/CeO_2 (HSA)	700	67.3	47.4	22.6	22.3	2.8	4.9	1.79
	800	78.3	60.6	20.4	18.7	~0	0.3	1.35
	900	82.5	70.1	19.3	10.6	~0	~0	1.08
	1000	86.9	76.6	16.6	6.8	~0	~0	0.82
Ni/CeO_2 (LSA)	700	49.7	41.4	18.9	27.8	3.3	8.6	3.02
	800	55.4	46.4	16.7	29.4	1.1	6.4	2.41
	900	61.1	53.9	15.8	26.3	~0	4.0	2.17
	1000	64.2	61.4	12.4	24.3	~0	1.9	2.09
Ni/Al_2O_3	700	48.1	33.1	19.7	17.7	10.3	19.2	4.97
	800	51.9	41.8	14.3	22.6	3.9	17.4	4.63
	900	57.2	49.7	10.0	24.4	1.4	14.5	4.52
	1000	59.8	59.5	9.7	20.9	~0	9.9	4.22

Table 7
Yield of H_2 production, deactivation percentages, and physicochemical properties of the catalysts after exposure in autothermal reforming of ethanol (with various inlet O_2/C_2H_5OH ratios) at 900ºC

Catalyst	Inlet O_2/C_2H_5OH molar ratio	Yield of H_2 (%) at steady state	Deactivation (%)	C formation (monolayers)	BET surface ($m^2\ g^{-1}$)	Ni-red. (Ni%)
Ni/CeO_2 (HSA)	0.0	82.5	8.2	1.08	23.1	90.2
	0.2	87.1	5.9	0.31	23.0	90.2
	0.4	90.1	3.4	~0	23.2	90.0
	0.6	81.7	4.3	~0	23.2	88.6
	0.8	74.9	3.9	~0	23.5	84.7
	1.0	72.2	3.9	~0	23.2	79.3
Ni/Al_2O_3	0.0	57.2	34.1	4.52	40.0	92.0
	0.2	60.7	30.9	3.16	39.6	91.6
	0.4	69.1	22.3	2.73	39.8	91.0
	0.6	75.8	17.5	2.14	40.0	90.8
	0.8	73.0	13.0	1.50	39.9	85.2
	1.0	65.1	8.2	1.03	39.9	81.6

Table 8
Product distributions and amount of carbon deposition after exposure in the steam reforming of ethanol (with various inlet H_2/C_2H_5OH ratios) at 900°C

Catalyst	Inlet H_2/C_2H_5OH molar ratio	Fraction of the carbon products (%)					C formation (monolayers)
		CO	CO_2	CH_4	C_2H_6	C_2H_4	
Ni/CeO_2 (HSA)	0.0	70.1	19.3	10.6	~0	~0	1.08
	0.5	70.8	19.6	9.6	~0	~0	0.72
	1.0	71.3	20.0	8.7	~0	~0	0.41
	2.0	72.7	20.7	6.6	~0	~0	0.39
	3.0	73.0	20.9	6.1	~0	~0	0.26
	4.0	73.3	19.8	6.9	~0	~0	0.22
	5.0	73.4	19.5	7.1	~0	~0	0.13
Ni/Al_2O_3	0.0	49.7	10.0	24.4	1.4	14.5	4.52
	0.5	51.1	10.7	24.0	0.6	13.6	3.97
	1.0	53.4	11.9	22.9	~0	11.8	2.69
	2.0	55.2	12.8	22.1	~0	9.9	2.41
	3.0	56.8	13.8	20.7	~0	8.7	2.06
	4.0	57.9	14.3	21.0	~0	6.8	1.87
	5.0	58.0	13.8	21.8	~0	6.4	1.62

RESEARCH IV

Catalytic steam reforming of dimethyl ether (DME) over high surface area Ce-ZrO_2 at SOFC operating temperature: The use of Ce-ZrO_2 as an internal pre-reforming catalyst

This study was aimed at developing a suitable reforming catalyst for later application in an indirect internal reforming Solid Oxide Fuel Cell (IIR-SOFC) fuelled by dimethyl ether (DME). It was found that, at temperature higher than 800°C, DME decomposed homogeneously, producing CH_4 and CH_3OH with small amount of CO, CO_2, and H_2. High surface area Ce-ZrO_2 can reform DME with steam efficiently at 900°C, producing high contents of H_2, CO, and CH_4 without the presence of CH_3OH in the product gas. The combination use of Ce-ZrO_2 (as a pre-reforming catalyst) and Ni/Al_2O_3 in the single unit was proven to significantly improve the reforming performance. According to this combination, the role of Ce-ZrO_2 is to first decompose CH_3OH and some CH_4 generated from the homogeneous decomposition of DME, while the role of Ni/Al_2O_3 is to reform CH_4 left from the pre-reforming section and to maximize the yield of H_2 production.

As another approach, IIR-SOFC model was studied using an annular ceramic reactor, in which DME initially reacted with steam on Ce-ZrO_2 + Ni/Al_2O_3 at the inner side of the reactor and then Ni/YSZ at the outer side. The stability and the yield of hydrogen production over this configuration were considerably higher than those of systems packed with single Ce-ZrO_2, single Ni/Al_2O_3, and without the filling of catalyst. In addition, the degree of carbon formation on the surface of Ni/YSZ was significantly low. The successful development of this reforming pattern improves the efficiency of IIR-SOFC fueled by DME by eliminating the requirement of an external reforming unit installation.

4.1 Introduction

Solid Oxide Fuel cell (SOFC) is an efficient electrochemical device that converts chemical energy to electrical energy with higher efficiency and lower pollutant emission compared to conventional processes [1]. H_2 and CO are the primary fuels for SOFC. Nevertheless, due to high operating temperature of SOFC (700-1100°C), it is known that some fuels (i.e. CH_4) can be directly fed to SOFC stacks; this operation is called a direct internal reforming SOFC (DIR-SOFC). According to this operation, the fuels are reformed at the anode producing H_2 and CO, which are electrochemically consumed for generating electricity simultaneously. An advantage of DIR-SOFC is that the H_2 consumption by the electrochemical reaction could promote the reforming or conversion of fuels at the anode side and consequently results in high conversion and efficiency [2].

DIR-SOFC operation requires an anode material that has good catalytic reforming and electrochemical reactivities. Ni/YSZ is the most common SOFC anode material due to its well-fitted properties for SOFC design requirement and its low cost compared with other supported metals (e.g. Co, Pt, Ru, and Rh). In addition, this material provides necessary catalytic reforming activity required for the DIR-SOFC operation. The nickel content for Ni/YSZ anode is usually 40 to 60% in order to match the thermal expansion of YSZ [3]. The major difficulty of DIR-SOFC operation over Ni/YSZ is the possible formation of carbon species on the surface of Ni due to the cracking of hydrocarbons. This formation could hinder gas access and degrade anode performance by blocking the catalyst active sites which resulted in the loss of cell performance and poor durability. Another alternative internal reforming operation is an indirect internal reforming (IIR-SOFC). By this operation, the reforming reaction takes place at a reformer located in close thermal contact with the anode side of SOFC. IIR-SOFC gives the advantage of good heat transfer between the reformer and the fuel cell and is expected to provide an autothermal operation. In addition, unlike DIR-SOFC, the reformer part and the anode side for IIR-SOFC operation are operated separately. Therefore, the catalyst for reforming reaction at the reformer part and the material for electrochemical reactions at the anode side of fuel cell can be optimized individually, preventing the possible degradation of anode from the carbon deposition.

Focusing on the fuel selection, methane is currently the major fuel for SOFC due to its well-developed supporting system and cost effectiveness. Nevertheless, the use of dimethyl ether (DME) should also be possible when operated as an internal or in-stack reforming. DME has several advantages; it is harmless and does not cause ozone layer destruction, and it is easy to handle like LPG. The approach in this work is to develop an indirect internal reforming operation that can reform DME efficiently at SOFC temperatures, 900ºC. The successful development of this operation would eliminate the requirement of the external reformer installation, making SOFC fueled by DME more efficient and attractive. Previously, hydrogen production from the reforming of DME has been studied over acid catalysts and Cu-based catalysts by several researchers; however, most of them have investigated the reforming of DME at low temperature [4-9].

In the present work, ceria-based catalyst was selected as the catalyst for the steam reforming of DME at SOFC operating temperature. Ceria-based catalysts have been commonly applied as catalysts in a wide variety of reactions involving oxidation or partial oxidation of hydrocarbons (e.g. automotive catalysis). A high oxygen mobility (redox property) [10], high oxygen storage capacity (OSC) [11], strong interaction with the supported metal (strong metal–support interaction) [12] and the modifiable ability [13] render this material very interesting for catalysis. Importantly, the reactivity toward methane steam reforming with high resistance toward carbon deposition over ceria has been observed [14-17]. Doped ceria with Zr (Ce-ZrO_2) has been reported to improve the specific surface area, oxygen storage capacity, redox property, thermal stability and catalytic activity. These benefits were associated with enhanced reducibility of cerium (IV) in CeO_2-ZrO_2 due to the high O^{2-} mobility inside the fluorite lattice. The reason for high mobility might be related to the lattice strain, which is generated by the introduction of a smaller isovalent Zr cation into the CeO_2 lattice (Zr^{4+} has a crystal ionic radius of 0.84 Å, which is smaller than 0.97 Å for Ce^{4+} in the same co-ordination environment) [18]. Therefore, Ce-ZrO_2 was selected for study in the present work. Furthermore, the benefit of applying Ce-ZrO_2 together with conventional Ni/Al_2O_3 was also studied.

As a next step, in order to study the possible use of Ce-ZrO_2 in IIR-SOFC, an annular ceramic reactor was designed and constructed. Details of this reactor

configuration will be described in Section 2.2. DME and steam were fed into this annular reactor packed with Ce-ZrO_2 and/or Ni/Al_2O_3, as reforming catalysts, and Ni/YSZ, an anode material of SOFC. The stability and reforming reactivity toward this operation was investigated compared to those without the use of reforming catalysts (DIR operation).

4.2 Experimental

4.2.1 Material preparation and characterization

Ce-ZrO_2 with different Ce/Zr molar ratios were prepared by co-precipitation of cerium nitrate ($Ce(NO_3)_3 \cdot H_2O$), and zirconium oxychloride ($ZrOCl_2 \cdot H_2O$) (from Aldrich). The ratio between both solutions was altered to achieve Ce/Zr molar ratios of 1/3, 1/1 and 3/1. It should be noted that aqueous solution of 0.1 M cetyltrimethylammonium bromide solution (from Aldrich) was also added in the cerium nitrate and zirconium oxychloride solution as a cationic surfactant. Our previous work reported that the preparation of ceria-based material by this surfactant-assisted method can achieve high surface area and high thermal stability due to the incorporation of surfactants during preparation, which reduces the interfacial energy and eventually decreases the surface tension of water contained in the pores [14, 19-20].

In the present work, the molar ratio of (([Ce]+[Zr])/ [cetyltrimethylammonium bromide] was kept constant at 0.8. The solid solution was formed by mixing 0.1 M of metal salt solution with 0.4 M of urea at a 2:1 volumetric ratio. This solution was stirred by a magnetic stirrer (100 rpm) for 3 h, and the precipitate was filtered and washed with deionised water and ethanol to prevent an agglomeration of the particles. It was dried overnight in an oven at 110°C, and then calcined in air at 1000°C for 6 h. Fig. 1 shows the SEM micrographs of Ce-ZrO_2 (with Ce/Zr = 3/1) synthesized by the above surfactant-assisted method (1a), compared to that synthesized by typical co-precipitation method (1b) (without the filling of cetyltrimethylammonium bromide solution). It is clear that the particle size of Ce-ZrO_2 synthesized by the surfactant-assisted method (Ce-ZrO_2 (High surface area; HSA)) is significantly smaller than that synthesized by typical co-precipitation method (Ce-ZrO_2 (Low surface area; LSA)).

Ni/Al_2O_3 catalysts were prepared by impregnating γ-Al_2O_3 with $Ni(NO_3)_2$ solution (Aldrich). The catalysts were reduced with 10%H_2/He before use. After reduction, the catalysts were characterized with several physicochemical methods. The weight content of Ni in Ni/Al_2O_3 was determined by X-ray fluorescence (XRF) analysis. The reducibility and dispersion percentages of nickel were measured from temperature-programmed reduction (TPR) with 5% H_2 in Ar and temperature-programmed desorption (TPD), respectively. The catalyst specific surface areas were obtained from BET measurements, which were carried out before and after calcination in order to determine its changes. All physicochemical properties of the synthesized catalysts are presented in Table 1. It should be noted that, after treatment, the degree of oxygen storage capacity (OSC) and redox reversibilities of all Ce-ZrO_2 (both HSA and LSA with different Ce/Zr ratios) were determined by the temperature programmed reduction (TPR-1) and temperature programmed oxidation (TPO) following with second time temperature programmed reduction (TPR-2), respectively, at the same conditions. Details of these measurements are given in Section 3.1.

4.2.2 Annular reactor configuration

An annular ceramic reactor was constructed in order to study the use of DME in IIR operation, Fig. 2. According to the design, the reforming catalysts (Ce-ZrO_2 and/or Ni/Al_2O_3) were packed at the inner side of the annular reactor, where the inlet gas was firstly introduced. At the end of the inner tube, all gas components flowed backward through the outer side of this annular reactor, where 300 mg of Ni/YSZ (with SiC) was packed. Therefore, both reforming catalysts and Ni/YSZ were operated at the same operating temperature. The main obligation of Ce-ZrO_2 and Ni/Al_2O_3 was to reform DME before reaching the surface of Ni/YSZ, preventing the possible degradation of Ni/YSZ by the carbon formation. It should be noted that Ni/YSZ in the present work was prepared by mixing NiO (42.86 vol%) with YSZ (57.14 vol%) with a ball milling for 18 h at room temperature. The catalyst was calcined in air at 1000°C for 6 h and then reduced with 10%H_2/Ar for 6 h before use.

4.2.3. Apparatus and Procedures

An experimental reactor system was constructed as shown in Fig. 3. The feed gases including the components of interest (DME and steam) and the carrier gas (helium) were introduced to the reaction section, in which either a quartz reactor (for primary study) or the annular ceramic reactor (for IIR study) was mounted vertically inside a furnace. Regarding the results in our previous publications [19-20], to avoid any limitations by external mass transfer, the total gas flow was 1000 cm^3 min^{-1} under a constant residence time of 5 x 10^{-4} g min cm^{-3} in all experiments. A Type-K thermocouple was placed into the annular space between the reactor and the furnace, while another Type-K thermocouple was inserted in the middle of the quartz tube in order to re-check the possible temperature gradient. The record showed that the maximum temperature fluctuation during the reaction was always ± 0.75°C or less from the temperature specified for the reaction. After the reactions, the exit gas mixture was transferred via trace-heated lines to the analysis section, which consisted of a Porapak Q column Shimadzu 14B gas chromatograph (GC) and a mass spectrometer (MS).

The steam reforming of DME reactivity and the product selectivity were studied. In order to study the formation of carbon species on catalyst surface, Temperature programmed Oxidation (TPO) was applied by introducing 10% O_2 in helium, after purging the system with helium. The operating temperature increased from 100 to 1000ºC at a rate of 20ºC min^{-1}. The amounts of carbon formation (mmol g_{cat}^{-1}) on the surface of catalysts were determined by measuring the CO and CO_2 yields from the TPO results (using Microcal Origin Software) [21].

In order to study the steam reforming reactivity, the rate of DME reforming was defined in terms of conversion denoted as X_{DME}, and product selectivities denoted as $S_{product}$. Selectivities of products (i.e. CO, CO_2, CH_4, and CH_3OH) were calculated by the carbon balance, defined as the ratios of the product moles to the consumed moles of hydrocarbon, accounting for stoichiometry. This information was presented in term of (relative) fraction of all by-product components, which are summed to 100%. H_2 selectivity was calculated by the H_2 balance, defined as the mole of H_2 produced to the total H_2 in the products.

$$X_{\mathrm{DME}} = \frac{100(\mathrm{DME}_{\mathrm{in}} - \mathrm{DME}_{\mathrm{out}})}{\mathrm{DME}_{\mathrm{in}}} \quad (1)$$

$$S_{\mathrm{Pr}\,oduct} = \frac{100(\mathrm{Mole\ of\ a\ specific\ product})}{(\mathrm{Total\ moles\ of\ all\ products})} \quad (2)$$

4.3 Results and Discussion

4.3.1 Oxygen storage capacities (OSC) and redox reversibility

The degree of oxygen storage capacities (OSC) for all Ce-ZrO_2 after calcination were investigated using TPR-1, which was performed by heating the catalysts up to 1000°C in a flow of 5%H_2 in He. The amount of H_2 uptake was correlated to the amount of oxygen stored in the catalysts. It should be noted that the test over Ni/Al_2O_3 was also performed for comparison. As shown in Fig. 4, the amount of H_2 uptakes over Ce-ZrO_2 (HSA) with Ce/Zr ratio of 3/1 are significantly higher than those observed over Ce-ZrO_2 (HSA) with Ce/Zr ratios of 1/1 and 1/3, suggesting its highest degree of OSC. In contrast, no H_2 consumption was observed from the TPR over Ni/Al_2O_3, indicating no occurrence of redox properties for this catalyst. It should also be noted that the amount of H_2 uptake over Ce-ZrO_2 (HSA) is significantly higher than that over Ce-ZrO_2 (LSA) at the same Ce/Zr ratio, suggesting the strong dependency of the degree of OSC on the specific surface area of Ce-ZrO_2. The benefit of OSC on the reforming reaction will be presented later in Section 3.3.

After the system was purged with helium, the redox reversibilities were then determined by applying TPO following with TPR-2. The TPO was carried out by heating the catalyst up to 1000°C in 10%O_2 in helium; the amounts of oxygen chemisorbed were then measured, Table 2. Regarding the TPR-2 results as also shown in Table 2, the amount of hydrogen uptakes for all catalysts were approximately similar to those from the first time reduction reaction (TPR-1), indicating the redox reversibility for these synthesized Ce-ZrO_2.

4.3.2 Homogenous (non catalytic) reaction

Before studying the catalytic performance, the homogeneous (non-catalytic) steam reforming of DME was primarily investigated. The inlet DME/H_2O in helium with the molar ratio of 1.0/3.0 (inlet DME partial pressure of 4 kPa) was introduced to the system, while the temperature increased from 100 to 1000ºC. As shown in Fig. 5, it was observed that DME was converted to methanol at the temperature above 800°C according to the hydration of DME (Eq. 3). CH_4, CO, CO_2, and H_2 were then observed at the temperature above 825°C from the decomposition of CH_3OH (Eq. 4), water gas shift (Eq. 5) and methanation reactions (Eq. 6). At 900°C, the conversion of DME is close to 100%.

$$CH_3OCH_3 + H_2O = 2CH_3OH \quad (3)$$

$$CH_3OH = 2H_2 + CO \quad (4)$$

$$CO + H_2O = H_2 + CO_2 \quad (5)$$

$$CO + 3H_2 = CH_4 + H_2O \quad (6)$$

It should be noted that the formations of higher molecular weight compounds such as formaldehyde, methyl formate and formic acid were found to be negligible.

4.3.3 Steam reforming of DME over Ce-ZrO_2

Ce-ZrO_2 with several Ce/Zr ratios were tested for the steam reforming of DME at 900°C with the inlet fuel/steam molar ratio of 1.0/3.0 (inlet DME partial pressure of 4 kPa). The reforming rate was measured as a function of time in order to indicate the stability and the deactivation rate. The variations in the hydrogen selectivity with time at 900°C are shown in Fig. 6. It was observed from the figure that Ce-ZrO_2 with Ce/Zr ratio of 3/1 provided the highest hydrogen selectivity. Consequently, Ce-ZrO_2 with Ce/Zr ratio of 3/1 was selected for further investigations. Catalyst stabilities expressed as deactivation percentages as well as the product selectivities are given in Table 3. It is clear that methane, hydrogen, carbon monoxide, and carbon dioxide are the main products, whereas the selectivity of methanol is closed to 0.

As shown in Fig. 4, according to the steam reforming of DME at 900°C, the main components present in the system are methanol and methane with some amounts of CO, CO_2, and H_2. The DME steam reforming reactivity for Ce-ZrO_2 is due to the gas-solid reactions between the above products generated from the homogenous DME steam reforming reaction and the lattice oxygen (O_O^x) at Ce-ZrO_2 surface. The redox mechanism between these gas components with the lattice oxygen (O_O^x) could be derived as illustrated below.

$$CH_3OH + S_{Ce} \Leftrightarrow CH_2\text{-}S_{Ce} + H_2O \quad (7)$$

$$CH_4 + 2S_{Ce} \Leftrightarrow CH_3\text{-}S_{Ce} + H\text{-}S_{Ce} \quad (8)$$

$$CH_3\text{-}S_{Ce} + S_{Ce} \Leftrightarrow CH_2\text{-}S_{Ce} + H\text{-}S_{Ce} \quad (9)$$

$$CH_2\text{-}S_{Ce} + S_{Ce} \Leftrightarrow CH\text{-}S_{Ce} + H\text{-}S_{Ce} \quad (10)$$

$$CH\text{-}S_{Ce} + S_{Ce} \Leftrightarrow C\text{-}S_{Ce} + H\text{-}S_{Ce} \quad (11)$$

$$C\text{-}S_{Ce} + O_O^x \Leftrightarrow CO + V_O^{\bullet\bullet} + 2\,e' + S_{Ce} \quad (12)$$

$$2H\text{-}S_{Ce} \Leftrightarrow H_2 + 2S_{Ce} \quad (13)$$

S_{Ce} is the Ce-ZrO_2 surface site and CH_x-S_{Ce} is an intermediate surface hydrocarbon species. S_{Ce} can be considered to be a unique site, or the same site as the lattice oxygen (O_O^x). $V_O^{\bullet\bullet}$ is an oxygen vacancy with an effective charge 2^+, e' is an electron which can either be more or less localized on a cerium ion or delocalized in a conduction band [22]. During the reaction, hydrocarbons are adsorbed on either a unique site (S_{Ce}) or the lattice oxygen (O_O^x). The lattice oxygen is then regenerated by reaction with oxygen containing compounds (i.e. steam) present in the system, Eq. 14.

$$H_2O + + V_O^{\bullet\bullet} + 2\,e' \Leftrightarrow H_2 + O_O^x \quad (14)$$

It should be noted that the measured value of the oxygen diffusion coefficient for ceria is high and the reaction rate is controlled by a surface reaction, not by diffusion of oxygen from the bulk of the solid particles to ceria surfaces [23].

After reaction, the post-reaction temperature-programmed oxidation (TPO) experiments were carried out to investigate the amount of carbon formation on the surface of Ce-ZrO_2. From the TPO results as shown in Fig. 7 and Table 3, some amounts of carbon deposition (mmol g_{cat}^{-1}) were observed over Ce-ZrO_2 with Ce/Zr ratios of 1/1 and 1/3, whereas significantly lower carbon formations were detected over Ce-ZrO_2 with Ce/Zr ratios of 3/1. It should be noted that the degree of carbon deposition observed from the steam reforming of DME over Ce-ZrO_2 was significantly lower than that observed over Ni/Al_2O_3 at the same operating conditions (Table 6). Theoretically, the carbon species can be formed during the steam reforming process by several reactions. Eqs. 15-18 below present the most probable reactions that could lead to carbon deposition from the system of the steam reforming:

$$CH_4 \Leftrightarrow 2H_2 + C \quad (15)$$

$$2CO \Leftrightarrow CO_2 + C \quad (16)$$

$$CO + H_2 \Leftrightarrow H_2O + C \quad (17)$$

$$CO_2 + 2H_2 \Leftrightarrow 2H_2O + C \quad (18)$$

C is the carbonaceous deposits. At low temperature, Eqs. (17-18) are favorable, while Eqs. (15-16) are thermodynamically unflavored [24]. The Boudouard reaction (Eq. 16) and the decomposition of methane (Eqs. 15) are the major pathways for carbon formation at such a high temperature as they show the largest change in Gibbs energy [25]. According to the range of temperature in this study, carbon formation would be formed via the decomposition of methane and Boudouard reaction.

The good steam reforming reactivity with high resistance toward carbon deposition for Ce-ZrO_2 is mainly related to its high oxygen storage capacity (OSC). By applying Ce-ZrO_2, both decomposition and Boudouard reactions (Eqs. 15 and 16) could be inhibited by the gas-solid redox reactions between methane and carbon monoxide with the lattice oxygen (O_O^x) at Ce-ZrO_2 surface (Eqs. 19 and 20), forming hydrogen and carbon dioxide, which are thermodynamically unflavored to form carbon species in this range of conditions.

$$CH_4 + O_O^x = CO + 2\,H_2 + V_O^{\bullet\bullet} + 2\,e' \quad (19)$$

$$CO + O_O^x = 2CO_2 + V_O^{\bullet\bullet} + 2\,e' \quad (20)$$

The highest reforming reactivity and greatest resistance toward carbon deposition for Ce-ZrO_2 (HSA) with Ce/Zr ratio of 3/1 is due to the significantly higher amount of lattice oxygen (O_O^x) on their surfaces, according to the results in Section 3.1. The high amount of lattice oxygen (O_O^x) promotes the redox reaction of intermediate surface hydrocarbon species (C-S_{Ce}) with the lattice oxygen (O_O^x) (Eq. 12) and also the redox reactions of methane and carbon monoxide with the lattice oxygen (Eqs. 19 and 20).

Table 4 and 5 present the effects of steam and temperature on the product contribution and degree of carbon deposition from the steam reforming of DME over Ce-ZrO_2. Clearly, hydrogen selectivity increased with increasing temperature, whereas methane and methanol selectivities decreased. Furthermore, the amount of carbon formation significantly decreased with increasing temperature. These are due to the higher reforming reactivity of methane and methanol at high temperature. It should be noted that the thermodynamic analysis for the steam reforming of DME at 900-1000°C were also performed using AspenPlus10.2 simulation program. At equilibrium condition, the main products from the steam reforming of DME in the range of temperature between 900-1000°C are only hydrogen, carbon monoxide, and carbon dioxide. Very few amount of methane ($3.7 \times 10^{-7} - 2.4 \times 10^{-6}$ kPa) was detected, whereas no formation of methanol was observed from the calculations. These calculated values are also presented in Table 5 (in the blanket). The deviations of the experimental results from the thermodynamic values are due to several side reactions. For instance, methanol can be formed by the hydration of DME, while methane can be generated from the reforming and decomposition of methanol as well as methanation reactions.

According to the effect of steam, hydrogen and carbon dioxide selectivities increased with increasing inlet steam concentration, whereas carbon monoxide selectivity decreased. The changes of hydrogen, carbon monoxide, and carbon dioxide selectivities are mainly due to the influence of mildly exothermic water-gas shift reaction, whereas the

decrease of methane production is due to the further reforming to carbon monoxide and hydrogen.

4.3.4 Steam reforming of DME over Ni/Al_2O_3 and ($Ce\text{-}ZrO_2$ + Ni/Al_2O_3)

The steam reforming of DME over Ni/Al_2O_3 was first studied at 900°C with the same inlet conditions as the case with $Ce\text{-}ZrO_2$. Table 6 presents the product selectivities from the steam reforming of DME over Ni/Al_2O_3 compared to those over $Ce\text{-}ZrO_2$ and without catalyst (homogeneous). Clearly, hydrogen selectivity observed from the steam reforming of DME over Ni/Al_2O_3 is lower than that over $Ce\text{-}ZrO_2$, whereas methanol selectivity is significantly higher.

As another approach of this work, $Ce\text{-}ZrO_2$ was then applied together with Ni/Al_2O_3 in the single unit either as the co-reforming catalyst by mixing both materials ($Ce\text{-}ZrO_2$ + Ni/Al_2O_3) or as the pre-reforming catalyst by packing in the different layers ($Ce\text{-}ZrO_2$ – Ni/Al_2O_3). It should be noted that the total weight was always kept constant at 500 mg in all experiments. In the case of combination pattern, 200 mg of $Ce\text{-}ZrO_2$ and 300 mg of Ni/Al_2O_3 were used. Fig. 8 shows the variations in the hydrogen selectivity with time at 900°C over both configurations compared to those from the systems with single Ni/Al_2O_3 and single $Ce\text{-}ZrO_2$. The hydrogen selectivities from the pre-reforming configuration ($Ce\text{-}ZrO_2$ – Ni/Al_2O_3) were significantly higher than those over the co-reforming configuration ($Ce\text{-}ZrO_2$ + Ni/Al_2O_3), single Ni/Al_2O_3 and single $Ce\text{-}ZrO_2$. In addition, the methane and methanol selectivities over this configuration were reduced, Table 6.

By applying $Ce\text{-}ZrO_2$ as the pre-reforming catalyst, the main purpose of $Ce\text{-}ZrO_2$ is to convert methanol (and some methane) from the homogenous decomposition of DME to methane, carbon monoxide, and hydrogen before these components reach the surface of Ni/Al_2O_3. Therefore, the main reaction over Ni/Al_2O_3 is the steam reforming of methane instead of the steam reforming of methanol or DME, which is thermodynamically unfavored to form carbon deposition.

4.3.5 Steam reforming with IIR-SOFC configuration

It is clear from the above observation that the use of Ce-ZrO_2 as the pre-reforming catalyst along with Ni/Al_2O_3 can catalyze the steam reforming of DME efficiently. The next approach is to investigate the possible use of this reforming operation for IIR-SOFC by applying the annular ceramic reactor as described above.

With the same feeding conditions, Fig. 9 and Table 7 respectively present the stability and the product selectivities at 900°C from the pre-reforming configuration (Ce-ZrO_2 – Ni/Al_2O_3) compared to those with the co-reforming configuration (Ce-ZrO_2 + Ni/Al_2O_3), single Ni/Al_2O_3 (Ni/Al_2O_3 / Ni/YSZ), with single Ce-ZrO_2 (Ce-ZrO_2 / Ni/YSZ), and without the filling of Ce-ZrO_2 and Ni/Al_2O_3 (Ni/YSZ).

The stability and the yield of hydrogen production from the steam reforming of DME over pre-reforming configuration were considerably higher than the others. At steady state, the yield of hydrogen production was close to the calculated equilibrium value. In addition, according to the results of TPO after reaction, the amount of carbon formation on the surface of Ni/YSZ was significantly low, Table 7. These improvements are due to the high conversions of methane and methanol, which are thermodynamically favored to form carbon deposition, by Ce-ZrO_2 and Ni/Al_2O_3 before these components reach the surface of Ni/YSZ at the outer side of the annular reactor.

4.4 Conclusion

DME can be decomposed homogeneously without the requirement of catalyst at high temperature, producing methane and methanol with small amount of carbon monoxide, carbon monoxide, and hydrogen. The use of Ce-ZrO_2 as the pre-reforming catalyst along with Ni/Al_2O_3 was an efficient way to catalyze the steam reforming of DME, producing high contents of hydrogen and carbon monoxide with low selectivity of by-products (i.e. methane). The role of Ce-ZrO_2 for the steam reforming of DME is to decompose methanol and some methane (generated by the homogeneous decomposition of DME), while the role of Ni/Al_2O_3 is to decompose methane left from the reforming over Ce-ZrO_2 to hydrogen and carbon monoxide.

By applying Ce-ZrO_2 and Ni/Al_2O_3 as internal pre-reforming catalysts, this reforming pattern provided good hydrogen selectivity and high resistance toward carbon

deposition on Ni/YSZ. It converts DME, methanol, and most of methane and maximizes the yield of hydrogen production. This successful development can improve the efficiency of IIR-SOFC fueled by DME by eliminating the requirement of an external pre-reforming unit installation.

References

[1] R. George, Fuel Cell Handbook, Sixth Edition, by EG&G Technical Services,Inc. Science Applications International Corp., Under Contract No. DE-AM-26-99FT40575, U.S. Dept. of Energy, Office of Fossil Energy, National Energy Technology Laboratory, Morgantown, W. Virginia.

[2] S.H. Clarke, A.L. Dicks, K. Pointon, T.A. Smith and A. Swann, Catalysis Today, 38(4), (1997), 411-423

[3] K.C. Wincewicz, and J.S. Cooper, J. Power Sources, 140, (2005), 280-296.

[4] K. Oka, T. Nishiguchi, H. Kanai, K. Utani and S. Imamura, Appl. Catal. A: General, 309(2), (2006), 187-191

[5] T.A. Semelsberger, K.C. Ott, R.L. Borup and H.L. Greene, Appl. Catal. A: General, 309(2), (2006), 210-223

[6] T. Kawabata, H. Matsuoka, T. Shishido, D. Li, Y. Tian, T. Sano and K. Takehira, Appl. Catal. A: General, 308, (2006), 82-90

[7] T.A. Semelsberger, K.C. Ott, R.L. Borup and H.L. Greene, Appl. Catal. B: Environmental, 65(3-4), (2006), 291-300

[8] K. Faungnawakij, Y. Tanaka, N. Shimoda, T. Fukunaga, S. Kawashima, R. Kikuchi and K. Eguchi, Appl. Catal. A: General, 304, (2006), 40-48

[9] T. Nishiguchi, K. Oka, T. Matsumoto, H. Kanai, K. Utani and S. Imamura, Appl. Catal. A: General, 301(1), (2006), 66-74

[10] P. Fornasiero, G. Balducci, R.D. Monte, J. Kaspar, V. Sergo, G. Gubitosa, A. Ferrero and M. Graziani. J. Catal. 164 (1996) 173.

[11] T. Miki, T. Ogawa, M. Haneda, N. Kakuta, A. Ueno, S. Tateishi, S. Matsuura and M. Sato, J. Phys. Chem. 94 (1990) 339.

[12] L. Fan and K. Fujimoto. J. Catal. 172 (1997) 238.

[13] M. Pijolat, M. Prin and M. Soustelle. J. Chem. Soc., Faraday Trans. 91 (1995) 3941.

[14] N. Laosiripojana and S. Assabumrungrat, Appl. Catal. B: Environ, 60 (2005) 107.

[15] N. Laosiripojana, W. Sutthisripok, and S. Assabumrungrat, Chem. Eng. Journal 112 (2005) 13-22.

[16] N. Laosiripojana, W. Sangtongkitcharoen, and S. Assabumrungrat, Fuel, In Press

[17] N. Laosiripojana and S. Assabumrungrat, Appl. Catal. A: General, 290 (2005) 200.

[18] D. Kim, J. Am. Ceram. Soc., 72, (1989), 1415

[19] N. Laosiripojana and S. Assabumrungrat, J. Power Sources, 158(2), (2006), 1348-1357.

[20] N. Laosiripojana and S. Assabumrungrat, Appl. Catal. B: Environmental, 66(1-2), (2006), 29-39

[21] E. Ramirez, A. Atkinson and D. Chadwick, Appl. Catal. B 36 (2002) 193–206.

[22] P.J. Gellings and H.J.M. Bouwmeester (2000), Solid state aspects of oxidation catalysis, Catalysis Today, 58, 1-53.

[23] B.C.H. Steele and J.M. Floyd. Proc. Br. Ceram. Soc. 19 (1971) 55.

[24] Y. Lwin, W.R.W. Daud, A.B. Mohamad and Z. Yaakob, Int. J. Hydrogen Energy, 25(1), (2000), 47-53.

[25] J.N. Amor, Appl. Catal. A 176 (1999) 159–176.

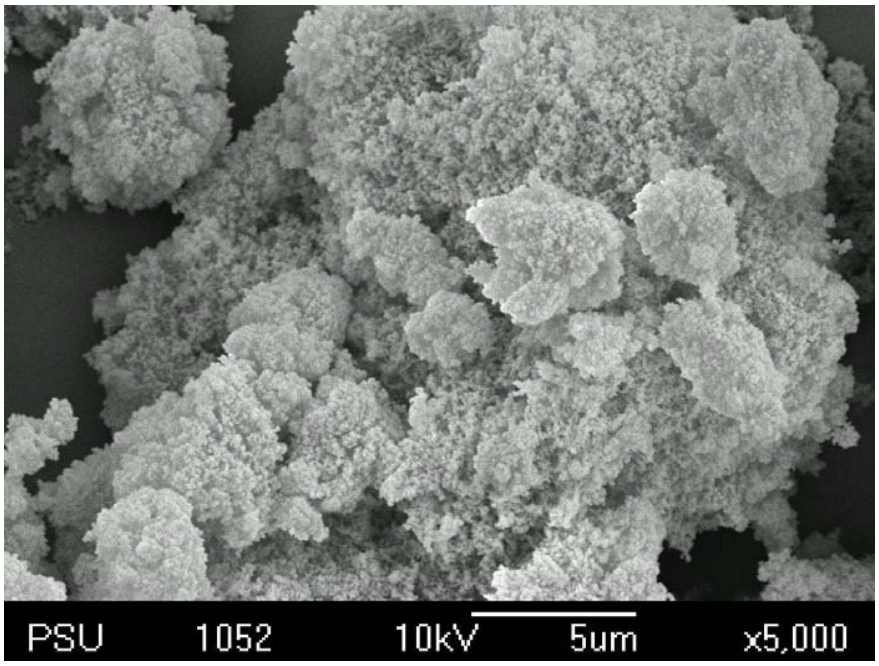

Fig. 1(a)

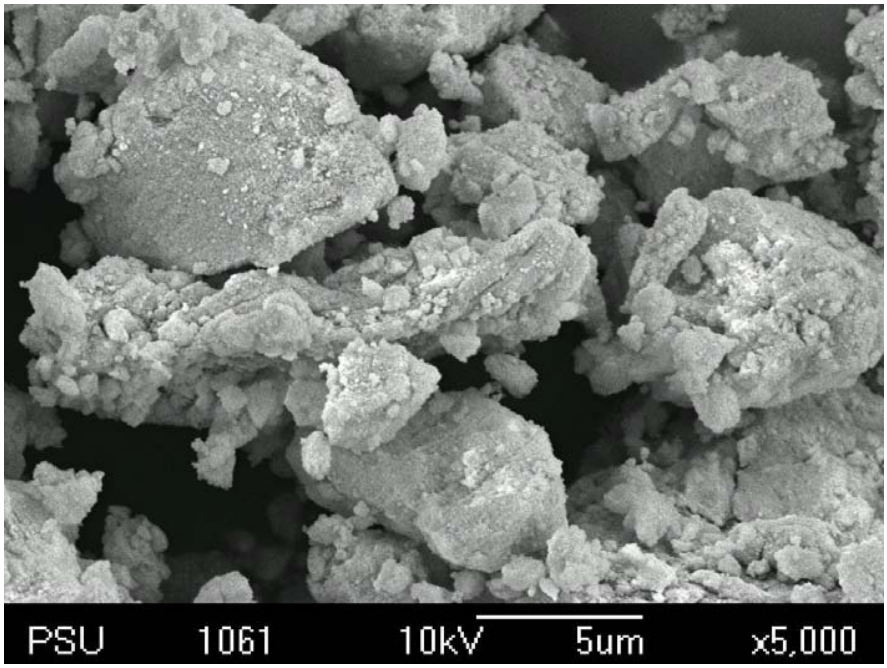

Fig. 1(b)

Fig. 1 SEM micrographs of (1a) Ce-ZrO_2 (with Ce/Zr = 3/1) synthesized by the surfactant-assisted method, and (1b) Ce-ZrO_2 synthesized by co-precipitation method

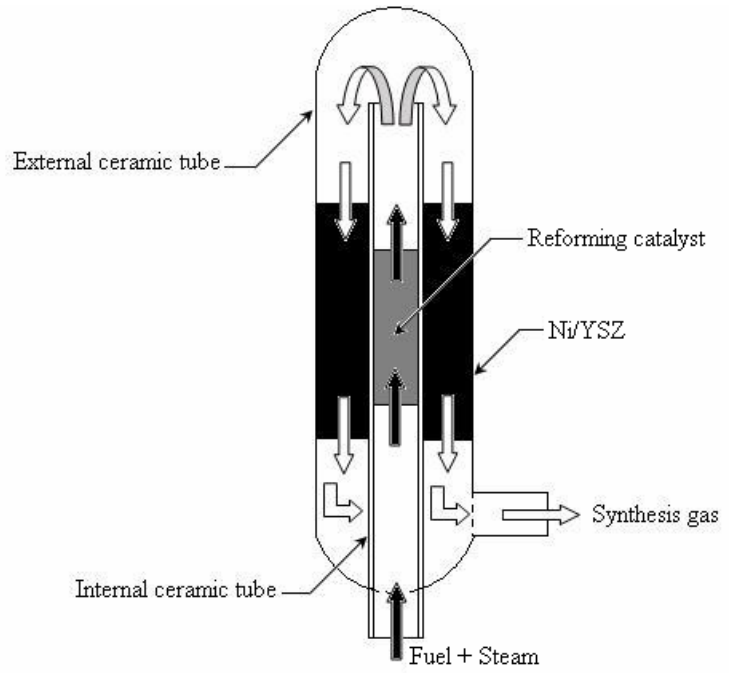

Fig. 2 Configuration of annular ceramic reactor for experiments under IIR operation.

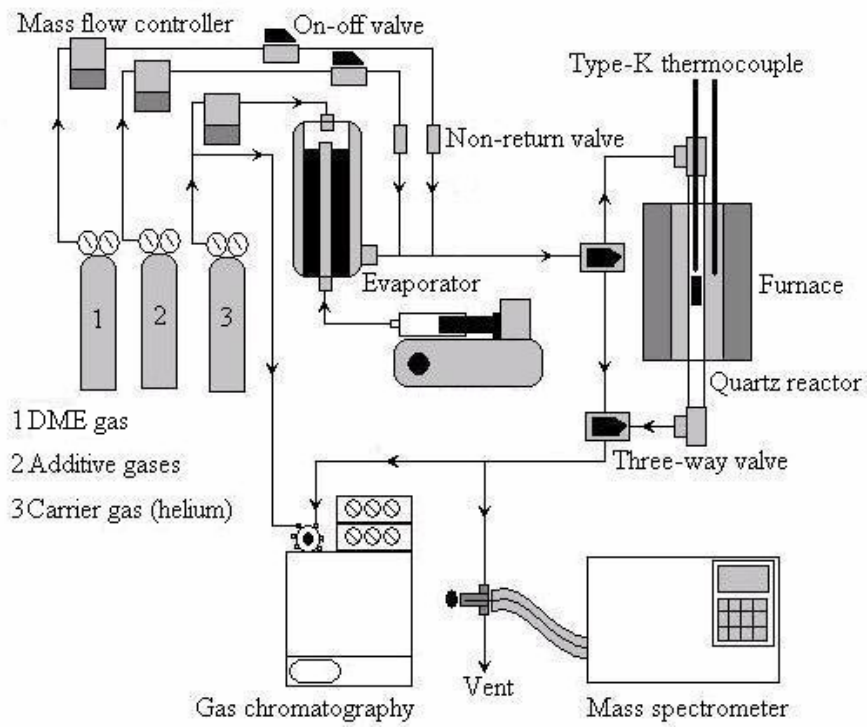

Fig. 3 Schematic diagram of the experimental set-up

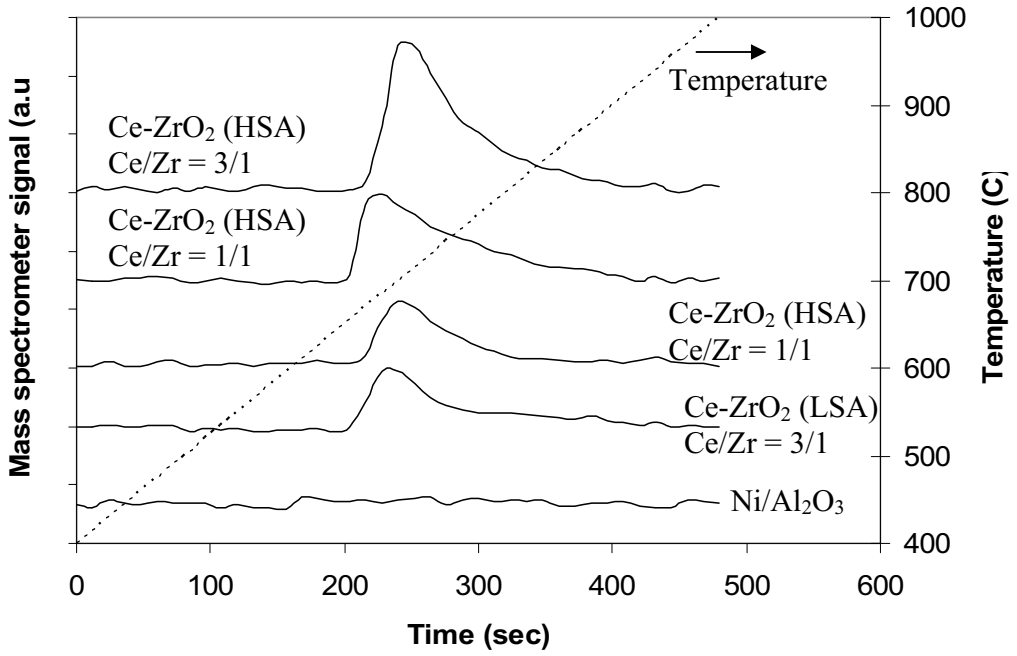

Fig. 4 Temperature Programmed Reduction (TPR-1) of several catalysts

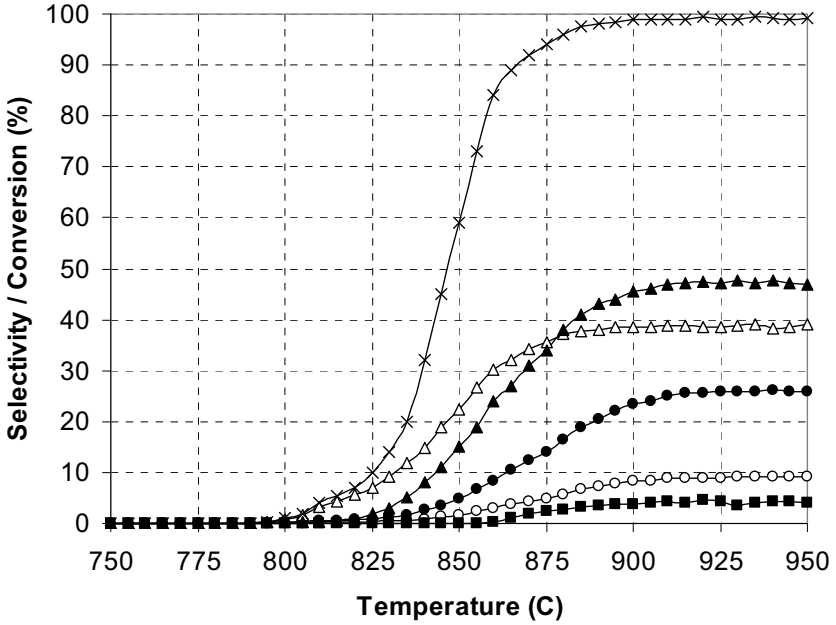

Fig. 5 Homogenous (in the absence of catalyst) reactivity of DME steam reforming (4 kPa DME, and 12 kPa H_2O) (DME (×), H_2 (●), CO (○), CO_2 (■), CH_4 (▲), and CH_3OH (△))

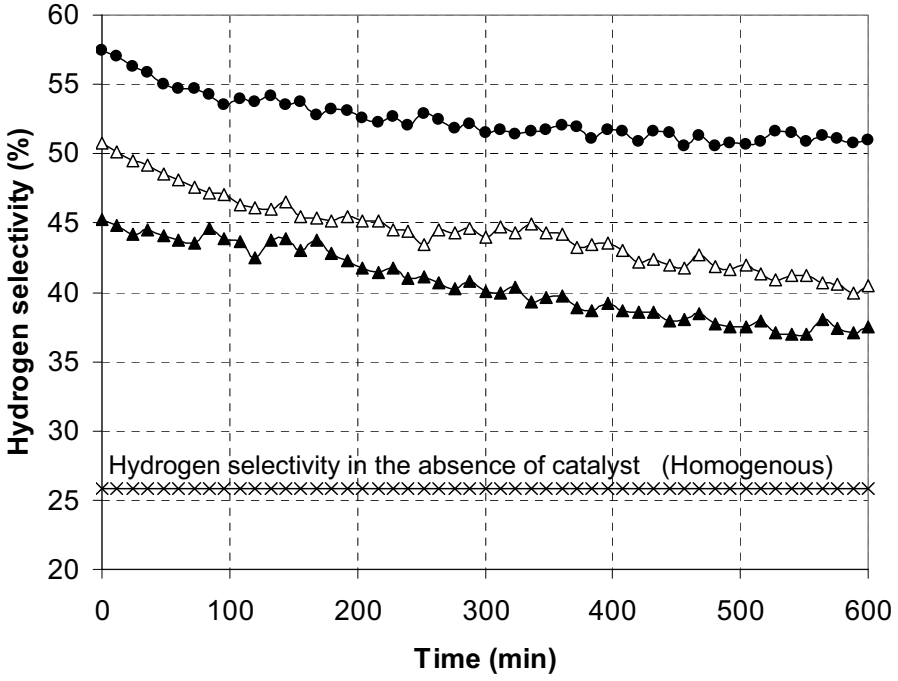

Fig. 6 Steam reforming of DME at 900°C for Ce-ZrO_2 (Ce/Zr=3/1) (●),Ce-ZrO_2 (Ce/Zr=1/1) (△), and Ce-ZrO_2 (Ce/Zr=1/3) (▲) (4 kPa C_2H_5OH, and 12 kPa H_2O)

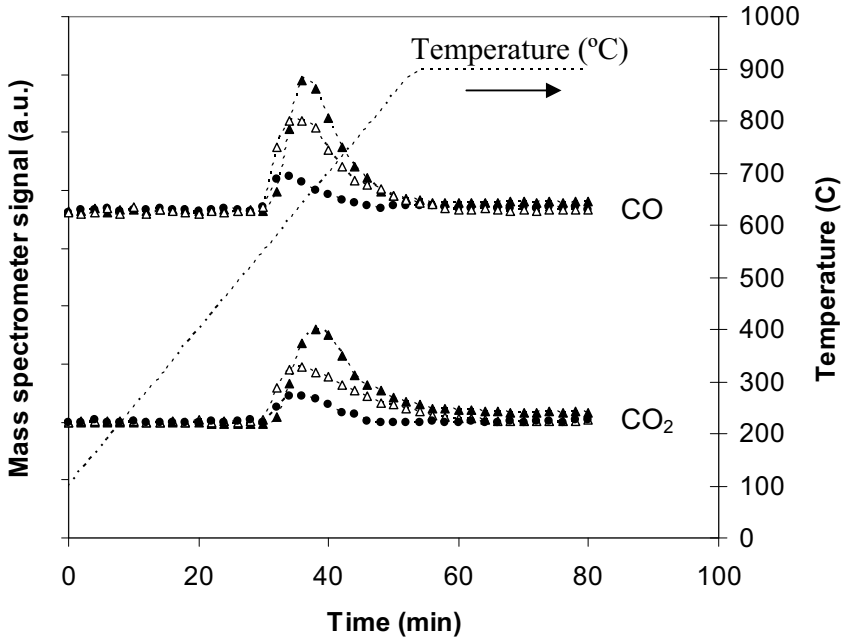

Fig. 7 Temperature Programmed Oxidation (TPO) of Ce-ZrO_2 (Ce/Zr=3/1) (●), Ce-ZrO_2 (Ce/Zr=1/1) (△), and Ce-ZrO_2 (Ce/Zr=1/3) (▲) after exposure in steam reforming of DME (4 kPa DME, and 12 kPa H_2O) for 10 h

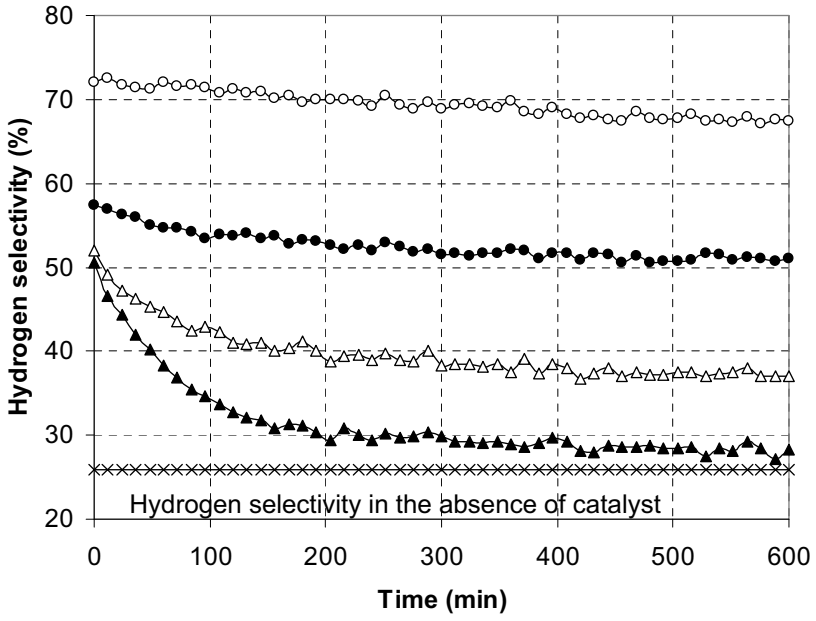

Fig. 8 Steam reforming of DME at 900°C for Ce-ZrO_2 (●), Ni/Al_2O_3 (▲), Ce-ZrO_2 + Ni/Al_2O_3 (△), and Ce-ZrO_2 - Ni/Al_2O_3 (○) (4 kPa DME, and 12 kPa H_2O)

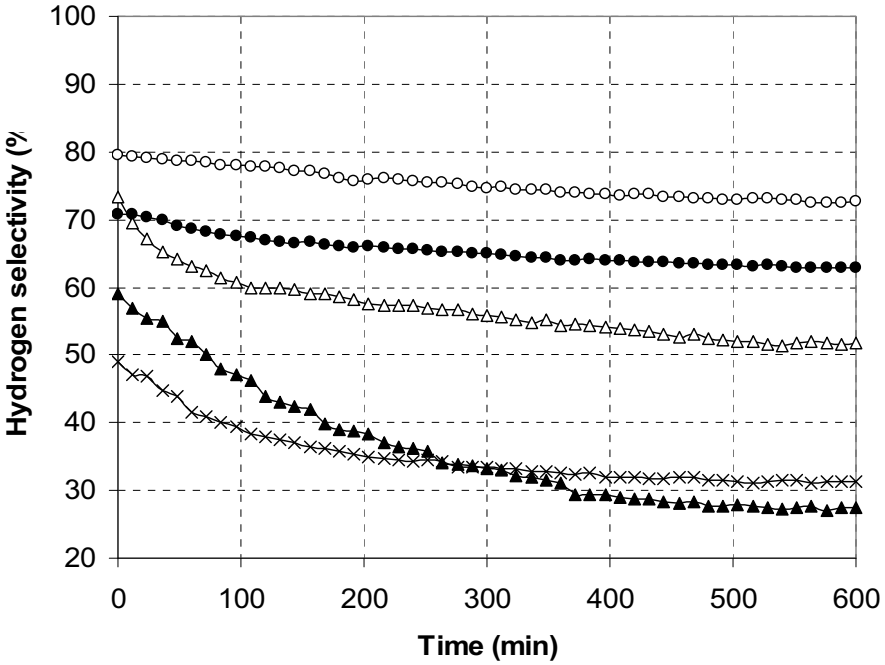

Fig. 9 Steam reforming of DME over IIR configuration at 900°C (Non-catalyst / Ni/YSZ (▲), Ce-ZrO_2 / Ni/YSZ (●), Ni/Al_2O_3 / Ni/YSZ (×), Ce-ZrO_2+Ni/Al_2O_3 / Ni/YSZ (△), and Ce-ZrO_2-Ni/Al_2O_3 / Ni/YSZ (○)) (4 kPa DME, and 12 kPa H_2O)

Table 1
Physicochemical properties of the synthesized catalysts

Catalyst	Metal-load[a] (wt.%)	BET Surface Area ($m^2 g^{-1}$)	Metal-reducibility[b] (%)	Metal-dispersion[c] (%)
Ni/Al_2O_3	5.0	67	94.5	4.93
$Ce\text{-}ZrO_2$ (Ce/Zr=1/3)	-	48	-	-
$Ce\text{-}ZrO_2$ (Ce/Zr=1/1)	-	45	-	-
$Ce\text{-}ZrO_2$ (Ce/Zr=3/1)	-	39.5	-	-

[a] Measured from X-ray fluorescence analysis.
[b] Measured from temperature-programmed reduction (TPR) with 5%hydrogen.
[c] Measured from temperature-programmed desorption (TPD) of hydrogen after TPR measurement.

Table 2
Results of TPR-1, TPO, TPR-2 analyses of $Ce\text{-}ZrO_2$ after calcination

Catalyst	Total H_2 Uptake from TPR-1 ($\mu mol\ g_{cat}^{-1}$)	Total O_2 Uptake from TPO ($\mu mol\ g_{cat}^{-1}$)	Total H_2 Uptake from TPR-2 ($\mu mol\ g_{cat}^{-1}$)
$Ce\text{-}ZrO_2$ (HSA) (Ce/Zr=1/3)	2899	1475	2876
$Ce\text{-}ZrO_2$ (HSA) (Ce/Zr=1/1)	3701	1862	3694
$Ce\text{-}ZrO_2$ (HSA) (Ce/Zr=3/1)	5247	2640	5250
$Ce\text{-}ZrO_2$ (LSA) (Ce/Zr=3/1)	2649	1328	2643
Ni/Al_2O_3	0	0	0

Table 3
Products and amount of carbon deposition from the steam reforming of DME over Ce-ZrO_2 with different Ce/Zr ratio at 900ºC

Catalyst	Deactivation (%)	Hydrogen selectivity (%)	Fraction of the by-products (%)				C formation (mmol g_{cat}^{-1})
			CO	CO_2	CH_4	CH_3OH	
Ce-ZrO_2 (Ce/Zr=1/3)	17.3	37.4	26.5	10.2	52.1	11.2	0.24
Ce-ZrO_2 (Ce/Zr=1/1)	20.4	40.5	30.2	14.3	51.6	3.9	0.20
Ce-ZrO_2 (Ce/Zr=3/1)	11.1	51.2	33.8	15.7	49.9	0.6	0.06

Table 4
Effect of inlet steam content on the products and amount of carbon deposition after exposure in the steam reforming of DME at 900ºC

DME/H_2O	Hydrogen selectivity (%)	Fraction of the by-products (%)				C formation (mmol g_{cat}^{-1})
		CO	CO_2	CH_4	CH_3OH	
1.0/3.0	51.2	33.8	15.7	49.9	0.6	0.06
1.0/5.0	52.8	32.5	19.6	47.6	0.3	0.06
1.0/7.0	53.0	31.0	21.6	47.1	0.3	0.04

Table 5
Effect of temperature on the products and amount of carbon deposition after exposure in the steam reforming of DME

Temperature (°C)	Hydrogen selectivity (%)	Fraction of the by-products (%)				C formation (mmol g_{cat}^{-1})
		CO	CO_2	CH_4	CH_3OH	
900	51.2 (73.9)	33.8[a] (78.2)[b]	15.7 (21.7)	49.9 (~0)	0.6 (~0)	0.06
925	53.9 (73.6)	38.4 (79.1)	19.5 (20.8)	42.1 (~0)	~0 (~0)	0.03
950	55.4 (73.3)	43.5 (80.0)	21.0 (19.9)	36.5 (~0)	~0 (~0)	~0
975	57.5 (73.0)	46.8 (80.7)	22.0 (19.1)	31.2 (~0)	~0 (~0)	~0
1000	59.0 (72.8)	51.9 (81.5)	23.7 (18.4)	24.4 (~0)	~0 (~0)	~0

[a] Observed from the Experiments
[b] Calculated from the thermodynamic analysis (at equilibrium)

Table 6
Products and amount of carbon deposition from the steam reforming of DME over several catalysts at 900ºC

Catalyst	Hydrogen selectivity (%)	Fraction of the by-products (%)				C formation (mmol g_{cat}^{-1})
		CO	CO_2	CH_4	CH_3OH	
Non-catalyst	25.8	9.0	4.0	47.1	38.9	
Ce-ZrO_2	51.2	33.8	15.7	49.9	0.6	0.06
Ni/Al_2O_3	28.3	9.6	5.2	49.5	35.7	4.20
Ce-ZrO_2 + Ni/Al_2O_3	37.1	17.4	8.9	54.2	19.5	2.08
Ce-ZrO_2 - Ni/Al_2O_3	67.4	43.9	24.5	31.6	~0	0.30

Table 7
Products and amount of carbon deposition from the steam reforming of DME over IIR-SOFC configuration (at 900ºC)

System	Hydrogen selectivity (%)	Fraction of the by-products (%)				C formation (mmol g_{cat}^{-1})
		CO	CO_2	CH_4	CH_3OH	
Non-catalyst / Ni/YSZ	27.3	10.4	4.0	51.7	33.9	4.03
Ce-ZrO_2 / Ni/YSZ	62.9	41.8	19.6	38.6	~0	0.20
Ni/Al_2O_3 / Ni/YSZ	31.2	11.2	10.4	48.0	31.4	4.43
Ce-ZrO_2+Ni/Al_2O_3 / Ni/YSZ	51.8	19.6	12.6	50.1	17.7	3.81
Ce-ZrO_2-Ni/Al_2O_3 / Ni/YSZ	72.5	51.3	27.8	20.9	~0	0.36

RESEARCH V

A study of high temperature desulphurization over nano-scale high surface area ceria for later application in SOFC

In the present work, the suitable absorbent material for high temperature desulphurization was investigated in order to apply internally in Solid Oxide Fuel Cell (SOFC). It was found that nano-scale high surface area CeO_2 has useful desulphurization activity and enables to remove H_2S from the feed gas efficiently in the range of temperature between 500 to 850^oC. In this range of temperature, compared to the conventional low surface area CeO_2, 80-85% of H_2S was removed by nano-scale high surface area CeO_2, whereas only 30-32% of H_2S was removed by conventional low surface area CeO_2. According to the XRD studies, the product formed after desulphurization over nano-scale high surface area CeO_2 was Ce_2O_2S. EDS mapping also suggested the uniform distribution of sulfur on the surface of CeO_2.

Regeneration experiments were then conducted by Temperature Programmed Oxidation (TPO) experiment. Ce_2O_2S can be recovered to CeO_2 after exposure in the oxidation condition at temperature above 600^oC. It should be noted that SO_2 is the product from this regeneration process. According to the SEM/EDS and XRD measurements, all Ce_2O_2S forming is converted to CeO_2 after oxidative regeneration. As the final step, a deactivation model considering the concentration and temperature dependencies on the desulphurization activity of CeO_2 was applied and the experimental results were fitted in this model for later application in SOFC model.

5.1 Introduction

Due to the present oil crisis and global warming problem, a great number of efforts have been focused on the use of alternative and renewable energy sources. Biogas is an important energy source due to its closed cycle operation and producible from biodegradable solid wastes such as cattle dung (diary wastes), piggery wastes, municipal solid wastes, and industrial effluents. Currently, there are numerous attempts to use biogas as a primary fuel for electrical generation by using several energy devices i.e. internal combustion engines and fuel cells. As biogas always contains high concentration of hydrogen sulfide (H_2S) (approximately 1000-2000 ppm depending on its source), it cannot be utilized directly to the energy devices. Biogas must be initially purified in order to remove H_2S which easily poisons the process reactor. In addition, the removal of H_2S would also help in preventing odors, safety hazards, and corrosion of the biogas transport equipment.

The appropriate technologies of desulphurization depend on the final applications as well as the operating conditions. Several researchers have studied the desulphurization by selective oxidation of H_2S over solid absorbents at low temperature (200-300°C). Park et al [1] investigated this reaction over $Bi_4V_{2-x}Sb_xO_{11-y}$ material and reported the good H_2S conversion with less than 2% of SO_2 selectivity in the temperature ranges of 220-260°C. Lee et al [2] also studied this desulphurization reaction on zeolite-NaX and zeolite-KX. They found that Zeolite-KX was superior to the zeolite-NaX in terms of selectivity to elemental sulfur and resistance to deactivation. In detail, elemental sulfur yield over zeolite-NaX was achieved about 90% at 225^{o}C for the first 4 hours, but gradually decreased to 55% after 40 hours, whereas the yield of elemental sulfur on zeolite-KX was obtained within the range of 86% at 250^{o}C after 40 hours.

It should be noted that the selective oxidation may not suitable for the high temperature applications i.e. coal or residual oil gasification, and fuel cell applications, which operated the temperature range of 400-1200°C, due to the large temperature differences in the process. Several high temperature desulfurization techniques are, therefore, desired for use in such applications [3]. Previously, the high temperature removal of hydrogen sulfide from simulated gas was carried out in batch type fluidized-bed reactor using natural manganese ore consisted of several metal oxides (MnO_x: 51.85%, FeO_y: 3.86%, CaO: 0.11%) [4]. It was found that H_2S removal efficiency increased with increasing temperature but decreased with increasing excess gas velocity. In addition, the breakthrough time for H_2S decreased as the gas velocity increased.

As another example of the high temperature application, fuel cell has drawn a great interest from many researchers as it can generate electricity at high efficiency. Various types of fuel cells are available, in that Solid Oxide Fuel Cell (SOFC) has taken much attention because of its large

electricity production capacity. To establish these highly efficient processes, it is necessary to develop a high temperature treatment process for the various feed stocks i.e. biogas and natural gas, which consist of significant amount of H_2S. To date fuel cell systems are relied mainly on batch operation of sorbent technology for sulfur removal. Although this technology possesses a necessary removal efficiency, the low capacity associated with the batchwise operation and the potential utilization of high sulfur hydrocarbon feed stocks greatly affect the fuel cell processor foot print, types of sorbent and sorbent maintenance interval [5]. A widely established metal oxide i.e. ZnO has been used as a high temperature desulphurization sorbent. ZnO has the most favorable thermodynamics for H_2S removal among sorbents that have been investigated. However, despite its attractive thermodynamic properties, the reduction of ZnO and subsequent vaporization of elemental zinc create a serious problem over many cycles of sulfidation/regeneration at high temperatures [6, 7]. As a result, alternate absorbents to minimize ZnO problems at high temperature ranges are needed.

Meng et al [8] and Kay et al [9] first described the use of cerium oxide (or ceria) sorbents for high-temperature desulfurization. It is well established that ceria and metal oxide (e.g. Gd, Nb, and Zr) doped cerias provide high oxygen storage capacity, which is beneficial in oxidation processes. Several researchers have also reported the benefit of adding or doping this material on the reforming and partial oxidation catalysts in terms of catalyst stability and the resistance toward carbon deposition [10, 11]. Focusing on the use of ceria as the sorbent for desulphurization, in laboratory-scaled fixed-bed reactor tests, the H_2S concentration was reduced from 1.2 v% to 3 ppmv at 872°C and 1 atm by using reduced ceria, CeO_n (n<2). However, only a few data were reported particularly on the material characterization and the mechanism of desulfurization. Abbasian et al [12] and Li et al [13] studied mixed-oxide sorbents containing cerium and copper oxides. Although some evidence of cerium sulfidation was reported, the primary function of the ceria was considered to be for maintaining the active copper in a highly dispersed form. Zeng et al [14] studied the H_2S removal in presence of hydrogen on CeO_2 sorbent. They reported complete conversion of CeO_2 to CeO_2S during sulfidation in the temperature range of 500-700^oC and regeneration of Ce_2O_2S to CeO_2 by using SO_2. According to phase diagrams, relevant reactions were reported by Kay et al [9] as:

Sulfidation

$$2CeO_2 + H_2S + H_2 \leftrightarrow Ce_2O_2S + 2H_2O \quad (1)$$

Regeneration

$$Ce_2O_2S + SO_2 \leftrightarrow 2CeO_2 + S_2 \quad (2)$$

It should be noted that the major limitations to apply CeO_2 in the high temperature process are its low specific surface and high surface area reduction percentage due to the high surface sintering. It was observed that from our previous work that the surface area reduction of CeO_2 after exposure in the reaction conditions at 900°C were 23% and 28%, respectively. The corresponding post-reaction specific surface areas were only 1.9 and 8.7 $m^2 g^{-1}$, respectively [15]. The use of high surface area CeO_2 would be a good alternative procedure to improve the performance of H_2S removal at high temperature. In this paper, nano-scale high surface area CeO_2 (from nano-Arc Company, US) was used as a sorbent for desulfurization process. The reactions during sulfidation and oxidative regeneration were investigated. Some analytical techniques were employed to characterize the sorbents at different stages of operation. In addition, the deactivation model considering the concentration dependency of the activity was developed and fitted with the experimental results to determine the kinetic parameters for the later application in SOFC model fueled by conventional fuel i.e. biogas and natural gas. Regarding the selection of the suitable model, it should be noted that the formation of a dense product layer over the solid reactant results in an additional diffusion resistance and is expected to cause a drop in the reaction rate. One would also expect it to cause significant changes in the pore structure, active surface area, and activity per unit area of solid reactant with reaction extent. These changes cause a decrease of the solid reactant activity with time. As reported in the literature, the deactivation model works well for such gas-solid reactions [16]. In this model, the effects of these factors on the diminishing rate of sulfur fixation were combined in a deactivation rate term [17].

5.2 Experimental

5.2.1. Fixed bed reactor setup

A laboratory-scaled fixed bed quartz reactor of 30 cm height and 0.635 cm internal diameter was installed vertically in an electric furnace with a programmable temperature controller. Nano-scale CeO_2 (from nano-Arc Company, US) was firstly calcined at 900^oC before packing between two layers of quartz wool. The physical and chemical properties of CeO_2 are provided in Table 1. A type K thermocouple was located externally at the centre of the catalyst to monitor the temperature of the reactor. Swagelok fittings and tubing were used to connect the reactor to the gas supply and gas sampling systems. Details of the reactor setup were shown in Figure 1.

5.2.2. Analytical methods

Pure CeO_2 and spent CeO_2 were characterized using X-ray diffractrometer (XRD) employing Cu 30 kW and 15 mA to determine the sulfur deposition on the sorbent. SEM and EDS analysis was also carried out to investigate the changes in morphology and sulfur distribution by elemental mapping. The conditions used were 40 kV and resolution of 4000.

5.2.3. Gas Analysis

Gas analysis was carried out using Shimadzu gas chromatography (GC-14B) equipped with a Porapak-Q column and a TCD detector. The H_2S peak was obtained using a linear temperature programming in the column oven. The temperature was increased from 40 to 200^oC at a ramp rate of 20^oC min^{-1}. The operating conditions of the GC are summarized in Table 2. It should be noted that the TCD calibration was carried out by mixing pure H_2S and N_2 at various ratios. Mixture of 0.01% (molar) H_2S balanced with nitrogen was used to calibrate the concentration by diluting with helium gas.

5.2.4. Procedures for sulfidation experiments

The sulfidation experiments were carried out in a fixed bed reactor. The experimental procedures were divided into the study of optimum temperature and the establishment of breakthrough curves for the adsorption of H_2S on CeO_2 sorbent.

Regarding the study of optimum temperature, a set of experiments was carried out to test the desulphurization activity of CeO_2 sorbent at various temperatures; i.e. 400, 500, 600, 700, 800 and 850^oC. The amount of CeO_2 was kept at 500 mg, while the total flow rate was 100 cm^3 min^{-1}. The temperature was increased linearly at a rate of 10^oC min^{-1} until reaching a desired temperature. The reactor was then kept under isothermal condition for 30 min. The exit gases from the reactor were connected to the gas chromatography (GC) equipped with TCD detector to detect the H_2S level after adsorption at each temperature level. The breakthrough curve experiments were then carried out at the suitable temperatures for the desulphurization. The reactor was operated using a feed gas (100 cm^3 min^{-1}) with H_2S concentration of 1000 ppm. The reactor was heated up to a desired temperature at a heating rate of 10^oC min^{-1}. The system was operated under isothermal until breakthrough of H_2S appeared at the exit of the bed.

5.2.5 Oxidative regeneration of sulfided CeO_2 by temperature programmed reaction study

The characteristics of the regeneration of the sulfided CeO_2 were examined using a temperature programmed oxidation (TPO) apparatus equipped with quadrupole mass spectrometer.

In the TPO examination, 10% oxygen balanced in helium or nitrogen was fed into the microreactor in the TPO apparatus at a flow rate of 100 cm^3 min^{-1}. A sample of 50 mg was packed into the micro reactor of ¼'' size. The sample was heated to 900^oC at a constant heating rate of 10^oC min^{-1}. The exit gases were monitored continuously using the mass spectrometer.

5.3 Results and discussion

5.3.1. Sulfidation results

Firstly, the effect of temperature on the desulphurization activity of nano-scale CeO_2 sorbent was studied in the range of 400 to 850^oC. The conversion of H_2S (X) defined in Eq. 3 was plotted with temperature as shown in Figure 2. It should be noted that the desulphurization activity of conventional low surface area CeO_2 (synthesized by the precipitation method with the specific surface area of 3.1 m^2 g^{-1}) was also performed for comparison.

$$X = \frac{Conc_{Initial} - Conc_{Exit}}{Conc_{Initial}} \times 100 \quad (3)$$

It was found that the H_2S conversion from the desulphurization over nano-scale CeO_2 is almost 3 times higher than that over conventional low surface area CeO_2. The conversion increases readily with increasing temperature and then became constant at the temperature higher than 600^oC. The breakthrough results for nano-scale CeO_2, which refers to a predetermined H_2S outlet condition when a certain concentration of H_2S cannot be removed by the catalyst bed [18], at several temperatures are presented in Figure 3. As seen from the figure, the breakthrough period increased with increasing temperature. It should be noted that a few bumps (higher H_2S concentration regions) appeared in some early part of the pre-breakthrough curves. These early bumps could be associated with incomplete reduction of ceria at the early state. Without pre-reduction, the reduction and sulfidation occurred simultaneously on the surface of ceria, as explained by Zeng et al [14]. It should be noted according to the gas product detecting from gas chromatography during the sulfidation testing that small amounts of hydrogen and oxygen were also detected along with steam, which could be formed by the combustion of hydrogen and oxygen.

5.3.2 Regeneration of sulfided CeO_2

Regeneration of sulfided CeO_2 was conducted by using 10% oxygen as a regeneration agent for two different samples sulfided at 700 and 800^oC. A sample was packed and heated in a micro

tube reactor installed in the furnace at a constant heating rate of 10°C min^{-1}. The amount of O_2 and SO_2 evolved at each temperature level were monitored by mass spectrometer. Figures 4 and 5 show the results of the samples sulfided at 700 and 800°C, respectively. Both figures indicate the consumption of O_2 and evolution of SO_2 during the temperature range of 600 and 800°C. The evolution temperature observed in the present work is in good agreement with several previous works in the literature [19, 20, 21], in which investigated the oxidation of Ce_2O_2S in the range of operating temperature between 600-800°C by TPO technique and observed the evolution of SO_2 around 800°C. According to the calculation of area under peaks from Figures 4 and 5, the amount of SO_2 evolved was approximately 1.25mol% from the sulfided sample at 700°C by consuming oxygen of 2% whereas the amount of SO_2 evolved from the sulfided sample at 800°C was about 3 mol% with the oxygen consuming of 4%. The difference in the amount of SO_2 evolution from the sulfidation at different temperatures, which was also observed by several researchers, could be mainly due to the increase of oxygen mobility on the surface of CeO_2 by increasing temperature. It is well established that ceria-based material contains a high concentration of highly mobile oxygen vacancies, which act as local sources or sinks for oxygen involved in reactions taking place on its surface. That high oxygen mobility, high oxygen storage capacity, and its modifiable ability render the ceria-based material very interesting for a wide range of catalytic applications. At higher temperature, the gas-solid reaction between the inlet sulfur compound and the bulk lattice oxygen on the surface of CeO_2 easily occurred and consequently results in the high sulfidation reaction [22]. It should be noted that the previous work from Zeng et al [14] also reported that the degree of sulfidation increases with increasing temperature.

5.3.3. Characterization of absorbent

Sulfided CeO_2 was subjected to its surface analysis by SEM/EDS and XRD measurements to determine the distribution of sulfur and the type of product formation on the surface of the CeO_2. From the SEM & EDS mapping as shown in Figure 6, sulfur distribution on the surface of the catalyst was detected. According to the sulfur distribution at 700 and 800°C as shown in Figures 6(a) and 6(b) respectively, the sulfur concentrations at 800°C are higher than those at 700°C, which is in good agreement with the observed SO_2 peaks shown in Figures 4 and 5. In addition, from the sulfur mapping observed by the EDS, it was found that the sulfur element is uniformly distributed over the surface of CeO_2. Larger particles in the figure are due to aggregation of smaller particles and the change in the porous structure. As CeO_2 consists of high surface oxygen ions, these ions make it become easily exchanged to sulfur upon H_2S adsorption [23].

In addition to the SEM/EDS measurement, sulfided CeO_2 was subjected to XRD studies to determine the type product formed. From the XRD analysis as shown in Figure 8, major phases of the sulfided CeO_2 is Ce_2O_2S (Pattern 26-1085). The pattern was compared with that of pure CeO_2 (pattern 34-0394) as shown in Figure 7. The XRD patterns of spent CeO_2 indicates that the cerium oxide sulfide (Ce_2O_2S) was formed from the reaction of CeO_2 with H_2S. Peaks of spent CeO_2 were decreased and peak broadening occurred at the CeO_2 peaks due to the formation of Ce_2O_2S. Sulfided CeO_2 was subjected to oxidative regeneration at a constant heating rate of $10^oC\ min^{-1}$ until 900^oC. The sample after regeneration was analysed by XRD to determine its potential reuse as a CeO_2. It was found that the regenerated CeO_2 shows peaks at the same two theta angles as those of pure CeO_2 as shown in Figure 9. This ensures the possible regeneration of sulfided CeO_2.

From the evidences of sulfidation, regeneration, and catalyst characterization, a sequence of reactions occurred during these processes can be proposed. The possible reaction mechanism of the sulfidation and regeneration can be predicted as follows:

$$2CeO_2 + H_2S \rightarrow Ce_2O_2S + H_2O + 0.5O_2 \quad (4)$$

$$Ce_2O_2S + 2O_2 \rightarrow SO_2 + 2CeO_2 \quad (5)$$

It should be noted that the detectable of steam from the desulphurization experiments and the observation of Ce_2O_2S phase from the XRD studies support this proposed sulfidation reaction mechanism. Regarding the regeneration reaction, as described, it was confirmed by the two techniques i.e. TPO and XRD analysis. The first experiment observed the formation of SO_2 from the regeneration process, while the second one confirmed that CeO_2 can be regenerated.

5.3.4 Deactivation model for CeO_2 absorbent

Deactivation models proposed in the literature [24] for gas-solid reactions with significant changes of activity of the solid due to textural changes, as well as product layer diffusion resistance during reaction were reported to be quite successful in predicting conversion-time data. In the early work of Orbey et al. [16] and in the recent work of Suyadal et al [25], deactivation models were used for the prediction of breakthrough curves in packed adsorption columns. In the present work, a deactivation model is proposed with following these assumptions i.e. isothermal condition, pseudo-steady-state condition, first-order deactivation of the absorbent with respect to the solid surface which can be described in terms of an exponential decrease with time in its available surface, and constant activity throughout the surface of absorbent. Combined equation of mole balance and rate law for the packed bed reactor is given below:

$$Vo.t\frac{dC_{H_2S}}{dt} = -k_o.a(t)C_{H_2S} \quad (6)$$

The boundary conditions are inlet concentrations are

At $t = 0$, $C_{H_2S} = C_{H_2Sin}$

At $t = t$, $C_{H_2S} = C_{H_2Sout}$

Therefore,

$$a(t) = \frac{Vo}{Wk} Ln\left(\frac{C_{H_2Sin}}{C_{H_2Sout}}\right) \quad (7)$$

The first order exponential decay is $a(t) = e^{-k_d t}$, substituting Eq. 6 to Eq. 8:

$$-k_d.t = \ln\frac{Vo}{Wk_o} + \ln\ln\left(\frac{C_{H_2Sin}}{C_{H_2Sout}}\right) \quad (8)$$

This equation is equivalent to the breakthrough [25]. Thus, when $\ln\ln\left(\frac{C_{H_2Sin}}{C_{H_2Sout}}\right)$ is plotted versus operating time (t), a straight line should be obtained with a slope equal to $-k_d$ and intercept equal to $\ln\frac{Vo}{Wk_o}$ as shown in Figure 10. Table 3 summarizes the model parameters determined at different temperatures. The fluctuation of 10 to 15% in correlation coefficient may be due to initial bumps. Advantages of deactivation model is the presence of only two adjustable parameters such as initial sorption rate constant K_o and the deactivation rate constant K_d. Both parameters showed increasing trend with respect to increase in the temperatures. Sorption rate constant K_o and the deactivation rate constant K_d were correlated as a function of temperature using Arrhenious equations (Eqs. 9 and 10).

$$K_o = k_o e^{-e/RT} \quad (9)$$

$$K_d = k_o e^{-e/RT} \quad (10)$$

The temeprature dependency was illustrated as shown in Figure 11. The activation energies of k_o and k_d were found to be 33.4 and 90 kJ mol^{-1}. These high values of the activation energies indicate that the H_2S sorption on CeO_2 is the chemical adsorption.

5.4 Conclusion

Nano-scale high surface area CeO_2 has useful desulphurization activity in the range of temperature between 500 to 850^oC. Compared to the conventional low surface area CeO_2, 80-85% of H_2S was removed by nano-scale high surface area CeO_2, whereas 30-32% of H_2S was removed by conventional low surface area CeO_2. According to the XRD and EDS mapping, the uniform Ce_2O_2S was formed after desulphurization. According to the TPO experiment, this component (Ce_2O_2S) can be recovered to CeO_2 after exposure in the oxidation condition at temperature above 600^oC. Furthermore, regarding the SEM/EDS and XRD measurements, all Ce_2O_2S forming is converted to CeO_2 after this oxidative regeneration.

As the final step, a deactivation model considering the concentration and temperature dependencies of the desulphurization activity was proposed for later application in SOFC model.

References

1. D.W. Park, B.H. Hwang, W.D. Ju, M.I. Kim, K.H. Kim, H.C. Woo, *Korean J. Chem. Eng*., **22**, 190 (2005).
2. J.D. Lee, J.H. Jun, N.K. Park, S.O. Ryu, T.J. Lee, *Korean J. Chem. Eng*., **22**, 36 (2005).
3. P.R. Westmoreland and D.P. Harrison, *Environ. Sci. Technol***.**, **10**, 559 (1976).
4. H.T. Jang, S.B. Kim, D.S. Doh, *Korean J. Chem*. *Eng*., **20**, 116 (2003).
5. T. H. Gardener, *Fuel*, **81**, 2157 (2002).
6. J. H. Swisher and K. Schwerdtfeger, *J. Mater. Eng. Perform.*, **1**, 399 (1992).
7. V. Patrick and G. R. Gavalas, *Ind. Eng. Chem. Res.,* **28**, 931 (1989).
8. V.V. Meng and D.A.R. Kay, *High Technology Ceramics*, Elsevier, Amsterdam, 2247 (1987).
9. D.A.R. Kay, W.G. Wilson, and V. Jalan, *J. Alloys and Compounds,* **192**, 11 (1993).
10. K.H. Kim, S.Y. Lee, and K.J. Yoon, *Korean J. Chem. Eng*., **23**, 356 (2006).
11. K.H. Kim, S.Y. Lee, S.W. Nam, T.H. Lim, S.A. Hong, K.J. Yoon, *Korean J. Chem. Eng*., **23**, 17 (2006).
12. J. Abbasian, A.H. Hill, M. Flytzani-Stephanopoulos, and Z. Li, Final Report, DE-FC22-92PC92521 (1994).

13. Z. Li, and M. Flytzani-Stephanopoulos, *Ind. Eng. Chem. Res.*, **36**, 187 (1997).
14. Y. Zeng, S. Zhang, F.R. Groves, and D.P. Harrison*, Chem. Eng. Sci*., **54**, 3007 (1999).
15. N. Laosiripojana and S. Assabumrungrat, *Applied Catal. B*, **60**, 107 (2005).
16. N. Orbey, G. Dogu, and T. Dogu, *Can. J. Chem. Eng.,* **60**, 314 (1982).
17. H.S. Fogler, Elements of chemical reaction engineering, Prentice-Hall Inc, Englewood Cliffs, New Jersey 07632, ISBN 0-13-263476-7 (1986).
18. M.P. Cal, B.W. Strickler, and A.A. Lizzio, *Carbon*, **38**, 1757 (2000).
19. R.M.Ferriz, R.J.Gorte, J.M.Vohs, *Applied Catal. B*, **43**, 273 (2003).
20. Z. Wang, M.Flytzani-Stephanopoulos, *Energy & Fuels*, **19**, 2093 (2005).
21. M.Flytzani-Stephanopoulos, Angela D. Surgenor, Report, NASA/TM—2007-214686.
22. S. Yasyerli, G. Dogu, and T. Dogu, *Catal. Today***, 117**, 271 (2006).
23. M. Ziolek, *J. Molecular catalysis A*, **97**, 49 (1995).
24. T. Dogu, *Chem. Eng. J*., **21**, 213 (1981).
25. Y. Suyadal, M. Erol, H. Oguz, *Ind. Eng. Chem. Res.,* **39**, 724 (2000).

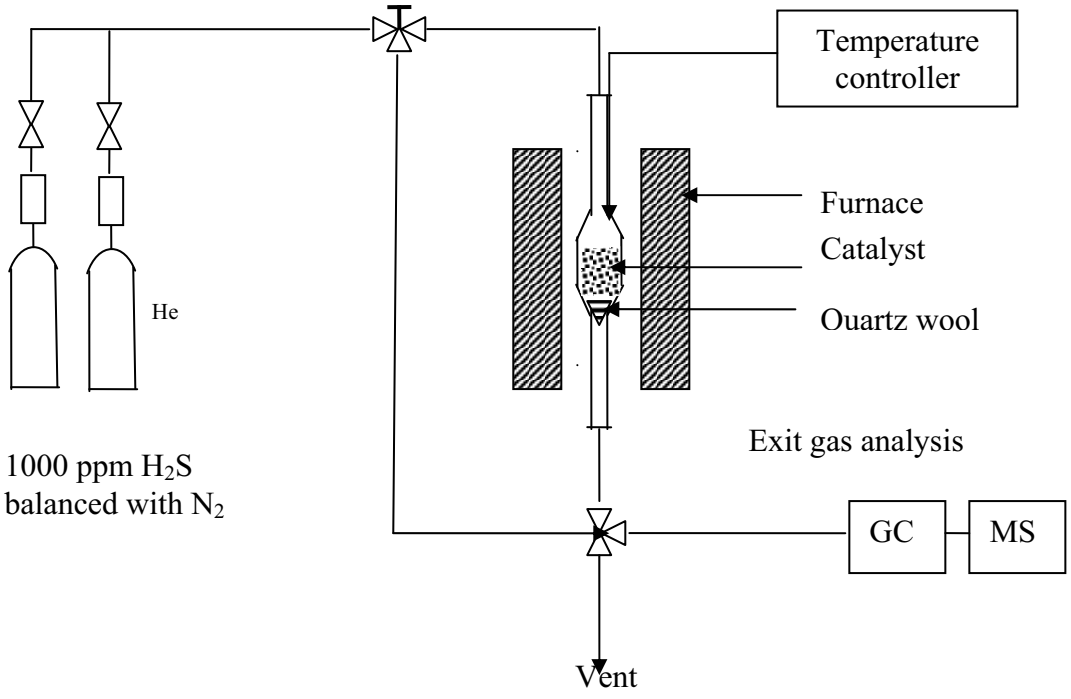

Figure 1 Schematic diagram of experimental setup.

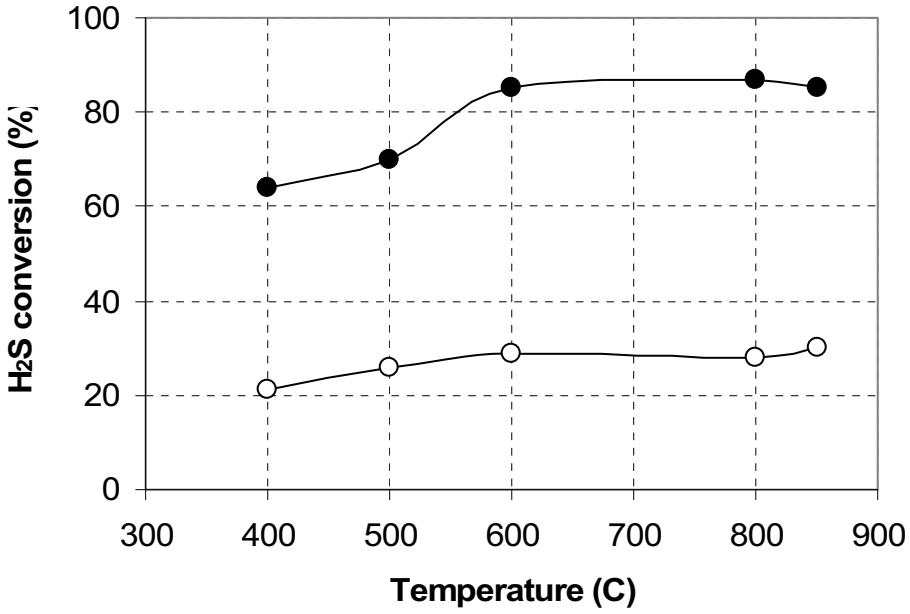

Figure 2 Conversions of H_2S at different temperatures (nano-scale high surface area CeO_2 (●), and conventional low surface area CeO_2 (○))

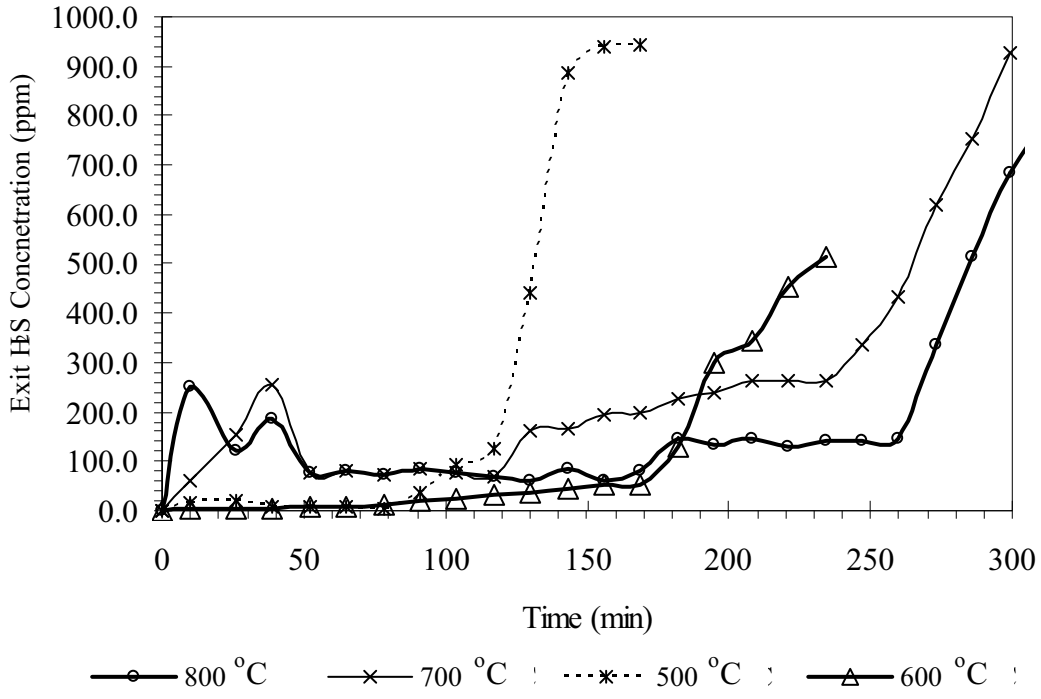

Figure 3 Sulfidation break through curves of CeO_2

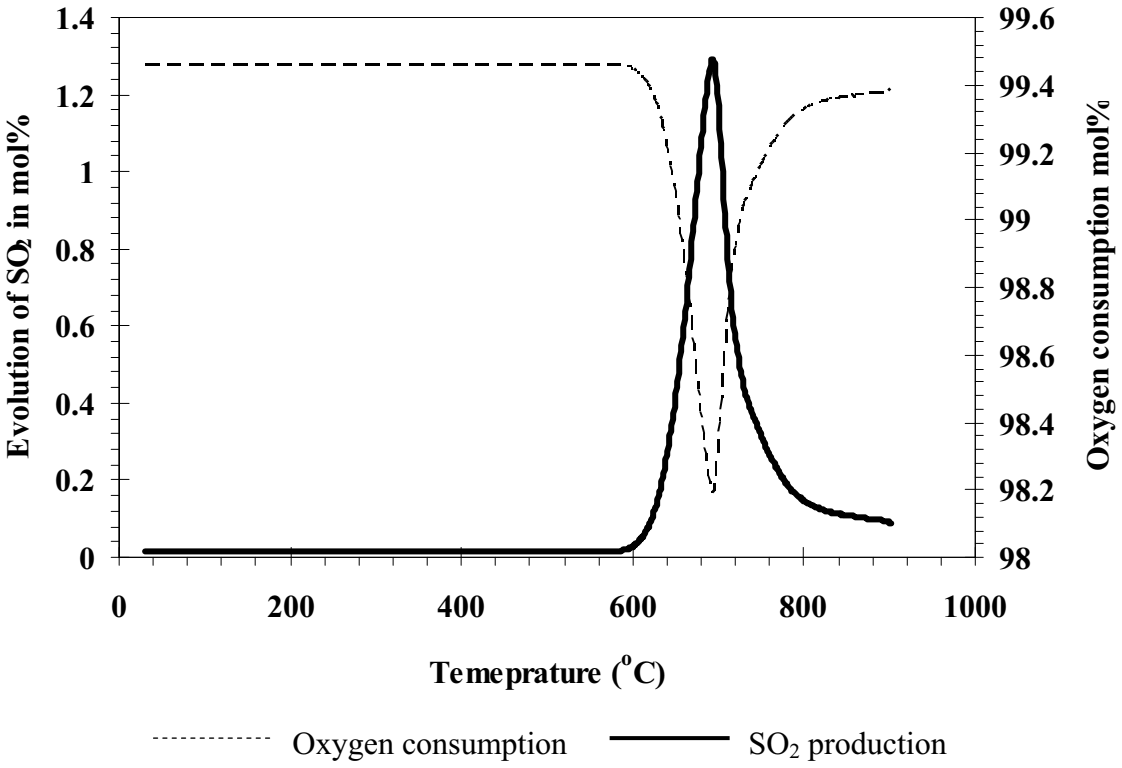

Figure 4 Oxidative regeneration of CeO_2 sulfided at 700°C.

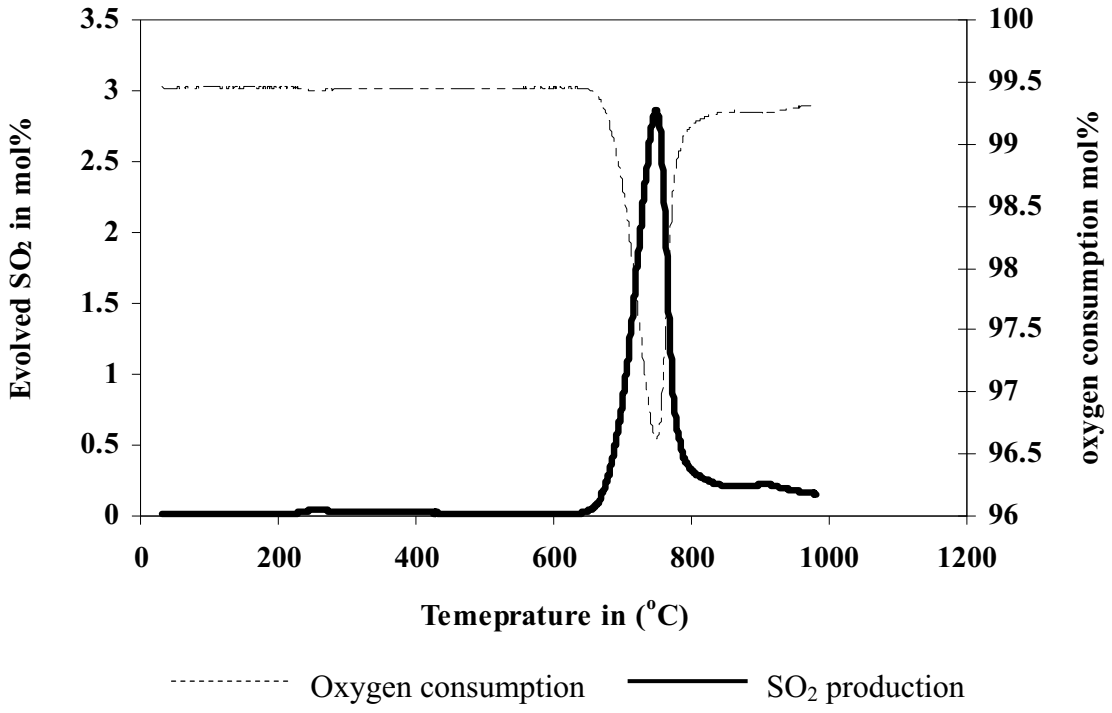

Figure 5 Oxidative regeneration of CeO_2 sulfided at 800°C.

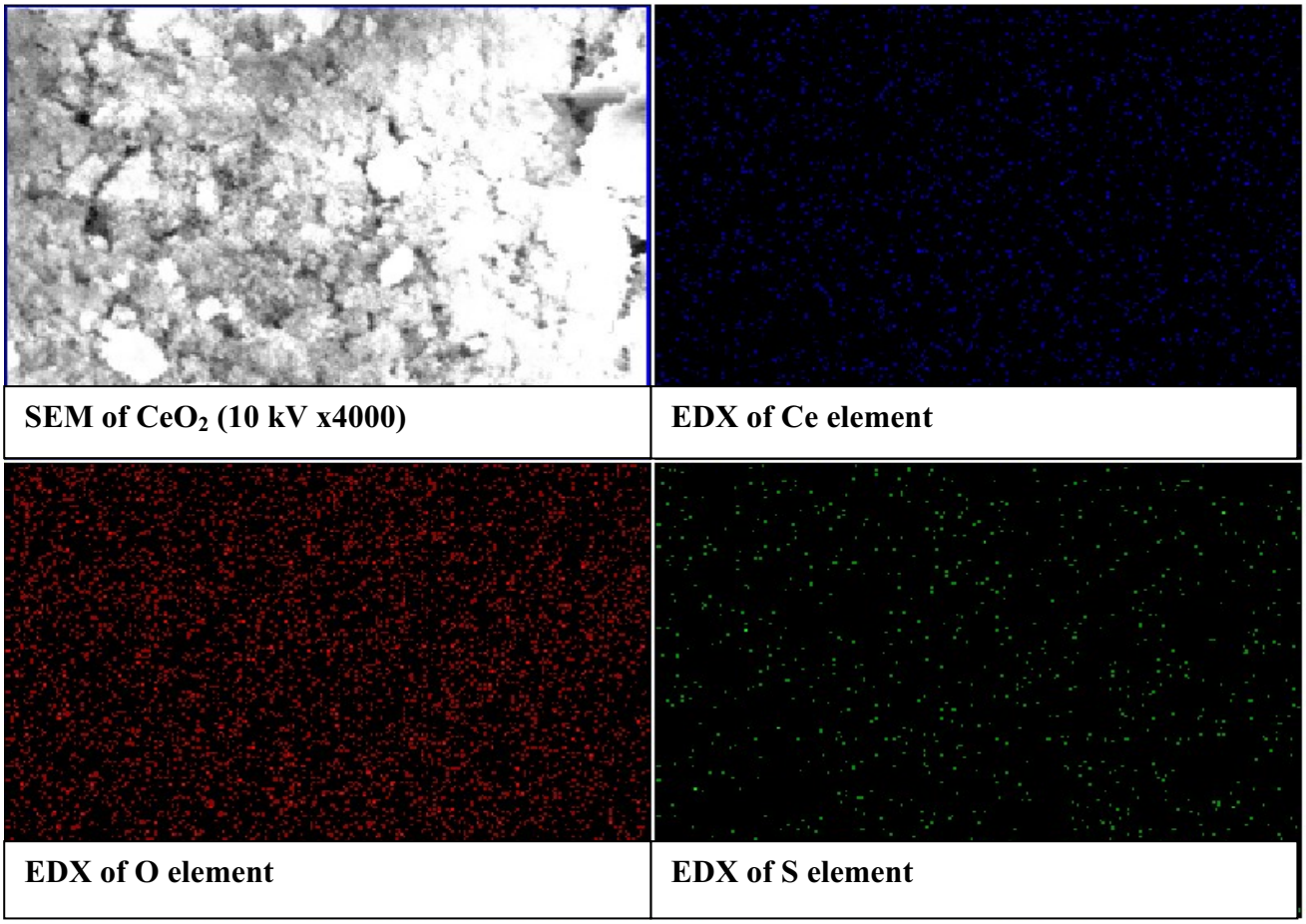

(a) SEM and elemental mapping of CeO_2 sulfided at 700^{o}C

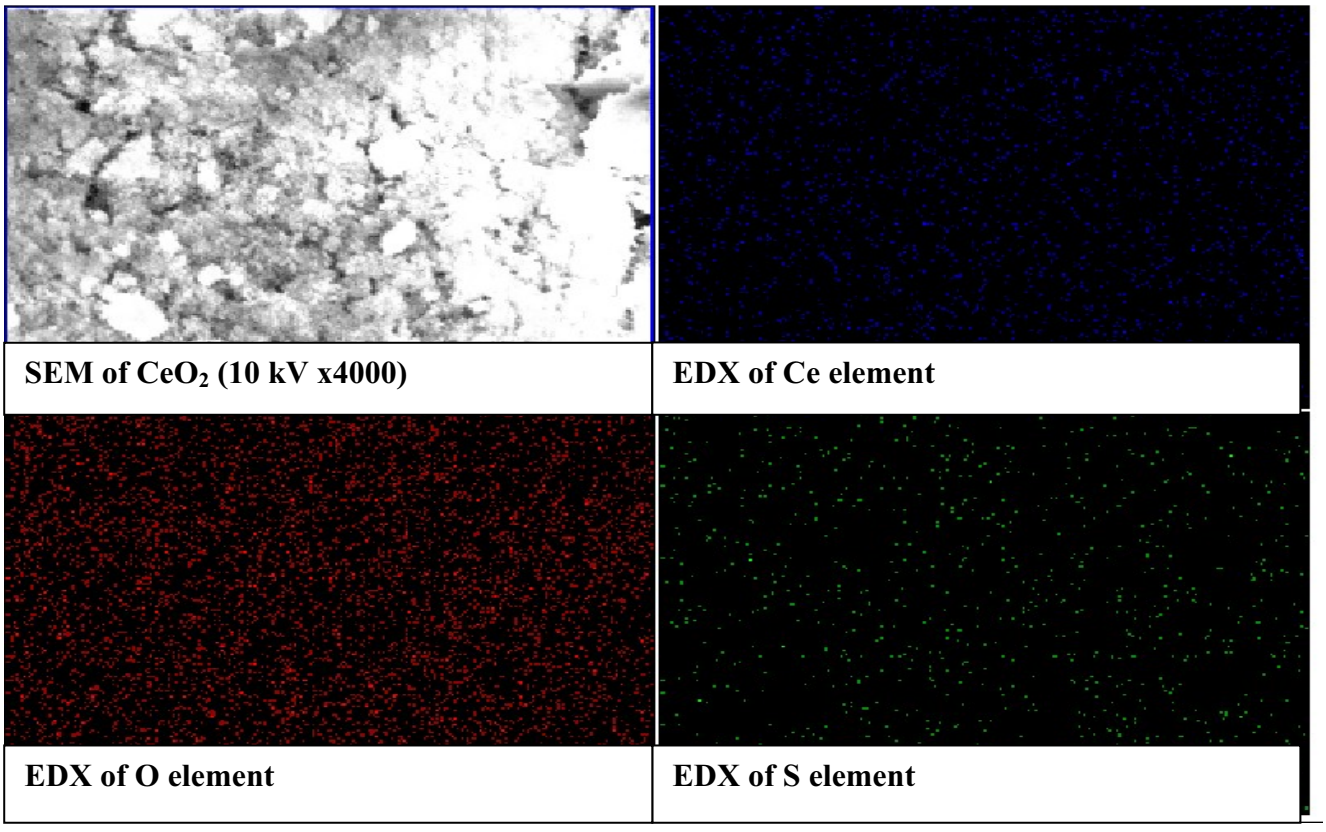

b) SEM and elemental mapping of CeO_2 sulfided at 800^{o}C

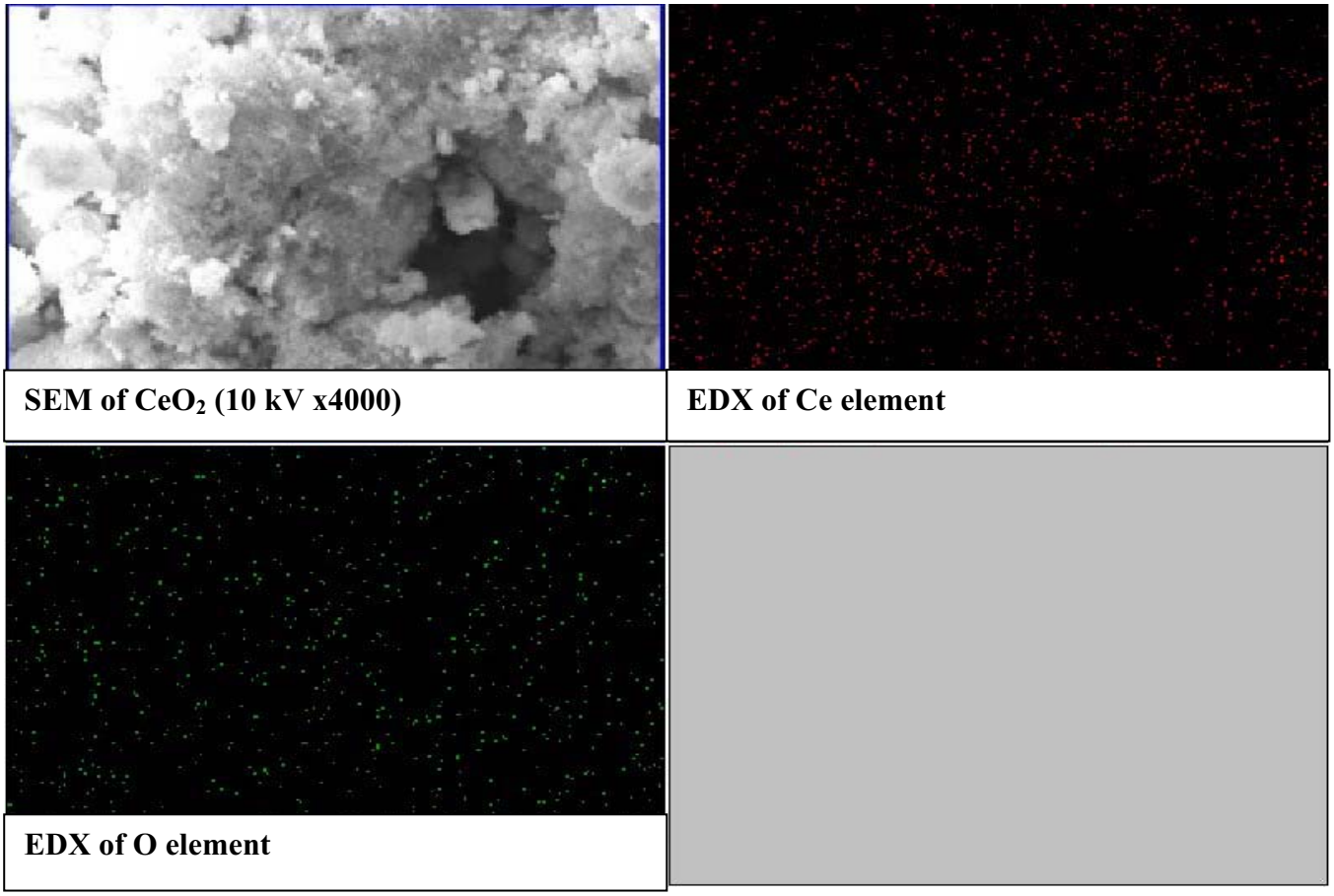

(c) SEM and elemental mapping of regenerated CeO_2

Figure 6 Mapping of sulfur, oxygen and cerium distribution on the sulfided CeO_2.

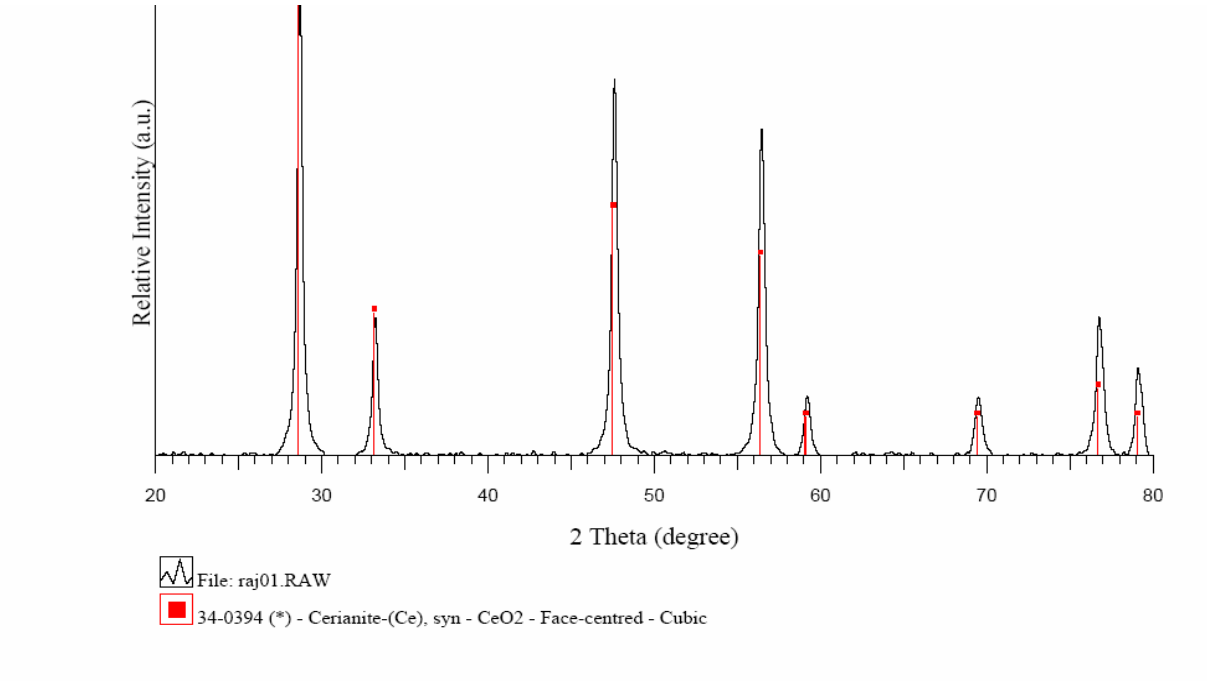

Figure 7 XRD pattern of pure CeO_2.

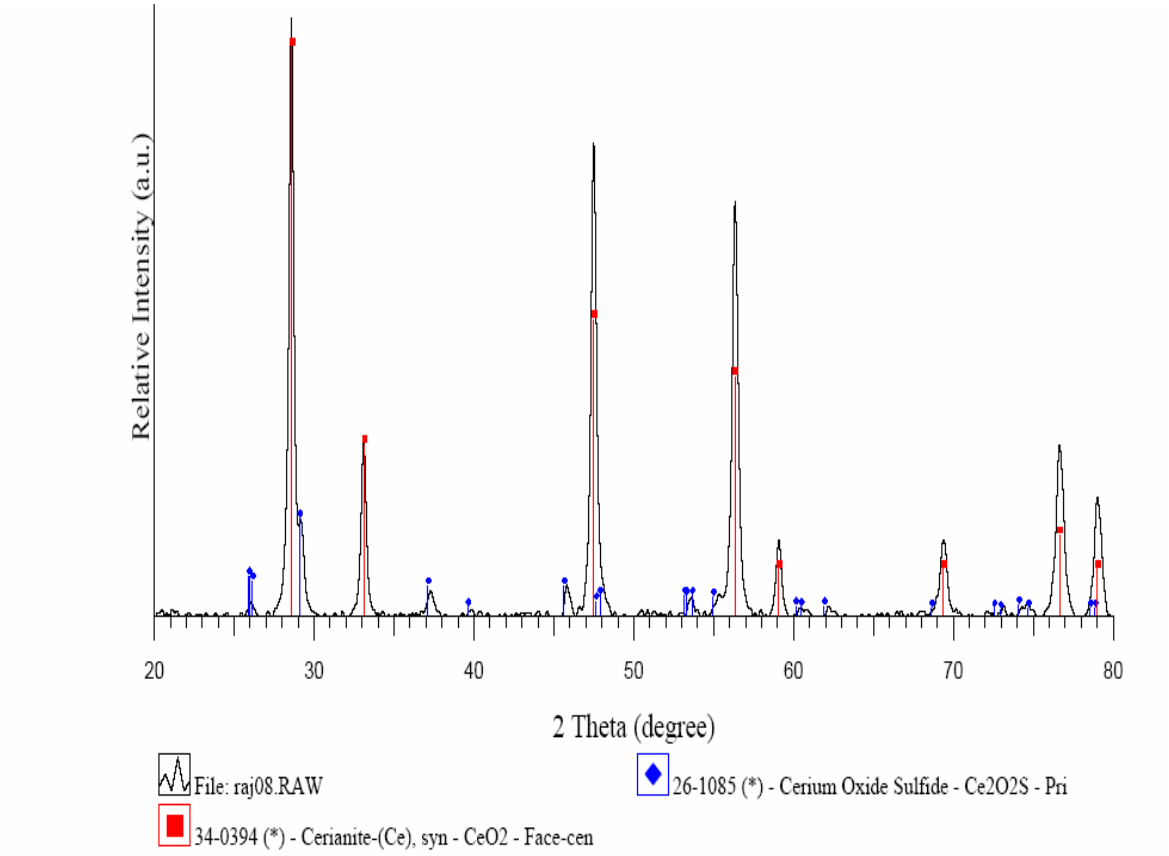

Figure 8 XRD pattern of CeO_2 sulfided at 800 ^{o}C (JCPDS-ICDD).

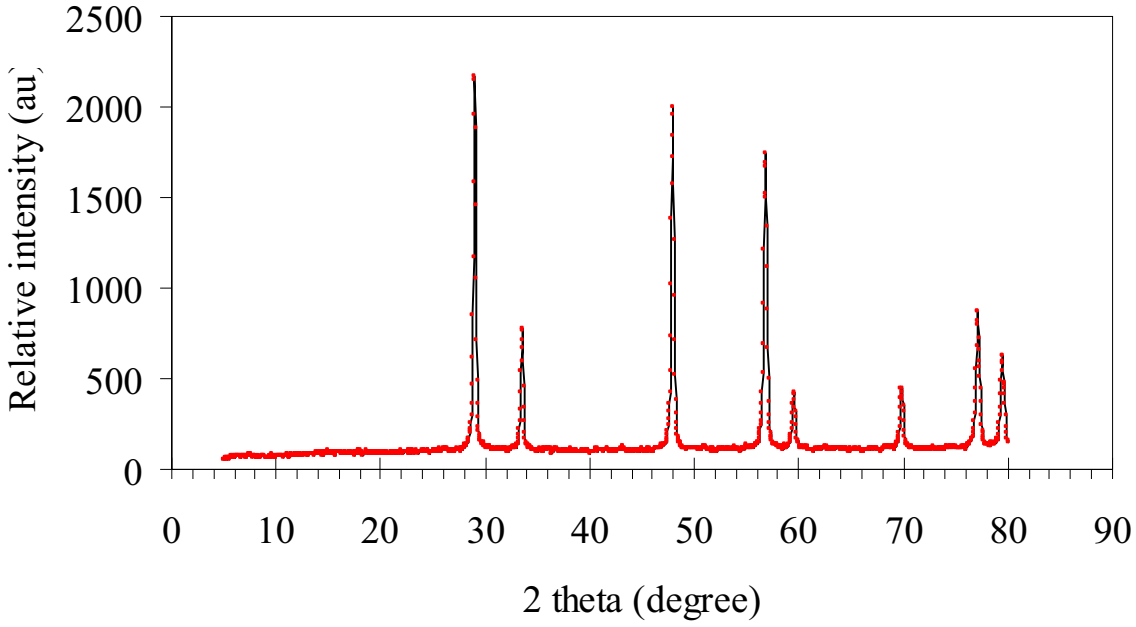

Figure 9 XRD pattern of regenerated sulfided CeO_2 (JCPDS-ICDD).

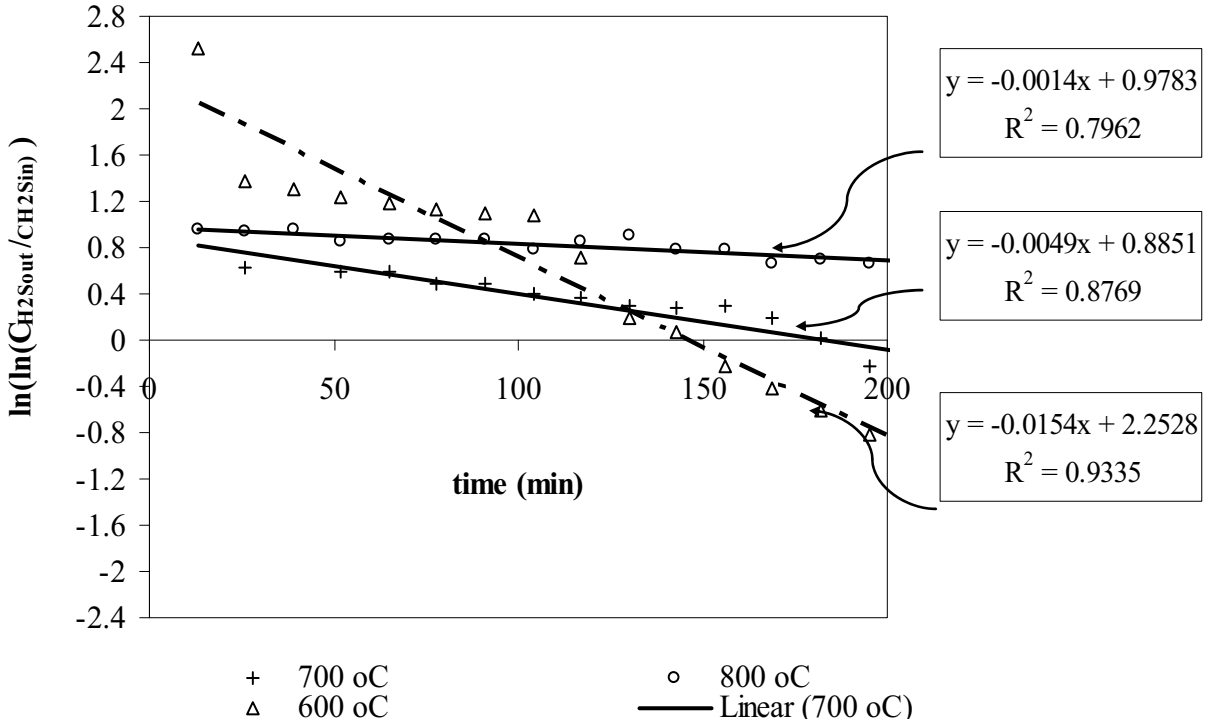

Figure 10 Test of deactivation model equation.

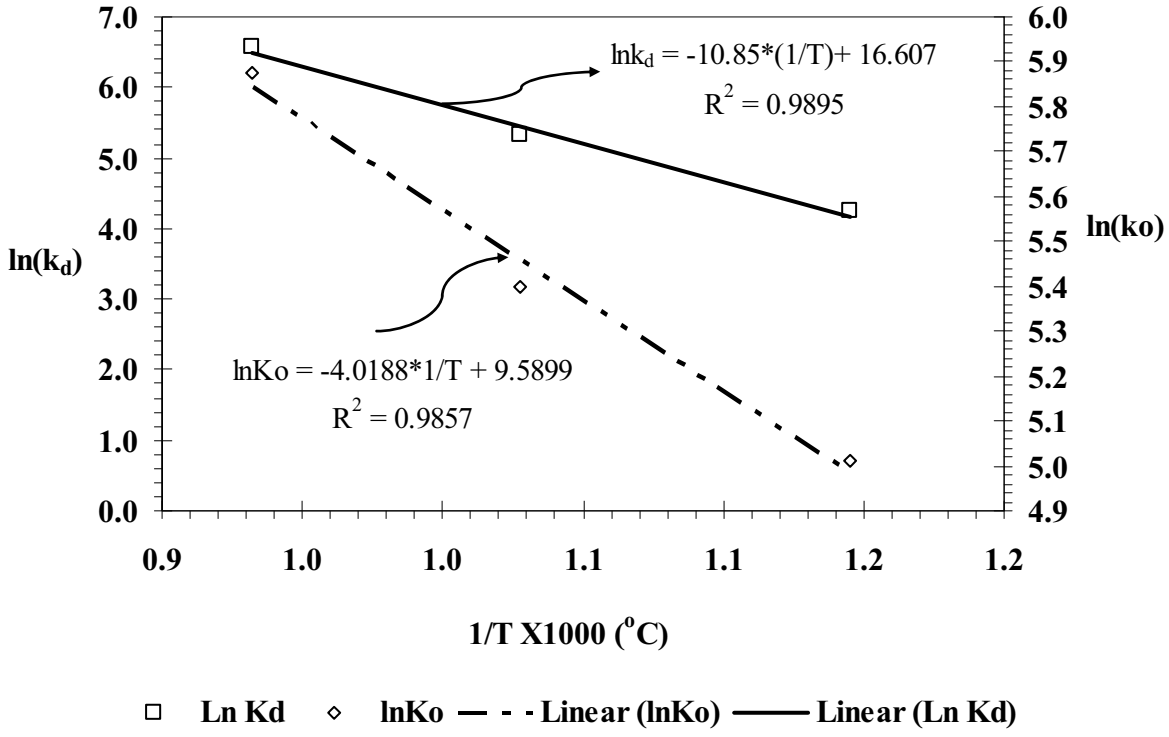

Figure 11 Arrhenious plots of sorption rate constants and deactivation rate constants.

Table 1

Physical and chemical properties of CeO_2

Surface area (m^2g^{-1})	42.819
Bulk density	9.102
Pore Volume	9.7443×10^{-2}

Table 2

Operating conditions of GC

Detector	TCD
Detector temperature (^oC)	150
Column	Porapak-Q
Oven temperature (^oC)	Linear programming @ $20^oC\ min^{-1}$
Current (mA)	150

Table 3 Summary of deactivation model parameters

Temperature (^oC)	$\frac{Vo}{Wk_o}$ **(-)**	k_o **($cm^3\ min^{-1}\ g^{-1}$)**	k_d **(min^{-1})**	**R^2 (-)**
600	2.55	3.566	0.0144	0.79
700	2.40	1.66	0.0049	0.89
800	2.66	1.503	0.0014	0.9351

RESEARCH IV

Reactivity of CeO_2 and Ce-ZrO_2 toward steam reforming of palm fatty acid distilled (PFAD) with co-fed oxygen and hydrogen

Steam reforming of three types free fatty acids (i.e. palmitic, oleic and linoleic acids) and palm fatty acid distilled (PFAD) were studied over ceria-based materials prepared by precipitation and cationic surfactant-assisted methods with/without Zr doping with an aim to develop good reforming catalyst for converting PFAD to hydrogen with high reforming reactivity and low carbon deposition. Among all catalysts, high surface area (HSA) Ce-ZrO_2 (with Ce/Zr ratio of 3/1) prepared by cationic surfactant-assisted method provided the highest steam reforming reactivity with greatest resistance toward carbon deposition; due to the high oxygen storage capacity (OSC) of this material. During steam reforming, the redox reactions between absorbed hydrocarbons (forming intermediate surface hydrocarbon species) with lattice oxygen (O_O^x) at Ce-ZrO_2 surface take place. The rapid redox reactions between surface carbon (C*) forming via the adsorptions of hydrocarbon with lattice oxygen (O_O^x) prevents the formation of carbon species from decomposition of hydrocarbons. At 1173 K, the main products from the steam reforming of PFAD over this catalyst are H_2, CO, and CO_2 with some amounts of CH_4 and C_2H_4 generated; the formations of these high hydrocarbons can be eliminated by increasing temperature up to 1273 K.

The addition of either oxygen or hydrogen together with PFAD and steam considerably reduced the degree of carbon deposition. The presence of oxygen also reduced the formations of hydrocarbons, on the other hand, these formations increased when hydrogen was introduced at the feed. The negative effect of hydrogen is due to hydrogenation reaction as well as the reduction of lattice oxygen by hydrogen, which consequently inhibits the reaction of lattice oxygen with surface hydrocarbon species.

6.1 Introduction

According to the current oil crisis and the shortage of fossil fuels, the development of the biomass-based fuels (or biofuel) attracts much attention. Nowadays, one of the most practical biofuels is biodiesel, which are produced from palm oil. It should be noted that, recently, there are also several attempts to convert lignocellulosic biomass to biofuels (i.e. BTL); this conversion will reduce the competition of fuel with food market, which results in the food shortage and the rising of food price. Nevertheless, this technology remains need further development to achieve high efficiency.

Focusing on palm oil, over the past 10 years, this compound has become one of the attractive resources for biodiesel production since it constitutes a renewable and sustainable source of energy. Importantly, palm oil always contain high amount of free fatty acid (FFA) and the presence of too high FFA easily results in high amounts of soap produced simultaneously with the transesterification reaction. Therefore, to avoid this reaction, most of FFA in palm oil must be firstly processed or removed (as called palm fatty acid distilled or PFAD). The conversion of this removed PFAD to valuable products or fuels (e.g. fatty acid methyl esters via esterification or even hydrogen) is an alternative way to reduce the cost for biodiesel production and consequently make biodiesel enable to compete economically with conventional petroleum diesel fuels. Among the prospective fuels, hydrogen is expected to be one of the most promising fuels in the near future. It is known as the zero-emission fuel and could be produced efficiently from the catalytic reforming of several hydrocarbon sources such as methane, methanol, bio-ethanol, gasoline and other oil derivatives. On this basis, the production of hydrogen from PFAD will provide the great benefit in terms of energy, environmental, and economical aspects.

Focusing on catalytic reforming process, steam reforming of several oxygenated hydrocarbons, e.g. methanol, acetic acid, ethanol, acetone, phenol or cresol as model compounds of bio-oils has widely been investigated [1-9]. Recently, many researchers have also investigated the addition of oxygen together with steam in a single process, calling an autothermal reforming, in order to reduce the degree of carbon formation as well as provide the thermal self-sustaining process. Until now, no literature work has reported the conversion fatty acids or PFAD to hydrogen by the catalytic reforming process; only few works have presented the catalytic reforming or

cracking of acetic acid to hydrogen [10-12]. PFAD normally consists mainly of palmitic acid ($C_{16}H_{32}O_2$; $CH_3(CH_2)_{14}COOH$), oleic acid ($C_{18}H_{34}O_2$; $CH_3(CH_2)_7CH=CH(CH_2)_7COOH$) and linoleic acid ($C_{18}H_{32}O_2$; $CH_3(CH_2)_4CH=CHCH_2CH=CH(CH_2)_7CO_2H$) with various ratios depending on the source of palm oils. The major difficulty to reform high hydrocarbon compounds like PFAD is the possible deactivation of the reforming catalyst due to the carbon deposition, as fatty acids can decompose homogenously and form carbon species on the surface of catalyst. In addition, from its thermal decomposition, several gaseous hydrocarbon elements, which act as very strong promoters for carbon formation, can be formed. Worldwide efforts are in progress to explore a novel catalyst with high activity and stability for the reforming of heavy hydrocarbon compounds.

Recently, it is established that ceria and metal oxide (e.g. Gd, Nb, and Zr) doped cerias provide high oxygen storage capacity, which is beneficial in oxidation and reforming processes [13]. The great benefit of ceria-based catalysts for the reforming reaction is their high resistance toward carbon deposition compared to the conventional metal catalysts i.e. Ni [13, 14]; however, the main weaknesses of the materials are their low specific surface area and high deactivation due to the thermal sintering particularly when operated at such a high temperature [15]. The preparation and use of high surface area ceria (CeO_2 (HSA; high surface area)) with high resistance toward the sintering would be a good alternative method to improve the catalytic reactivity [15]. Recently, Terribile et al. [16] synthesized CeO_2 (HSA) with improved textural, structural and chemical properties for environmental applications by using a novel cationic surfactant-assisted approach. They reported that the reaction of cerium salts under basic conditions with ammonia in the presence of a cationic surfactant results in the precipitation of a gelatinous hydrous cerium oxide/surfactant mixture, which after calcination gives high surface area, fluorite-structured CeO_2 with good homogeneity and stability. They suggested that the cationic surfactant acts as a surface area enhancer by incorporation into the hydrous oxide and lowering of the surface tension of water in the pores during drying.

In addition to the investigation on preparation method, the addition of zirconium oxide (ZrO_2) has also been reported to improve the specific surface area, oxygen storage capacity, redox property, thermal stability and catalytic activity of ceria [17-22]. These benefits were associated with enhanced reducibility of cerium

(IV) in Ce-ZrO_2, which is a consequence of high O^{2-} mobility inside the fluorite lattice. The reason for the increasing mobility might be related to the lattice strain, which is generated by the introduction of a smaller isovalent Zr cation into the CeO_2 lattice (Zr^{4+} has a crystal ionic radius of 0.84 Å, which is smaller than 0.97 Å for Ce^{4+} in the same co-ordination environment) [23].

In the present work, it is aimed to develop the reforming catalysts that can convert PFAD to hydrogen with high reforming activity and great resistance toward carbon formation. CeO_2 and Ce-ZrO_2 prepared by 2 different methods i.e. typical (co-) precipitation and cationic surfactant-assisted methods were selected as the catalyst in the present work. The steam reforming of palmitic acid, oleic acid and linoleic acid (as main components in PFAD) over these catalysts were firstly studied and compared to conventional Ni/Al_2O_3. The steam reforming of PFAD over selected catalyst was then carried out. The effects of temperature, oxygen adding and hydrogen adding on the reforming reactivity were also investigated. Lastly, the possible mechanism for steam reforming of PFAD over ceria-based catalysts was discussed.

6.2 Experimental methods

6.2.1. Raw material and Chemicals

In the present work, palm fatty acid distillate (PFAD) was obtained from Chumporn Palm Oil Industry Public Company Limited., Thailand. It consists of 93 wt% free fatty acid (FFA) (mainly contains 46% palmitic acid, 34% oleic acid and 8% linoleic acid with small amount of other fatty acids i.e. stearic, myristic, tetracosenoic, linolenic, ecosanoic, ecosenoic, and palmitoleic acid). The rest elements are triglycerides, diglycerides (DG), monoglycerides (MG) and traces of impurities. The lab grade palmitic acid, oleic acid, and linoleic acid were supplied from Aldrich.

6.2.2 Material synthesis and characterization

In the present work, CeO_2 was synthesized by precipitation (CeO_2 (LSA)) and cationic surfactant-assisted (CeO_2 (HSA)) methods. CeO_2 (LSA) was prepared by the precipitation of cerium nitrate ($Ce(NO_3)_3 \cdot H_2O$) from Aldrich. The starting solution was prepared by slowly adding of 0.4 M ammonia (with flow rate of 0.254 $cm^3\ h^{-1}$) to 0.1 M of cerium nitrate solution until reaching volumetric ratio of 2:1. This solution

was stirred by magnetic stirring (100 rpm) for 3 h, then sealed and placed in a thermostatic bath maintained at 363 K for 3 days to prevent an agglomeration of the particles. The precipitate was filtered and washed with deionised water and acetone to remove the free surfactant. It was dried overnight in an oven at 383 K, and then calcined at 1173 K for 6 h. Following to the work from Terribile et al. [16], CeO_2 (HSA) were prepared by adding an aqueous solution of the appropriate cationic surfactant, 0.1 M cetyltrimethylammonium bromide solution from Aldrich, to a 0.1 M cerium nitrate. The molar ratio of ([Ce])/[cetyltrimethylammonium bromide] was kept constant at 0.8. The mixture was stirred and then aqueous ammonia was slowly added with vigorous stirring until the pH was 11.5 [16]. After treatment with the same procedure as CeO_2 (LSA), fluorite-structured CeO_2 with good homogeneity were obtained.

$Ce_{1-x}Zr_xO_2$ (or Ce-ZrO_2) with different Ce/Zr molar ratios were also prepared by either co-precipitation or surfactant-assisted method of cerium nitrate ($Ce(NO_3)_3 \cdot H_2O$), and zirconium oxychloride ($ZrOCl_2 \cdot H_2O$) (from Aldrich). The ratio between each metal salt was altered to achieve nominal Ce/Zr molar ratios: $Ce_{1-x}Zr_xO_2$, where x = 0.25, 0.50, and 0.75 respectively. After treatment, the specific surface areas of all CeO_2 and Ce-ZrO_2 were achieved from BET measurement. As presented in Table 1, after drying in the oven, surface areas of 105 and 55 $m^2\ g^{-1}$ were observed for CeO_2 (HSA) and CeO_2 (LSA), respectively and, as expected, the surface area decreased at high calcination temperatures. However, the value for CeO_2 (HSA) is still appreciable after calcination at 1173 K. The achievement of high surface area material by surfactant-assisted procedure is due to the interaction of hydrous oxide with cationic surfactants under basic conditions during the preparation [16]. At high pH value, conducting the precipitation of hydrous oxide in the presence of cationic surfactant allows cation exchange process between H^+ and the surfactant, resulting in a developed pore structure with an increase in surface area [16]. It can also be seen that the introduction of ZrO_2 stabilizes the surface area of ceria, which is in good agreement with several previous reports [24-26].

For comparison, Ni/Al_2O_3 (5wt% Ni) was also prepared by impregnating γ-Al_2O_3 (from Aldrich) with $Ni(NO_3)_2$ solution (from Aldrich). After stirring, the solution was dried and calcined at 1173 K for 6 h. The catalyst powder was reduced with 10%H_2/Ar at 773 K for 6 h before use. After reduction, Ni/Al_2O_3 was

characterized by several physicochemical methods. The weight contents of Ni were determined by X-ray fluorescence (XRF) analysis. The reducibility percentage of nickel was measured and calculated from the degree of H_2 uptakes from temperature-programmed reduction (TPR) test using 5% H_2 with the total flow rate of 100 cm^3 min^{-1} and temperature from room temperature to 773 K, while the dispersion percentage of nickel was identified from temperature-programmed desorption (TPD) by measuring the volumetric H_2 chemisorbed. All physicochemical properties of the synthesized catalysts are presented in Table 2.

6.2.3 Apparatus and Procedures

To undergoing the catalytic testing, an experimental reactor system was constructed. The feed including palmitic acid, oleic acid and linoleic acid, PFAD and deionized H_2O was introduced via a heated syringe pump passing through our design quartz vaporizer-mixer system, where the inlet fatty acids are injected as droplet before vaporized and mixed with steam/carrier gas. All inlet components were introduced to a 10-mm diameter quartz reactor, which is mounted vertically inside tubular furnace. The catalyst (100 mg) was loaded in the quartz reactor, which was packed with a small amount of quartz wool to prevent the catalyst from moving. Preliminary experiments were carried out to find suitable conditions in which internal and external mass transfer effects are not predominant. Considering the effect of external mass transfer, the total gas flow rate was varied between 10-150 cm^3 min^{-1} under a constant residence time of 10^{-3} g min cm^{-3}. It was found that the reforming rate was independent of gas velocity when the gas flow rate was higher than 70 cm^3 min^{-1}, indicating the absence of external mass transfer effects at this high velocity. Furthermore, the reactions on different average sizes of catalysts (up to 500 μm) were carried out to confirm that the experiments were in the region of intrinsic kinetics. It was observed that the catalysts with the particle size less than 200 μm showed no intraparticle diffusion limitation in the range of conditions studied. Therefore, the total flow rate was kept constant at 100 cm^3 min^{-1} whereas catalyst diameter was between 100-200 μm in all experiments.

In our system, a Type-K thermocouple was placed into the annular space between the reactor and the furnace. This thermocouple was mounted on the tubular reactor in close contact with the catalyst bed to minimize the temperature difference

between the catalyst bed and the thermocouple. Another Type-K thermocouple was inserted in the middle of the quartz tube in order to re-check the possible temperature gradient. It is noted that the inner-system thermocouple is covered with small closed-end quartz rod to prevent the catalytic reactivity of thermocouple during reaction. After the reactions, the exit gas mixture was transferred via trace-heated lines to the analysis section, which consists of a Porapak Q column Shimadzu 14B gas chromatograph (GC) and a mass spectrometer (MS). The mass spectrometer in which the sampling of the exit gas was done by a quartz capillery and differential pumping was used for the transient and carbon formation experiments, whereas the gas chromatography was applied in order to investigate the steady state condition experiments and to recheck the results from MS. In the present work the reactivity of catalyst toward the reaction was defined in terms of hydrogen and other gaseous hydrocarbon by-product selectivities (based on carbon balance).

6.2.4 Measurement of carbon formation

In order to investigate the amount of carbon formed on catalyst surface, the oxidation reaction was applied by introducing 10% O_2 in helium into the system at isothermal condition (1173 K), after purging the system with helium. The amount of carbon formation on the surface of catalysts was determined by measuring the areas under peak of CO and CO_2 from the test compared with those from the calibrations of these components. It is noted that the calibrations of CO and CO_2 were performed by injecting a known amount of these calibration gases from a loop, in an injection valve in the bypass line.

6.3 Results and Discussion

6.3.1 Redox properties and redox reversibility

After treatment, the degrees of oxygen storage capacity (OSC) for fresh ceria-based materials were investigated using reduction measurement (R-1), which was performed by purging the catalysts with 5%H_2 in helium at 1173 K. The amount of H_2 uptake is correlated to the amount of oxygen stored in the catalysts. As presented in Table 3, the amount of H_2 uptakes over high surface area Ce-ZrO_2 and CeO_2 are significantly higher than those over the low surface area cerias, suggesting the

increasing of OSC with the doping of Zr and the increasing of material specific surface area. The benefit of OSC on the reforming reaction will be later presented in Section 4. After purged with helium, the redox reversibilities were then determined by applying oxidation measurement (Ox-1) following with second time reduction measurement (R-2). The amounts of O_2 chemisorbed and H_2 uptake are presented in Table 3. Regarding the results as also shown in Table 3, the amount of hydrogen uptakes for all materials were approximately identical to those from the R-1, indicating the reversibility of OSC for these synthesized ceria-based materials.

6.3.2 Reactivity toward the steam reforming of fatty acids

Before undergoing the tests on PFAD, the steam reforming of palmitic acid, oleic acid and linoleic acid were firstly investigated as these three hydrocarbons are the main components in PFAD. The experiments were carried out at 1173 K by introducing each fatty acid along with steam as co-reactant. It should be noted that the reactions for Ce-ZrO_2 with different Ce/Zr ratios (1/3, 1/1, and 3/1) were preliminary done over palmitic acid and the results revealed that Ce-ZrO_2 with Ce/Zr ratio of 3/1 synthesized from both techniques shows the best performance in terms of stability, activity and product selectivities. Therefore, we report here detailed reactivity of Ce-ZrO_2 only with Ce/Zr ratio of 3/1.

Table 4 presents the summarize of gaseous product distribution from the steam reforming of palmitic acid, oleic acid and linoleic acid over CeO_2 and Ce-ZrO_2 prepared by 2 techniques, while Fig. 1 shows the variations in hydrogen selectivity (%) with time (under the period of 48 h) from the steam reforming of palmitic acid over these catalysts. It is noted that the product distribution in the present work is reported in term of selectivity, as the conversion of fatty acids are always 100% in the range of conditions studied. It can be seen from Fig. 1 that no significant deactivation was detected from these 4 catalysts indicating their good stability toward the reactions. From Table 4, apart from H_2, CO, and CO_2 productions, significant amount of CH_4, C_2H_4, C_2H_6, and C_3H_6 were also detected from the reactions. The production of CO_2 indicates the contribution of the water-gas shift at this high temperature, while the presenting of gaseous hydrocarbons (i.e. CH_4, C_2H_4, C_2H_6, and C_3H_6) comes from the decomposition of these fatty acids (Eq. 1 in the discussion section). Between these three fatty acids, palmitic acid provides highest hydrogen production, whereas

hydrogen production from oleic acid is slightly higher than that from linoleic acid. Furthermore, compared between four catalysts (CeO_2 (HSA), CeO_2 (LSA), Ce-ZrO_2 (HSA), and Ce-ZrO_2 (LSA)), Ce-ZrO_2 (HSA) presents the highest hydrogen production with considerably lower formations of CH_4, C_2H_4, C_2H_6, and C_3H_6. It should be noted that, for comparison, the steam reforming of palmitic acid over conventional Ni/Al_2O_3 was tested at 1173 K. As seen in Fig. 2, unstable profiles of hydrogen production yield, which related to the formation of carbon species on the surface of catalyst, were observed.

After purging in helium, the post-reaction oxidation experiments were carried out by introducing of 10% oxygen in helium to determine the amount of carbon formation occurred in the system. The oxidation measurement detected some amount of carbon on the surface of ceria-based catalysts (between 5.0-5.5 mmol g_{cat}^{-1} for high surface area materials and between 5.9-7.0 mmol g_{cat}^{-1} for low surface area one), whereas significantly higher amount of carbon was found over Ni/Al_2O_3, Table 5, indicating the greater resistance toward carbon deposition of ceria-based catalysts. The explanation for the steam reforming reactivity of ceria-based catalysts with high resistance toward carbon deposition will be given in the discussion section.

6.3.3 Reactivity toward the steam reforming of PFAD

From the results in section 3.1, among all ceria-based catalysts, Ce-ZrO_2 (HSA) with Ce/Zr ratios of 3/1 showed the greatest reactivities toward the steam reforming of palmitic acid, oleic acid and linoleic acid. Therefore, it was chosen for the further study to investigate the reactivity toward the steam reforming of PFAD. Instead of individual fatty acid, the feed was PFAD/H_2O in helium with the steam/carbon ratio of 3.0. It is noted that, before studying the catalyst performance, homogeneous (non-catalytic) steam reforming of PFAD (with above steam/carbon ratio) was also investigated at 1123 K. It was found that at this temperature PFAD were all homogeneously converted to CH_4, C_2H_6, C_2H_4, C_3H_6, CO, CO_2 and H_2 (with H_2 selectivity of 41.3% and CH_4, C_2H_6, C_2H_4, C_3H_6, CO, CO_2 selectivities of 22.3, 10.3, 16.8, 5.0, 16.4, 29.2% respectively). It should also be noted that significant amount of carbon was also detected in the blank reactor after exposure for 10 h.

As for the catalyst testing, the variations in hydrogen production and gaseous by-product selectivities with time from the steam reforming of PFAD over Ce-ZrO_2 at

1123 K are shown in Fig. 3. Similar trend as all three fatty acids was observed; the main products are H_2, CO, and CO_2 with some amounts of CH_4, C_2H_4, C_2H_6, and C_3H_6. The post reaction oxidation measurement indicated that the amount of carbon deposition on the surface of Ce-ZrO_2 after exposure in reforming condition for 48 h is 5.1 mmol g_{cat}^{-1}. As the next step, the effects of inlet steam/carbon ratio and temperature on the reforming reactivity were then studied by varying the inlet steam/carbon ratio from 3.0 to 5.0, 7.0, 9.0 and 11.0, and increasing the operating temperature from 1173 K to 1198 K, 1223 K, 1248 K and 1273 K. Fig. 4 presents the effect of inlet steam/carbon ratio on the hydrogen production and other by-product selectivities (after held the system for 10 h at each condition to ensure that the reaction reactivity is stable), whereas Table 6 presents the degree of carbon deposition observed from the post reaction oxidation measurement. It can be seen that hydrogen and carbon dioxide increase with increasing steam content, whereas carbon monoxide decreases; this could be mainly due to the contribution of the water gas shift reaction. Nevertheless, all hydrocarbon (CH_4, C_2H_4, and C_2H_6) selectivities remain unchanged with increasing steam content and the amount of carbon deposition was relatively unaffected by the increasing of steam. Fig. 5 illustrates the influence of temperature on the hydrogen yield and gaseous product selectivities. Clearly, the activities of catalyst increased with increasing temperature. At 1273 K, the main products from the steam reforming of PFAD over Ce-ZrO_2 were H_2, CO, CO_2, and CH_4, with insignificant amounts of C_2H_4, C_2H_6, and C_3H_6. Table 6 also presents the effect of temperature on the degree of carbon deposition; it can be seen that the amount of carbon formation on Ce-ZrO_2 surface decreased with increasing temperature.

6.3.4 Reactivity towards reforming of PFAD with co-fed oxygen

According to the results in Section 3.3, Ce-ZrO_2 can reform PFAD efficiently with high resistance toward carbon formation compared to conventional Ni/Al_2O_3. Nevertheless, the major consideration for ceria-based catalyst is its relatively low reforming reactivity, which results in the remains of high hydrocarbons in the product due to the incomplete reforming reaction particularly at low operating temperature (1173-1198 K). These formations could be minimized by increasing the temperature to 1273 K, which means significantly high energy input is required for the system. As an alternative procedure to reduce the formations of these hydrocarbons, oxygen was

added in the feed together with PFAD and steam as autothermal reforming operation. In the present work, the inlet steam/carbon molar ratio was kept constant at 3.0, while the inlet O_2/carbon molar ratios were varied from 0.2, 0.4, 0.6, 0.8, to 1.0. The effect of oxygen concentration on product selectivities at 1173 K (after held the system for 10 h at each condition to ensure that the reaction reactivity is stable) is shown in Fig. 6.

It can be seen that hydrogen selectivity increased with increasing O_2/carbon molar ratio until the ratio reached 0.8, then oxygen showed no effect on the hydrogen production at higher inlet O_2/carbon molar ratio values. It should be noted that the conversion of O_2 was always closed to 100% in all testing. Fig. 6 also indicates that the dependence of oxygen on CH_4 production is non-monotonic. At suitable O_2/carbon molar ratio, higher H_2, CO, and CO_2 were observed from the autothermal reforming of PFAD, whereas no formation of C_2H_6, C_2H_4, and C_3H_6 was found compared to the steam reforming at the same operating conditions. The post-reaction oxidation measurement was then carried out to determine the degree of carbon formation on catalyst surface. From the oxidation measurement results shown in Table 7, significantly less quantities of carbon deposited were observed at high O_2/carbon molar ratio.

6.3.5 Reactivity towards reforming of PFAD with co-fed hydrogen

Previously, we reported that the addition of hydrogen as co-feeding along with oxyhydrocarbon (i.e. ethanol) and steam over Ni catalysts could reduce the degree of carbon formation in the system as well as minimize the presences of intermediate hydrocarbon i.e. C_2H_4 and C_2H_6 occurring form the decomposition of ethanol during reaction [27]. Here, we thereby investigated the reactivity of Ce-ZrO_2 towards reforming of PFAD with co-fed hydrogen. The inlet steam/carbon molar ratio was kept constant at 3.0, while the inlet H_2/carbon molar ratios were varied from 0.5-5.0. As hydrogen was used as the feed, the effect of this component on the catalyst performance was investigated in term of gaseous hydrocarbon (i.e. CH_4, C_2H_6, C_2H_4, and C_3H_6) distribution instead of hydrogen production selectivity. Fig. 7 presents all product distribution from the steam reforming of PFAD in the presence of hydrogen over Ce-ZrO_2 (after held the system for 10 h at each condition to ensure that the

reaction reactivity is stable), while Table 7 also reports the effect of hydrogen adding on the amount of carbon formation.

It was found that, with the presence of hydrogen, less amount of carbon deposited were observed on the surface of Ce-ZrO_2. However, the formations of hydrocarbon particularly CH_4 in the product increased with increasing H_2 content. Thus, the adding of hydrogen as co-fed is not the suitable procedure for improving the steam reforming performance of PFAD over Ce-ZrO_2.

6.4 Discussion

Ce-ZrO_2 (HSA) was found in this study to have good reactivity toward the steam reforming of PFAD with excellent resistance towards carbon deposition compared to conventional Ni/Al_2O_3. Although Ni/Al_2O_3 provided higher initial H_2 yield, the reactivity decreases rapidly with time due to the significant carbon formation on its surface resulting in the low H_2 yield at steady state condition (Fig. 2, Table 4 and Table 5). It is noted that Ce-ZrO_2 (HSA) also presented good reactivity toward steam reforming of palmitic, oleic, and linoleic acids. Among these three fatty acids, the steam reforming of palmitic acid provided highest hydrogen production with lowest presence of hydrocarbons (i.e. CH_4, C_2H_6, C_2H_4, and C_3H_6) in the product; this could be due to the lighter carbon molecule of palmitic acid (C_{16}) compared to oleic and linoleic acids (C_{18}). Nevertheless, the differences are not much significant. At the temperature of 1173 K, the main products from the reforming of PFAD over Ce-ZrO_2 (HSA) were H_2, CO, CO_2, and CH_4 with some amounts of C_2H_6, C_2H_4, and C_3H_6. According to the mechanistic viewpoint, the overall reactions involved in the steam reforming of PFAD are very complex. At such a high operating temperature in the present work, the thermal decomposition of PFAD can take place producing several gaseous products (i.e. hydrogen, carbon monoxide, carbon dioxide, light hydrocarbons (C_nH_m) and oxygenates ($C_nH_mO_x$)) as well as carbon species forming on the surface of catalyst. By feeding steam, the steam reforming of hydrocarbons and oxygenates can then occur along with some side-reactions (e.g. water gas shift reaction and methanation).

$$C_nH_m + nH_2O \rightarrow nCO + (n + 0.5m)H_2 \quad (1)$$

$$C_nH_mO_x + (n\text{-}x)H_2O \rightarrow nCO + (n - x + 0.5m)H_2 \quad (2)$$

$$nCO + nH_2O \rightarrow nCO_2 + nH_2 \quad (3)$$

$$nCO + 3nH_2 \rightarrow nCH_4 + nH_2O \quad (4)$$

$$nCO_2 + 4nH_2 \rightarrow nCH_4 + 2nH_2O \quad (5)$$

Previously, we have proposed the redox mechanism to explain the reforming behavior of ceria-based catalysts by indicating that the reforming reaction mechanism involves the reaction between methane, or an intermediate surface hydrocarbon species, and lattice oxygen at the ceria-based material surface [28]. During reforming reaction, the isothermal reaction rate reaches steady-state where co-reactant i.e. steam provides a continuing source of oxygen. We also proposed that the controlling step is the reaction of methane with ceria, and that oxygen is replenished by a significantly more facile surface reaction of the ceria with steam [28]. Therefore, we suggested here that the reaction pathway for steam reforming of PFAD over ceria-based materials involves the reaction between absorbed hydrocarbons (forming intermediate surface hydrocarbon species) with the lattice oxygen (O_O^x) at CeO_2 surface, as illustrated schematically below.

C_nH_m adsorption

$$C_nH_m + (n+m)^* \rightarrow (CH_x^*) + (H^*) \rightarrow n(C^*) + m(H^*) \quad (6)$$

Co-reactant (H_2O) adsorption

$$H_2O + 2^* \Leftrightarrow OH^* + H^* \quad (7)$$

$$OH^* + {}^* \Leftrightarrow H^* + O^* \quad (8)$$

Redox reactions of lattice oxygen (O_O^x) with C and O**

$$C^* + O_O^x \rightarrow CO^* + V_O^{\bullet\bullet} + 2\,e' \quad (9)$$

$$V_O^{\bullet\bullet} + 2\,e' + O^* \Leftrightarrow O_O^x + {}^* \quad (10)$$

Desorption of products (CO and H_2)

$$CO^* \Leftrightarrow CO + {}^* \quad (11)$$

$$2(H^*) \Leftrightarrow H_2 + 2^* \quad (12)$$

Using the Kroger–Vink notation, $V_O^{\bullet\bullet}$ denotes as an oxygen vacancy with an effective charge 2^+, and e' is an electron which can either be more or less localized on a cerium ion or delocalized in a conduction band. * is the surface active site of ceria-based materials, there are two possibilities for this scheme depending on what is assumed for the catalyst active site. It can be a unique site, or can also be considered to be the same site as the catalyst oxidised site (O_x) [28]. During the reactions, hydrocarbons adsorbed on * forming intermediate surface hydrocarbon species (CH_x*) (Eq. 6) and later reacted with the lattice oxygen (O_O^x) (Eq. 9). The steady state reforming rate is due to the continuous supply of the oxygen source by H_2O (Eqs. 7-8) that reacted with the reduced-state catalyst to recover lattice oxygen (O_O^x) (Eq. 10).

The high resistance towards carbon deposition for ceria-based catalysts particularly Ce-ZrO_2 (HSA) is mainly due to the high oxygen storage capacity (OSC) of material. Previously, we reported the excellent resistance towards carbon deposition for CeO_2 especially for high surface area CeO_2 [28]. CeO_2 contains a high concentration of highly mobile oxygen vacancies and thus acts as a local source or sink for oxygen on its surface. It has been reported that at high temperature the lattice oxygen (O_O^x) at the CeO_2 surface can oxidize gaseous hydrocarbons (methane [28], propane and butane [29]). Although conventional CeO_2 (CeO_2 (LSA)) has also been reported to provide high resistance towards carbon formation, the major weaknesses of CeO_2 (LSA) are its low specific surface area and also high size reduction due to the thermal sintering impact, resulting in its significant lower redox properties than CeO_2 (HSA). These disadvantages result in the low steam reforming reactivity for CeO_2 (LSA). It was also concluded here that the addition of ZrO_2 on CeO_2 promoted the reforming reactivity, which is in good agreement with the literatures.

According to our interested reaction (steam reforming of PFAD), carbon formation could occur from the decompositions of fatty acids and gaseous hydrocarbon products. Theoretically, it can also occur from the Boudouard reaction (Eq. 13) especially at low inlet steam/carbon molar ratio.

$$2CO \quad \Leftrightarrow \quad CO_2 + C \qquad (13)$$

These reactions could be inhibited by the redox reaction between the surface carbon (C) with the lattice oxygen (O_O^x) at CeO_2 surface (Eq. 17).

$$C + O_O^x \rightarrow CO + V_O^{\bullet\bullet} + 2\,e' \qquad (17)$$

The greater resistance toward carbon deposition for high surface area ceria-based catalyst particularly Ce-ZrO_2 (HSA) is due to the significant higher amount of lattice oxygen (O_O^x) on their surfaces, according to the results in Section 3.1.

It was also observed from the study that the addition of either oxygen or hydrogen together with PFAD and steam reduced the degree of carbon deposition. By addition of oxygen along with PFAD and steam as autothermal reforming, the partial oxidation of fatty acids takes place and fatty acids could possibly oxidize to methane and carbon monoxide; thus, the rate of fatty acid decomposition reduces and less C_2H_6, C_2H_4, and C_3H_6 are generated, which consequently results in the lower degree of carbon deposition on the surface of catalyst. In addition, oxygen also prevents the formation of carbon species via the hydrocarbon depositions by oxidizing these hydrocarbons to gaseous elements that are unfavored to form carbon species. Importantly, the presence of oxygen also helps steam to regenerate the lattice oxygen (O_O^x) on CeO_2 surface ($0.5O_2 + V_O^{\bullet\bullet} + 2\,e' \rightarrow O_O^x$), which eventually help promoting the reforming reactivity of ceria. It is noted that the major consideration of the autothermal reforming operation is the O_2/carbon ratio. The presence of too high oxygen concentration could oxidize hydrogen produced from the reaction and generate more steam.

By adding hydrogen at the feed, the degree of carbon formation also reduced due to the hydrogenation reaction. Nevertheless, it was found that in the presence of hydrogen at the feed the formations of hydrocarbon particularly CH_4 in the product increased. This negative effect of hydrogen appearance on CH_4, C_2H_4, and C_2H_6 conversions could be due to the hydrogenation of adsorbed CH_x species with this adding hydrogen and also from reduction of lattice oxygen by hydrogen and consequently inhibits the reaction of the lattice oxygen with the surface hydrocarbon species. This explanation is in good agreement with our previous studies [28] which

studied kinetics parameters for the methane steam reforming on ceria-based materials and reported the negative effect of hydrogen on methane conversion.

6.5 Conclusion

Steam reforming of free fatty acids (i.e. palmitic, oleic and linoleic acids) and palm fatty acid distilled (PFAD) were tested over ceria-based materials prepared by precipitation and cationic surfactant-assisted methods with/without Zr doping. Among all ceria-based catalysts, Ce-ZrO_2 (with Ce/Zr ratio of 3/1) from cationic surfactant-assisted method (Ce-ZrO_2 (HSA)) provided the highest degree of oxygen storage capacity (OSC) and steam reforming reactivity with greatest resistance toward carbon deposition. At 1173 K, the main products from the steam reforming of PFAD over Ce-ZrO_2 (HSA) are H_2, CO, and CO_2 with some amounts of CH_4, C_2H_4, C_2H_6, and C_3H_6; the formations of high hydrocarbon can be eliminated by increasing the operating temperature up to 1273 K.

The addition of either oxygen or hydrogen together with PFAD and steam reduced the degree of carbon deposition. The presence of oxygen also reduced the formations of C_2H_6, C_2H_4, and C_3H_6 due to the possible oxidation of fatty acids, which is eventually converted to methane and carbon monoxide. At suitable O_2/H_2O/PFAD ratio, high H_2 selectivity without the formation of C_{2+} hydrocarbon was achieved. On the other hand, in the presence of hydrogen at the feed the formations of hydrocarbon in the product increased. This negative effect of hydrogen appearance on CH_4, C_2H_4, and C_2H_6 conversions is due to hydrogenation reaction and the reduction of lattice oxygen by hydrogen, which consequently inhibits the reaction of the lattice oxygen with the surface hydrocarbon species.

References

[1] A.C. Basagiannis and X.E. Verykios, Appl. Catal. A 308 (2006), p. 182.

[2] J.R. Galdámez, L. García and R. Bilbao, Energy Fuels 19 (2005), p. 1133.

[3] S. Czernik, R.J. French, K.A. Magrini-Bair and E. Chornet, Energy Fuels 18 (2004), p. 1738.

[4] D. Wang, S. Czernik, D. Montané, M. Mann and E. Chornet, Ind. Eng. Chem. Res. 36 (1997), p. 1507.

[5] D. Wang, D. Montané and E. Chornet, Appl. Catal. A 143 (1996), p. 245.

[6] K. Polychronopoulou, C.N. Costa and A.M. Efstathiou, Appl. Catal. A 272 (2004), p. 37.

[7] K. Takanabe, K. Aika, K. Seshan and L. Lefferts, J. Catal. 227 (2004), p. 101.

[8] A.N. Fatsikostas, D.I. Kondarides and X.E. Verykios, Catal. Today 75 (2002), p. 145.

[9] D.K. Liguras, D.I. Kondarides and X.E. Verykios, Appl. Catal. B: Environ. 43 (2003), p. 345.

[10] A.C. Basagiannis, X.E. Verykios, Appl. Catal. B, In Press

[11] A.C. Basagiannis, X.E. Verykios, International Journal of Hydrogen Energy 32 (2007) p. 3343.

[12] T. Davidian, N. Guilhaume, C. Daniel, C. Mirodatos, Appl. Catal. A 335 (2008) p. 64.

[13] E. Ramirez, A. Atkinson and D. Chadwick, Appl. Catal. B 36 (2002), p. 193.

[14] E. Ramírez-Cabrera, N. Laosiripojana, A. Atkinson and D. Chadwick, Catal. Today, 78 (2003), 433.

[15] D. Terribile, A. Trovarelli, J. Llorca, C. Leitenburg and G. Dolcetti, J. Catal., 178 (1998), 299.

[16] D. Terribile, A. Trovarelli, J. Llorca, C. Leitenburg and G. Dolcetti, Catal. Today, 43 (1998), 79-88.

[17] M. Ozawa, M. Kimura, A. Isogai, J. Alloys Comp., 193 (1993) 73.

[18] G. Balducci, J. Kaspar, P. Fornasiero, M. Graziani, M.S. Islam, J. Phys. Chem. B, 102 (1998) 557.

[19] G. Vlaic, P. Fornasiero, S. Geremia, J. Kaspar, M. Graziani, J. Catal., 168 (1997) 386.

[20] G.R. Rao, J. Kaspar, S. Meriani, R. Dimonte, M. Graziani, Catal. Lett., 24 (1994) 107.

[21] P. Fornasiero, R. Dimonte, G.R. Rao, J. Kaspar, S. Meriani, A. Trovarelli, M. Graziani, J. Catal., 151 (1995) 168.

[22] M.H. Yao, T.E. Hoost, R.J. Baird, F.W. Kunz, J. Catal., 166 (1997) 67.

[23] D. Kim, J. Am. Ceram. Soc., 72 (1989) 1415.

[24] N. Kruse, A. Frennet, J.M. Bastin (Eds.), Catalysis and Automotive Pollution Control IV, Elsevier, Amsterdam, 1998

[25] J. Kaspar, P. Fornasiero and M. Graziani. Catal. Today 50 (1999), 285.

[26] H.S. Roh, H.S. Potdar and K.W. Jun, Catal. Today 93–95 (2004), 39.

[27] N. Laosiripojana, S. Assabumrungrat, S. Charojrochkul, Appl. Catal. A 327 (2007) p. 180.

[28] N. Laosiripojana and S. Assabumrungrat, Appl. Catal. B: Environ, 60 (2005) 107.

[29] N. Laosiripojana, S. Assabumrungrat, J Power Sources 158 (2006) 1348.

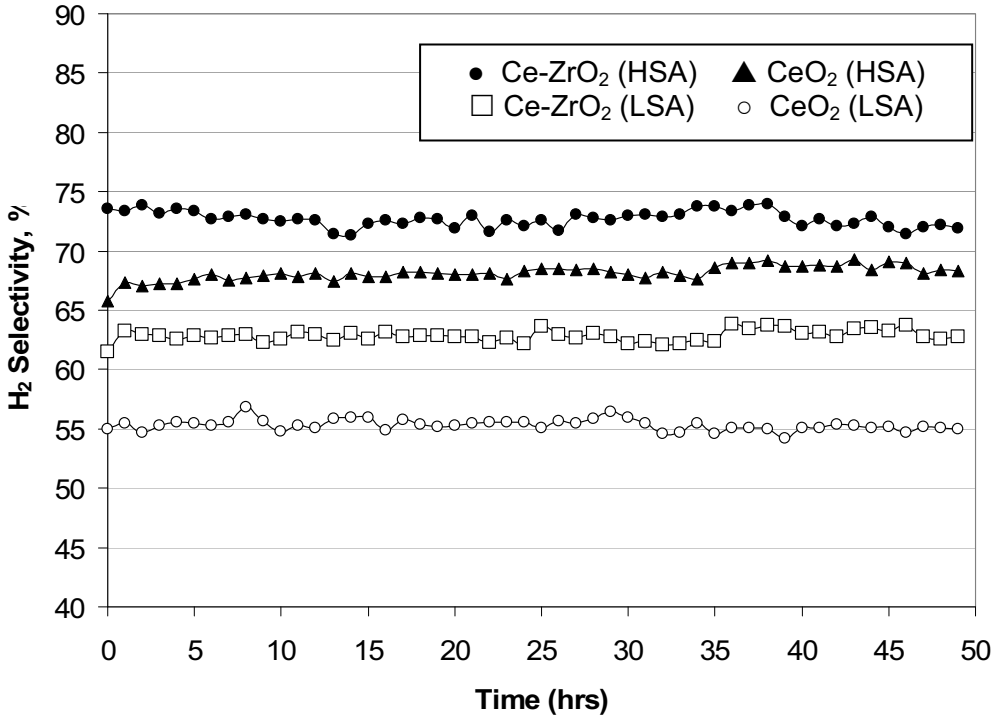

Fig. 1 Variation in hydrogen selectivities with time from steam reforming of palmitic acid at 1173 K over several catalysts

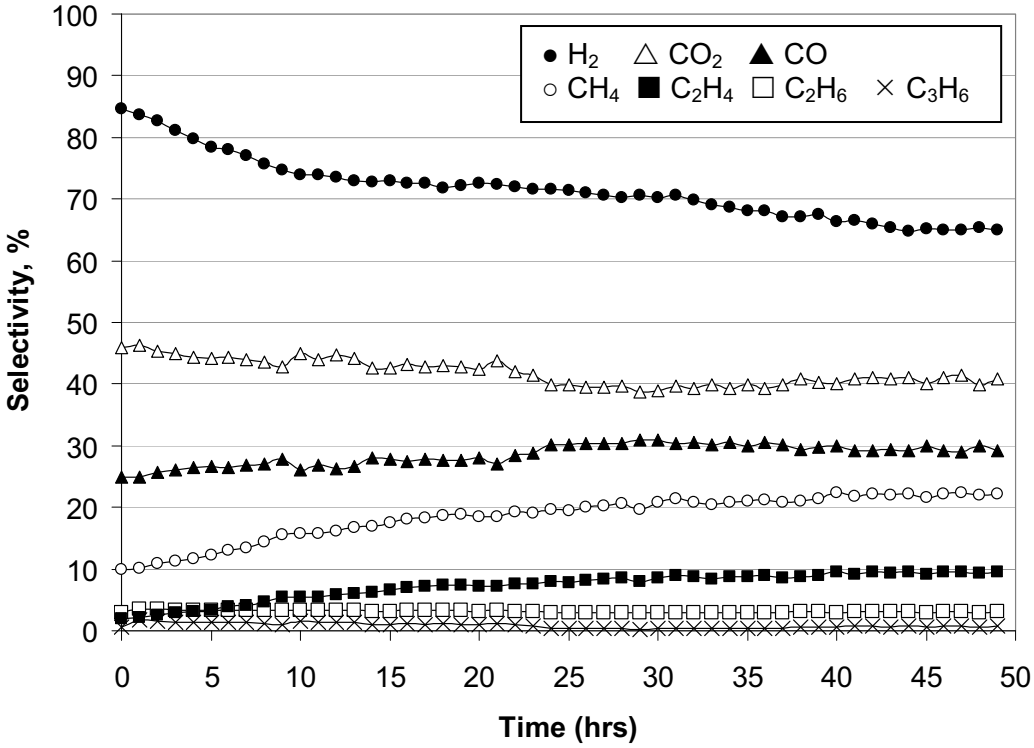

Fig. 2 Variations in hydrogen and other gaseous product selectivities with time from steam reforming of palmitic acid at 1173 K over Ni/Al_2O_3

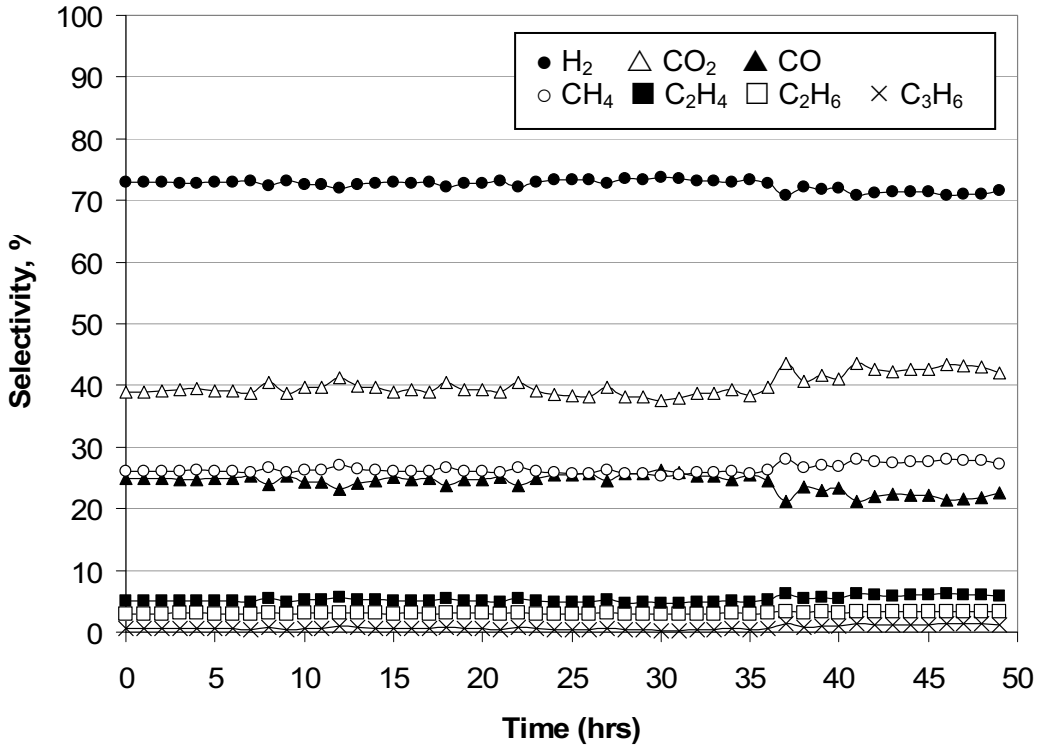

Fig. 3 Variations in hydrogen and other gaseous product selectivities with time from steam reforming of PFAD at 1173 K over Ce-ZrO_2 with Ce/Zr ratio of 3/1

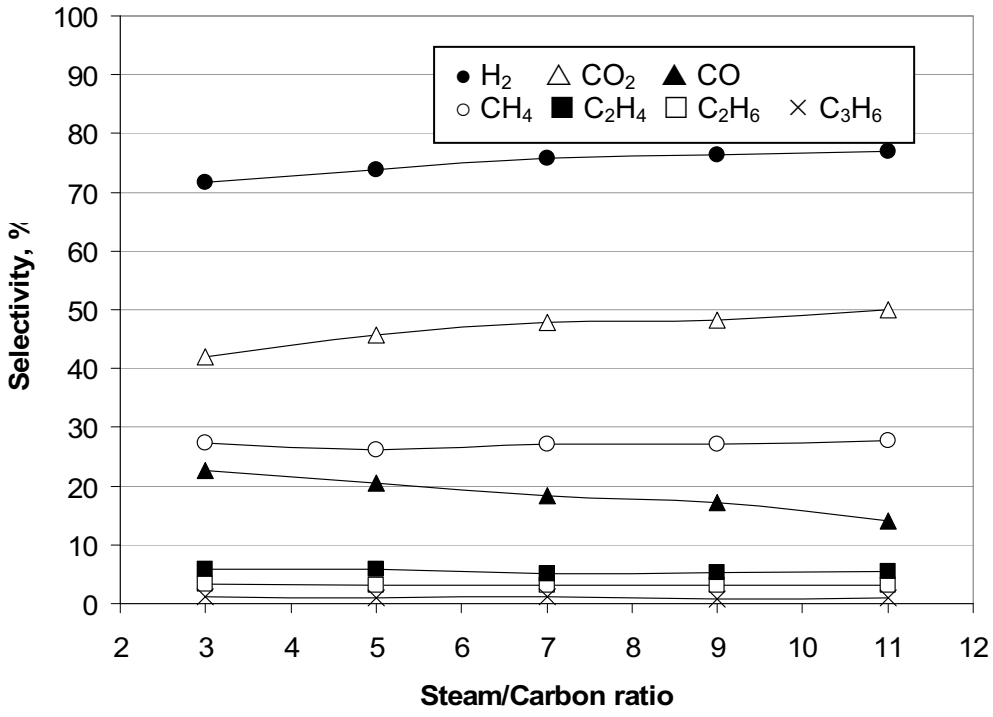

Fig. 4 Effect of inlet steam/carbon molar ratio on gaseous product selectivities from steam reforming of PFAD at 1173 K over Ce-ZrO_2 with Ce/Zr ratio of 3/1

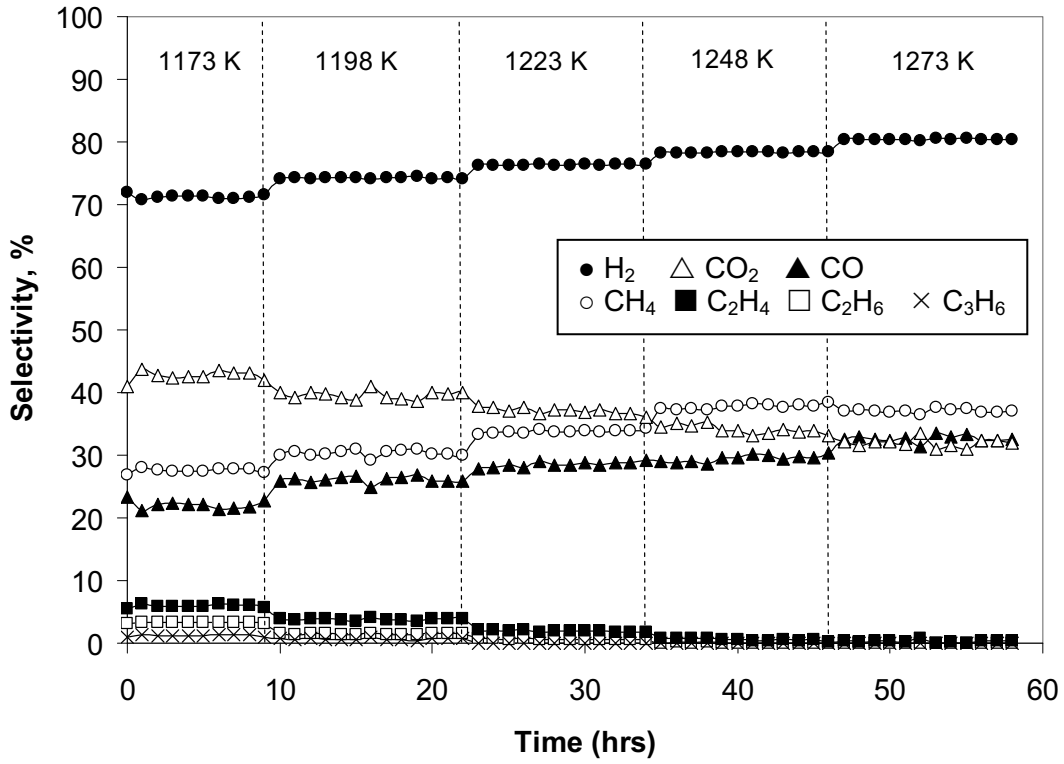

Fig. 5 Effect of temperature on hydrogen and other gaseous product selectivities with time from steam reforming of PFAD over Ce-ZrO_2 with Ce/Zr ratio of 3/1

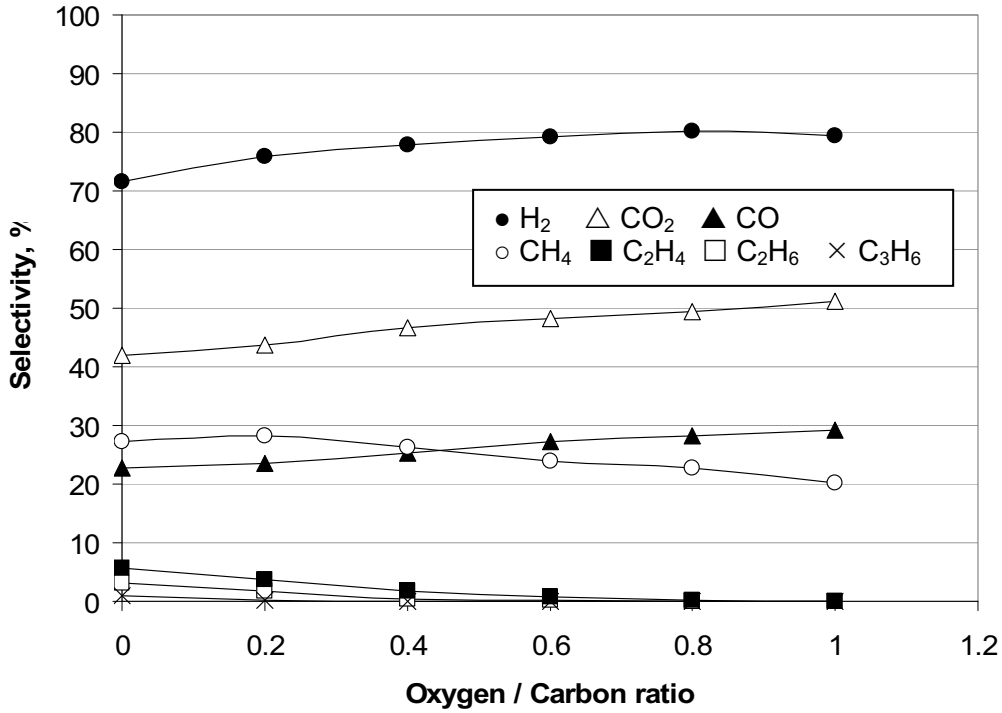

Fig. 6 Effect of inlet oxygen/carbon molar ratio on gaseous product selectivities from steam reforming of PFAD at 1173 K over Ce-ZrO_2 with Ce/Zr ratio of 3/1

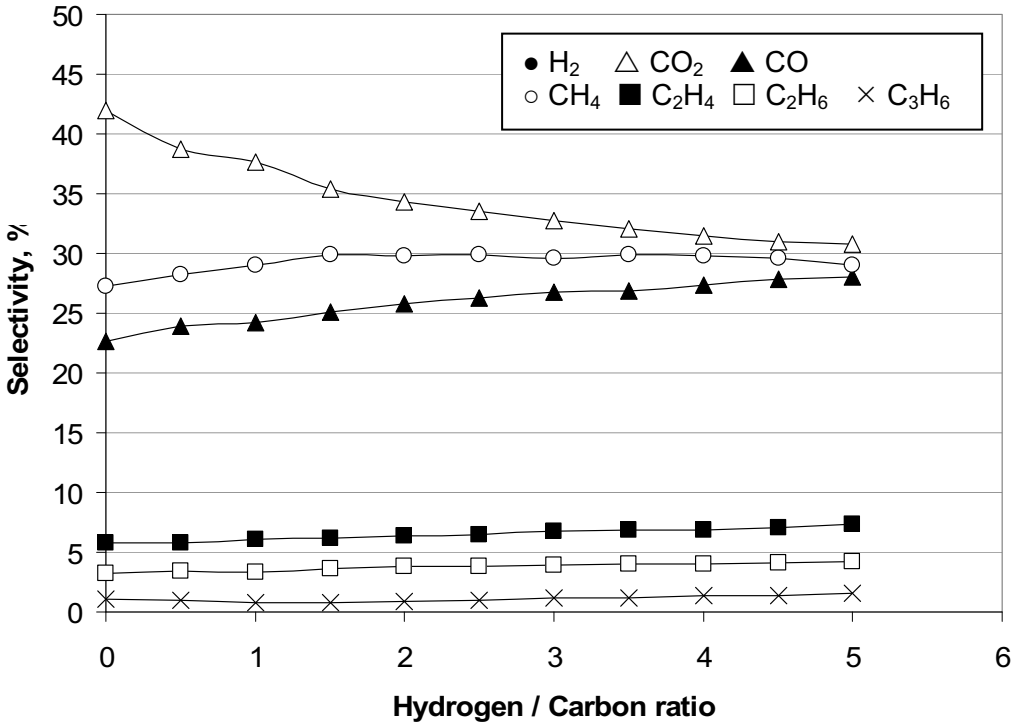

Fig. 7 Effect of inlet hydrogen/carbon molar ratio on gaseous product selectivities from steam reforming of PFAD at 1173 K over Ce-ZrO_2 with Ce/Zr ratio of 3/1

Table 1 Specific surface area of CeO_2 and Ce-ZrO_2 before and after calcination at 1173 K

Catalysts	Surface area after drying ($m^2\ g^{-1}$)	Surface area after calcination ($m^2\ g^{-1}$)
CeO_2 (HSA)	105	29
Ce-ZrO_2 (HSA) (Ce/Zr=1/3)	135	49
Ce-ZrO_2 (HSA) (Ce/Zr=1/1)	120	47
Ce-ZrO_2 (HSA) (Ce/Zr=3/1)	115	46.5
CeO_2 (LSA)	55	11
Ce-ZrO_2 (LSA) (Ce/Zr=1/3)	82	22
Ce-ZrO_2 (LSA) (Ce/Zr=1/1)	74	20.5
Ce-ZrO_2 (LSA) (Ce/Zr=3/1)	70	20

Table 2 Physicochemical properties of Ni/Al_2O_3 after reduction

Catalyst	Metal-load[a] (wt.%)	BET Surface Area ($m^2\ g^{-1}$)	Metal-reducibility[b] (%)	Metal-dispersion[c] (%)
Ni/Al_2O_3	4.9	40	92.1	4.87

[a] Measured from X-ray fluorescence analysis.
[b] Measured from temperature-programmed reduction (TPR) with 5%hydrogen.
[c] Measured from temperature-programmed desorption (TPD) of hydrogen after TPR measurement.

Table 3 R-1, Ox-1, R-2 analyses of ceria-based materials after calcination

Catalyst	Total H_2 Uptake from R-1 ($\mu mol/g_{cat}$)*	Total O_2 Uptake from Ox-1 ($\mu mol/g_{cat}$)*	Total H_2 Uptake from R-2 ($\mu mol/g_{cat}$)*
CeO_2 (HSA)	4087	2012	4077
Ce-ZrO_2 (HSA) (Ce/Zr=1/3)	2883	1423	2879
Ce-ZrO_2 (HSA) (Ce/Zr=1/1)	3692	1848	3687
Ce-ZrO_2 (HSA) (Ce/Zr=3/1)	5221	2620	5213
CeO_2 (LSA)	1789	884	1780
Ce-ZrO_2 (LSA) (Ce/Zr=1/3)	1087	551	1075
Ce-ZrO_2 (LSA) (Ce/Zr=1/1)	1701	709	1694
Ce-ZrO_2 (LSA) (Ce/Zr=3/1)	2625	1305	2621

* Deviation = ± 3%

Table 4
Hydrogen selectivity and distribution of other gaseous by-products from the steam reforming of fatty acids over several catalysts at 1173 K

Fuel	Catalyst	Hydrogen Selectivity (%)	Distribution of the by-products (%)					
			CO	CO_2	CH_4	C_2H_6	C_2H_4	C_3H_6
Palmitic acid	Ce-ZrO_2 (HSA)	71.8	24.1	44.7	25.4	1.9	3.7	0.2
	CeO_2 (HSA)	68.3	21.4	39.1	30.7	2.5	5.8	0.5
	Ce-ZrO_2 (LSA)	62.7	19.2	38.6	31.7	3.3	6.3	0.9
	CeO_2 (LSA)	54.9	18.1	35.5	34.8	3.5	7.1	1.0
Oleic acid	Ce-ZrO_2 (HSA)	69.2	22.2	40.9	28.3	2.5	5.3	0.8
	CeO_2 (HSA)	61.9	19.1	38.2	33.8	2.6	5.4	0.9
	Ce-ZrO_2 (LSA)	60.4	18.9	37.6	33.3	2.9	6.7	0.6
	CeO_2 (LSA)	52.3	17.4	32.2	36.4	3.9	8.9	1.2
Linoleic acid	Ce-ZrO_2 (HSA)	67.4	21.8	39.5	27.6	3.8	5.9	1.4
	CeO_2 (HSA)	63.8	20.1	37.5	29.0	3.7	8.5	1.2
	Ce-ZrO_2 (LSA)	57.8	19.7	36.1	30.2	3.9	8.7	1.4
	CeO_2 (LSA)	51.5	18.7	32.0	35.1	3.7	9.2	1.3
Palmitic acid	Ni/Al_2O_3	65.5	29.8	40.1	22.2	3.9	9.8	1.4

Table 5
Amount of carbon deposition on the surface of each catalyst after exposure in the steam reforming of fatty acids at 1173 K for 48 h

Fuel	Catalyst	Carbon formation (mmol g_{cat}^{-1})
Palmitic acid	Ce-ZrO_2 (HSA)	5.0
	CeO_2 (HSA)	5.3
	Ce-ZrO_2 (LSA)	5.9
	CeO_2 (LSA)	6.4
Oleic acid	Ce-ZrO_2 (HSA)	5.1
	CeO_2 (HSA)	5.5
	Ce-ZrO_2 (LSA)	6.4
	CeO_2 (LSA)	6.9
Linoleic acid	Ce-ZrO_2 (HSA)	5.4
	CeO_2 (HSA)	5.5
	Ce-ZrO_2 (LSA)	6.6
	CeO_2 (LSA)	7.0
Palmitic acid	Ni/Al_2O_3	9.5

Table 6
Effects of inlet steam/carbon molar ratio and temperature on the degree of carbon formation after exposure in steam reforming of PFAD for 10 h

Catalyst	Steam/carbon molar ratio	Temperature (K)	Carbon formation (mmol g_{cat}^{-1})
Ce-ZrO_2 (Ce/Zr=3/1)	3.0	1173	5.1
	5.0	1173	5.0
	7.0	1173	5.2
	9.0	1173	5.1
	11.0	1173	5.0
	3.0	1198	4.7
	3.0	1223	4.3
	3.0	1248	3.9
	3.0	1273	3.5

Table 7
Effects of inlet oxygen/carbon and hydrogen/carbon molar ratio on the degree of carbon formation after exposure in steam reforming of PFAD at 1023 K for 10 h

Catalyst	Oxygen/carbon molar ratio	Hydrogen/carbon molar ratio	Carbon formation (mmol g_{cat}^{-1})
Ce-ZrO_2 (Ce/Zr=3/1)	0.2	-	4.7
	0.4	-	4.1
	0.6	-	3.6
	0.8	-	3.2
	1.0	-	3.0
	-	0.5	4.8
	-	1.0	4.5
	-	1.5	4.4
	-	2.0	4.2
	-	2.5	4.1
	-	3.0	3.9
	-	3.5	3.9
	-	4.0	3.8
	-	4.5	3.9
	-	5.0	3.8

Output from the research project

1. **N. Laosiripojana** and S. Assabumrungrat, *Catalytic steam reforming of methane, methanol, and ethanol over Ni/YSZ: the possible use of these fuels in internal reforming SOFC*. Journal of Power Sources **2007**; 163: 943-951
   (Impact factor 2007 = 2.809)

2. **N. Laosiripojana** and S. Assabumrungrat, *Catalytic steam reforming of dimethyl ether (DME) over high surface area Ce-ZrO_2 at SOFC temperature: The possible use of DME in indirect internal reforming operation (IIR-SOFC)*. Applied Catalysis A: General **2007** 320: 105-113
   (Impact factor 2007 = 3.166)

3. **N. Laosiripojana**, W. Sutthisripok and S. Assabumrungrat, *Reactivity of high surface area CeO_2 synthesized by surfactant-assisted method to ethanol decomposition with and without steam*, Chemical Engineering Journal **2007**; 127: 31-38
   (Impact factor 2007 = 1.707)

4. **N. Laosiripojana**, S. Assabumrungrat, and S. Charojrochkul, *Steam reforming of ethanol with co-fed oxygen and hydrogen over Ni on high surface area ceria support*. Applied Catalysis A: General **2007**; 327: 180-188
   (Impact factor 2007 = 3.166)

5. W. Sutthisripok, **N. Laosiripojana** and L. Srikong, Effect of specific surface area and Zr doping content on oxygen storage capacity (OSC) and methane steam reforming reactivity of CeO2-ZrO_2, *ECS Transactions*, 7(1), **2007**; 1769
   (Impact factor 2007 = -)

6. **N. Laosiripojana**, S. Assabumrungrat, and S. Charojrochkul, Steam reforming of ethanol over Ni on high surface area ceria support: Influence of redox properties on the catalyst stability and product selectivities, *ECS Transactions*, 7(1), **2007**; 1717
   (Impact factor 2007 = -)

7. **N. Laosiripojana**, D. Chadwick, S. Assabumrungrat, *Effect of high surface area CeO_2 and Ce-ZrO_2 supports over Ni catalyst on CH_4 reforming with H_2O in the presences of O_2, H_2, and CO_2*. Chemical Engineering Journal **2008**;138: 264-273
   (Impact factor 2007 = 1.707)

8. R. Kempegowda, **N. Laosiripojana**, and S. Assabumrungrat, *A study of high temperature desulphurization over nano-scale high surface area ceria for later application in SOFC*. Korean Journal of Chemical Engineering, **2008**; 25: 223-230
   (Impact factor 2007 = 0.747)

9. **N. Laosiripojana** and S. Assabumrungrat, *Kinetic dependencies and reaction pathways in hydrocarbon and oxyhydrocarbon conversions catalyzed by ceria-based materials*. Applied Catalysis B: Environmental **2008**; 82: 103-113
   (Impact factor 2007 = 4.651)

10. A. Shotipruk, S. Assabumrungrat, P. Pavasant, and **N. Laosiripojana**, "*Reactivity of CeO_2 and $Ce\text{-}ZrO_2$ toward the steam reforming of palm fatty acid distillate (PFAD) with co-fed oxygen and hydrogen*", Chemical Engineering Science **2009**, 64: 459-466
   (Impact factor 2007 = 1.775)

รางวัลที่ได้รับจากผลงานวิจัยจากทุนพัฒนาอาจารย์รุ่นกลาง ปี 2549

- 2008 Young Scientist Award 2007 Young Scientist Award from the Foundation for the Promotion of Science and Technology under Patronage of His Majesty the King

- Finalist for *2008 ASEAN Young Scientist and Technologist Award* from ASEAN National Committee on Science & Technology

- 2008 TRF-CHE Mid-research career award

ภาคผนวก

Available online at www.sciencedirect.com
ScienceDirect
Applied Catalysis A: General 320 (2007) 105–113
APPLIED CATALYSIS A: GENERAL
www.elsevier.com/locate/apcata

Catalytic steam reforming of dimethyl ether (DME) over high surface area Ce–ZrO_2 at SOFC temperature: The possible use of DME in indirect internal reforming operation (IIR-SOFC)

N. Laosiripojana [a,*], S. Assabumrungrat [b]

[a] *The Joint Graduate School of Energy and Environment, King Mongkut's University of Technology Thonburi, Bangkok 10140, Thailand*
[b] *Center of Excellence on Catalysis and Catalytic Reaction Engineering, Department of Chemical Engineering, Chulalongkorn University, Bangkok 10330, Thailand*

Received 14 September 2006; received in revised form 14 December 2006; accepted 24 December 2006
Available online 11 January 2007

Abstract

This study was aimed at developing a suitable reforming catalyst for later application in an indirect internal reforming solid oxide fuel cell (IIR-SOFC) fuelled by dimethyl ether (DME). It was found that, at temperature higher than 800 °C, DME decomposed homogeneously, producing CH_4 and CH_3OH with small amount of CO, CO_2, and H_2. High surface area Ce–ZrO_2 can reform DME with steam efficiently at 900 °C, producing high contents of H_2, CO, and CH_4 without the presence of CH_3OH in the product gas. The combination use of Ce–ZrO_2 (as a pre-reforming catalyst) and Ni/Al_2O_3 in the single unit was proven to significantly improve the reforming performance. According to this combination, the role of Ce–ZrO_2 is to first decompose CH_3OH and some CH_4 generated from the homogeneous decomposition of DME, while the role of Ni/Al_2O_3 is to reform CH_4 left from the pre-reforming section and to maximize the yield of H_2 production.

As another approach, IIR-SOFC model was studied using an annular ceramic reactor, in which DME initially reacted with steam on Ce–ZrO_2 + Ni/Al_2O_3 at the inner side of the reactor and then Ni/YSZ at the outer side. The stability and the yield of hydrogen production over this configuration were considerably higher than those of systems packed with single Ce–ZrO_2, single Ni/Al_2O_3, and without the filling of catalyst. In addition, the degree of carbon formation on the surface of Ni/YSZ was significantly low. The successful development of this reforming pattern improves the efficiency of IIR-SOFC fueled by DME by eliminating the requirement of an external reforming unit installation.

Keywords: Indirect internal reforming; Dimethyl ether; Ce–ZrO_2; Solid oxide fuel cell

1. Introduction

Solid oxide fuel cell (SOFC) is an efficient electrochemical device that converts chemical energy to electrical energy with higher efficiency and lower pollutant emission compared to conventional processes [1]. H_2 and CO are the primary fuels for SOFC. Nevertheless, due to high operating temperature of SOFC (700–1100 °C), it is known that some fuels (i.e. CH_4) can be directly fed to SOFC stacks; this operation is called a direct internal reforming SOFC (DIR-SOFC). According to this operation, the fuels are reformed at the anode producing H_2 and CO, which are electrochemically consumed for generating electricity simultaneously. An advantage of DIR-SOFC is that the H_2 consumption by the electrochemical reaction could promote the reforming or conversion of fuels at the anode side and consequently results in high conversion and efficiency [2].

DIR-SOFC operation requires an anode material that has good catalytic reforming and electrochemical reactivities. Ni/YSZ is the most common SOFC anode material due to its well-fitted properties for SOFC design requirement and its low cost compared with other supported metals (e.g. Co, Pt, Ru, and Rh). In addition, this material provides necessary catalytic reforming activity required for the DIR-SOFC operation. The nickel content for Ni/YSZ anode is usually 40–60% in order to match the thermal expansion of YSZ [3]. The major difficulty of DIR-SOFC operation over Ni/YSZ is the possible formation of carbon species on the surface of Ni due to the cracking of hydrocarbons. This formation could hinder gas access and

* Corresponding author. Tel.: +66 2 8729014; fax: +66 2 8726736.
E-mail address: navadol_l@jgsee.kmutt.ac.th (N. Laosiripojana).

0926-860X/$ – see front matter © 2007 Elsevier B.V. All rights reserved.
doi:10.1016/j.apcata.2006.12.018

degrade anode performance by blocking the catalyst active sites, which resulted in the loss of cell performance and poor durability. Another alternative internal reforming operation is an indirect internal reforming (IIR-SOFC). By this operation, the reforming reaction takes place at a reformer located in close thermal contact with the anode side of SOFC. IIR-SOFC gives the advantage of good heat transfer between the reformer and the fuel cell and is expected to provide an autothermal operation. In addition, unlike DIR-SOFC, the reformer part and the anode side for IIR-SOFC operation are operated separately. Therefore, the catalyst for reforming reaction at the reformer part and the material for electrochemical reactions at the anode side of fuel cell can be optimized individually, preventing the possible degradation of anode from the carbon deposition.

Focusing on the fuel selection, methane is currently the major fuel for SOFC due to its well-developed supporting system and cost effectiveness. Nevertheless, the use of dimethyl ether (DME) should also be possible when operated as an internal or in-stack reforming. DME has several advantages; it is harmless and does not cause ozone layer destruction, and it is easy to handle like LPG. The approach in this work is to develop an indirect internal reforming operation that can reform DME efficiently at SOFC temperatures, 900 °C. The successful development of this operation would eliminate the requirement of the external reformer installation, making SOFC fueled by DME more efficient and attractive. Previously, hydrogen production from the reforming of DME has been studied over acid catalysts and Cu-based catalysts by several researchers; however, most of them have investigated the reforming of DME at low temperature [4–9].

In the present work, ceria-based catalyst was selected as the catalyst for the steam reforming of DME at SOFC operating temperature. Ceria-based catalysts have been commonly applied as catalysts in a wide variety of reactions involving oxidation or partial oxidation of hydrocarbons (e.g. automotive catalysis). A high oxygen mobility (redox property) [10], high oxygen storage capacity (OSC) [11], strong interaction with the supported metal (strong metal–support interaction) [12] and the modifiable ability [13] render this material very interesting for catalysis. Importantly, the reactivity toward methane steam reforming with high resistance toward carbon deposition over ceria has been observed [14–17]. Doped ceria with Zr (Ce–ZrO_2) has been reported to improve the specific surface area, oxygen storage capacity, redox property, thermal stability and catalytic activity. These benefits were associated with enhanced reducibility of cerium (IV) in CeO_2–ZrO_2 due to the high O^{2-} mobility inside the fluorite lattice. The reason for high mobility might be related to the lattice strain, which is generated by the introduction of a smaller isovalent Zr cation into the CeO_2 lattice (Zr^{4+} has a crystal ionic radius of 0.84 Å, which is smaller than 0.97 Å for Ce^{4+} in the same co-ordination environment) [18]. Therefore, Ce–ZrO_2 was selected for study in the present work. Furthermore, the benefit of applying Ce–ZrO_2 together with conventional Ni/Al_2O_3 was also studied.

As a next step, in order to study the possible use of Ce–ZrO_2 in IIR-SOFC, an annular ceramic reactor was designed and constructed. Details of this reactor configuration will be described in Section 2.2. DME and steam were fed into this annular reactor packed with Ce–ZrO_2 and/or Ni/Al_2O_3, as reforming catalysts, and Ni/YSZ, an anode material of SOFC. The stability and reforming reactivity toward this operation was investigated compared to those without the use of reforming catalysts (DIR operation).

2. Experimental

2.1. Material preparation and characterization

Ce–ZrO_2 with different Ce/Zr molar ratios were prepared by co-precipitation of cerium nitrate ($Ce(NO_3)_3{\cdot}H_2O$), and zirconium oxychloride ($ZrOCl_2{\cdot}H_2O$) (from Aldrich). The ratio between both solutions was altered to achieve Ce/Zr molar ratios of 1/3, 1/1 and 3/1. It should be noted that aqueous solution of 0.1 M cetyltrimethylammonium bromide solution (from Aldrich) was also added in the cerium nitrate and zirconium oxychloride solution as a cationic surfactant. Our previous work reported that the preparation of ceria-based material by this surfactant-assisted method can achieve high surface area and high thermal stability due to the incorporation of surfactants during preparation, which reduces the interfacial energy and eventually decreases the surface tension of water contained in the pores [14,19,20].

In the present work, the molar ratio of ([Ce] + [Zr])/[cetyltrimethylammonium bromide] was kept constant at 0.8. The solid solution was formed by mixing 0.1 M of metal salt solution with 0.4 M of urea at a 2:1 volumetric ratio. This solution was stirred by a magnetic stirrer (100 rpm) for 3 h, and the precipitate was filtered and washed with deionised water and ethanol to prevent an agglomeration of the particles. It was dried overnight in an oven at 110 °C, and then calcined in air at 1000 °C for 6 h. Fig. 1 shows the SEM micrographs of Ce–ZrO_2 (with Ce/Zr = 3/1) synthesized by the above surfactant-assisted method (1a), compared to that synthesized by typical co-precipitation method (1b) (without the filling of cetyltrimethylammonium bromide solution). It is clear that the particle size of Ce–ZrO_2 synthesized by the surfactant-assisted method (Ce–ZrO_2 (high surface area; HSA)) is significantly smaller than that synthesized by typical co-precipitation method (Ce–ZrO_2 (low surface area; LSA)).

Ni/Al_2O_3 catalysts were prepared by impregnating γ-Al_2O_3 with $Ni(NO_3)_2$ solution (Aldrich). The catalysts were reduced with 10%H_2/He before use. After reduction, the catalysts were characterized with several physicochemical methods. The weight content of Ni in Ni/Al_2O_3 was determined by X-ray fluorescence (XRF) analysis. The reducibility and dispersion percentages of nickel were measured from temperature programmed reduction (TPR) with 5% H_2 in Ar and temperature programmed desorption (TPD), respectively. The catalyst specific surface areas were obtained from BET measurements, which were carried out before and after calcination in order to determine its changes. All physicochemical properties of the synthesized catalysts are presented in Table 1. It should be noted that, after treatment, the degree of oxygen storage capacity (OSC) and redox reversibilities of all

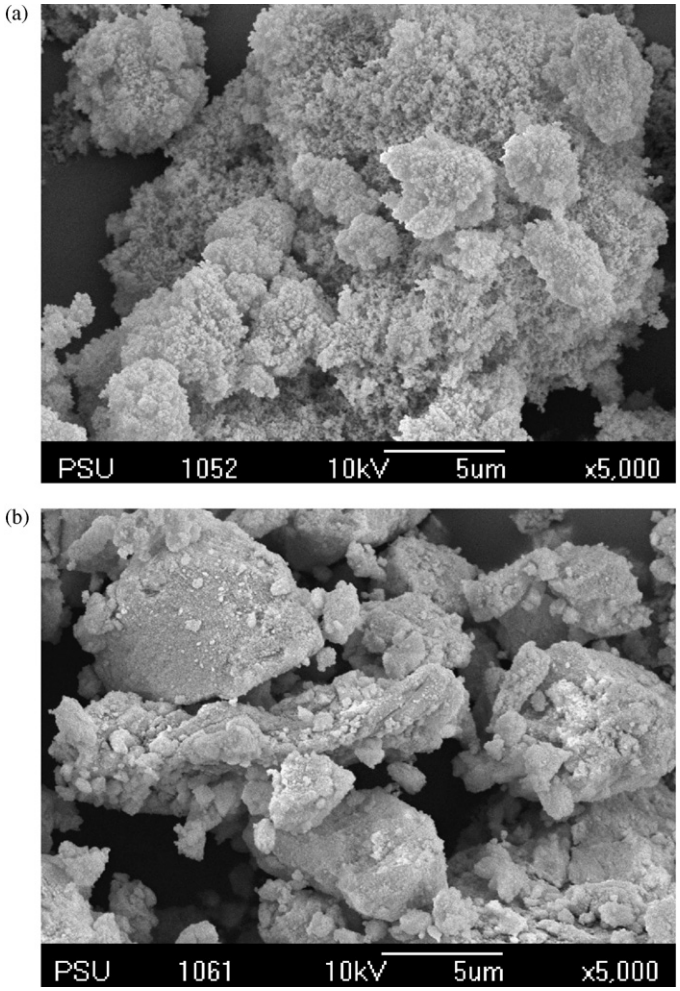

Fig. 1. SEM micrographs of Ce–ZrO_2 (with Ce/Zr = 3/1) synthesized by the surfactant-assisted method (a), compared to that synthesized by typical co-precipitation method (b).

Ce–ZrO_2 (both HSA and LSA with different Ce/Zr ratios) were determined by the temperature programmed reduction (TPR-1) and temperature programmed oxidation (TPO) following with second time temperature programmed reduction (TPR-2), respectively, at the same conditions. Details of these measurements are given in Section 3.1.

2.2. Annular reactor configuration

An annular ceramic reactor was constructed in order to study the use of DME in IIR operation, Fig. 2. According to the design, the reforming catalysts (Ce–ZrO_2 and/or Ni/Al_2O_3) were packed at the inner side of the annular reactor, where the inlet gas was firstly introduced. At the end of the inner tube, all gas components flowed backward through the outer side of this annular reactor, where 300 mg of Ni/YSZ (with SiC) was packed. Therefore, both reforming catalysts and Ni/YSZ were operated at the same operating temperature. The main obligation of Ce–ZrO_2 and Ni/Al_2O_3 was to reform DME before reaching the surface of Ni/YSZ, preventing the possible degradation of Ni/YSZ by the carbon formation. It should be noted that Ni/YSZ in the present work was prepared by mixing NiO (42.86 vol%) with YSZ (57.14 vol%) with a ball milling for 18 h at room temperature. The catalyst was calcined in air at 1000 °C for 6 h and then reduced with 10%H_2/Ar for 6 h before use.

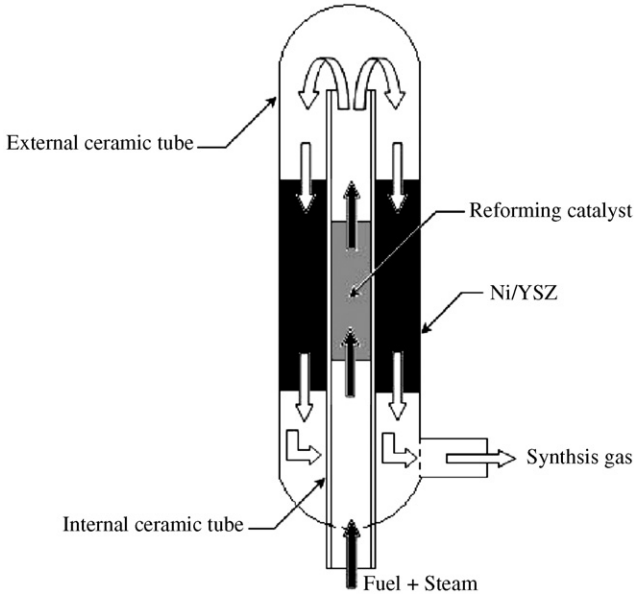

Fig. 2. Configuration of annular ceramic reactor for experiments under IIR operation.

2.3. Apparatus and procedures

An experimental reactor system was constructed as shown in Fig. 3. The feed gases including the components of interest (DME and steam) and the carrier gas (helium) were introduced to the reaction section, in which either a quartz reactor (for primary study) or the annular ceramic reactor (for IIR study) was mounted vertically inside a furnace. Regarding the results in our previous publications [19,20], to avoid any limitations by external mass

Table 1
Physicochemical properties of the synthesized catalysts

Catalyst	Metal-load[a] (wt.%)	BET surface area ($m^2\ g^{-1}$)	Metal-reducibility[b] (%)	Metal-dispersion[c] (%)
Ni/Al_2O_3	5.0	67	94.5	4.93
Ce–ZrO_2 (Ce/Zr = l/3)	–	48	–	–
Ce–ZrO_2 (Ce/Zr = l/1)	–	45	–	–
Ce–ZrO_2 (Ce/Zr = 3/1)	–	39.5	–	–

[a] Measured from X-ray fluorescence analysis.
[b] Measured from temperature programmed reduction (TPR) with 5%hydrogen.
[c] Measured from temperature programmed desorption (TPD) of hydrogen after TPR measurement.

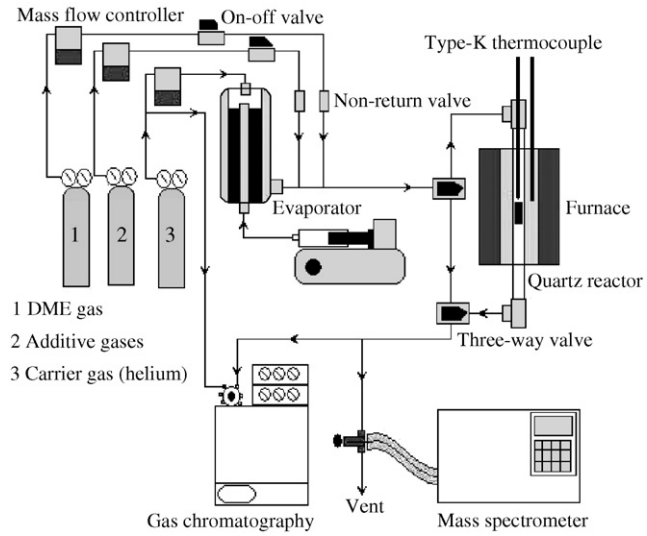

Fig. 3. Schematic diagram of the experimental set-up.

transfer, the total gas flow was 1000 $cm^3\ min^{-1}$ under a constant residence time of 5×10^{-4} g min cm^{-3} in all experiments. A Type-K thermocouple was placed into the annular space between the reactor and the furnace, while another Type-K thermocouple was inserted in the middle of the quartz tube in order to re-check the possible temperature gradient. The record showed that the maximum temperature fluctuation during the reaction was always ±0.75 °C or less from the temperature specified for the reaction. After the reactions, the exit gas mixture was transferred via trace-heated lines to the analysis section, which consisted of a Porapak Q column Shimadzu 14B gas chromatograph (GC) and a mass spectrometer (MS).

The steam reforming of DME reactivity and the product selectivity were studied. In order to study the formation of carbon species on catalyst surface, temperature programmed oxidation (TPO) was applied by introducing 10% O_2 in helium, after purging the system with helium. The operating temperature increased from 100 to 1000 °C at a rate of 20 °C min^{-1}. The amounts of carbon formation (mmol g_{cat}^{-1}) on the surface of catalysts were determined by measuring the CO and CO_2 yields from the TPO results (using Microcal Origin Software) [21].

In order to study the steam reforming reactivity, the rate of DME reforming was defined in terms of conversion denoted as X_{DME}, and product selectivities denoted as $S_{product}$. Selectivities of products (i.e. CO, CO_2, CH_4, and CH_3OH) were calculated by the carbon balance, defined as the ratios of the product moles to the consumed moles of hydrocarbon, accounting for stoichiometry. This information was presented in term of (relative) fraction of all by-product components, which are summed to 100%. H_2 selectivity was calculated by the H_2 balance, defined as the mole of H_2 produced to the total H_2 in the products.

$$X_{DME} = \frac{100(DME_{in} - DME_{out})}{DME_{in}} \quad (1)$$

$$S_{Product} = \frac{100(\text{Mole of a specific product})}{(\text{Total moles of all products})} \quad (2)$$

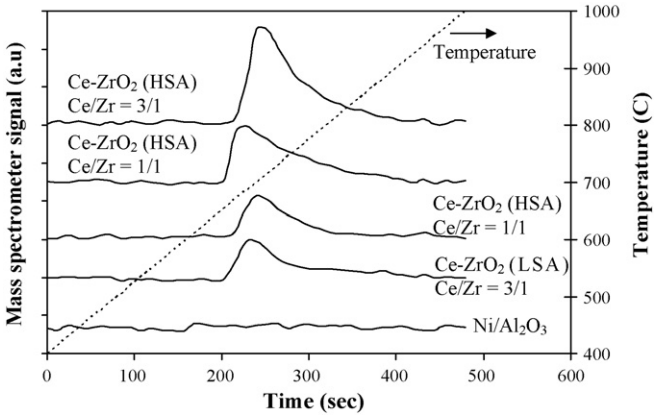

Fig. 4. Temperature programmed reduction (TPR-1) of several catalysts.

3. Results and discussion

3.1. Oxygen storage capacities (OSC) and redox reversibility

The degree of oxygen storage capacities (OSC) for all Ce–ZrO_2 after calcination were investigated using TPR-1, which was performed by heating the catalysts up to 1000 °C in a flow of 5%H_2 in He. The amount of H_2 uptake was correlated to the amount of oxygen stored in the catalysts. It should be noted that the test over Ni/Al_2O_3 was also performed for comparison. As shown in Fig. 4, the amount of H_2 uptakes over Ce–ZrO_2 (HSA) with Ce/Zr ratio of 3/1 are significantly higher than those observed over Ce–ZrO_2 (HSA) with Ce/Zr ratios of 1/1 and 1/3, suggesting its highest degree of OSC. In contrast, no H_2 consumption was observed from the TPR over Ni/Al_2O_3, indicating no occurrence of redox properties for this catalyst. It should also be noted that the amount of H_2 uptake over Ce–ZrO_2 (HSA) is significantly higher than that over Ce–ZrO_2 (LSA) at the same Ce/Zr ratio, suggesting the strong dependency of the degree of OSC on the specific surface area of Ce–ZrO_2. The benefit of OSC on the reforming reaction will be presented later in Section 3.3.

After the system was purged with helium, the redox reversibilities were then determined by applying TPO following with TPR-2. The TPO was carried out by heating the catalyst up to 1000 °C in 10%O_2 in helium; the amounts of oxygen chemisorbed were then measured, Table 2. Regarding the TPR-2 results as also shown in Table 2, the amount of hydrogen uptakes for all catalysts were approximately similar to those from the first time reduction reaction (TPR-1), indicating the redox reversibility for these synthesized Ce–ZrO_2.

3.2. Homogenous (non-catalytic) reaction

Before studying the catalytic performance, the homogeneous (non-catalytic) steam reforming of DME was primarily investigated. The inlet DME/H_2O in helium with the molar ratio of 1.0/3.0 (inlet DME partial pressure of 4 kPa) was introduced to the system, while the temperature increased from 100 to

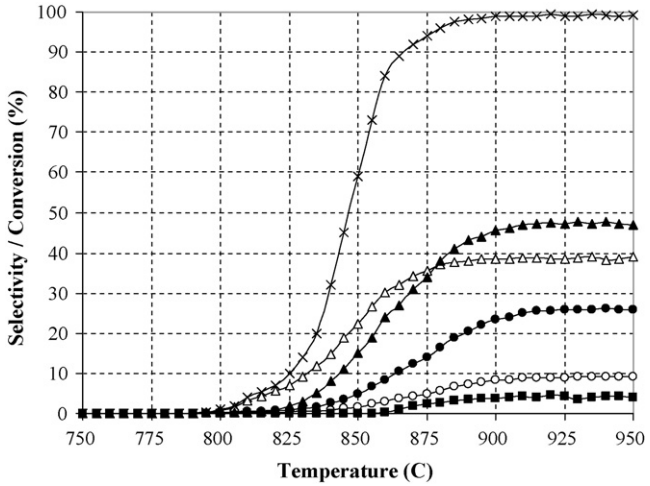

Fig. 5. Homogenous (in the absence of catalyst) reactivity of DME steam reforming (4 kPa DME, and 12 kPa H_2O) (DME (×), H_2 (●), CO (○), CO_2 (■), CH_4 (▲), and CH_3OH (△)).

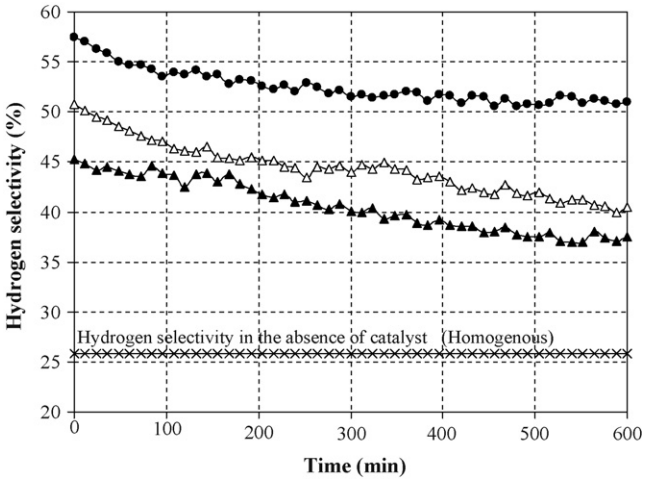

Fig. 6. Steam reforming of DME at 900 °C for Ce–ZrO_2 (Ce/Zr = 3/1) (●), Ce–ZrO_2 (Ce/Zr=1/1) (△), and Ce–ZrO_2 (Ce/Zr=1/3) (▲) (4 kPa C_2H_5OH, and 12 kPa H_2O).

1000 °C. As shown in Fig. 5, it was observed that DME was converted to methanol at the temperature above 800 °C according to the hydration of DME (Eq. (3)). CH_4, CO, CO_2, and H_2 were then observed at the temperature above 825 °C from the decomposition of CH_3OH (Eq. (4)), water gas shift (Eq. (5)) and methanation reactions (Eq. (6)). At 900 °C, the conversion of DME is close to 100%.

$$CH_3OCH_3 + H_2O = 2CH_3OH \quad (3)$$

$$CH_3OH = 2H_2 + CO \quad (4)$$

$$CO + H_2O = H_2 + CO_2 \quad (5)$$

$$CO + 3H_2 = CH_4 + H_2O \quad (6)$$

It should be noted that the formations of higher molecular weight compounds such as formaldehyde, methyl formate and formic acid were found to be negligible.

3.3. Steam reforming of DME over Ce–ZrO_2

Ce–ZrO_2 with several Ce/Zr ratios were tested for the steam reforming of DME at 900 °C with the inlet fuel/steam molar ratio of 1.0/3.0 (inlet DME partial pressure of 4 kPa). The reforming rate was measured as a function of time in order to indicate the stability and the deactivation rate. The variations in the hydrogen selectivity with time at 900 °C are shown in Fig. 6. It was observed from the figure that Ce–ZrO_2 with Ce/Zr ratio of 3/1 provided the highest hydrogen selectivity. Consequently, Ce–ZrO_2 with Ce/Zr ratio of 3/1 was selected for further investigations. Catalyst stabilities expressed as deactivation percentages as well as the product selectivities are given in Table 3. It is clear that methane, hydrogen, carbon monoxide, and carbon dioxide are the main products, whereas the selectivity of methanol is closed to 0.

As shown in Fig. 5, according to the steam reforming of DME at 900 °C, the main components present in the system are methanol and methane with some amounts of CO, CO_2, and H_2. The DME steam reforming reactivity for Ce–ZrO_2 is due to the gas–solid reactions between the above products generated from the homogenous DME steam reforming reaction and the lattice oxygen (O_O^x) at Ce–ZrO_2 surface. The redox mechanism between these gas components with the lattice oxygen (O_O^x) could be derived as illustrated below.

$$CH_3OH + S_{Ce} = CH_2{-}S_{Ce} + H_2O \quad (7)$$

$$CH_4 + 2S_{Ce} = CH_3{-}S_{Ce} + H{-}S_{Ce} \quad (8)$$

$$CH_3{-}S_{Ce} + S_{Ce} = CH_2{-}S_{Ce} + H{-}S_{Ce} \quad (9)$$

$$CH_2{-}S_{Ce} + S_{Ce} = CH{-}S_{Ce} + H{-}S_{Ce} \quad (10)$$

$$CH{-}S_{Ce} + S_{Ce} = C{-}S_{Ce} + H{-}S_{Ce} \quad (11)$$

Table 2
Results of TPR-1, TPO, TPR-2 analyses of Ce–ZrO_2 after calcination

Catalyst	Total H_2 uptake from TPR-1 (μmol g_{cat}^{-1})	Total O_2 uptake from TPO (μmol g_{cat}^{-1})	Total H_2 uptake from TPR-2 (μmol g_{cat}^{-1})
Ce–ZrO_2 (HSA) (Ce/Zr = l/3)	2899	1475	2876
Ce–ZrO_2 (HSA) (Ce/Zr = l/1)	3701	1862	3694
Ce–ZrO_2 (HSA) (Ce/Zr = 3/1)	5247	2640	5250
Ce–ZrO_2 (LSA) (Ce/Zr = 3/1)	2649	1328	2643
Ni/Al_2O_3	0	0	0

Table 3
Products and amount of carbon deposition from the steam reforming of DME over Ce–ZrO_2 with different Ce/Zr ratio at 900 °C

Catalyst	Deactivation (%)	Hydrogen selectivity (%)	Fraction of the by-products (%)				C formation (mmol g_{cat}^{-1})
			CO	CO_2	CH_4	CH_3OH	
Ce–ZrO_2 (Ce/Zr = l/3)	17.3	37.4	26.5	10.2	52.1	11.2	0.24
Ce–ZrO_2 (Ce/Zr = l/1)	20.4	40.5	30.2	14.3	51.6	3.9	0.20
Ce–ZrO_2 (Ce/Zr = 3/1)	11.1	51.2	33.8	15.7	49.9	0.6	0.06

$$C{-}S_{Ce} + O_O{}^x = CO + V_O{}^{\bullet\bullet} + 2e' + S_{Ce} \quad (12)$$

$$2H\text{-}S_{Ce} = H_2 + 2S_{Ce} \quad (13)$$

S_{Ce} is the Ce–ZrO_2 surface site and CH_x–S_{Ce} is an intermediate surface hydrocarbon species. S_{Ce} can be considered to be a unique site, or the same site as the lattice oxygen ($O_O{}^x$). $V_O{}^{\bullet\bullet}$ is an oxygen vacancy with an effective charge 2^+, e' is an electron which can either be more or less localized on a cerium ion or delocalized in a conduction band [22]. During the reaction, hydrocarbons are adsorbed on either a unique site (S_{Ce}) or the lattice oxygen ($O_O{}^x$). The lattice oxygen is then regenerated by reaction with oxygen containing compounds (i.e. steam) present in the system, Eq. (14).

$$H_2O + + V_{O\bullet\bullet} + 2e' = H_2 + O_O{}^x \quad (14)$$

It should be noted that the measured value of the oxygen diffusion coefficient for ceria is high and the reaction rate is controlled by a surface reaction, not by diffusion of oxygen from the bulk of the solid particles to ceria surfaces [23].

After reaction, the post-reaction temperature programmed oxidation (TPO) experiments were carried out to investigate the amount of carbon formation on the surface of Ce–ZrO_2. From the TPO results as shown in Fig. 7 and Table 3, some amounts of carbon deposition (mmol g_{cat}^{-1}) were observed over Ce–ZrO_2 with Ce/Zr ratios of 1/1 and 1/3, whereas significantly lower carbon formations were detected over Ce–ZrO_2 with Ce/Zr ratios of 3/1. It should be noted that the degree of carbon deposition observed from the steam reforming of DME over

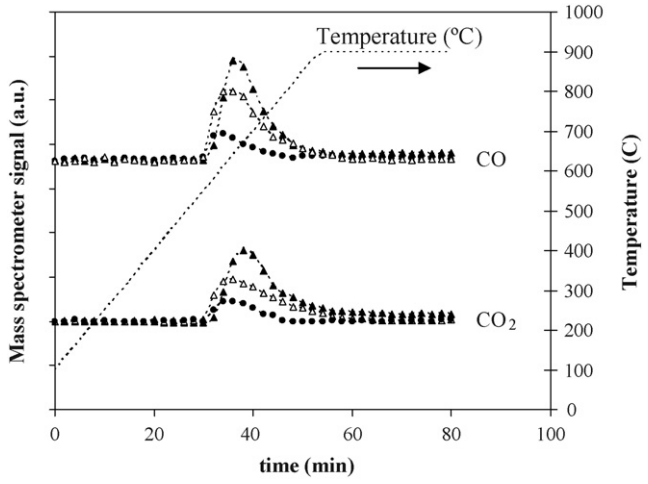

Fig. 7. Temperature programmed oxidation (TPO) of Ce–ZrO_2 (Ce/Zr = 3/1) (●), Ce–ZrO_2 (Ce/Zr = 1/1) (△), and Ce–ZrO_2 (Ce/Zr = 1/3) (▲) after exposure in steam reforming of DME (4 kPa DME, and 12 kPa H_2O) for 10 h.

Ce–ZrO_2 was significantly lower than that observed over Ni/Al_2O_3 at the same operating conditions (Table 6). Theoretically, the carbon species can be formed during the steam reforming process by several reactions. Eqs. (15)–(18) present the most probable reactions that could lead to carbon deposition from the system of the steam reforming:

$$CH_4 = 2H_2 + C \quad (15)$$

$$2CO = CO_2 + C \quad (16)$$

$$CO + H_2 = H_2O + C \quad (17)$$

$$CO_2 + 2H_2 = 2H_2O + C \quad (18)$$

C is the carbonaceous deposits. At low temperature, Eqs. (17)–(18) are favorable, while Eqs. (15)–(16) are thermodynamically unflavored [24]. The Boudouard reaction (Eq. (16)) and the decomposition of methane (Eqs. (15)) are the major pathways for carbon formation at such a high temperature as they show the largest change in Gibbs energy [25]. According to the range of temperature in this study, carbon formation would be formed via the decomposition of methane and Boudouard reaction.

The good steam reforming reactivity with high resistance toward carbon deposition for Ce–ZrO_2 is mainly related to its high oxygen storage capacity (OSC). By applying Ce–ZrO_2, both decomposition and Boudouard reactions (Eqs. (15) and (16)) could be inhibited by the gas–solid redox reactions between methane and carbon monoxide with the lattice oxygen ($O_O{}^x$) at Ce–ZrO_2 surface (Eqs. (19) and (20)), forming hydrogen and carbon dioxide, which are thermodynamically unflavored to form carbon species in this range of conditions.

$$CH_4 + O_O{}^x = CO + 2H_2 + V_{O\bullet\bullet} + 2e' \quad (19)$$

$$CO + O_O{}^x = 2CO_2 + V_{O\bullet\bullet} + 2e' \quad (20)$$

The highest reforming reactivity and greatest resistance toward carbon deposition for Ce–ZrO_2 (HSA) with Ce/Zr ratio of 3/1 is due to the significantly higher amount of lattice oxygen ($O_O{}^x$) on their surfaces, according to the results in Section 3.1. The high amount of lattice oxygen ($O_O{}^x$) promotes the redox reaction of intermediate surface hydrocarbon species (C–S_{Ce}) with the lattice oxygen ($O_O{}^x$) (Eq. (12)) and also the redox reactions of methane and carbon monoxide with the lattice oxygen (Eqs. (19) and (20)).

Tables 4 and 5 present the effects of steam and temperature on the product contribution and degree of carbon deposition from the steam reforming of DME over Ce–ZrO_2. Clearly,

Table 4
Effect of inlet steam content on the products and amount of carbon deposition after exposure in the steam reforming of DME at 900 °C

DME/H_2O	Hydrogen selectivity (%)	Fraction of the by-products (%)				C formation (mmol g_{cat}^{-1})
		CO	CO_2	CH_4	CH_3OH	
1.0/3.0	51.2	33.8	15.7	49.9	0.6	0.06
1.0/5.0	52.8	32.5	19.6	47.6	0.3	0.06
1.0/7.0	53.0	31.0	21.6	47.1	0.3	0.04

Table 5
Effect of temperature on the products and amount of carbon deposition after exposure in the steam reforming of DME

Temperature (°C)	Hydrogen selectivity (%)	Fraction of the by-products (%)				C formation (mmol g_{cat}^{-1})
		CO	CO_2	CH_4	CH_3OH	
900	51.2 (73.9)	33.8[a] (78.2)[b]	15.7 (21.7)	49.9 (∼0)	0.6 (∼0)	0.06
925	53.9 (73.6)	38.4(79.1)	19.5 (20.8)	42.1 (∼0)	∼0 (∼0)	0.03
950	55.4 (73.3)	43.5 (80.0)	21.0 (19.9)	36.5 (∼0)	∼0 (∼0)	∼0
975	57.5 (73.0)	46.8 (80.7)	22.0 (19.1)	31.2 (∼0)	∼0 (∼0)	∼0
1000	59.0 (72.8)	51.9(81.5)	23.7 (18.4)	24.4 (∼0)	∼0 (∼0)	∼0

[a] Observed from the experiments.
[b] Calculated from the thermodynamic analysis (at equilibrium).

hydrogen selectivity increased with increasing temperature, whereas methane and methanol selectivities decreased. Furthermore, the amount of carbon formation significantly decreased with increasing temperature. These are due to the higher reforming reactivity of methane and methanol at high temperature. It should be noted that the thermodynamic analysis for the steam reforming of DME at 900–1000 °C were also performed using AspenPlus10.2 simulation program. At equilibrium condition, the main products from the steam reforming of DME in the range of temperature between 900 and 1000 °C are only hydrogen, carbon monoxide, and carbon dioxide. Very few amount of methane (3.7×10^{-7} to 2.4×10^{-6} kPa) was detected, whereas no formation of methanol was observed from the calculations. These calculated values are also presented in Table 5 (in the blanket). The deviations of the experimental results from the thermodynamic values are due to several side reactions. For instance, methanol can be formed by the hydration of DME, while methane can be generated from the reforming and decomposition of methanol as well as methanation reactions.

According to the effect of steam, hydrogen and carbon dioxide selectivities increased with increasing inlet steam concentration, whereas carbon monoxide selectivity decreased. The changes of hydrogen, carbon monoxide, and carbon dioxide selectivities are mainly due to the influence of mildly exothermic water–gas shift reaction, whereas the decrease of methane production is due to the further reforming to carbon monoxide and hydrogen.

3.4. Steam reforming of DME over Ni/Al_2O_3 and ($Ce–ZrO_2$ + Ni/Al_2O_3)

The steam reforming of DME over Ni/Al_2O_3 was first studied at 900 °C with the same inlet conditions as the case with $Ce–ZrO_2$. Table 6 presents the product selectivities from the steam reforming of DME over Ni/Al_2O_3 compared to those over $Ce–ZrO_2$ and without catalyst (homogeneous). Clearly, hydrogen selectivity observed from the steam reforming of DME over Ni/Al_2O_3 is lower than that over $Ce–ZrO_2$, whereas methanol selectivity is significantly higher.

As another approach of this work, $Ce–ZrO_2$ was then applied together with Ni/Al_2O_3 in the single unit either as the co-reforming catalyst by mixing both materials ($Ce–ZrO_2$ + Ni/Al_2O_3) or as the pre-reforming catalyst by packing in the different layers ($Ce–ZrO_2$–Ni/Al_2O_3). It should be noted that the total weight was always kept constant at 500 mg in all experiments. In the case of combination pattern, 200 mg of $Ce–ZrO_2$ and 300 mg of Ni/Al_2O_3 were used. Fig. 8 shows the

Table 6
Products and amount of carbon deposition from the steam reforming of DME over several catalysts at 900 °C

Catalyst	Hydrogen selectivity (%)	Fraction of the by-products (%)				C formation (mmol g_{cat}^{-1})
		CO	CO_2	CH_4	CH_3OH	
Non-catalyst	25.8	9.0	4.0	47.1	38.9	
$Ce–ZrO_2$	51.2	33.8	15.7	49.9	0.6	0.06
Ni/Al_2O_3	28.3	9.6	5.2	49.5	35.7	4.20
$Ce–ZrO_2$ + Ni/Al_2O_3	37.1	17.4	8.9	54.2	19.5	2.08
$Ce–ZrO_2$–Ni/Al_2O_3	67.4	43.9	24.5	31.6	∼0	0.30

Table 7
Products and amount of carbon deposition from the steam reforming of DME over IIR-SOFC configuration (at 900 °C)

System	Hydrogen selectivity (%)	Fraction of the by-products (%)				C formation (mmol g_{cat}^{-1})
		CO	CO_2	CH_4	CH_3OH	
Non-catalyst/Ni/YSZ	27.3	10.4	4.0	51.7	33.9	4.03
Ce–ZrO_2/Ni/YSZ	62.9	41.8	19.6	38.6	~0	0.20
Ni/Al_2O_3/Ni/YSZ	31.2	11.2	10.4	48.0	31.4	4.43
Ce–ZrO_2 + Ni/Al_2O_3/Ni/YSZ	51.8	19.6	12.6	50.1	17.7	3.81
Ce–ZrO_2–Ni/Al_2O_3/Ni/YS2	72.5	51.3	27.8	20.9	~0	0.36

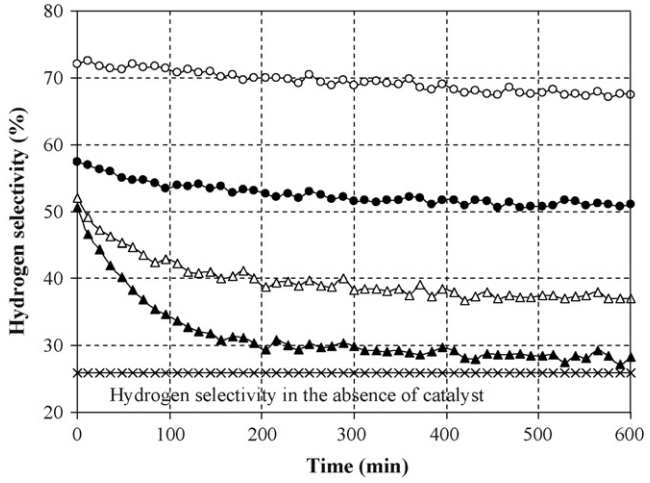

Fig. 8. Steam reforming of DME at 900°C for Ce–ZrO_2 (●), Ni/Al_2O_3 (▲), Ce–ZrO_2 + Ni/Al_2O_3 (△), and Ce–ZrO_2–Ni/Al_2O_3 (○) (4 kPa DME, and 12 kPa H_2O).

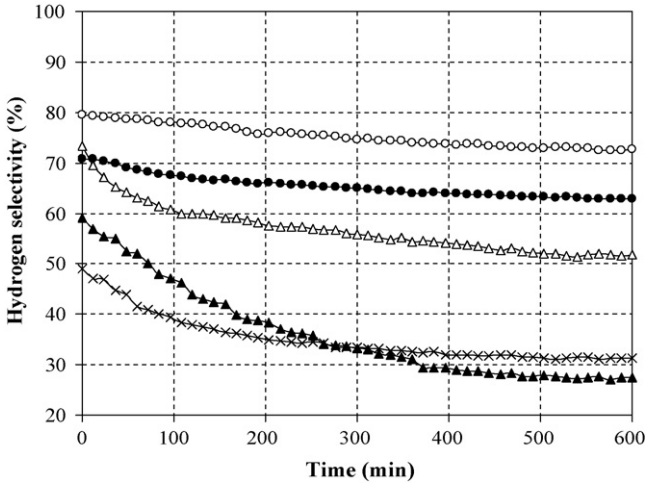

Fig. 9. Steam reforming of DME over IIR configuration at 900 °C (non-catalyst/Ni/YSZ (▲), Ce–ZrO_2/Ni/YSZ (●), Ni/Al_2O_3/Ni/YSZ (×), Ce–ZrO_2 + Ni/Al_2O_3/Ni/YSZ (△), and Ce–ZrO_2–Ni/Al_2O_3/Ni/YSZ (○)) (4 kPa DME, and 12 kPa H_2O).

variations in the hydrogen selectivity with time at 900 °C over both configurations compared to those from the systems with single Ni/Al_2O_3 and single Ce–ZrO_2. The hydrogen selectivities from the pre-reforming configuration (Ce–ZrO_2–Ni/Al_2O_3) were significantly higher than those over the co-reforming configuration (Ce–ZrO_2 + Ni/Al_2O_3), single Ni/Al_2O_3 and single Ce–ZrO_2. In addition, the methane and methanol selectivities over this configuration were reduced, Table 6.

By applying Ce–ZrO_2 as the pre-reforming catalyst, the main purpose of Ce–ZrO_2 is to convert methanol (and some methane) from the homogenous decomposition of DME to methane, carbon monoxide, and hydrogen before these components reach the surface of Ni/Al_2O_3. Therefore, the main reaction over Ni/Al_2O_3 is the steam reforming of methane instead of the steam reforming of methanol or DME, which is thermodynamically unfavored to form carbon deposition.

3.5. Steam reforming with IIR-SOFC configuration

It is clear from the above observation that the use of Ce–ZrO_2 as the pre-reforming catalyst along with Ni/Al_2O_3 can catalyze the steam reforming of DME efficiently. The next approach is to investigate the possible use of this reforming operation for IIR-SOFC by applying the annular ceramic reactor as described above.

With the same feeding conditions, Fig. 9 and Table 7 respectively present the stability and the product selectivities at 900 °C from the pre-reforming configuration (Ce–ZrO_2–Ni/Al_2O_3) compared to those with the co-reforming configuration (Ce–ZrO_2 + Ni/Al_2O_3), single Ni/Al_2O_3(Ni/Al_2O_3/Ni/YSZ), with single Ce–ZrO_2(Ce–ZrO_2/Ni/YSZ), and without the filling of Ce–ZrO_2 and Ni/Al_2O_3(Ni/YSZ).

The stability and the yield of hydrogen production from the steam reforming of DME over pre-reforming configuration were considerably higher than the others. At steady state, the yield of hydrogen production was close to the calculated equilibrium value. In addition, according to the results of TPO after reaction, the amount of carbon formation on the surface of Ni/YSZ was significantly low, Table 7. These improvements are due to the high conversions of methane and methanol, which are thermodynamically favored to form carbon deposition, by Ce–ZrO_2 and Ni/Al_2O_3 before these components reach the surface of Ni/YSZ at the outer side of the annular reactor.

4. Conclusion

DME can be decomposed homogeneously without the requirement of catalyst at high temperature, producing methane and methanol with small amount of carbon monoxide, carbon monoxide, and hydrogen. The use of Ce–ZrO_2 as the pre-reforming catalyst along with Ni/Al_2O_3 was an efficient way to

catalyze the steam reforming of DME, producing high contents of hydrogen and carbon monoxide with low selectivity of by-products (i.e. methane). The role of $Ce–ZrO_2$ for the steam reforming of DME is to decompose methanol and some methane (generated by the homogeneous decomposition of DME), while the role of Ni/Al_2O_3 is to decompose methane left from the reforming over $Ce–ZrO_2$ to hydrogen and carbon monoxide.

By applying $Ce–ZrO_2$ and Ni/Al_2O_3 as internal pre-reforming catalysts, this reforming pattern provided good hydrogen selectivity and high resistance toward carbon deposition on Ni/YSZ. It converts DME, methanol, and most of methane and maximizes the yield of hydrogen production. This successful development can improve the efficiency of IIR-SOFC fueled by DME by eliminating the requirement of an external pre-reforming unit installation.

Acknowledgements

The financial support from The Thailand Research Fund (TRF) throughout this project is gratefully acknowledged. The authors would also like to express gratitude to Mr. Pakorn Philunrekekun for the thermodynamic analysis.

References

[1] R. George, Fuel Cell Handbook, 6th ed., EG&G Technical Services, Inc. Science Applications International Corp., Under Contract No. DE-AM-26-99FT40575, U.S. Dept. of Energy, Office of Fossil Energy, National Energy Technology Laboratory, Morgantown, W. Virginia.
[2] S.H. Clarke, A.L. Dicks, K. Pointon, T.A. Smith, A. Swann, Catal. Today 38 (4) (1997) 411–423.
[3] K.C. Wincewicz, J.S. Cooper, J. Power Sources 140 (2005) 280–296.
[4] K. Oka, T. Nishiguchi, H. Kanai, K. Utani, S. Imamura, Appl. Catal. A: Gen. 309 (2) (2006) 187–191.
[5] T.A. Semelsberger, K.C. Ott, R.L. Borup, H.L. Greene, Appl. Catal. A: Gen. 309 (2) (2006) 210–223.
[6] T. Kawabata, H. Matsuoka, T. Shishido, D. Li, Y. Tian, T. Sano, K. Takehira, Appl. Catal. A: Gen. 308 (2006) 82–90.
[7] T.A. Semelsberger, K.C. Ott, R.L. Borup, H.L. Greene, Appl. Catal. B: Environ. 65 (3–4) (2006) 291–300.
[8] K. Faungnawakij, Y. Tanaka, N. Shimoda, T. Fukunaga, S. Kawashima, R. Kikuchi, K. Eguchi, Appl. Catal. A: Gen. 304 (2006) 40–48.
[9] T. Nishiguchi, K. Oka, T. Matsumoto, H. Kanai, K. Utani, S. Imamura, Appl. Catal. A: Gen. 301 (1) (2006) 66–74.
[10] P. Fornasiero, G. Balducci, R.D. Monte, J. Kaspar, V. Sergo, G. Gubitosa, A. Ferrero, M. Graziani, J. Catal. 164 (1996) 173.
[11] T. Miki, T. Ogawa, M. Haneda, N. Kakuta, A. Ueno, S. Tateishi, S. Matsuura, M. Sato, J. Phys. Chem. 94 (1990) 339.
[12] L. Fan, K. Fujimoto, J. Catal. 172 (1997) 238.
[13] M. Pijolat, M. Prin, M. Soustelle, J. Chem. Soc., Faraday Trans. 91 (1995) 3941.
[14] N. Laosiripojana, S. Assabumrungrat, Appl. Catal. B: Environ. 60 (2005) 107.
[15] N. Laosiripojana, W. Sutthisripok, S. Assabumrungrat, Chem. Eng. J. 112 (2005) 13–22.
[16] N. Laosiripojana, W. Sangtongkitcharoen, S. Assabumrungrat, Fuel 85 (2006) 323–332.
[17] N. Laosiripojana, S. Assabumrungrat, Appl. Catal. A: Gen. 290 (2005) 200.
[18] D. Kim, J. Am. Ceram. Soc. 72 (1989) 1415.
[19] N. Laosiripojana, S. Assabumrungrat, J. Power Sources 158 (2) (2006) 1348–1357.
[20] N. Laosiripojana, S. Assabumrungrat, Appl. Catal. B: Environ. 66 (1–2) (2006) 29–39.
[21] E. Ramirez, A. Atkinson, D. Chadwick, Appl. Catal. B 36 (2002) 193–206.
[22] P.J. Gellings, H.J.M. Bouwmeester, Catal. Today 58 (2000) 1–53.
[23] B.C.H. Steele, J.M. Floyd, Proc. Br. Ceram. Soc. 19 (1971) 55.
[24] Y. Lwin, W.R.W. Daud, A.B. Mohamad, Z. Yaakob, Int. J. Hydrogen Energy 25 (1) (2000) 47–53.
[25] J.N. Amor, Appl. Catal. A 176 (1999) 159–176.

Available online at www.sciencedirect.com
ScienceDirect
Applied Catalysis A: General 327 (2007) 180–188
APPLIED CATALYSIS A: GENERAL
www.elsevier.com/locate/apcata

Steam reforming of ethanol with co-fed oxygen and hydrogen over Ni on high surface area ceria support

N. Laosiripojana [a,*], S. Assabumrungrat [b], S. Charojrochkul [c]

[a] *The Joint Graduate School of Energy and Environment, King Mongkut's University of Technology Thonburi, Bangkok, Thailand*
[b] *Center of Excellence in Catalysis and Catalytic Reaction Engineering, Department of Chemical Engineering, Faculty of Engineering, Chulalongkorn University, Bangkok, Thailand*
[c] *National Metal and Materials Technology Center (MTEC), Bangkok, Thailand*

Received 6 February 2007; received in revised form 26 April 2007; accepted 1 May 2007
Available online 5 May 2007

Abstract

Ethanol steam reforming with/without co-fed oxygen and hydrogen over Ni on high surface area (HSA) CeO_2 support, synthesized via a surfactant-assisted method, (Ni/CeO_2 (HSA)) was studied under solid oxide fuel cell (SOFC) operating conditions for later application as an in-stack reforming catalyst. The catalyst provides considerably higher reforming reactivity and excellent resistance towards carbon deposition in comparison with Ni/Al_2O_3 and Ni on conventional ceria (Ni/CeO_2 (low surface area; LSA)). At the temperature above 800 °C, the main products from the reforming processes over Ni/CeO_2 (HSA) were H_2, CO, and CO_2 with some amount of CH_4 depending on the inlet steam/ethanol and co-fed reactant (i.e. O_2 and H_2)/ethanol ratios, whereas high hydrocarbon compound i.e. C_2H_4 was also observed from the reforming of ethanol over Ni/CeO_2 (LSA) and Ni/Al_2O_3. An addition of O_2 (as oxidative steam reforming) and H_2 significantly reduced the degree of carbon deposition. The presence of both reactants also promoted the conversions of hydrocarbon presented in the system (i.e. CH_4 and C_2H_4) to CO and H_2. The major consideration of these additions is the suitable co-fed reactant/C_2H_5OH ratio. The presence of too high oxygen concentration could oxidize Ni particles to NiO, which resulted in a lower reforming reactivity, and also combusts H_2 to H_2O. The suitable O_2/C_2H_5OH molar ratio for the oxidative steam reforming of Ni/CeO_2 was 0.4, which is less than that of Ni/Al_2O_3. An addition of too high hydrogen content slightly decreased the catalyst activity, which could be due to the active site competition of nickel particle and the inhibition of gas–solid redox reactions between the gaseous hydrocarbon components with the lattice oxygen (O_O^x) on the surface of CeO_2 support in the case of Ni/CeO_2.

Keywords: Ethanol; Steam reforming; Hydrogen; Oxidative steam reforming; Ceria

1. Introduction

A mixture of hydrogen and carbon monoxide (so-called synthesis gas) is a major fuel for solid oxide fuel cell (SOFC). Nevertheless, the use of other hydrocarbon fuel such as methane, methanol, ethanol, gasoline, and other oil derivatives is also possible when operated as an internal or in-stack reforming (IR-SOFC) [1]. According to the global environmental problems and current fossil fuel crisis, the development of IR-SOFC fed by biomass or renewable based fuels, attracts more attention as an alternative method for power generation in the near future. Among renewable sources, bio-ethanol is a promising candidate since it is readily produced by fermentation of biomasses and has reasonably high hydrogen content. In addition, ethanol is also safe and simple to handle, transport and store [2,3]. The major difficulty for a reforming of ethanol is the deactivation of the reforming catalyst due to a possible carbon deposition during ethanol decomposition, particularly at high temperature.

Previously, a steam reforming of ethanol has been studied by several researchers [4–11]. Most of them have investigated the reforming of ethanol over noble metal catalysts on several oxide supports [4–7]. Verykios et al. [8,9] reported that Rh based catalyst provides significantly higher activity and stability towards the steam reforming of ethanol compared with Ru, Pt, Pd, and also Ni. Similarly, Freni et al. [4,6,7] presented that Rh/Al_2O_3 provides the highest reforming reactivity among noble metal catalysts (e.g. Rh, Ru, Pt, Pd)

* Corresponding author. Tel.: +66 2 8729014; fax: +66 2 8726736.
E-mail address: navadol_l@jgsee.kmutt.ac.th (N. Laosiripojana).

0926-860X/$ – see front matter © 2007 Elsevier B.V. All rights reserved.
doi:10.1016/j.apcata.2007.05.001

on several oxide supports (e.g. Al_2O_3, MgO, SiO_2, TiO_2). Sobyanin et al. [10] studied the decomposition of ethanol in the presence of steam over Pd supported on a porous carbonaceous material. They presented that the catalyst exhibits a high activity and long-term stability. Burch et al. [11] found that the order of ethanol steam reforming reactivity over metals was Rh > Pd > Ni = Pt, and also reported the important role of the catalyst support. Verykios et al. [8,9] also investigated the steam reforming of ethanol over Ni based catalyst on several oxide supports (e.g. La_2O_3, Al_2O_3, YSZ, and MgO). They revealed that Ni/La_2O_3 and Ni/La_2O_3/Al_2O_3 exhibit high activity and stability.

According to these previous publications, an extensive formation of encapsulated carbon was always observed from the steam reforming of ethanol even if the noble metal catalysts were applied. This carbon formation was mainly due to the decomposition of ethanol-forming high hydrocarbons (e.g. acetaldehyde, ethylene, and ethane), which easily formed the carbonaceous deposits. An addition of oxygen to perform an oxidative steam reforming (or autothermal reforming) was proven to provide great benefits in terms of catalyst stability and coke suppression [12]. However, the yield of hydrogen production could be minimized due to the oxidation of hydrogen from added oxygen. The attractive characteristic of the autothermal reforming operation is that the exothermic heat from the partial oxidation can directly supply the energy required for the endothermic steam reforming reaction, and it is considered to be a thermally self-sustaining process.

In this work, it is aimed at developing an alternative catalyst, which can reform ethanol with high stability and activity at such a high temperature (700–1000 °C) for later application in IR-SOFC. According to the economical point of view, Ni was selected as a catalyst rather than other precious metals such as Pt, Rh, and Ru. Although the precious metals have been reported to be active for the reforming reactions and more resistant to the carbon formation than Ni [13,14], the current prices of these metals are very high for commercial uses, and the availability of some precious metals such as ruthenium was too low to have a major impact on the total reforming catalyst market [15]. A selection of the support material is a major consideration of this work. It has been widely reported that metal catalysts are not very active for the steam reforming when supported on inert oxides [16]. Various supports have been investigated, e.g. α-Al_2O_3 [17], γ-Al_2O_3 and γ-Al_2O_3 with alkali metal oxide and rare earth metal oxide [18], $CaAl_2O_4$ [19] and CeO_2 based supports [20]. A promising catalyst system for the reforming reactions appeared to be a metal on CeO_2 based supports, where metals can be Ni, Pt or Pd [17–19]. Therefore, CeO_2 was chosen as a catalyst support over Ni in this work.

CeO_2 (or called ceria) is an important material for a variety of catalytic reactions involving oxidation of hydrocarbons (e.g. automobile exhaust catalysts). It contains a high concentration of highly mobile oxygen vacancies, which act as local sources or sinks for oxygen involved in reactions taking place on its surface. Recently, the high resistance toward carbon deposition over ceria has been reported [20–22]. However, the major considerations of applying CeO_2 in the high temperature steam reforming reaction are their low specific surface and their percentage of high surface area (HSA) reduction due to the high surface sintering. The use of HSA ceria-based materials as the catalyst support would be a good alternative procedure to improve the reforming performance. Several methods have recently been described for the preparation of HSA CeO_2. Among these methods, the surfactant-assisted approach was reported to provide CeO_2 HSA with improved textural, structural, and chemical properties [23]. Our previous publication [20] also presented the achievement of CeO_2 with HSA and good stability after thermal treatment by this preparation method.

In the present work, the stability and activity toward the steam reforming of ethanol over Ni on HSA CeO_2 support (Ni/CeO_2 (HSA)) was firstly studied and compared with Ni on conventional LSA CeO_2 support (Ni/CeO_2 (LSA)), and Ni/Al_2O_3. The resistance toward carbon formation and the influences of inlet C_2H_5OH/H_2O molar ratio and temperature on the product selectivity over these catalysts were also studied. As the next step, the addition of co-fed reactant (i.e. O_2 and H_2) was then investigated. An improvement of the resistance toward carbon deposition by the presence of these components and the suitable inlet co-fed reactant/C_2H_5OH molar ratio were eventually determined.

2. Experimental

2.1. Catalyst preparation and characterization

Conventional CeO_2 support (CeO_2 (LSA)) was prepared by a precipitation method. The mixture of 0.1 M cerium nitrate ($Ce(NO_3)_3 \cdot H_2O$) (from Aldrich) and 0.4 M of urea at a 2:1 volumetric ratio was prepared and stirred using a magnetic stirrer (100 rpm) for 3 h. The precipitate was filtered and washed with deionized water and ethanol to prevent an agglomeration of particles. It was dried overnight in an oven at 110 °C, and then calcined in air at 1000 °C for 6 h.

CeO_2 (HSA) support was prepared by adding an aqueous solution of an appropriate cationic surfactant, 0.1 M cetyltrimethylammonium bromide solution from Aldrich, to a 0.1 M cerium nitrate. The molar ratio of ([Ce])/[cetyltrimethylammonium bromide] was kept constant at 0.8. The mixture was stirred and then aqueous ammonia was slowly added with vigorous stirring until the pH was 11.5. The mixture was continually stirred for 3 h, then sealed and placed in a thermostatic bath maintained at 90 °C for 3 days. Next, the mixture was cooled and the resulting precipitate was filtered and washed repeatedly with water and acetone. The filtered powder was then treated under the same procedures as CeO_2 (LSA). BET measurements of CeO_2 (both LSA and HSA) were carried out at different calcination temperatures to determine the decrease in specific surface area due to the thermal sintering. As presented in Table 1, after drying, surface areas of 105 and 55 $m^2\,g^{-1}$ were observed for CeO_2 (HSA) and conventional CeO_2, respectively. As expected, the surface area dramatically decreased at high calcination temperatures. However, the value for CeO_2 (HSA) is still appreciable after

Table 1
Specific surface area of CeO_2 (HSA and LSA) after drying and calcinations for 6 h at different temperatures

Catalyst	BET surface area ($m^2\ g^{-1}$) after drying or calcination at						
	100 °C	200 °C	400 °C	600 °C	800 °C	900 °C	1000 °C
CeO_2 (LSA)[a]	55	49	36	21	15	11	8.5
CeO_2 (HSA)[b]	105	97	69	48	35	29	24

[a] Conventional LSA CeO_2 prepared by the precipitation method.
[b] HSA CeO_2 prepared by the surfactant-assisted approach.

calcination at 1000 °C and it is almost three times of that for the conventional CeO_2.

Ni/CeO_2 (5 wt.% Ni) was then prepared by impregnating CeO_2 (both LSA and HSA) with a $Ni(NO_3)_2$ solution (from Aldrich). The catalyst was reduced with 10% H_2 at 500 °C for 6 h before use. For comparison, a conventional Ni/Al_2O_3 (5 wt.% Ni) was also prepared by impregnating α-Al_2O_3 (from Aldrich) with $Ni(NO_3)_2$. After reduction, the catalyst was characterized by several physicochemical methods. The weight contents of Ni in Ni/Al_2O_3 and Ni/CeO_2 were determined by X-ray fluorescence (XRF) analysis. The reducibility percentage of nickel was measured and calculated from the degree of H_2 uptakes from the temperature-programmed reduction (TPR) test using 5% H_2 with the total flow rate of 100 $cm^3\ min^{-1}$ and temperature from room temperature to 500 °C, while the dispersion percentage of nickel was identified from the volumetric H_2 chemisorption measurement using chemisorption analyzer. According to this measurement, the H_2 chemisorption and backsorption isotherms were measured and their difference was used to calculate strongly chemisorbed H_2 uptakes, from which Ni dispersions were obtained by assuming 1:1 stoichiometry of adsorbed H and metal surface atoms [24,25]. The catalyst specific surface areas were obtained from BET measurement. All physicochemical properties of the synthesized catalysts are presented in Table 2.

As described in Section 1, the advantage of CeO_2 as the support is mainly due to its high redox properties. In addition to the above characterizations, the redox properties and redox reversibilities of synthesized Ni/CeO_2 (both LSA and HSA) and Ni/Al_2O_3 were also determined by the TPR and the temperature programmed oxidation (TPO). Regarding these experiments, 5% H_2 and 10% O_2 were used for the TPR and TPO, respectively, while the temperature of the system increased from room temperature to 900 °C for both experiments.

2.2. Apparatus and procedures

An experimental reactor system was constructed as presented elsewhere [20–22]. The feed gases including the components of interest (ethanol and steam from the evaporator, oxygen and hydrogen as the additive gas), and the carrier gas (helium) were introduced to the reaction section, in which a 10-mm diameter quartz reactor was mounted vertically inside a furnace. The catalyst was loaded in the quartz reactor, which was packed with a small amount of quartz wool to prevent the catalyst from moving. Regarding the results in our previous publications [20–22], in order to avoid any limitations by intraparticle diffusion, the weight of catalyst loading was kept constant at 50 mg, while the total gas flow rate was 100 $cm^3\ min^{-1}$ under a constant residence time of 3×10^{-2} g s cm^{-3} in all experiments. A Type-K thermocouple was placed into an annular space between the reactor and the furnace. This thermocouple was mounted on the tubular reactor in close contact with the catalyst bed to minimize the temperature difference between the catalyst bed and the thermocouple. Another Type-K thermocouple was inserted in the middle of the quartz tube to recheck the possible temperature gradient.

After the reactions, the exit gas mixture was transferred via trace-heated lines to the analysis section, which consists of a Porapak Q column Shimadzu 14B gas chromatograph (GC) and a mass spectrometer (MS). The gas chromatography was applied to investigate the steady state condition experiments, whereas the mass spectrometer in which the sampling of the exit gas was done by a quartz capillery and differential pumping was used for the transient carbon formation experiment. To study the formation of carbon species on catalyst surface, TPO was applied by introducing 10% O_2 in He (with the flow rate of 100 $cm^3\ min^{-1}$) 1) into the system, after being purged with He. The operating temperature increased from room temperature to 900 °C with a rate of 10 °C min^{-1}. The amount of carbon formation on the surface of catalysts were determined by measuring the CO and CO_2 yields from the TPO results (using microcal origin software) assuming a value of 0.026 nm^2 for the area occupied by a carbon atom in a surface monolayer of the basal plane in graphite [26]. In addition to the TPO method, the amount of carbon deposition was confirmed by the calculation of carbon balance in the system. The amount of carbon deposited on the surface of catalyst is theoretically equal to the difference between the inlet carbon

Table 2
Physicochemical properties of the catalysts after reduction

Catalyst	Ni-load (wt.%)	BET surface area ($m^2\ g^{-1}$)	Ni-reducibility (Ni%)	Ni-dispersion (Ni%)
Ni/CeO_2 (HSA)	5.0	24	92.2	6.41
Ni/CeO_2 (LSA)	4.8	8.5	91.3	3.12
Ni/Al_2O_3	5.0	40	94.5	4.85

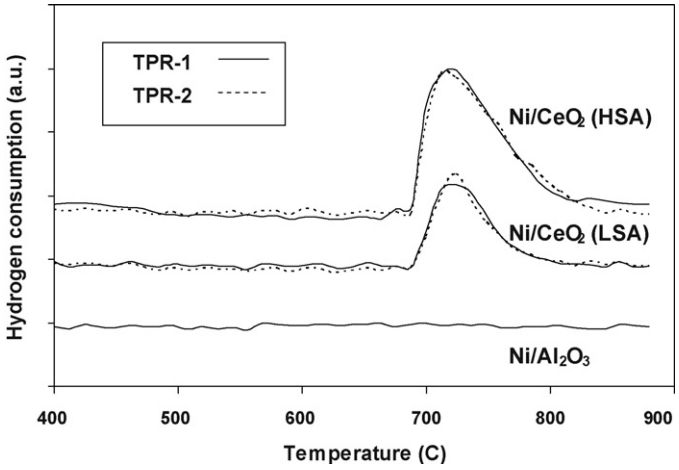

Fig. 1. TPR-1 of fresh catalysts after reduction and second time temperature programmed reduction (TPR-2) of Ni/CeO_2 (HSA and LSA).

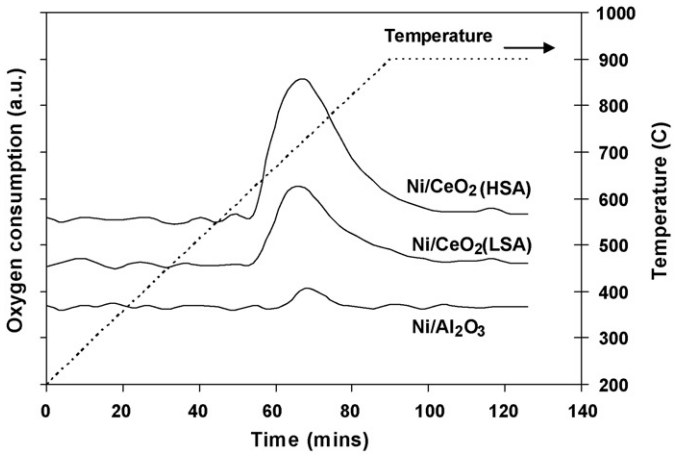

Fig. 2. TPO of Ni/CeO_2 (HSA and LSA) and Ni/Al_2O_3 after TPR-1.

containing components (C_2H_5OH) and the outlet carbon containing components (CO, CO_2, CH_4, C_2H_6, C_2H_4, and C_2H_4O). The amount of carbon deposited per gram of catalyst is given by the following equation:

$$C_{\text{deposition}} = \frac{\text{mole}_{\text{carbon(in)}} - \text{mole}_{\text{carbon(out)}}}{m_{\text{catalyst}}} \quad (1)$$

To study the steam reforming reactivity, the rate of ethanol steam reforming was defined in terms of conversion and product distribution. The yield of hydrogen production was calculated by the hydrogen balance, defined as the molar fraction of hydrogen produced to the total hydrogen in the products. Distributions of other by-products (i.e. CO, CO_2, CH_4, C_2H_6, C_2H_4, and C_2H_4O) were calculated by the carbon balance, defined as the ratios of the product moles to the consumed moles of hydrocarbon, accounting for stoichiometry. This information was presented in terms of relative fractions of all by-product components (i.e. CO, CO_2, CH_4, C_2H_6, C_2H_4, and C_2H_4O), which are summed to 100%.

3. Results

3.1. Redox properties and redox reversibility of the synthesized catalysts

After reducing, the oxygen storage capacities (OSC) and the degree of redox properties for Ni/CeO_2 (both LSA and HSA) and Ni/Al_2O_3 were investigated using a TPR-1, which was performed by heating the catalysts up to 900 °C in 5% H_2-He. The amount of hydrogen uptake is correlated to the amount of oxygen stored and enabled to consume in the ceria-based supports. The solid lines in Fig. 1 represent the results of TPR-1 for these three catalysts. It is apparent that the greater amount of hydrogen uptake is detected from Ni/CeO_2 (HSA) compared to Ni/CeO_2 (LSA), suggesting that the OSC strongly depends on the specific surface area of CeO_2. In contrast, hydrogen consumption was not observed from the TPR over Ni/Al_2O_3, indicating no occurrence of redox properties for this catalyst. After being purged with He, the redox reversibilities for Ni/CeO_2 (both LSA and HSA) were then determined by applying a TPO following with the second time TPR-2. Regarding the TPO and TPR-2 results as shown in Figs. 1 (dotted lines), 2 and Table 3, the amount of hydrogen uptakes for Ni/CeO_2 (both LSA and HSA) were approximately similar to those from TPR-1, indicating their redox reversibilities. It should be noted that the TPO over Ni/Al_2O_3 was also carried out to clarify the effect of Ni oxidation on the TPO spectra. As seen in Fig. 2, insignificant amount of oxygen uptake was observed over Ni/Al_2O_3, indicating that the observed oxygen uptakes for Ni/CeO_2 (both LSA and HSA) were mostly related to the redox property of CeO_2. The insignificant oxygen uptake for Ni/Al_2O_3 during TPO could be due to the presence of only small amount of Ni in the catalyst (5 wt.%).

3.2. Homogenous (noncatalytic) reaction

Before studying performances of the catalysts, homogeneous (noncatalytic) reactions were investigated. Previously,

Table 3
Results of TPR-1, TPO, TPR-2 analyses of Ni/CeO_2 (both CeO_2(HSA), CeO_2(LSA))

Catalyst	Total H_2 uptake from TPR-1[a] ($\mu mol/g_{cat}$)	Total O_2 uptake from TPO[b] ($\mu mol/g_{cat}$)	Total H_2 uptake from TPR-2[c] ($\mu mol/g_{cat}$)
Ni/CeO_2 (HSA)	2104	1031	2100
Ni/CeO_2 (LSA)	1018	506	1015

[a] TPR of the reduced catalysts.
[b] TPO after TPR-1.
[c] Re-TPR after TPO.

we reported the product distribution at different temperatures (150–1000 °C) from the homogeneous steam reforming of ethanol [22]. Here, the homogeneous steam reforming of ethanol in the presence of oxygen (as oxidative steam reforming) was further investigated. A similar trend as the steam reforming was observed. Firstly, ethanol was converted to acetaldehyde, and hydrogen at the temperature above 200 °C via the dehydrogenation of ethanol (Eq. (2)). Simultaneously, methane and carbon monoxide productions were initially observed at the temperature around 250–300 °C via the fast decomposition of acetaldehyde (Eq. (3)).

$$C_2H_5OH \rightarrow C_2H_4O + H_2 \quad (2)$$

$$C_2H_4O \rightarrow CH_4 + CO \quad (3)$$

The concentration of acetaldehyde significantly dropped at the temperature of 550 °C and approached zero at the temperature of 650 °C. In this range of temperature, the formations of ethane and ethylene were observed. Ethane is formed by the dehydration of ethanol (Eq. (4)) whereas the production of ethane is from ethylene hydrogenation (Eq. (5)). This phenomenon is confirmed by the observation of lower H_2 selectivity compared to CO selectivity.

$$C_2H_5OH \rightarrow C_2H_4 + H_2O \quad (4)$$

$$C_2H_4 + H_2 \rightarrow C_2H_6 \quad (5)$$

The concentration of carbon monoxide, carbon dioxide, methane, ethane, and ethylene remained almost constant at temperatures higher than 650 °C. It should be noted that, when compared to the homogeneous (noncatalytic) ethanol steam reforming at the same operating temperatures in our previous report [22], the addition oxygen along with ethanol and steam as autothermal reforming, increased the conversion of ethanol and reduced the formations of ethane and ethylene. These are due to the possible oxidation of ethanol in the presence of oxygen forming more acetaldehyde (Eq. (6)), which is eventually converted to methane and carbon monoxide. This oxidation reduces the degree of ethanol dehydration and consequently, less ethylene and ethane were generated.

$$C_2H_5OH + \frac{1}{2}O_2 \rightarrow C_2H_4O + H_2O \quad (6)$$

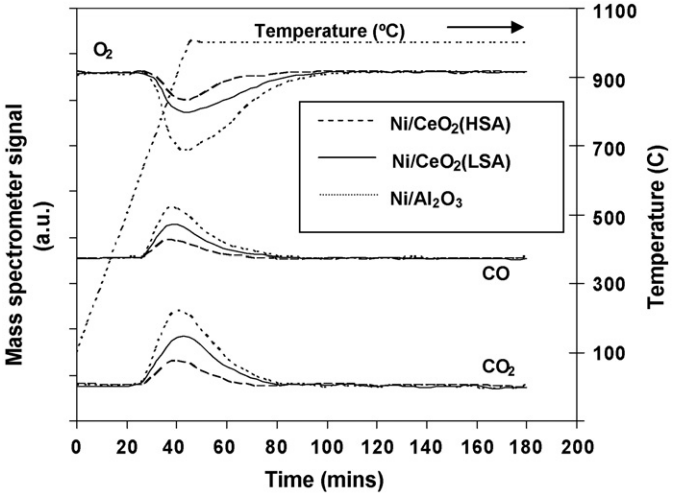

Fig. 3. TPO of Ni/CeO_2 (HSA), Ni/CeO_2 (LSA), and Ni/Al_2O_3 after exposure in steam reforming of ethanol (4 kPa C_2H_5OH, and 12 kPa H_2O) for 10 h.

Nevertheless, significant amount of ethylene and ethane (12–18%) remains observed from the homogeneous autothermal reforming of ethanol.

3.3. Reactivity towards ethanol steam reforming

The steam reforming of ethanol over Ni/CeO_2 (both LSA and HSA) and conventional Ni/Al_2O_3 without co-fed reactant were firstly tested at 900 °C by introducing C_2H_5OH/H_2O in helium with the molar ratios of 1.0/1.0, 1.0/2.0, and 1.0/3.0 to the catalyst-bed. After 10 h operation, the catalyst reactivity expressed as yield of hydrogen production and the post reaction characterizations were measured, as presented in Table 4. The postreaction TPO experiments were also carried out after a helium purge by introducing 10% O_2 in He in order to determine the degree of carbon formation. From the TPO results shown in Fig. 3, small peaks of carbon dioxide and carbon monoxide were observed for Ni/CeO_2 (HSA) and Ni/CeO_2 (LSA), whereas huge amount of carbon dioxide and carbon monoxide formations were detected for Ni/Al_2O_3. The amount of carbon formations were then determined by measuring the CO and CO_2 yields from these TPO results. Using a value of 0.026 nm^2 for the area occupied by a carbon atom in a surface monolayer of the basal

Table 4
Yield of H_2 production and the physicochemical properties of catalysts after exposure in the steam reforming of ethanol at 900 °C with different inlet C_2H_5OH/H_2O ratios

Catalyst	C_2H_5OH/H_2O ratio	Yield of H_2 production (%)	BET surface ($m^2\ g^{-1}$)	Ni-load (wt.%)	Ni-red. (Ni%)	Ni-disp. (Ni%)
Ni/CeO_2 (HSA)	1.0/3.0	82.5	23.2	4.9	90.2	6.39
	1.0/2.0	76.4	23.1	4.8	90.5	6.41
	1.0/1.0	65.5	23.2	4.8	90.4	6.37
Ni/CeO_2 (LSA)	1.0/3.0	61.1	9.8	4.8	89.2	3.11
	1.0/2.0	57.3	9.8	4.8	89.6	3.10
	1.0/1.0	54.6	9.5	4.7	89.7	3.12
Ni/Al_2O_3	1.0/3.0	57.2	40.0	4.9	92.0	4.85
	1.0/2.0	54.2	39.5	4.9	91.7	4.81
	1.0/1.0	53.1	40.0	4.8	91.8	4.83

Table 5
Dependence of inlet C_2H_5OH/H_2O ratio on the amount of carbon formation remaining on the catalyst surface

C_2H_5OH/H_2O ratio	Total carbon formation (monolayers)		
	Ni/CeO_2 (HSA)	Ni/CeO_2 (LSA)	Ni/Al_2O_3
1.0/3.0	1.08[a] (1.08)[b]	2.17 (2.15)	4.52 (4.54)
1.0/2.0	1.19 (1.17)	2.23 (2.21)	4.76 (4.78)
1.0/1.0	1.24 (1.26)	2.31 (2.34)	4.81 (4.79)

[a] Calculated using CO and CO_2 yields from TPO with 10% oxygen.
[b] Calculated from the balance of carbon in the system.

plane in graphite [26], the quantities of carbon deposited over Ni/CeO_2 (HSA), Ni/CeO_2 (LSA), and Ni/Al_2O_3 were observed to be approximately 1.08, 2.17, and 4.52 monolayers, respectively, for the inlet C_2H_5OH/H_2O ratio of 1.0/3.0. It should be noted that these values were found to decrease with increasing inlet H_2O concentration as shown in Table 5. In addition to the TPO method, the total amounts of carbon deposited were ensured by the calculations of carbon balance of the system. Regarding the calculations, the moles of carbon deposited per gram of Ni/CeO_2 (HSA), Ni/CeO_2 (LSA), and Ni/Al_2O_3 were 1.12, 2.19, and 4.55 mmol g^{-1}, respectively. Using the same assumption for the area occupied by a carbon atom [26], these values are equal to 1.08, 2.15, and 4.54 monolayers respectively, which is in good agreement with the values observed from the TPO method described above. These results clearly indicated the highest resistance towards carbon formation for Ni/CeO_2 (HSA).

The influence of operating temperature on the product distribution over Ni/CeO_2 (HSA), Ni/CeO_2 (LSA), and Ni/Al_2O_3 were further studied by varying temperature from 700 to 1000 °C. All product distributions over these catalysts at different temperature are presented in Table 6. It was found that the main products from the ethanol steam reforming over Ni/CeO_2 (HSA) were H_2, CO, CO_2, and CH_4, with small amounts of C_2H_4 and C_2H_6 depending on the operating temperature. In contrast, significant amounts of C_2H_4 and C_2H_6 were also observed as well as other chemical components from the ethanol steam reforming over Ni/CeO_2 (LSA) and Ni/Al_2O_3 in the range of conditions studied.

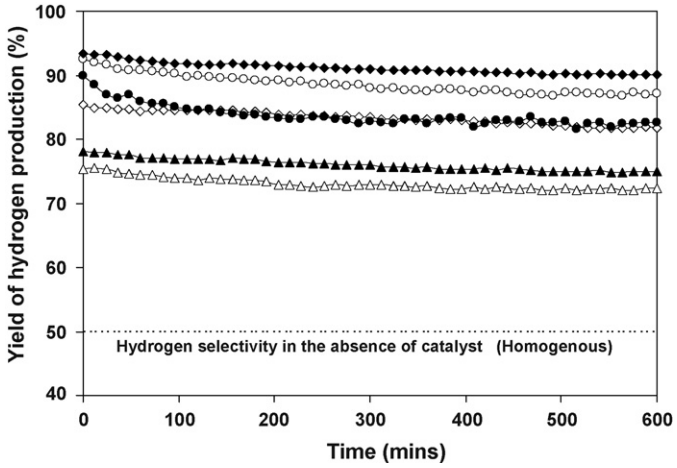

Fig. 4. Autothermal reforming of ethanol at 900 °C for Ni/CeO_2 (HSA) with the inlet O_2/C_2H_5OH ratios of 0 (●), 0.2 (○), 0.4 (◆), 0.6 (◇), 0.8 (▲), and 1.0 (Δ)) (4 kPa C_2H_5OH, and 12 kPa H_2O).

3.4. Reactivity towards reforming of ethanol with co-fed oxygen

Ni/CeO_2 (HSA) and Ni/Al_2O_3 were selected for further studied by adding oxygen together with ethanol and steam as autothermal reforming operation. The inlet C_2H_5OH/H_2O molar ratio was kept constant at 1.0/3.0, while the inlet O_2/C_2H_5OH molar ratios were varied from 0.2, 0.4, 0.6, 0.8, to 1.0. The effect of oxygen concentration on the variations in hydrogen yield (%) with time at 900 °C for Ni/CeO_2 (HSA) and Ni/Al_2O_3 are shown in Figs. 4 and 5. The dependences of oxygen on the yield of hydrogen production are nonmonotonic. The yield of hydrogen production increased with increasing O_2/C_2H_5OH molar ratio until the ratio reached 0.4 for Ni/CeO_2 (HSA) and 0.6 for Ni/Al_2O_3. Then, oxygen presented a negative effect on the hydrogen yield at higher inlet O_2/C_2H_5OH molar ratio values.

Fig. 6(a) and (b) presents the comparison between the product distribution from the autothermal reforming of ethanol (with the suitable O_2/C_2H_5OH molar ratio for each catalyst) and

Table 6
Products and amount of carbon deposition after exposure in the steam reforming of ethanol at different temperatures (with inlet C_2H_5OH/H_2O ratio of 1.0/3.0)

Catalyst	Temperature (°C)	Yield of H_2 production (%)	Fraction of the by-products (%)					C formation (monolayers)
			CO	CO_2	CH_4	C_2H_6	C_2H_4	
Ni/CeO_2 (HSA)	700	67.3	47.4	22.6	22.3	2.8	4.9	1.79
	800	78.3	60.6	20.4	18.7	~0	0.3	1.35
	900	82.5	70.1	19.3	10.6	~0	~0	1.08
	1000	86.9	76.6	16.6	6.8	~0	~0	0.82
Ni/CeO_2 (LSA)	700	49.7	41.4	18.9	27.8	3.3	8.6	3.02
	800	55.4	46.4	16.7	29.4	1.1	6.4	2.41
	900	61.1	53.9	15.8	26.3	~0	4.0	2.17
	1000	64.2	61.4	12.4	24.3	~0	1.9	2.09
Ni/Al_2O_3	700	48.1	33.1	19.7	17.7	10.3	19.2	4.97
	800	51.9	41.8	14.3	22.6	3.9	17.4	4.63
	900	57.2	49.7	10.0	24.4	1.4	14.5	4.52
	1000	59.8	59.5	9.7	20.9	~0	9.9	4.22

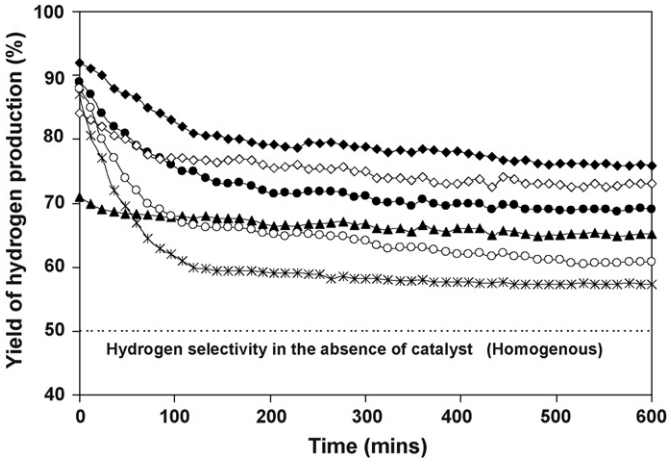

Fig. 5. Autothermal reforming of ethanol at 900 °C for Ni/Al_2O_3 with the inlet O_2/C_2H_5OH ratios of 0 (×), 0.2 (○), 0.4 (● 0.6 (◆), 0.8 (◇), and 1.0 (▲)) (4 kPa C_2H_5OH, and 12 kPa H_2O).

those from the steam reforming over Ni/CeO_2 (HSA) and Ni/Al_2O_3 at different temperatures (700–1000 °C). It was found that the main products from the autothermal reforming of ethanol over both catalysts are similar to the steam reforming (e.g., H_2, CO, CO_2, and CH_4). Nevertheless, higher H_2, CO, and CO_2 were observed from the autothermal reforming, whereas less CH_4, C_2H_6, and C_2H_4 were found compared to the steam reforming at the same operating conditions.

The postreaction TPOs were then carried out to determine the degree of carbon formation on catalyst surface. From the TPO results shown in Table 7, significantly less quantities of carbon deposited were observed for both Ni/CeO_2 (HSA) and Ni/Al_2O_3. No carbon formation was detected on Ni/CeO_2 (HSA) when the inlet O_2/C_2H_5OH molar ratio reached 0.4.

Regarding the TPR experiments over the spent catalysts after exposure in autothermal reforming condition, the addition of too high oxygen content (higher than 0.4 for Ni/CeO_2 and 0.6 for Ni/Al_2O_3) results in the oxidation of Ni to NiO as shown in the last column of Table 7 and it consequently reduces the reforming reactivity of the catalysts. Therefore, in order to produce hydrogen from the autothermal reforming of ethanol,

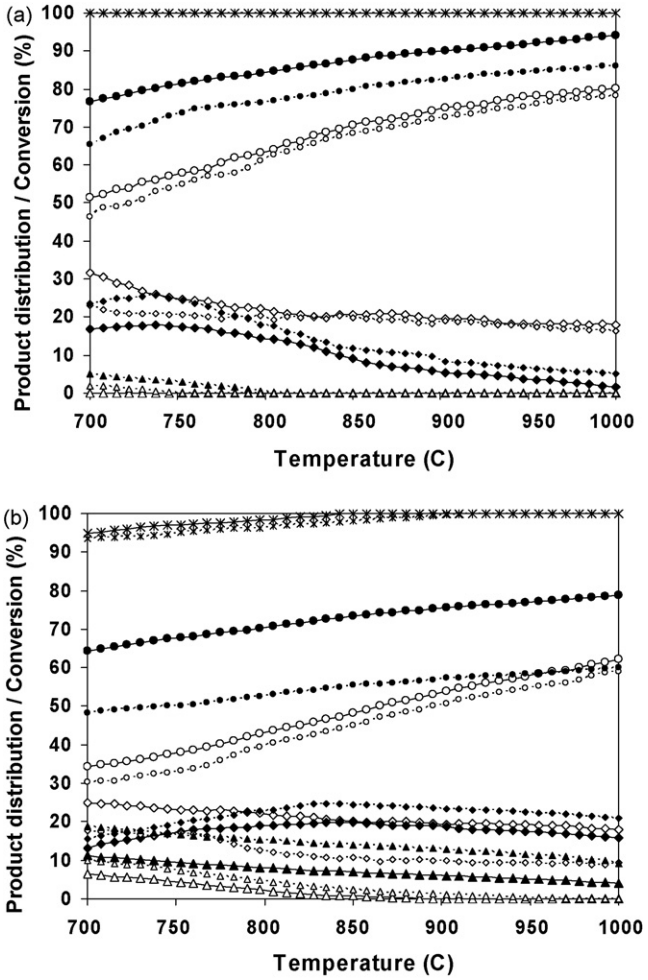

Fig. 6. Comparison of the conversion and product distributions (EtOH (×), H_2 (●), CO (○), CO_2 (◇), CH_4 (◆), C_2H_6 (Δ), and C_2H_4 (▲)) from steam reforming (small symbols with dot lines) (4 kPa C_2H_5OH, and 12 kPa H_2O) and autothermal reforming (large symbols with solid lines) (4 kPa C_2H_5OH, 12 kPa H_2O, and 1.6 kPa O_2) of ethanol over Ni/CeO_2 (HSA) (Fig. 6a) and Ni/Al_2O_3 (Fig. 6b).

the inlet O_2/C_2H_5OH molar ratios of 0.4 for Ni/CeO_2 (HSA) and 0.6 for Ni/Al_2O_3 are the optimum ratio, which provide the highest resistance towards carbon deposition and are able to operate without the oxidation of Ni.

Table 7
Yield of H_2 production, deactivation percentages, and physicochemical properties of the catalysts after exposure in autothermal reforming of ethanol (with various inlet O_2/C_2H_5OH ratios) at 900 °C

Catalyst	Inlet O_2/C_2H_5OH molar ratio	Yield of H_2 (%) at steady state	Deactivation (%)	C formation (monolayers)	BET surface ($m^2\,g^{-1}$)	Ni-red. (Ni%)
Ni/CeO_2 (HSA)	0.0	82.5	8.2	1.08	23.1	90.2
	0.2	87.1	5.9	0.31	23.0	90.2
	0.4	90.1	3.4	~0	23.2	90.0
	0.6	81.7	4.3	~0	23.2	88.6
	0.8	74.9	3.9	~0	23.5	84.7
	1.0	72.2	3.9	~0	23.2	79.3
Ni/Al_2O_3	0.0	57.2	34.1	4.52	40.0	92.0
	0.2	60.7	30.9	3.16	39.6	91.6
	0.4	69.1	22.3	2.73	39.8	91.0
	0.6	75.8	17.5	2.14	40.0	90.8
	0.8	73.0	13.0	1.50	39.9	85.2
	1.0	65.1	8.2	1.03	39.9	81.6

Table 8
Product distributions and amount of carbon deposition after exposure in the steam reforming of ethanol (with various inlet H_2/C_2H_5OH ratios) at 900 °C

Catalyst	Inlet H_2/C_2H_5OH molar ratio	Fraction of the carbon products (%)					C formation (monolayers)
		CO	CO_2	CH_4	C_2H_6	C_2H_4	
Ni/CeO_2 (HSA)	0.0	70.1	19.3	10.6	~0	~0	1.08
	0.5	70.8	19.6	9.6	~0	~0	0.72
	1.0	71.3	20.0	8.7	~0	~0	0.41
	2.0	72.7	20.7	6.6	~0	~0	0.39
	3.0	73.0	20.9	6.1	~0	~0	0.26
	4.0	73.3	19.8	6.9	~0	~0	0.22
	5.0	73.4	19.5	7.1	~0	~0	0.13
Ni/Al_2O_3	0.0	49.7	10.0	24.4	1.4	14.5	4.52
	0.5	51.1	10.7	24.0	0.6	13.6	3.97
	1.0	53.4	11.9	22.9	~0	11.8	2.69
	2.0	55.2	12.8	22.1	~0	9.9	2.41
	3.0	56.8	13.8	20.7	~0	8.7	2.06
	4.0	57.9	14.3	21.0	~0	6.8	1.87
	5.0	58.0	13.8	21.8	~0	6.4	1.62

3.5. Reactivity towards reforming of ethanol with co-fed hydrogen

As a next step, hydrogen was added as co-feeding along with ethanol and steam at the feed. The inlet C_2H_5OH/H_2O molar ratio was kept constant at 1.0/3.0, while the inlet H_2/C_2H_5OH molar ratios were varied from 0.5 to 5.0. As hydrogen is a feed, the effect of this component on the catalyst performance was investigated in term of hydrocarbon (i.e. CH_4, C_2H_4, and C_2H_6) distribution instead of the yield of hydrogen production. Table 8 presents all product distribution from the steam reforming of ethanol in the presence of hydrogen for Ni/CeO_2 (HSA) and Ni/Al_2O_3. Apparently, the production of CH_4, C_2H_4, and C_2H_6 decreases with increasing H_2/C_2H_5OH molar ratio, which means the higher CH_4, C_2H_4, and C_2H_6 conversions occurred, until the ratio reached 3.0. Then, the effect of hydrogen becomes less pronounced at higher inlet H_2/C_2H_5OH ratio and eventually the CH_4 concentration slightly grows up. The postreaction TPO were also carried out to determine the degree of carbon formation. From the TPO results as also shown in Table 8, with the presence of hydrogen, less amount of carbon deposited were observed for both Ni/CeO_2 (HSA) and Ni/Al_2O_3.

4. Discussion

According to the homogeneous (noncatalytic) oxidative steam-reforming test, significant amount of ethylene and ethane were observed at the temperatures above 650 °C. These formations are the major difficulties for the catalytic reforming of ethanol, as it has been widely established that at such a high temperature ethane and ethylene can easily decompose and form carbon species on the surface of catalyst ($C_nH_m \rightarrow 0.5\ mH_2 + nC$). Furthermore, in this range of temperature, in addition to the decomposition of ethane and ethylene, carbon formation can also be formed via the Boudouard reaction ($2CO \Leftrightarrow CO_2 + C$) during the catalytic steam reforming of ethanol. By increasing an inlet steam to ethanol molar ratio, the degree of carbon formation from the steam reforming of ethanol decreases, as the equilibrium of water–gas shift reaction moves forward producing more CO_2 rather than CO and eventually avoids carbon deposition via the Boudouard reaction. However, significant amount of carbon remains detected due to the decomposition of ethane, ethylene, and methane.

Ni/CeO_2 (HSA) was found in this study to have excellent resistance towards carbon deposition compared to conventional Ni/CeO_2 (LSA) and Ni/Al_2O_3. At the temperature above 800 °C, the main products from the reforming of ethanol over Ni/CeO_2 (HSA) were H_2, CO, CO_2, and small amount of methane; neither ethylene nor ethane was observed from the system over this catalyst. The high resistance towards carbon deposition for Ni/CeO_2 (HSA) is mainly due to the high OSC of ceria support. We previously reported the excellent resistance towards carbon deposition for CeO_2 especially for HSA CeO_2 [20]. CeO_2 contains a high concentration of highly mobile oxygen vacancies and thus acts as a local source or sink for oxygen on its surface. It has been reported that at high temperature the lattice oxygen (O_O^x) at the CeO_2 surface can oxidize gaseous hydrocarbons (methane [20], ethane, [22] and propane [22]). Although conventional CeO_2 (CeO_2 (LSA)) has also been reported to provide high resistance towards carbon formation, the major weaknesses of CeO_2 (LSA) are its low specific surface area and also high size reduction due to the thermal sintering impact, resulting in its significant lower redox properties than CeO_2 (HSA) and its lower Ni dispersion percentage on the surface compared to Ni/CeO_2 (HSA) and Ni/Al_2O_3. These disadvantages result in the low ethanol steam reforming reactivity for Ni/CeO_2 (LSA). By using Ni/CeO_2 (HSA) as a catalyst, in addition to the reaction on Ni surface, ethane and ethylene formations and the possible carbon depositions from these hydrocarbons could be inhibited by the gas–solid reactions between these hydrocarbons and the lattice oxygen (O_O^x) at CeO_2 surface forming hydrogen and carbon dioxide, which are thermodynamically unflavored to form carbon species. The lattice oxygen can then be regenerated by

reaction with oxygen containing compounds (steam) present in the system.

It was also observed from the study that the addition of either oxygen or hydrogen together with ethanol and steam reduced the degree of carbon deposition. As described, the oxidation of oxygen with ethanol can prevent the formation of ethylene and ethane via the dehydration of ethanol. In addition, oxygen can prevent the formation of carbon species via the hydrocarbon depositions by oxidizing these hydrocarbons producing the elements that are unflavored to form carbon species. In the case of Ni/CeO_2, the presence of oxygen also helps steam to regenerate the lattice oxygen (O_O^x) on CeO_2 surface ($0.5O_2 + V_O^{\bullet\bullet} + 2\,e' \rightarrow O_O^x$). The major consideration of the autothermal reforming operation is the O_2/C_2H_5OH ratio. The presence of too high oxygen concentration could oxidize Ni particles to NiO, which has low reforming reactivity. The suitable oxygen concentration for the autothermal reforming of Ni/CeO_2 (O_2/C_2H_5OH molar ratio of 0.4) is lower than that of Ni/Al_2O_3 (O_2/C_2H_5OH molar ratio of 0.6) due to the high OSC of CeO_2.

By adding hydrogen at the feed, the degree of carbon formation can be reduced by the hydrogenation reaction. The positive effect of hydrogen appearance on CH_4, C_2H_4, and C_2H_6 conversions could be due to the reduction of oxidized state on the surface active site of nickel (*) by hydrogen ($H_2 + O\text{-}* \Leftrightarrow H_2O + *$), whereas the increase in CH_4 selectivity at high hydrogen partial pressure could be due to the promotion of the methanation, the reverse water–gas shift reactions and the reverse methane steam reforming [27,28]. In addition, the occupying of hydrogen atom on some active sites of nickel particle ($H_2 + 2* \Leftrightarrow 2H\text{-}*$) could also lead to the decrease in methane conversion, as explained by Xu and Froment [27,28]. It should be noted, in addition, that the increase in CH_4 selectivity at high hydrogen partial pressure for Ni/CeO_2 could also be due to the reduction of lattice oxygen by hydrogen via the reverse of Eq. (21) and consequently inhibits the reaction of the lattice oxygen with the surface hydrocarbon species. This explanation is in good agreement with the previous studies [20,26], which studied kinetics parameters for the methane steam reforming on ceria-based materials and reported the negative effect of hydrogen on methane conversion over these materials.

5. Conclusions

Ni on HSA CeO_2 support (Ni/CeO_2 (HSA)) provides excellent reactivity towards the steam reforming of ethanol with high resistance toward carbon deposition and better product selectivity compared to Ni/Al_2O_3 and Ni on conventional LSA ceria (Ni/CeO_2 (LSA)). The great benefits of Ni/CeO_2 (HSA) in terms of stability and reactivity towards ethanol reforming, high resistance towards carbon deposition, and good product selectivities are due to the high redox property of CeO_2 (HSA).

An addition of oxygen (as autothermal reforming) and hydrogen can reduce the degree of carbon deposition and promote the conversions of hydrocarbons (i.e. CH_4 and C_2H_4) presented in the system to CO and H_2. The major consideration in adding these co-fed reactants is the suitable co-fed reactant/C_2H_5OH ratio. The presence of too high oxygen could reduce the yield of H_2 production, while too high hydrogen content could slightly decrease the catalyst activity.

Acknowledgements

The financial support from The Thailand Research Fund (TRF) and National Metal and Materials Technology Center (MTEC) throughout this project is gratefully acknowledged.

References

[1] P. Aguiar, D. Chadwick, L. Kershenbaum, Chem. Eng. Sci. 57 (2002) 1665.
[2] S. Cavallaro, S. Freni, Int. J. Hydrogen Energy 21 (6) (1996) 465.
[3] N.F. Athanasio, X.E. Verykios, J. Catal. 225 (4) (2004) 39.
[4] S. Cavallaro, S. Freni, Int. J. Hydrogen Energy 21 (1996) 465.
[5] S. Cavallaro, Energy Fuels 14 (2000) 1195.
[6] S. Freni, J. Power Sources 94 (2001) 14.
[7] S. Freni, S. Cavallaro, N. Mondello, L. Spadaro, F. Frusteri, J. Power Sources 108 (2002) 53.
[8] A. Fatsikostas, D. Kondarides, X. Verykios, Catal. Today 75 (2002) 145.
[9] D. Liguras, D. Kondarides, X. Verykios, Appl. Catal. B 43 (2003) 345.
[10] V.V. Galvita, V.D. Balyaer, V.A. Semikolenov, P. Tsiakaras, A. Frumin, V.A. Sobyanin, React. Kinet. Catal. Lett. 76 (2002) 343.
[11] J.P. Breen, R. Burch, H.M. Coleman, Appl. Catal. B 39 (2002) 65.
[12] N. Laosiripojana, S. Assabumrungrat, Appl. Catal. A Gen. 290 (2005) 200.
[13] L.V. Mattos, E. Rodino, D.E. Resasco, F.B. Possos, F.B. Noronha, Fuel Process. Technol. 83 (2003) 147.
[14] H.S. Roh, K.W. Jun, S.E. Park, Appl. Catal. A Gen. 251 (2003) 275.
[15] J.R. Rostrup-Nielsen, J.-H. Bak-Hansen, J. Catal. 144 (1993) 38.
[16] X. Wang, R.J. Gorte, Appl. Catal. A Gen. 224 (2002) 209.
[17] A.A. Lemonidou, M.A. Goula, I.A. Vasalos, Catal. Today 46 (1987) 175.
[18] T. Takeguchi, S.N. Furukawa, M. Inoue, J. Catal. 202 (2001) 14.
[19] J. Sfeir, P.A. Philippe, P. Moseki, N. Xanthopoulos, R. Vasquez, J.M. Hans, V.H. Jan, K.R. Thampi, J. Catal. 202 (2001) 229.
[20] N. Laosiripojana, S. Assabumrungrat, Appl. Catal. B 60 (2005) 107.
[21] N. Laosiripojana, W. Sutthisripok, S. Assabumrungrat, Chem. Eng. J. 112 (2005) 13.
[22] N. Laosiripojana, S. Assabumrungrat, Appl. Catal. B 66/(1–2) (2006) 29.
[23] D. Terribile, A. Trovarelli, J. Llorca, C. de Leitenburg, G. Dolcetti, Catal. Today 43 (1998) 79.
[24] C. Force, A. Ruiz Paniego, J.M. Guil, J.M. Gatica, C. Lopez-Cartes, S. Bernal, J. Sanz, Langmuir 17 (2001) 2720.
[25] J. Wei, E. Iglesia, J. Catal. 225 (2004) 116.
[26] E. Ramirez, A. Atkinson, D. Chadwick, Appl. Catal. B 36 (2002) 193.
[27] J. Xu, G.F. Froment, AIChE J. 35 (1989) 88.
[28] J. Xu, G.F. Froment, AIChE J. 35 (1989) 97.

Effect of specific surface area and Zr doping content on oxygen storage capacity (OSC) and methane steam reforming reactivity of CeO_2-ZrO_2

W. Sutthisripok[a], N. Laosiripojana[b] and S. Assabumrungrat[c]

[a] Department of Mining and Materials Engineering,
Faculty of Engineering, Prince of Songkla University, Songkla, Thailand
[b] The Joint Graduate School of Energy and Environment,
King Mongkut's University of Technology Thonburi, Thailand
[c] Center of Excellence in Catalysis and Catalytic Reaction Engineering,
Department of Chemical Engineering, Faculty of Engineering,
Chulalongkorn University, Thailand

This paper investigated the effect of specific surface area and Zr doping content on oxygen storage capacity (OSC) and methane steam reforming reactivity of CeO_2 and Ce-ZrO_2. It was found that the specific surface area of ceria and the doping of Zr present important role on the oxygen storage capacity (OSC) and the reactivity toward methane steam reforming. After calcination at 900°C, ceria prepared by Surfactant-assisted method (SF) was observed from the present work to have significantly higher surface area than those prepared by Templating (TP) and Precipitation (PP) methods; this material showed strong OSC and better reforming reactivity compared to others. In detail, the degree of OSC was measured by the number of hydrogen uptake from the temperature programmed reduction (TPR). It was found that the value of hydrogen uptake from the TPR of ceria prepared by SF was 2084 mmol/g, whereas those of ceria prepared by TP and PP were 1724 and 781 mmol/g, respectively. According to the reactivity toward methane steam reforming, after purging in 3 kPa methane at 900°C for 8h, the methane conversion for ceria prepared by SF was approximately 38%, whereas those of ceria prepared by TP and PP were 22%.

Introduction

Cerium oxide (or ceria) based material is an important catalyst for a variety of reactions involving oxidation of hydrocarbons. It is also being used as a promoter or support in several industrial processes and as a key component in the formulation of catalysts for controlling noxious emissions from transportation section. Ceria have attracted much attention due to their unique redox properties and high oxygen storage capacity (OSC) (1-2). This type of material contains high concentration of mobile oxygen vacancies; this catalyst therefore acts as a local source or sinks for oxygen involved in reactions taking place on its surface or on other catalytic materials supported. It can store oxygen under oxidising conditions and releases that oxygen under reducing conditions in order to continue the oxidation of hydrocarbons.

Ceria-based materials are also applied as catalyst in a wide variety of reactions involving the oxidation, and partial oxidation of hydrocarbons. In addition, this type of catalyst is applied as an automotive catalyst, which is used to oxidise unburnt hydrocarbons, convert CO to CO_2, and reduce NO_x. There is now increasing interest in applying ceria in more reducing conditions such as in methane reforming at the anodes (direct reforming) of Solid Oxide Fuel Cell (SOFC), where the potential for deactivation by carbon formation is much greater. Importantly, this material has been reported to have the reactivity toward the methane steam reforming reaction with excellent resistance toward carbon deposition at such a high temperature (800-1000ºC) (3-4). It has been well established that the gas–solid reaction between CeO_2 and CH_4 produces synthesis gas with H_2/CO ratio of two, according to the following reaction (5):

$$CH_4 + O^{O}_{x} = 2\,H_2 + CO + VO^{\bullet\bullet} + 2\,e' \quad (1)$$

O^{O}_{x} is the lattice oxygen on ceria surface, $VO^{\bullet\bullet}$ denotes as an oxygen vacancy with an effective charge 2^{+}, and e' is an electron which can either be more or less localized on a cerium ion or delocalized in a conduction band. It was also demonstrated that the reactions of the reduced ceria with co-reactants i.e. CO_2 and H_2O produced CO and H_2 and regenerated the CeO_2 surface (6-7):

$$VO^{\bullet\bullet} + 2\,e' + CO_2 = O^{O}_{x} + CO \quad (2)$$
$$VO^{\bullet\bullet} + 2\,e' + H_2O = O^{O}_{x} + H_2 \quad (3)$$

The great benefit of ceria-based catalysts for the cracking and reforming reactions is their high resistance toward carbon deposition compared to the conventional metal catalysts i.e. Ni (3-4); however, the main weaknesses of the materials are their low specific surface area and high deactivation due to the thermal sintering particularly when operated at such a high temperature. The use of high surface area CeO_2 would be a good alternative method to minimize the sintering impact and consequently improve the stability and steady state activity. Recently, Terribile et al. (8) synthesized CeO_2 (HSA) with improved textural, structural and chemical properties for environmental applications by using a surfactant-assisted approach. The materials with good homogeneity and stability especially after thermal treatments were achieved. Apart from the investigation on preparation method, the addition of zirconium oxide (ZrO_2) has also been reported to improve the specific surface area, oxygen storage capacity, redox property, thermal stability and catalytic activity of ceria (9-10). These benefits were associated with enhanced reducibility of cerium (IV) in Ce-ZrO_2, which is a consequence of high O_2^{-} mobility inside the fluorite lattice. The reason for the increasing mobility might be related to the lattice strain, which is generated by the introduction of a smaller isovalent Zr cation into the CeO_2 lattice (Zr^{4+} has a crystal ionic radius of 0.84 Å, which is smaller than 0.97 Å for Ce^{4+} in the same co-ordination environment).

In the present work, CeO_2 and Ce-ZrO_2 were synthesized by several methods i.e. precipitation, templating, and the surfactant-assisted approach. The oxygen storage capacity (OSC) of these synthesized materials was studied in terms of redox properties and redox reversibility. Furthermore, the methane steam reforming reactivity over these synthesized materials was carried out in order to determine the effect of specific surface area and the doping of Zr on the reactivity toward this reaction.

Experimental

Material preparation and characterizations

Conventional CeO_2 (CeO_2 (PP)) was prepared by co-precipitation of cerium nitrate from Aldrich. The starting solution was prepared by mixing 0.1 M of metal salt solutions with 0.4 M of ammonia at a 2 to 1 volumetric ratio. This solution was stirred by magnetic stirring (100 rpm) for 3 h. The precipitate was filtered and washed with deionised water and acetone to remove the free surfactant. It was dried overnight in an oven at 110°C, and then calcined in air at 900°C for 6 h.

CeO_2 was then prepared by the templating, and surfactant-assisted methods (CeO_2 (TP) and CeO_2 (SF), respectively). According to the surfactant-assisted method, an aqueous solution of an appropriate cationic surfactant and 0.1 M cetyltrimethylammonium bromide solution from Aldrich were added to an 0.1 M aqueous solution. The molar ratio of ((Ce))/(cetyltrimethylammonium bromide) was kept constant at 0.8. The mixture was stirred and then aqueous ammonia was slowly added with vigorous stirring. The mixture was continually stirred for 3 h. After that, the mixture was cooled and the resulting precipitate was filtered and washed repeatedly with water and acetone. The filtered powder was dried in the oven at 110°C for one day and then calcined in air at 900°C for 6 h. According to the templating method, the preparation procedures are almost the same as surfactant-assisted method, but cellulose acetate was used as the additive precursor instead of cetyltrimethylammonium bromide.

$Ce_{1-x}Zr_xO_2$ (or Ce-ZrO_2) with different Ce/Zr molar ratios were then prepared by either co-precipitation, templating, or surfactant-assisted methods of cerium nitrate ($Ce(NO_3)_3 \bullet H_2O$), and zirconium oxychloride ($ZrOCl_2 \bullet H_2O$) (from Aldrich). The ratio between each metal salt was altered to achieve nominal Ce/Zr molar ratios: $Ce_{1-x}Zr_xO_2$, where x = 0.25, 0.50, and 0.75 respectively. After preparation, the catalyst specific surface areas were obtained from BET measurement. In addition, as described in the introduction section, the advantage of ceria-based materials is related to its high redox properties, therefore, the degree of oxygen storage capacity (OSC) of all synthesized CeO_2 and Ce-ZrO_2 were determined by the temperature programmed reduction (TPR). Regarding the experiment, 5% H_2/Ar was used, while the temperature of the system increased from room temperature to 900ºC. Finally, the reactivity toward methane steam reforming and the resistance toward carbon formation over selected materials were then carried out.

Experimental Set-up

In order to study the methane steam reforming reaction, the experimental reactor system was set up, as shown in Figure 1. This system consists of three main sections: feed, reaction, and analysis sections. The main obligation of the feed section is to supply the components of interest such as CH_4, and H_2O to the reaction section, where an 8-mm internal diameter and 40-cm length quartz reactor was mounted vertically inside a furnace. The catalyst was loaded in the quartz reactor, which was already packed with a small amount of quartz wool to prevent the catalyst from moving. The residence time was kept constant at 5×10^{-4} g min cm^{-3}. The weight of catalyst loading was 100 mg, while a typical range of total gas flow was 100 cm^3 min^{-1}. The gas mixture was flowed though

the catalyst bed in the quartz reactor. A type-K thermocouple was inserted into the annular space between the reactor and the furnace. The thermocouple was mounted on the reactor in close contact with the catalyst bed to minimize the temperature difference between the catalyst bed and the thermocouple. After the reactions, the exit gas was transferred via trace-heated lines to the analysis section, which consists of a Porapak Q column Shimadzu 14B gas chromatography (GC) and a mass spectrometer (MS). The gas chromatography was applied in order to investigate the steady state condition experiments, whereas the mass spectrometer was used for the carbon formation experiments. In the present work, the outlet of the GC column was directly connected to a thermal conductivity detector (TCD).

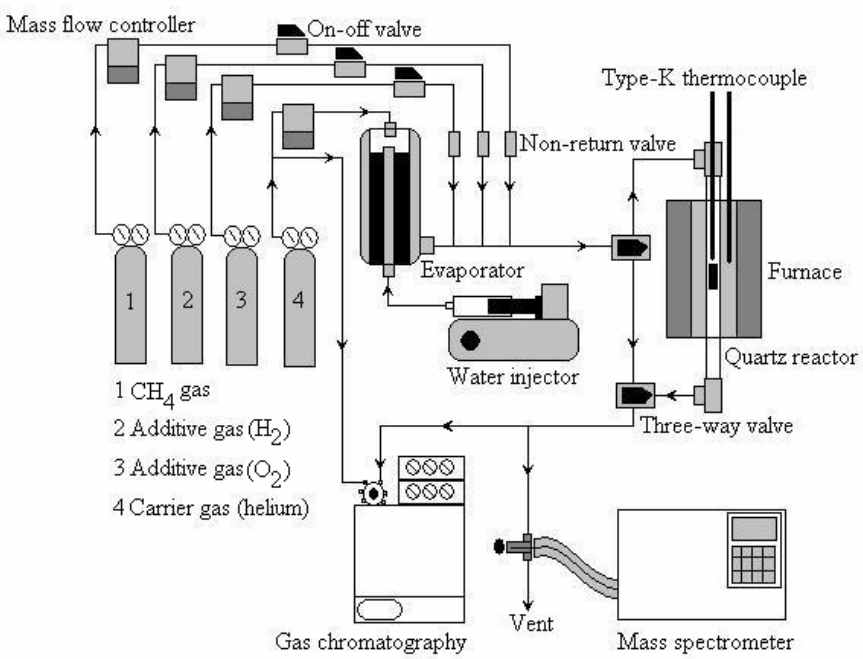

Figure 1 Schematic diagram of the experimental set-up

Results and Discussion

Physicochemical properties of the synthesized catalysts

The BET measurements of CeO_2 (PP, TP, and SF) were carried out before and after the calcinations at different temperatures in order to determine the specific surface area. The values are presented in Table 1. After drying in oven, the specific surface area of CeO_2 prepared by templating and surfactant assisted methods are in the same range and significantly higher than those prepared by precipitation method. As expected, the surface area dramatically decreased at high calcination temperatures particularly those prepared by templating. However, the values for CeO_2 (TP, and SF) are still appreciable after calcination at 900°C. By using the surfactant-assisted method, CeO_2 with surface area of 17.8 m^2 g^{-1} were obtained after calcination at 900°C. They are 3 times higher than CeO_2 (PP). It was also proven by the SEM experiments that the particle size of CeO_2 (SF) is significantly smaller than that of CeO_2 (PP), Figure 2 (a and b).

Table 1 BET surface area of ceria sample prepared by different preparation process.

Catalysts	After drying at 110°C	After calcination at 900°C
	BET ($m^2 g^{-1}$)	BET ($m^2 g^{-1}$)
CeO_2 (PP)	46.3	5.31
CeO_2 (SF)	98.1	17.8
CeO_2 (TP)	95.4	9.12
Ce-ZrO_2 (SF) (Ce/Zr=1/3)	135	49
Ce-ZrO_2 (SF) (Ce/Zr=1/1)	120	47
Ce-ZrO_2 (SF) (Ce/Zr=3/1)	115	46.5
Ce-ZrO_2 (PP) (Ce/Zr=1/3)	82	22
Ce-ZrO_2 (PP) (Ce/Zr=1/1)	74	20.5
Ce-ZrO_2 (PP) (Ce/Zr=3/1)	70	20

PP = Precipitation Method ; SF = Surfactant Assisted Method; TP = Templating Method

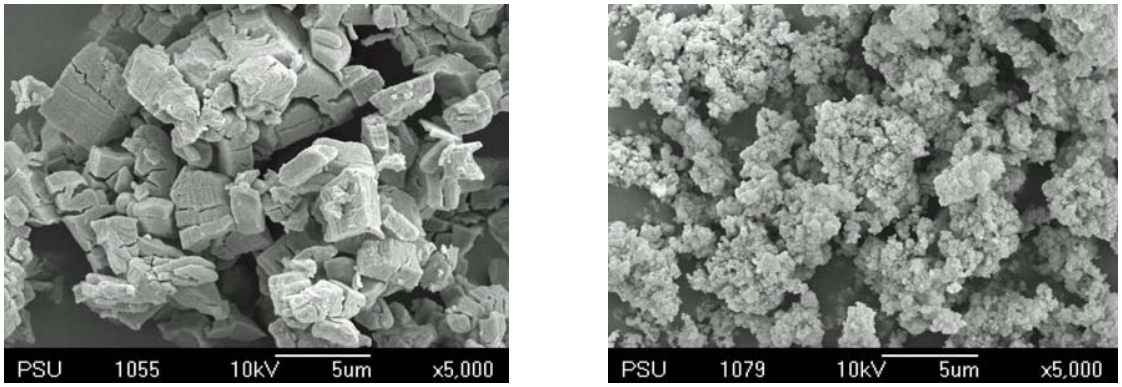

Figure 2 (a) SEM micrograph of CeO_2 (PP) after calcined at 900°C (b) SEM micrograph of CeO_2 (SF) after calcined at 900°C.

Oxygen Storage Capacity (OSC) of the synthesized catalysts

The oxygen storage capacities (OSC) and the degree of redox properties for all ceria-based materials were investigated using temperature programmed reduction (TPR), which was performed by heating the reduced catalysts up to 900°C in 5%H2 in argon. As shown in Figure 3, hydrogen uptakes are detected from CeO_2 at the temperature above 700°C. The amount of hydrogen uptake over CeO_2 (SF) is significantly higher than that over other CeO_2, suggesting the OSC strongly depends on the specific surface area of CeO_2.

The amount of hydrogen uptake is correlated to the amount of oxygen stored in the catalysts. As presented in Table 2, the amount of hydrogen uptakes over Ce-ZrO_2 and CeO_2 (SF) are significantly higher than that observed over other cerias, suggesting the improvement of OSC and redox properties by the doping of Zr and the increasing of catalyst specific surface area. The benefit of OSC on the reforming reaction will be later presented in the next section.

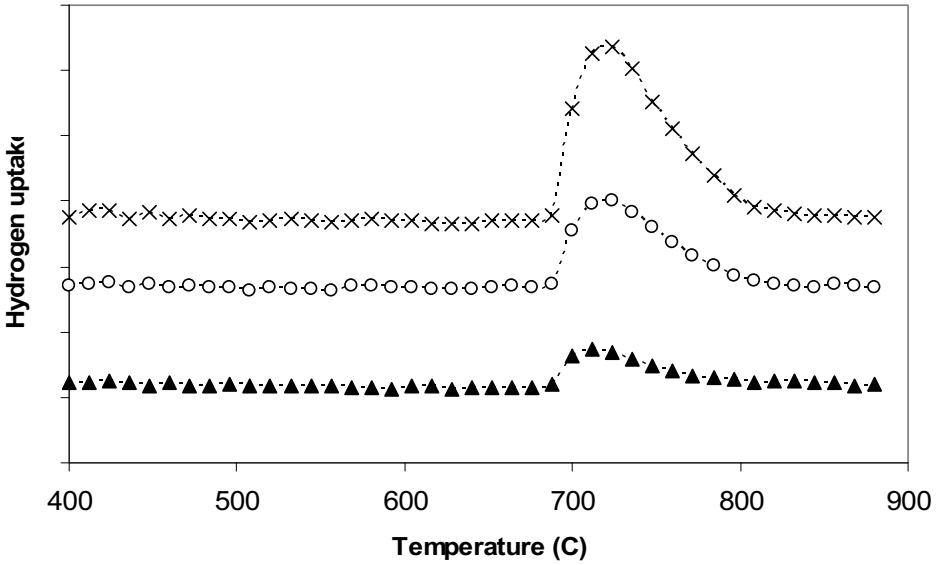

Figure 3 Temperature Programmed Reduction (TPR) of ceria prepared by cationic surfactant assisted method (×), ceria prepared by templating pathway (○), and ceria prepared by precipitation method (▲).

Table 2 Results of TPR of ceria-based materials after calcination.

Catalyst	Total H_2 Uptake from TPR ($\mu mol/g_{cat}$)
CeO_2 (SF)	4105
CeO_2 (PP)	1794
CeO_2 (TP)	1724
Ce-ZrO_2 (SF) (Ce/Zr=1/3)	3701
Ce-ZrO_2 (SF) (Ce/Zr=1/1)	5247
Ce-ZrO_2 (SF) (Ce/Zr=3/1)	1794
Ce-ZrO_2 (PP) (Ce/Zr=1/3)	1097
Ce-ZrO_2 (PP) (Ce/Zr=1/1)	1745
Ce-ZrO_2 (PP) (Ce/Zr=3/1)	2649

Stability and activity toward methane steam reforming

Firstly, the methane steam reforming reactivities over all CeO_2 were tested by introducing CH_4/H_2O in helium with the inlet ratio of 1.0/3.0 at 900°C. The main products from the reactions over these catalysts were H_2 and CO with some CO_2, indicating a contribution from the water-gas shift, and the reverse methanation at this high temperature. The steam reforming rate was measured as a function of time in order to indicate the stability and the deactivation rate. The variations in relative reforming activity with time for different catalysts are shown in Figure 4. At steady state, CeO_2 (SF) presented significant higher reactivity toward the methane steam reforming than CeO_2 (TP), and CeO_2 (PP).

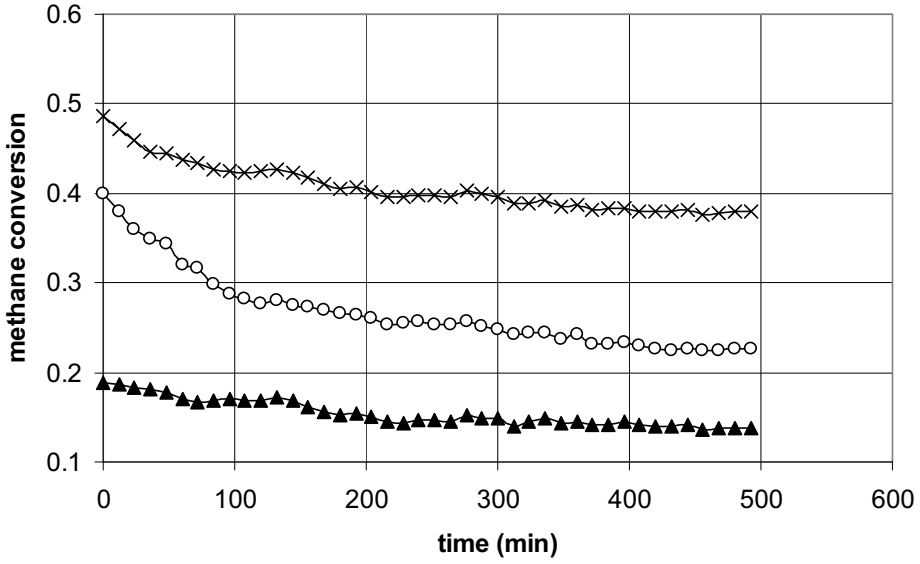

Figure 4 Methane conversion at 900°C of methane steam reforming in He over ceria prepared by cationic surfactant assisted method (×), ceria prepared by templating pathway (○), and ceria prepared by precipitation method (▲).

The steam reforming activities of CeO_2 (TP) and CeO_2 (PP) significantly declined with time before reaching a new steady-state rate at a much lower value, while the activity of CeO_2 (SF) declined slightly. Catalyst stabilities expressed as a deactivation percentage are given in Table 3. In order to investigate the reason of the catalyst deactivation, the post-reaction temperature-programmed oxidation (TPO) experiments were then carried out. TPO experiments detected slight carbon formation on the surface of ceria, particularly CeO_2 (SF), Figure 5.

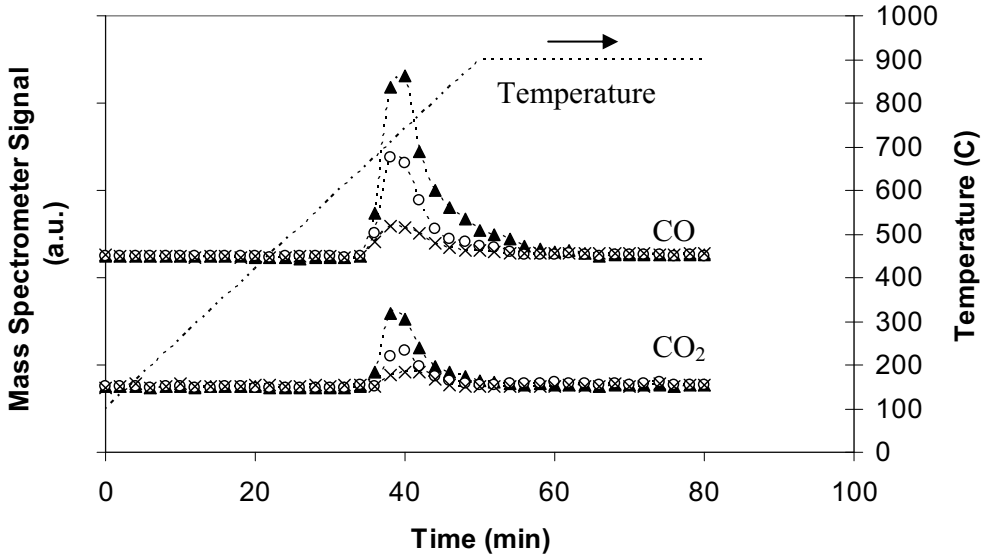

Figure 5 TPO of ceria prepared by cationic surfactant assisted method (×), ceria prepared by templating pathway (○), and ceria prepared by precipitation method (▲).

The methane steam reforming over Ce-ZrO_2 with different Ce/Zr ratios were then tested at the same conditions. The results revealed that Ce-ZrO_2 with Ce/Zr ratio of 3/1 shows the best performance in terms of stability and activity with no carbon deposition observed, according to the TPO experiment, Table 3.

Table 3 CH_4 reaction rate, rate constant and activation energies for CH_4 reactions on ceria-based materials (1048 K, 10 kPa CH_4 balance in He).

Catalysts	Methane conversion (%)	Amount of carbon formation (mmol/g_{cat})
CeO_2 (SF)	39.1	~0
CeO_2 (PP)	13.4	0.21
CeO_2 (TP)	22.3	0.19
Ce-ZrO_2 (SF) (Ce/Zr=1/3)	35.2	0.06
Ce-ZrO_2 (SF) (Ce/Zr=1/1)	49.8	0.08
Ce-ZrO_2 (SF) (Ce/Zr=3/1)	17.1	~0
Ce-ZrO_2 (PP) (Ce/Zr=1/3)	10.6	0.16
Ce-ZrO_2 (PP) (Ce/Zr=1/1)	16.7	0.18
Ce-ZrO_2 (PP) (Ce/Zr=3/1)	25.6	0.14

The good resistance toward carbon deposition for ceria-based materials, which has been widely reported by previous researchers, is mainly due to their sufficient oxygen storage capacity (OSC). It should be noted that we observed high amount of carbon formation on the surface of Ni catalysts after exposure in the same reforming conditions as ceria-based materials. Regarding the possible carbon formation during the reforming processes, the following reactions are theoretically the most probable reactions that could lead to carbon formation:

$$2CO \rightarrow CO_2 + C \quad (4)$$

$$CH_4 \rightarrow 2H_2 + C \quad (5)$$

$$CO + H_2 \rightarrow H_2O + C \quad (6)$$

$$CO_2 + 2H_2 \rightarrow 2H_2O + C \quad (7)$$

At low temperature, reactions (6)–(7) are favorable, while reaction (4) is thermodynamically unflavored (11). The Boudouard reaction (Eq. 4) and the decomposition of CH_4 (Eq. 5) are the major pathways for carbon formation at such a high temperature as they show the largest change in Gibbs energy (12). According to the range of temperature in this study, carbon formation would be formed via the decomposition of CH_4 and Boudouard reactions especially at high inlet CH_4/steam ratio. By applying CeO_2, both reactions (Eqs. 4 and 5) could be inhibited by the redox reaction between the surface carbon (C) forming via the adsorptions of CH_4 and CO (produced during the reforming process) with the lattice oxygen (O^{O}_{x}) at CeO_2 surface (Eq. 8).

$$C + O^{O}_{x} \rightarrow CO + V_O^{\bullet\bullet} + 2\,e' \quad (8)$$

The greater resistance toward carbon deposition for high surface area ceria-based catalyst particularly Ce-ZrO_2 (HSA) is due to the significant higher amount of lattice oxygen (O^{O}_{x}) on their surfaces

Conclusion

The specific surface area of ceria-based materials and the doping of Zr play an important role on the oxygen storage capacity (OSC), the reforming reactivity, and the resistance toward carbon deposition of this material. CeO_2 and Ce-ZrO_2 synthesized by surfactant assisted method was found to be a good candidate catalyst for the steam reforming of methane at such a high temperature (900°C) due to its significant higher steam reforming activity and its excellent resistances toward the thermal sintering and the carbon formation compared to other preparation methods i.e. conventional precipitation and templating methods.

Acknowledgments

The supports from the Thailand Research Fund (TRF) and National Metal and Materials Technology Center (MTEC) are gratefully acknowledged.

References

1. P. Fornasiero, G. Balducci, R.D. Monte, J. Kaspar, V. Sergo, G. Gubitosa, A. Ferrero and M. Graziani. *J. Catal*. **164**, 173 (1996).
2. T. Miki, T. Ogawa, M. Haneda, N. Kakuta, A. Ueno, S. Tateishi, S. Matsuura and M. Sato, *J. Phys. Chem*. **94**, 339 (1990).
3. E. Ramírez-Cabrera, A. Atkinson and D. Chadwick, *Appl. Catal. B* **36**, 193 (2002).
4. E. Ramírez-Cabrera, N. Laosiripojana, A. Atkinson and D. Chadwick, *Catal. Today* **78**, 433 (2003).
5. K. Otsuka, M. Hatano and A. Morikawa, *J. Catal*. **79**, 493 (1983).
6. K. Otsuka, M. Hatano and A. Morikawa, *Inorganica Chimica Acta* **109**, 193 (1985).
7. P.J. Gellings and H.J.M. Bouwmeester, *Catal. Today* **58**, 1 (2000).
8. D. Terribile, A. Trovarelli, J. Llorca, C. Leitenburg and G. Dolcetti, *J. Catal*. **178**, 299 (1998).
9. M. Ozawa, M. Kimura, A. Isogai, *J. Alloys Comp*. **193**, 73 (1993).
10. G. Vlaic, P. Fornasiero, S. Geremia, J. Kaspar, M. Graziani, *J. Catal*. **168**, 386 (1997).
11. Y. Lwin, W.R.W. Daud, A.B. Mohamad and Z. Yaakob, *Int. J. Hydrogen Energy* **25**, 47 (2000).
12. J.N. Amor, *Appl. Catal. A* **176**, 159 (1999).

Steam reforming of ethanol over Ni on high surface area ceria support: Influence of redox properties on the catalyst stability and product selectivities

N. Laosiripojana[a,†], S. Assabumrungrat[b], and S. Charojrochkul[c]

[a] The Joint Graduate School of Energy and Environment,
King Mongkut's University of Technology Thonburi, Thailand
[b] Center of Excellence in Catalysis and Catalytic Reaction Engineering,
Department of Chemical Engineering, Faculty of Engineering,
Chulalongkorn University, Thailand
[c] National Metal and Materials Technology Center (MTEC), Thailand

([†] Corresponding authors: navadol_l@jgsee.kmutt.ac.th)

The steam reforming of ethanol over Ni on high surface area CeO_2 support, synthesized by a surfactant-assisted approach, (Ni/CeO_2 (HSA)) were studied under solid oxide fuel cell (SOFC) operating conditions. The catalyst provides significantly higher reforming reactivity and excellent resistance toward carbon deposition compared to Ni/Al_2O_3 and Ni on conventional ceria (Ni/CeO_2 (LSA)) under the same conditions. At the temperature above 800°C, the main products from the reforming processes over Ni/CeO_2 (HSA) were H_2, CO, and CO_2 with small amount of CH_4 depending on the inlet ethanol/steam ratio, whereas high hydrocarbon compounds i.e., C_2H_4 and C_2H_6 were also observed from the reforming of ethanol over Ni/CeO_2 (LSA) and Ni/Al_2O_3 in the range of conditions studied (700-1000°C). The excellent ethanol reforming performances of Ni/CeO_2 (HSA) in terms of stability, reactivity, and product selectivities are due to the high redox property of CeO_2 (HSA). During the ethanol reforming process, in addition to the reactions on Ni surface, the gas-solid reactions between the gaseous components presented in the system (C_2H_5OH, C_2H_6, C_2H_4, CH_4, CO_2, CO, H_2O, and H_2) and the lattice oxygen (O_x) on ceria surface also take place. Among these redox reactions, the reactions of adsorbed surface hydrocarbons with the lattice oxygen (O_x) can eliminate the formation of high hydrocarbons (C_2H_6 and C_2H_4), which easily decompose and form carbon species on Ni surface.

Introduction

Solid Oxide Fuel Cell (SOFC) is a promising energy conversion unit that produces electrical energy and heat with greater energy efficiency and lower pollutant emission than combustion processes. Hydrogen is a major fuel for SOFC. Nevertheless, the use of other hydrocarbon fuels such as methane, methanol, ethanol, gasoline and other oil derivatives is also possible when operated as an internal or in-stack reforming (IR-SOFC) (1). Regarding the global environmental problems and current fossil fuel crisis, the

development of IR-SOFC fed by biomass or renewable based fuels attracts more attention to be an alternative method for power generation in the near future. Among renewable sources, bio-ethanol is a promising candidate, since it is readily produced by fermentation of biomasses and has reasonably high hydrogen content, in addition, ethanol is also safe to handle, transport and store (2,3).

Previously, steam reforming of ethanol has been studied by several researchers, most of them have investigated the reforming of ethanol over noble metal catalysts (e.g. Rh, Ru, Pt, Pd) on several oxide supports (e.g. Al_2O_3, MgO, SiO_2, TiO_2) (4-7). In this work, it is aimed at the development of an alternative catalyst for both steam and autothermal reforming of ethanol, which provided high stability and activity toward this reaction at such a high temperature (700-1000°C) for later application in IR-SOFC. According to the economical point of view, Ni was selected as a catalyst rather than other precious metals such as Pt, Rh and Ru. Although the precious metals have been reported to be active for the reforming reactions and resistant to the carbon formation than Ni, the current prices of these metals are very high for commercial uses, and the availability of some precious metals such as ruthenium was too low to have a major impact on the total reforming catalyst market. Selection of a support material is the major consideration of this work. CeO_2 was chosen as catalyst support over Ni in this work. This material (called ceria) is an important material for a variety of catalytic reactions involving oxidation of hydrocarbons (e.g. automobile exhaust catalysts). It contains a high concentration of highly mobile oxygen vacancies, which act as local sources or sinks for oxygen involved in reactions taking place on its surface. Recently, the high resistance toward carbon deposition over ceria has been reported (8-10). However, the major considerations of applying CeO_2 in the high temperature steam reforming reaction are their low specific surface and their high surface area reduction percentage due to the high surface sintering. The use of high surface area (HSA) ceria-based materials as the catalyst support would be a good alternative procedure to improve the reforming performance. Several methods have recently been described for the preparation of high surface area CeO_2. Among these methods, the surfactant-assisted approach was reported to provide CeO_2 (HSA) with improved textural, structural, and chemical properties (11). Our previous publication (7) also presented the achievement of CeO_2 with high surface area and good stability after thermal treatment by this preparation method.

In the present work, the stability and activity toward the steam reforming of ethanol over Ni on high surface area CeO_2 support (Ni/CeO_2 (HSA)) was studied and compared to Ni on conventional low surface area CeO_2 support (Ni/CeO_2 (LSA)), and Ni/Al_2O_3. The resistance toward carbon formation and the influence of temperature on the product selectivities over these catalysts were studied.

Experimental

Material preparation and characterizations

Conventional CeO_2 support (CeO_2 (LSA)) was prepared by the precipitation method. The mixture of 0.1 M cerium nitrate ($Ce(NO_3)_3 \cdot H_2O$) (from Aldrich) and 0.4 M of urea at a 2 to 1 volumetric ratio was prepared and stirred by magnetic stirring (100 rpm) for 3 h. The precipitate was filtered and washed with deionised water and ethanol to prevent an

agglomeration of the particles. It was dried overnight in an oven at 110°C, and then calcined in air at 1000°C for 6 h.

High surface area CeO_2 support (CeO_2 (HSA)) was prepared by adding an aqueous solution of the appropriate cationic surfactant, 0.1 M cetyltrimethylammonium bromide solution from Aldrich, to a 0.1 M cerium chloride. The molar ratio of ((Ce))/(cetyltrimethylammonium bromide) was kept constant at 0.8. The mixture was stirred and then aqueous ammonia was slowly added with vigorous stirring until the pH was 11.5 (48). The mixture was continually stirred for 3 h, then sealed and placed in the thermostatic bath maintained at 90°C for 3 days. After that, the mixture was cooled and the resulting precipitate was filtered and washed repeatedly with water and acetone. The filtered powder was then treated under the same procedures as CeO_2 (LSA). BET measurements of CeO_2 (both LSA and HSA) were carried out at different calcinations temperatures in order to determine the decreasing in specific surface area due to the thermal sintering. As presented in Table 1, after drying, surface areas of 105 and 55 $m^2 g^{-1}$ were observed for CeO_2 (HSA) and conventional CeO_2, respectively and, as expected, the surface area dramatically decreased at high calcination temperatures. However, the value for CeO_2 (HSA) is still appreciable after calcination at 1000°C and it is almost 3 times of that for the conventional CeO_2.

Table 1 Specific surface area of CeO_2 (HSA and LSA) after drying and calcinations at different temperatures

Catalyst	BET surface area ($m^2 g^{-1}$) after drying or calcination at						
				600ºC	800ºC	900ºC	1000ºC
CeO_2 (LSA.)[a]	55	49	36	21	15	11	8.5
CeO_2 (HSA)[b]	105	97	69	48	35	29	24

[a] conventional low surface area CeO_2 prepared by the precipitation method
[b] high surface area CeO_2 prepared by the surfactant-assisted approach

Ni/CeO_2 was then prepared by impregnating CeO_2 (both LSA and HSA) with a $Ni(NO_3)_2$ solution (from Aldrich). The catalyst was reduced with 10%H_2/Ar at 500ºC for 6 h before use. For comparison, conventional Ni/Al_2O_3 was also prepared by impregnating α-Al_2O_3 (from Aldrich) with $Ni(NO_3)_2$. After reduction, the catalyst was characterized by several physicochemical methods. The weight contents of Ni in Ni/Al_2O_3 and Ni/CeO_2 were determined by X-ray fluorescence (XRF) analysis. The reducibility and dispersion percentages of nickel were measured from temperature-programmed reduction (TPR) with 5% H_2 in Ar and temperature-programmed desorption (TPD) respectively. The catalyst specific surface areas were obtained from BET measurement.

Apparatus and Procedures

An experimental reactor system was constructed. The feed gases including the components of interest (ethanol and steam) and the carrier gas (helium) were introduced to the reaction section, in which either a quartz reactor was mounted vertically inside a

furnace. A Type-K thermocouple was placed into the annular space between the reactor and the furnace, while another Type-K thermocouple was inserted in the middle of the quartz tube in order to re-check the possible temperature gradient. The record showed that the maximum temperature fluctuation during the reaction was always ± 0.75°C or less from the temperature specified for the reaction. After the reactions, the exit gas mixture was transferred via trace-heated lines to the analysis section, which consisted of gas chromatograph (GC) and mass spectrometer (MS).

In order to study the steam reforming reactivity, the rate of ethanol reforming was defined in terms of conversion denoted as X_{Ethanol}, and product selectivities denoted as S_{product}. Selectivities of products (i.e. CO, CO_2, CH_4, C_2H_6, C_2H_4, and C_2H_4O) were calculated by the carbon balance, defined as the ratios of the product moles to the consumed moles of hydrocarbon, accounting for stoichiometry. This information was presented in term of (relative) fraction of all by-product components, which are summed to 100%. H_2 selectivity was calculated by the H_2 balance, defined as the mole of H_2 produced to the total H_2 in the products.

$$X_{Ethanol} = \frac{100(\%Ethanol_{in} - \%Ethanol_{out})}{\%Ethanol_{in}} \quad (1)$$

$$S_{\text{Pr}oduct} = \frac{100(\text{Mole of a specific product})}{(\text{Total moles of all products})} \quad (2)$$

Temperature programmed Oxidation (TPO) was applied to study the formation of carbon species on catalyst surface by introducing 10% O_2 in helium, after purging the system with helium. The operating temperature increased from 100 to 1000ºC at a rate of 20ºC min^{-1}. The amounts of carbon formation (mmol g_{cat}^{-1}) on the surface of catalysts were determined by measuring the CO and CO_2 yields from the TPO results.

Results and Discussion

Homogenous (non catalytic) reaction

Before studying performances of the catalysts, homogeneous (non-catalytic) steam reforming and autothermal reforming of ethanol were primary investigated. Regarding the steam reforming testing, inlet C_2H_5OH/H_2O in helium with the molar ratio of 1.0/3.0 was introduced to the system, while the temperature increased from 100ºC to 950ºC. As shown in Figure 1, it was observed that ethanol was converted to acetaldehyde, and hydrogen at the temperature above 200°C. Methane and carbon monoxide productions were initially observed at the temperature around 250-300°C. The selectivity of acetaldehyde significantly dropped at the temperature of 550°C and approached zero at the temperature of 650°C. In this range of temperature, the formations of ethane and ethylene were observed. The selectivities of carbon monoxide, carbon dioxide, methane, ethane and ethylene remained almost constant at temperatures higher than 650°C.

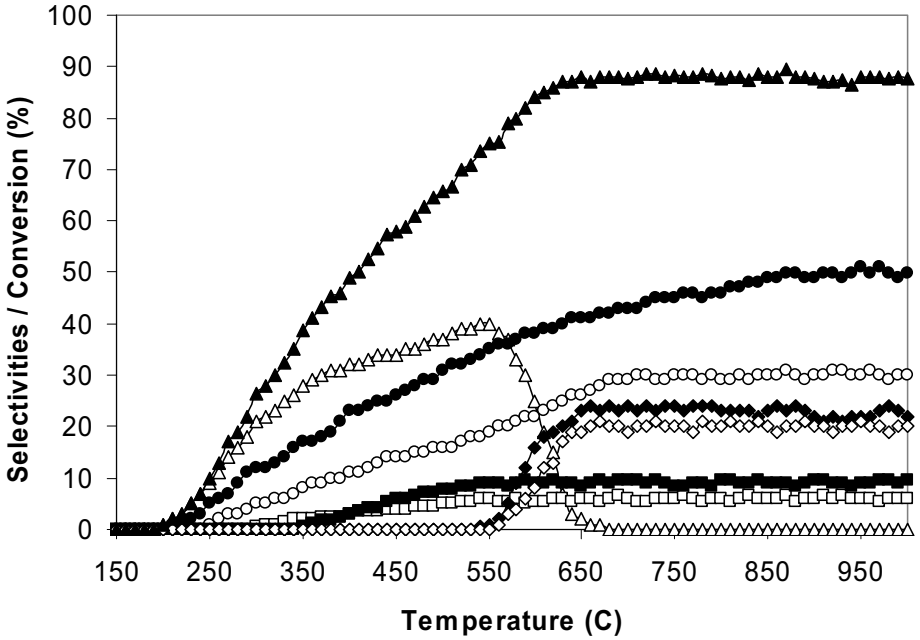

Figure 1 Homogenous (in the absence of catalyst) reactivity of ethanol steam reforming (4 kPa C_2H_5OH, and 12 kPa H_2O) (EtOH (▲), H_2 (●), CO (○), CO_2 (■), CH_4 (□), CH_3CHO (△), C_2H_6 (◇), and C_2H_4 (◆)).

Steam reforming of Ethanol over several catalysts

The steam reforming of ethanol over Ni/CeO_2 (both LSA and HSA) and conventional Ni/Al_2O_3 were studied at 900°C. The feed was C_2H_5OH/H_2O in helium with the molar ratios of 1.0/1.0, 1.0/2.0, and 1.0/3.0. The variations in hydrogen selectivities (%) with time at 900°C for different catalysts and different inlet C_2H_5OH/H_2O ratio are shown in Figure 2. After 10 h operation, the hydrogen selectivities of Ni/CeO_2 (HSA) were significantly higher than those of Ni/CeO_2 (LSA) and Ni/Al_2O_3 in all conditions. However, the deactivations were also observed in all catalysts.

The post-reaction temperature-programmed oxidation (TPO) experiments were then carried out after a helium purge by introducing 10% oxygen in helium in order to determine whether the observed deactivation is due to the carbon formation. From the TPO results shown in Figure 3, small peaks of carbon dioxide and carbon monoxide were observed for Ni/CeO_2 (HSA) and Ni/CeO_2 (LSA), whereas huge amount of carbon dioxide and carbon monoxide formations were detected for Ni/Al_2O_3. The amount of carbon formations can be determined by measuring the CO and CO_2 yields from these TPO results. Using a value of 0.026 nm^2 for the area occupied by a carbon atom in a surface monolayer of the basal plane in graphite, the quantities of carbon deposited over Ni/CeO_2 (HSA), Ni/CeO_2 (LSA), and Ni/Al_2O_3 were observed to be approximately 1.08, 2.17, and 4.52 monolayers, respectively, for the inlet C_2H_5OH/H_2O ratio of 1.0/3.0. It should be noted that the degree of carbon formation was found to decrease with increasing inlet H_2O concentration. Regarding the TPO, the results clearly indicated the highest resistance toward carbon formation for Ni/CeO_2 (HSA).

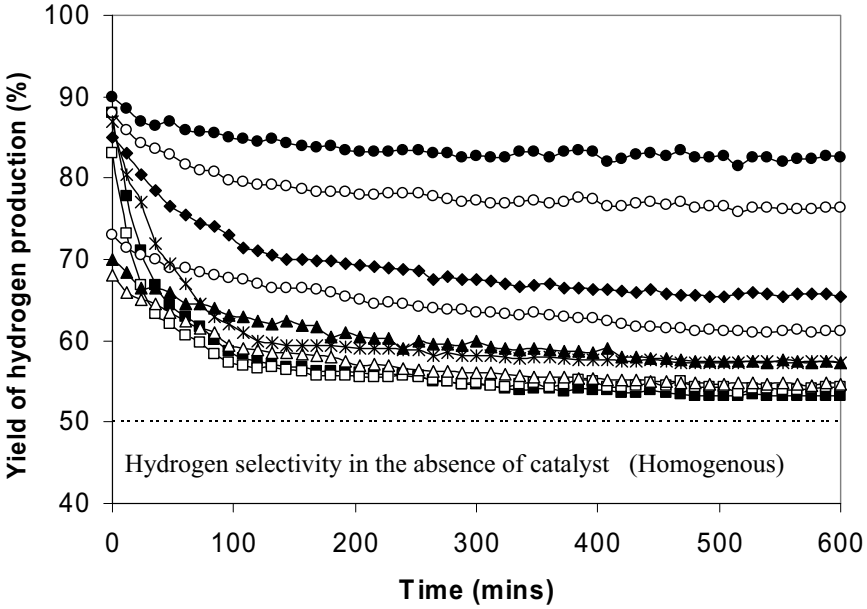

Figure 2 Steam reforming of ethanol at 900°C (Ni/CeO_2 (HSA) with 1/3 of $EtOH/H_2O$ (●), Ni/CeO_2 (HSA) with 1/2 of $EtOH/H_2O$ (○),Ni/CeO_2 (HSA) with 1/1 of $EtOH/H_2O$ (◆), Ni/CeO_2 (LSA) with 1/3 of $EtOH/H_2O$ (◇), Ni/CeO_2 (LSA) with 1/2 of $EtOH/H_2O$ (▲), Ni/CeO_2 (LSA) with 1/1 of $EtOH/H_2O$ (△),Ni/Al_2O_3 with 1/3 of $EtOH/H_2O$ (×), Ni/Al_2O_3 with 1/2 of $EtOH/H_2O$ (□), and Ni/Al_2O_3 with 1/1 of $EtOH/H_2O$ (■).

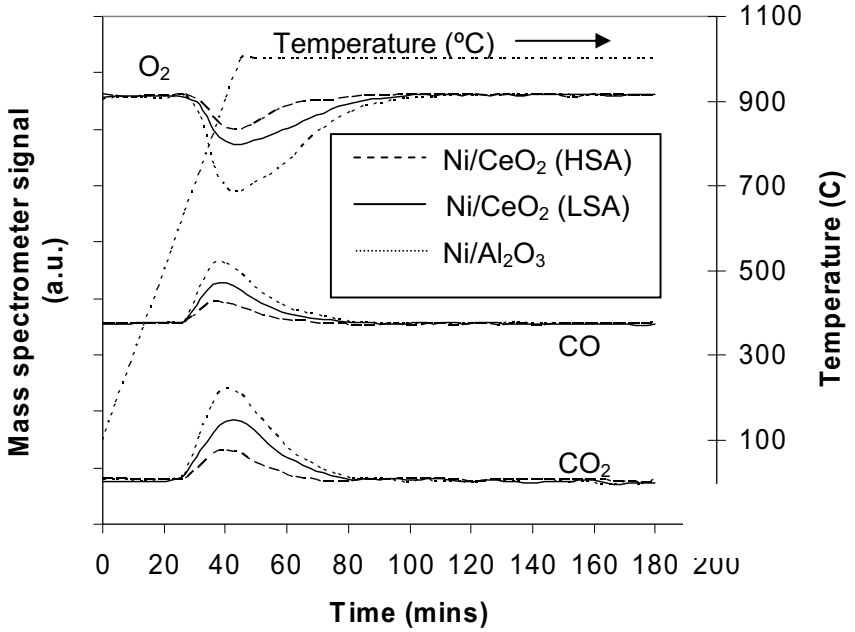

Figure 3 Temperature Programmed Oxidation (TPO) of Ni/CeO_2 (HSA), Ni/CeO_2 (LSA), and Ni/Al_2O_3 after exposure in steam reforming of ethanol

The influence of operating temperature on the product selectivities over Ni/CeO_2 (HSA), Ni/CeO_2 (LSA), and Ni/Al_2O_3 at different inlet C_2H_5OH/H_2O molar ratios were further studied by varying temperature from 700°C to 1000°C. As shown in Figure 4, it

was found that, the main products from the ethanol steam reforming over Ni/CeO_2 (HSA) were H_2, CO, CO_2, and CH_4, with small amounts of C_2H_4 and C_2H_6 depending on the operating temperature. In contrast, significant amounts of C_2H_4 and C_2H_6 were also observed as well as other chemical components from the ethanol steam reforming over Ni/CeO_2 (LSA) and Ni/Al_2O_3 in the range of conditions studied. Consequently, less H_2, CO, and CO_2 selectivities were achieved over these catalysts.

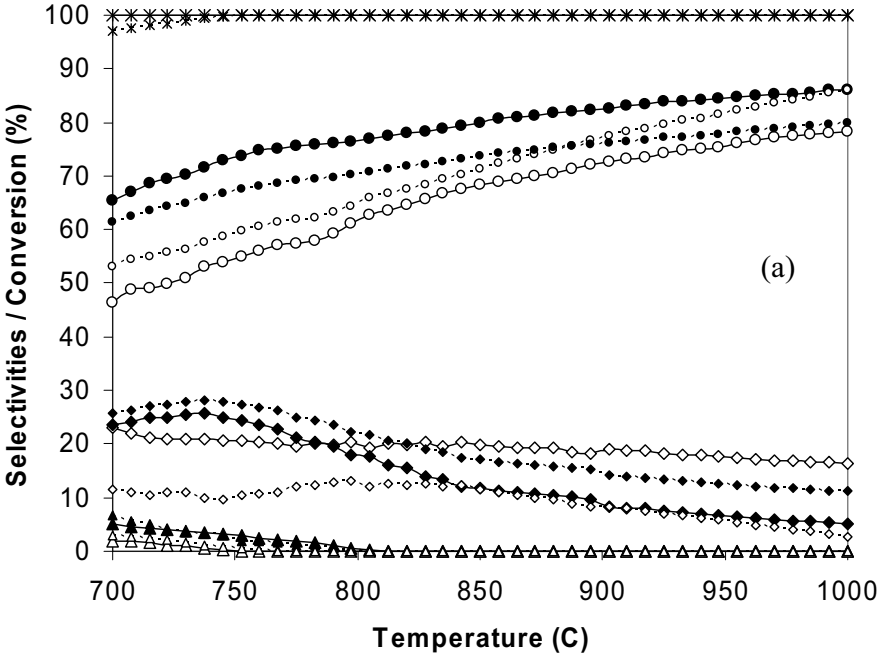

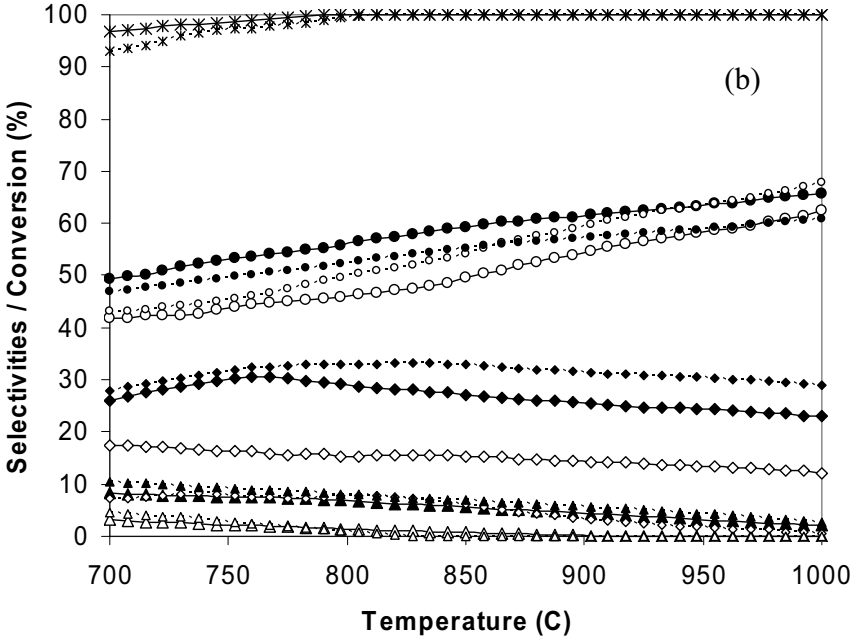

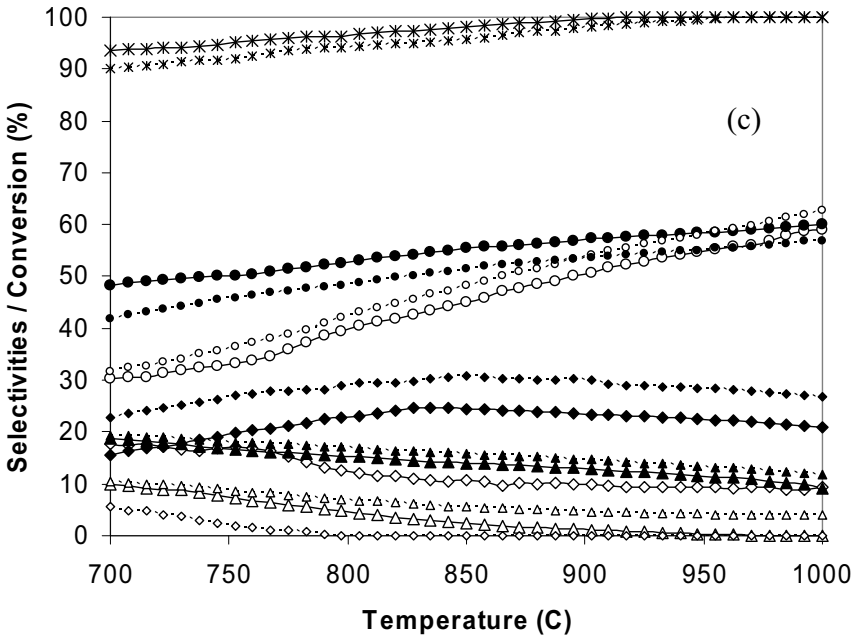

Figure 4 Effect of temperature on the conversion and product selectivities (EtOH (×), H_2 (●), CO (○), CO_2 (◇), CH_4 (◆), C_2H_6 (△), and C_2H_4 (▲)) from ethanol steam reforming over Ni/CeO_2 (HSA) (a), Ni/CeO_2 (LSA) (b), and Ni/Al_2O_3 (c) with inlet EtOH/H_2O ratios of 1/3 (large symbols with solid lines) and 1/2 (small symbols with dot lines).

It can be concluded that Ni/CeO_2 (HSA) was found in this study to be a promising catalyst for the steam reforming of ethanol. This catalyst provided excellent resistance toward carbon deposition compared to conventional Ni/CeO_2 (LSA) and Ni/Al_2O_3. At the temperature higher than 800ºC, the main products from the reforming of ethanol over Ni/CeO_2 (HSA) were H_2, CO, CO_2, and small amount of CH_4; neither C_2H_4 nor C_2H_6 was observed from the system over this catalyst. In contrast, the steam reforming of ethanol over Ni/CeO_2 (LSA) and Ni/Al_2O_3 formed significant amounts of C_2H_4 and C_2H_6, in addition, high amount of carbon deposition was also observed over these catalysts. The high resistance toward carbon deposition for CeO_2 especially high surface area CeO_2 was reported in our previous publications and is mainly due to the high oxygen storage capacity (OSC) of this material. CeO_2 contains a high concentration of highly mobile oxygen vacancies and thus acts as a local source or sink for oxygen on its surface. It has been reported that at high temperature the lattice oxygen (O_x) at the CeO_2 surface can oxidize gaseous hydrocarbons (methane, ethane, and propane). Although conventional CeO_2 (CeO_2 (LSA)) has also been reported to provide high resistance toward carbon formation, the major weaknesses of CeO_2 (LSA) are its low specific surface area and also high size reduction due to the thermal sintering impact, resulting in its significant lower redox properties than CeO_2 (HSA), and its lower Ni dispersion percentage on the surface compared to Ni/CeO_2 (HSA) and Ni/Al_2O_3. These disadvantages result in the low ethanol steam reforming reactivity for Ni/CeO_2 (LSA). By using Ni/CeO_2 (HSA) as the catalyst, in addition to the reaction on Ni surface, ethane and ethylene formations and the possible carbon depositions from these hydrocarbons could be inhibited by the gas-solid reactions between these hydrocarbons and the lattice oxygen (O_x) at CeO_2 surface forming hydrogen and carbon dioxide, which are thermodynamically unflavored to form carbon species, as illustrated schematically below.

$C_2H_6 + 2S \Leftrightarrow 2(CH_3\text{-}S)$ (1)

$C_2H_4 + 2S \Leftrightarrow 2(CH_2\text{-}S)$ (2)

$CH_4 + 2S \Leftrightarrow CH_3\text{-}S + H\text{-}S$ (3)

$CH_3\text{-}S + S \Leftrightarrow CH_2\text{-}S + H\text{-}S$ (4)

$CH_2\text{-}S + S \Leftrightarrow CH\text{-}S + H\text{-}S$ (5)

$CH\text{-}S + S \Leftrightarrow C\text{-}S + H\text{-}S$ (6)

$C\text{-}S + O_x \Leftrightarrow CO + O_{x-1} + S$ (7)

$2H\text{-}S \Leftrightarrow H_2 + 2S$ (8)

S is the catalyst surface site and CH_x-S is an intermediate surface hydrocarbon species. During the steam reforming, the lattice oxygen is regenerated by reaction with oxygen containing compounds (steam) present in the system.

Conclusion

Ni on high surface area CeO_2 support (Ni/CeO_2 (HSA)) provides excellent reactivity toward the steam and autothermal reforming of ethanol with high resistance toward carbon deposition and better product selectivities compared to Ni/Al_2O_3 and Ni on conventional low surface area ceria (Ni/CeO_2 (LSA)). The main products from these reforming processes over Ni/CeO_2 (HSA) were H_2, CO, and CO_2 with small amount of CH_4, whereas the formations of C_2H_4 and C_2H_6 were also observed together with the above gas components from the reactions over Ni/CeO_2 (LSA) and Ni/Al_2O_3 in the range of conditions studied. The great benefits of Ni/CeO_2 (HSA) in terms of stability and reactivity toward ethanol reforming, high resistance toward carbon deposition, and good product selectivities are due to the high redox property of CeO_2 (HSA).

Acknowledgments

The supports from the Thailand Research Fund (TRF) and National Metal and Materials Technology Center (MTEC) are gratefully acknowledged.

References

1. P. Aguiar, D. Chadwick and L. Kershenbaum, *Chem. Eng. Sci*. **57**, 1665 (2002).
2. S. Cavallaro, S. Freni, *Int. J. Hydrogen Energy* **21**, 465 (1996).
3. N.F. Athanasio, X.E. Verykios, *J. Catal*. **225**, 39 (2004).
4. S. Cavallaro and S. Freni. *Int. J. Hydrogen Energy* **21**, 465 (1996).
5. S. Cavallaro. *Energy and Fuels* **14**, 1195 (2000).
6. S. Freni. *J. Power Sour*. **94**, 14 (2001).
7. S. Freni, S. Cavallaro, N. Mondello, L. Spadaro, F. Frusteri. *J. Power Sour*. **108**, 53 (2002).
8. N. Laosiripojana and S. Assabumrungrat, *Appl. Catal. B: Environ*. **60**, 107 (2005).
9. N. Laosiripojana, W. Sutthisripok, and S. Assabumrungrat, *Chem. Eng. J.* **112**, 13 (2005).
10. N. Laosiripojana, W. Sangtongkitcharoen, and S. Assabumrungrat, *Fuel* **85**, 323 (2006).
11. D. Terribile, A. Trovarelli, J. Llorca, C. de Leitenburg and G. Dolcetti, *Catal. Today* **43**, 88 (1998).

ELSEVIER

Chemical Engineering Journal 138 (2008) 264–273

Chemical Engineering Journal

www.elsevier.com/locate/cej

Effect of high surface area CeO_2 and Ce-ZrO_2 supports over Ni catalyst on CH_4 reforming with H_2O in the presence of O_2, H_2, and CO_2

N. Laosiripojana [a,*], D. Chadwick [b], S. Assabumrungrat [c]

[a] *The Joint Graduate School of Energy and Environment, King Mongkut's University of Technology Thonburi, Bangkok 10140, Thailand*
[b] *Department of Chemical Engineering, Imperial College London SW7 2AZ, UK*
[c] *Center of Excellence on Catalysis and Catalytic Reaction Engineering, Department of Chemical Engineering, Chulalongkorn University, Bangkok 10330, Thailand*

Received 31 January 2007; received in revised form 9 May 2007; accepted 17 May 2007

Abstract

Methane steam reforming over Ni on high surface area (HSA) CeO_2 and Ce-ZrO_2 supports, synthesized by surfactant-assisted method, was studied and compared to conventional Ni/CeO_2, Ni/Ce-ZrO_2, and Ni/Al_2O_3. It was firstly observed that Ni/Ce-ZrO_2 (HSA) with the Ce/Zr ratio of 3/1 showed the best performance in terms of activity and stability. This catalyst presented considerably better resistance toward carbon formation than conventional Ni/CeO_2, Ni/Ce-ZrO_2, and Ni/Al_2O_3; and the minimum inlet H_2O/CH_4 ratio requirement to operate without the detectable of carbon are significantly lower. These benefits are related to the high oxygen storage capacity (OSC) of high surface area Ce-ZrO_2 support. During the reforming process, in addition to the reactions on Ni surface, the redox reactions between the absorbed CH_4 and the lattice oxygen (O_x) on CeO_2 and Ce-ZrO_2 surface also take place, which effectively prevent the formation of carbon on the surface of Ni.

The effects of possible inlet co-reactant, i.e. H_2O, H_2, CO_2, and O_2 on the conversion of CH_4 were also studied. It was found that H_2 presented positive effect on the CH_4 conversion when small amount of H_2 was introduced; nevertheless, this positive effect became less pronounced and eventually inhibited the conversion of CH_4 at high inlet H_2 concentration particularly for Ni/CeO_2 (HSA) and Ni/Ce-ZrO_2 (HSA). The dependence of H_2O on the rate was non-monotonic due to the competition of the active sites, as have also been presented by Xu [1], Xu and Froment [2,3], Elnashaie et al. [4] and Elnashaie and Elshishini [5]. Addition of CO_2 inhibited the reforming rate, whereas addition of O_2 promoted the CH_4 conversion but reduced both CO and H_2 productions.

Keywords: Methane steam reforming; Carbon formation; CeO_2; Ce-ZrO_2

1. Introduction

Methane steam reforming is a widely practiced technology to produce hydrogen or synthesis gas for utilization in chemical processes and solid oxide fuel cells (SOFCs). Three main reactions take place as in the following equations.

$$CH_4 + H_2O = CO + 3H_2 \quad (1)$$

$$CO + H_2O = CO_2 + H_2 \quad (2)$$

$$CH_4 + 2H_2O = CO_2 + 4H_2 \quad (3)$$

Both the water-gas shift reaction (Eq. (2)) and reverse methanation (Eq. (3)) are always associated with catalytic steam reforming at elevated temperatures. Due to their overall high endothermic nature, these reactions are carried out at high-temperature (700–900 °C) to achieve high conversions.

Commercial catalysts for the methane steam reforming reaction are nickel on supports, such as Al_2O_3, MgO, $MgAl_2O_4$ or their mixtures. Selection of a support material is an important issue as it has been evident that metal catalysts are not very active for the steam reforming when supported on inert oxides [6]. Various support materials have been tested, for example, α-Al_2O_3 [7], γ-Al_2O_3 and γ-Al_2O_3 with alkali metal oxide and rare earth metal oxide [8], $CaAl_2O_4$ [9] and Ce-ZrO_2 [10]. A promising catalyst system for the reforming reactions appears to be a metal on Ce-ZrO_2 support, where the metal can be Ni, Pt or Pd [11–19]. Ni/Ce-ZrO_2 has also been successfully applied to partial oxidation and autothermal reforming of methane [20].

It is well-established that cerium oxide (CeO_2) and ceria-zirconia (Ce-ZrO_2) are useful in a wide variety of applications

* Corresponding author.
E-mail address: navadol_l@jgsee.kmutt.ac.th (N. Laosiripojana).

1385-8947/$ – see front matter © 2007 Elsevier B.V. All rights reserved.
doi:10.1016/j.cej.2007.05.035

involving oxidation or partial oxidation of hydrocarbons (e.g. automotive catalysis) and as components of anodes for SOFCs. This material has high oxygen storage capacity, which is beneficial in oxidation processes and carbon combustion. The excellent resistance toward carbon formation from methane cracking reaction over CeO_2 compared to commercial Ni/Al_2O_3 was also reported recently [21]. The addition of zirconium oxide (ZrO_2) to cerium oxide (CeO_2) has been found to improve the oxygen storage capacity, redox property, thermal stability, and catalytic activity [22–31]. Nevertheless, the major limitations for applying CeO_2 and to a lesser extent Ce-ZrO_2 in high-temperature steam reforming are their low specific surface and surface area reduction due to sintering [21]. Therefore, the use of high surface area (HSA) ceria-based materials as the catalyst support would be a good alternative to improve the methane steam reforming performance. Several methods have been described recently for the preparation of high surface area (HSA) CeO_2 and Ce-ZrO_2 solid solutions. Most interest is focused on the preparation of transition-metal oxides using templating pathways [32–34]. However, only a few of these composites showed a regular pore structure after calcination [35–37]. A surfactant-assisted approach was employed to prepare high surface area CeO_2 and Ce-ZrO_2 with improved textural, structural and chemical properties for environmental applications [38]. They were prepared by reacting a cationic surfactant with a hydrous mixed oxide produced by co-precipitation under basic conditions. By this preparation procedure, materials with good homogeneity and stability especially after thermal treatments were achieved.

In the present work, high surface area (HSA) CeO_2 and Ce-ZrO_2 were synthesized by the surfactant-assisted approach. Ni was selected as a metal catalyst and impregnated on these high surface area CeO_2 and Ce-ZrO_2. It should be noted that, for Ni/Ce-ZrO_2, different ratios of Ce/Zr were firstly investigated to determine a suitable composition ratio. The stability and activity of Ni on high surface area CeO_2 and Ce-ZrO_2 were then studied and compared to Ni on low surface area CeO_2 and Ce-ZrO_2, and also conventional Ni/Al_2O_3. Furthermore, the resistance toward carbon formation and the influences of possible inlet co-reactant, i.e. H_2, H_2O, CO_2, and O_2 (as oxidative steam reforming) on the methane steam reforming over these catalysts were determined by adding and varying the partial pressures of these components at the inlet feed, as these are important issues in the industrial applications.

2. Experimental

2.1. Material preparation and characterization

Conventional Ce-ZrO_2 supports (Ce-ZrO_2 (LSA)) with different Ce/Zr molar ratios were prepared by co-precipitation of cerium chloride ($CeCl_3{\cdot}7H_2O$), and zirconium oxychloride ($ZrOCl_2{\cdot}8H_2O$) from Aldrich. The starting solution was prepared by mixing 0.1 M of metal salt solutions with 0.4 M of ammonia at a 2 to 1 volumetric ratio. This solution was stirred by magnetic stirring (100 rpm) for 3 h, then sealed and placed in a thermostatic bath maintained at 90 °C. The ratio between each metal salt was altered to achieve nominal Ce/Zr molar ratios of 1/3, 1/1 and 3/1. The precipitate was filtered and washed with deionised water and acetone to remove the free surfactant. It was dried overnight in an oven at 110 °C, and then calcined in air at 1000 °C for 6 h.

High surface area (HSA) Ce-ZrO_2 supports were prepared by the surfactant-assisted method [38]. An aqueous solution of an appropriate cationic surfactant and 0.1 M cetyltrimethylammonium bromide solution from Aldrich were added to an 0.1 M aqueous solution containing $CeCl_3{\cdot}7H_2O$ and $ZrOCl_2{\cdot}8H_2O$ in a desired molar ratio. The molar ratio of ([Ce] + [Zr])/[cetyltrimethylammonium bromide] was kept constant at 0.8. The mixture was stirred and then aqueous ammonia was slowly added with vigorous stirring. The mixture was continually stirred for 3 h, then sealed and placed in the thermostatic bath maintained at 90 °C. After that, the mixture was cooled and the resulting precipitate was filtered and washed repeatedly with water and acetone. The filtered powder was dried in the oven at 110 °C for 1 day and then calcined in air at 1000 °C for 6 h. Similarly, CeO_2 (LSA and HSA) were prepared using the same procedures as Ce-ZrO_2, but without the addition of $ZrOCl_2{\cdot}8H_2O$.

Ni/Ce-ZrO_2, Ni/CeO_2 and Ni/Al_2O_3 with 5 wt.% Ni were prepared by impregnating the respective supports with $NiCl_3$ solution at room temperature. These solutions were stirred by magnetic stirring (100 rpm) for 6 h. The solution was dried overnight in the oven at 110 °C, calcined in air at 1000 °C and reduced with 10%H_2 for 6 h. The BET measurements of all synthesized Ni/CeO_2 and Ni/Ce-ZrO_2 were then carried out in order to determine the specific surface area. These values as well as the observed pore volume and pore size of the catalysts are presented in Table 1. It can be seen that the introduction of

Table 1
Specific surface areas, pore volume, and pore size of catalysts after treatments

Catalysts	Surface area after calcination ($m^2\ g^{-1}$)	Pore volume ($cm^3\ g^{-1}$)	Pore size (Å)
Ni/Ce-ZrO_2 (HSA) (Ce/Zr = 1/3)	45	0.15	63.71
Ni/Ce-ZrO_2 (HSA) (Ce/Zr = 1/1)	44	0.14	63.90
Ni/Ce-ZrO_2 (HSA) (Ce/Zr = 3/1)	41.5	0.14	63.15
Ni/CeO_2 (HSA)	24	0.13	63.02
Ni/Ce-ZrO_2 (LSA) (Ce/Zr = 1/3)	20	0.13	63.67
Ni/Ce-ZrO_2 (LSA) (Ce/Zr = 1/1)	18	0.11	61.19
Ni/Ce-ZrO_2 (LSA) (Ce/Zr = 3/1)	19	0.11	62.42
Ni/CeO_2 (LSA)	8.5	0.08	61.20

Table 2
Physicochemical properties of the synthesized catalysts

Catalyst	Metal-load (wt.%)	Metal-reducibility (%)	Ni-dispersion (%)
Ni/Ce-ZrO_2 (HSA) (Ce/Zr = 1/3)	4.9	91.8	9.67
Ni/Ce-ZrO_2 (HSA) (Ce/Zr = 1/1)	4.9	91.0	8.82
Ni/Ce-ZrO_2 (HSA) (Ce/Zr = 3/1)	5.0	92.6	8.95
Ni/CeO_2 (HSA)	5.0	92.2	6.41
Ni/Ce-ZrO_2 (LSA) (Ce/Zr = 1/3)	4.8	90.8	4.69
Ni/Ce-ZrO_2 (LSA) (Ce/Zr = 1/1)	4.9	91.6	4.73
Ni/Ce-ZrO_2 (LSA) (Ce/Zr = 3/1)	4.9	92.1	4.68
Ni/CeO_2 (LSA)	5.0	91.3	3.12
Ni/Al_2O_3	5.0	94.5	4.85

ZrO_2 stabilizes the surface area of catalyst, which is in good agreement with the results obtained on catalysts prepared by conventional routes [21]. It should be noted that the catalysts were also characterized with several physicochemical methods after reduction. The weight content of Ni in Ni/Al_2O_3, Ni/Ce-ZrO_2 (with different Ce/Zr ratio), and Ni/CeO_2 were determined by X-ray fluorescence (XRF) analysis. The reducibility and dispersion percentages of nickel were measured from temperature programmed reduction (TPR) with 5% H_2 in Ar and temperature programmed desorption (TPD), respectively. All physicochemical properties of the synthesized catalysts are presented in Table 2.

2.2. Experimental set-up

Fig. 1 shows the schematic diagram of the experimental reactor system. It consists of three main sections: feed, reaction, and analysis sections. The main obligation of the feed section is to supply the components of interest, such as CH_4, H_2O, H_2, or O_2 to the reaction section, where an 8 mm internal diameter and 40 cm length quartz reactor was mounted vertically inside a furnace. The catalyst (with the weight of 50 mg) was loaded in the quartz reactor, which was packed with a small amount of quartz wool to prevent the catalyst from moving. Preliminary experiments were carried out to find suitable conditions in which internal and external mass transfer effects are not predominant. Considering the effect of external mass transfer, the total flow rate was kept constant at 100 $cm^3\,min^{-1}$ at a constant residence time of 5×10^{-4} g min cm^{-3} in all testing. The suitable average sizes of catalysts were also verified in order to confirm that the experiments were carried out within the region of intrinsic kinetics. In our system, a Type-K thermocouple was placed into the annular space between the reactor and furnace. This thermocouple was mounted in close contact with the catalyst bed to minimize the temperature difference. Another Type-K thermocouple, covering by closed-end quartz tube, was inserted in the middle of the quartz reactor in order to re-check the possible temperature gradient.

After the reactions, the exit gas was transferred via trace-heated lines to the analysis section, which consists of a Porapak Q column Shimadzu 14B gas chromatography (GC) and a mass spectrometer (MS). The gas chromatography was applied in order to investigate the steady state condition experiments, whereas the mass spectrometer was used for the transient carbon formation and water-gas shift reaction experiments.

2.3. Temperature programmed techniques (TP)

In the present work, temperature programmed technique (TP) was applied for studying carbon formation and water-gas shift reaction experiments. Temperature programmed methane adsorption (TPMA) was done in order to investigate the reaction of methane with the surface of catalyst. Five percent CH_4 in He with the total flow rate of 100 $cm^3\,min^{-1}$ was introduced into the system, while the operating temperature increased from room temperature to 900 °C by the rate of 10 °C min^{-1}. Then, the system was cooled down to the room temperature under helium flow. After the TPMA experiment, the carbon deposited on the catalyst was investigated by the temperature programmed oxidation (TPO). Ten percent O_2 in He with the total flow rate of 100 $cm^3\,min^{-1}$ was introduced into the system, after a He purge. Similar to TPMA, the temperature was increased from room temperature to 900 °C. The amount of carbon formation on the surface of each catalyst was then determined by measuring the CO and CO_2 yield obtained from the TPO result.

The temperature programmed reaction (TPR_x) of CO/H_2O/He gas mixture was also carried out in order to investigate the water-gas shift reaction. The mixture of 5%CO and 10%H_2O in He was introduced into the system during heating up period by the rate of 10 °C min^{-1} before reaching the isothermal condition at 900 °C.

3. Results

3.1. Selection of suitable Ce/Zr ratio for Ni/Ce-ZrO_2

Ni/Ce-ZrO_2 catalysts with different Ce/Zr ratios (1/3, 1/1, and 3/1) were firstly tested in methane steam reforming conditions at 900 °C for both HSA and LSA materials in order to select the most suitable ratio of Ce/Zr for the main studies. The results shown in Fig. 2 revealed that at steady state, the Ni/Ce-ZrO_2 with Ce/Zr ratio of 3/1 shows the best performance in terms of stability and activity for both high and low surface areas. Consequently, Ni/Ce-ZrO_2 with Ce/Zr ratio of 3/1 was selected for further investigations.

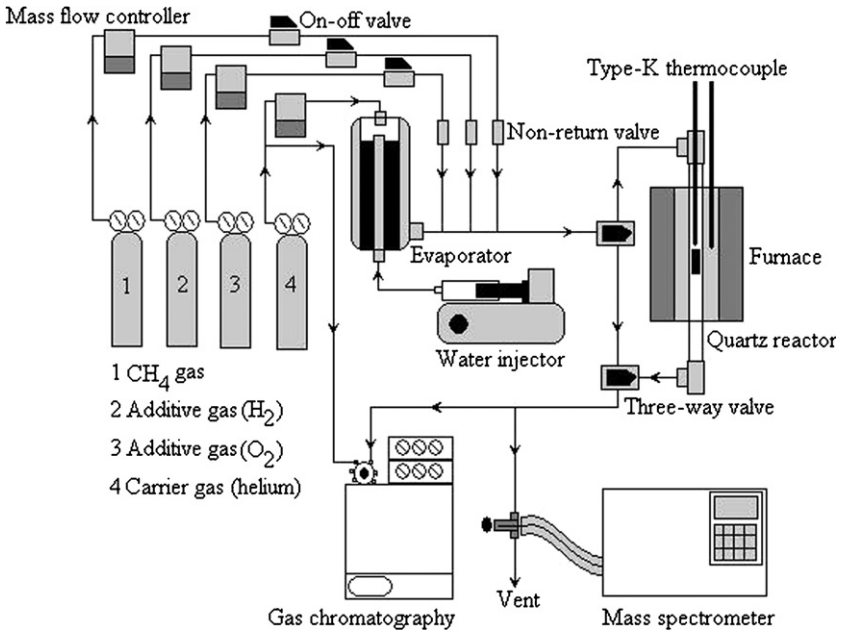

Fig. 1. Schematic diagram of the experimental set-up.

3.2. Stability and activity toward methane steam reforming

The reactivity of methane steam reforming over Ni/CeO_2 (HSA), $Ni/Ce\text{-}ZrO_2$ (HSA) with Ce/Zr ratio of 3/1, Ni/Al_2O_3, $Ni/Ce\text{-}ZrO_2$ (LSA) and Ni/CeO_2 (LSA) were then tested. The inlet components were $CH_4/H_2O/H_2$ in helium with the inlet ratio of 1.0/3.0/0.2 (with the inlet CH_4 partial pressure of 4 kPa). The main products from the reactions over these catalysts were H_2 and CO with some CO_2, indicating a contribution from the water-gas shift, and the reverse methanation at this high-temperature. The steam reforming rate was measured as a function of time in order to indicate the stability and the deactivation rate. The variations in CH_4 conversion with time for different catalysts are shown in Fig. 3. At steady state, Ni/CeO_2 (HSA) and $Ni/Ce\text{-}ZrO_2$ (HSA) presented much higher reactivity toward the methane steam reforming than Ni/Al_2O_3, $Ni/Ce\text{-}ZrO_2$ (LSA), and Ni/CeO_2 (LSA). As seen from the figure, the steam reforming activities of Ni/CeO_2 (LSA) and Ni/Al_2O_3 significantly declined with time before reaching a new steady state rate at a much lower value, while the activity of Ni/CeO_2 (HSA), $Ni/Ce\text{-}ZrO_2$ (HSA), and $Ni/Ce\text{-}ZrO_2$ (LSA) declined slightly. Catalyst stabilities expressed as a deactivation percentage are given in Table 3. In order to investigate the reason of the catalyst deactivation, the post-reaction temperature programmed oxidation (TPO) experiments were then carried out. TPO experiments detected small amount of carbon formation on the surface of Ni over ceria-based supports, whereas significant amount of carbon deposited was observed from the TPO over Ni/Al_2O_3 (1.31 mmol g_{cat}^{-1}). According to these TPO results, the deacti-

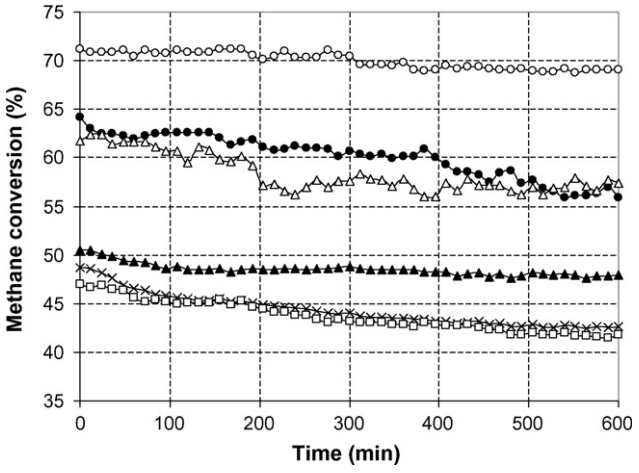

Fig. 2. Steam reforming of methane at 900 °C for $Ni/Ce\text{-}ZrO_2$ with different Ce/Zr ratios using the inlet $CH_4/H_2O/H_2$ ratio of 1.0/3.0/0.2 ($Ni/Ce\text{-}ZrO_2$ (HSA) Ce/Zr = 3/1 (◯), $Ni/Ce\text{-}ZrO_2$ (HSA) Ce/Zr = 1/1 (●), $Ni/Ce\text{-}ZrO_2$ (HSA) Ce/Zr = 1/3 (△), $Ni/Ce\text{-}ZrO_2$ (LSA) Ce/Zr = 3/1 (▲), $Ni/Ce\text{-}ZrO_2$ (LSA) Ce/Zr = 1/1 (×), and $Ni/Ce\text{-}ZrO_2$ (LSA) Ce/Zr = 1/3 (□)).

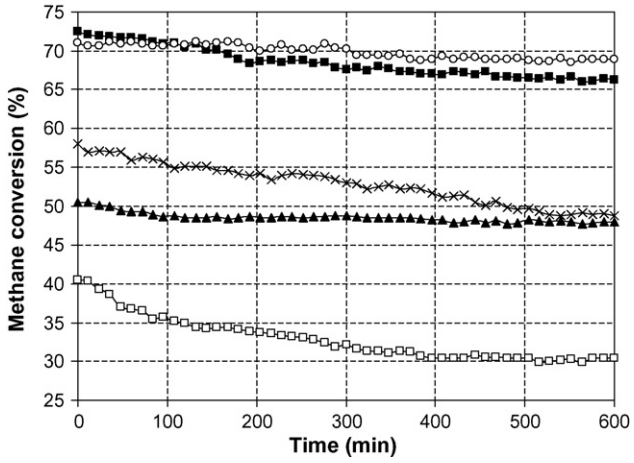

Fig. 3. Steam reforming of methane at 900 °C for different catalysts using the inlet $CH_4/H_2O/H_2$ ratio of 1.0/3.0/0.2 ($Ni/Ce\text{-}ZrO_2$ (HSA) (◯), Ni/CeO_2 (HSA) (■), Ni/Al_2O_3 (×), $Ni/Ce\text{-}ZrO_2$ (LSA) (▲), and Ni/CeO_2 (LSA) (□)).

Table 3
Physicochemical properties of the synthesized catalysts after running the reaction at 900 °C for 10 h

Catalyst	Deactivation (%)	Surface area after reaction ($m^2\ g^{-1}$)	C. formation[a] (mmol g_{cat}^{-1})	Ni-dispersion (%)
Ni/Ce-ZrO_2 (HSA) (Ce/Zr = 1/3)	7.0	42	0.08	9.62
Ni/Ce-ZrO_2 (HSA) (Ce/Zr = 1/1)	12	40	0.11	8.71
Ni/Ce-ZrO_2 (HSA) (Ce/Zr = 3/1)	3.0	40	~0	8.75
Ni/CeO_2 (HSA)	8.7	22	~0	6.33
Ni/Ce-ZrO_2 (LSA) (Ce/Zr = 1/3)	11	18	0.21	4.52
Ni/Ce-ZrO_2 (LSA) (Ce/Zr = 1/1)	12	15	0.19	4.61
Ni/Ce-ZrO_2 (LSA) (Ce/Zr = 3/1)	5.1	18	~0	4.62
Ni/CeO_2 (LSA)	24	6.2	0.14	3.06
Ni/Al_2O_3	16	40	1.31	4.81

[a] Measured from temperature programmed oxidation (TPO).

vation of Ni/Al_2O_3 during the methane steam reforming was mainly related to the carbon formation. In contrast, the deactivations of Ni/CeO_2 and Ni/Ce-ZrO_2 were not caused by the carbon formation; the BET measurement (Table 3) suggested that the deactivations of Ni/CeO_2 and Ni/Ce-ZrO_2, particularly for the low surface area supports, could be due to reduction of surface area. The lower magnitude of the reduction for Ni/CeO_2 (HSA) and Ni/Ce-ZrO_2 (HSA) than for the LSA materials indicates a higher thermal stability for CeO_2 (HSA) and Ce-ZrO_2 (HSA). It should be noted from the BET and TPO studies that although Ni/Al_2O_3 was thermally stable at high operating temperature, it was more susceptible to carbon formation which led to the catalyst deactivation.

3.3. Resistance toward carbon formation

More investigations on the resistance toward the formation of carbon species for all catalysts were investigated by Temperature programmed techniques, i.e. TPMA and TPO. In order to provide the best conditions for testing and obtain the actual resistance toward carbon formation, the influences of exposure time and methane concentration on the amount of carbon formation were firstly determined. Five percent CH_4 in He was fed to the catalyst bed at the isothermal condition (900 °C) for several exposure times (15, 30, 60, 90, 120, 150, and 180 min). The profiles of carbon formation over different catalysts with several exposure times are shown in Fig. 4. Clearly, the quantity of carbon formed on the catalyst surface increased with increasing CH_4 exposure time, and reached its maximum value after 120 min for all catalysts. The influence of inlet CH_4 concentration on the amount of carbon formation was then investigated by introducing different inlet methane partial pressures (2.0–10.0 kPa) with the constant exposure time of 120 min. The amount of carbon deposition seemed to be independent of the inlet methane partial pressure at the same operating conditions. It should be noted that although the rate of carbon formation reaction ($CH_4 \rightarrow C + H_2$) should vary with the methane partial pressure, the reaction time of 120 min may be sufficiently long enough to achieve its maximum carbon formation on the surface of each catalyst and, therefore, the influence of methane partial pressure on coke deactivation was not obviously observed. Therefore, in all experiments, TPMA was carried out by introducing 5% CH_4 in He for 120 min before investigating the degree

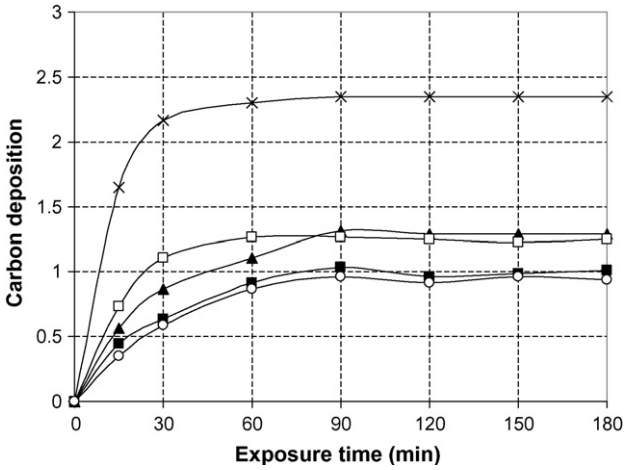

Fig. 4. Influence of exposure time on the amount of carbon formation (mmol g_{cat}^{-1}) for different catalysts at 900 °C (Ni/Ce-ZrO_2 (HSA) (◯), Ni/CeO_2 (HSA) (■), Ni/Al_2O_3 (×), Ni/Ce-ZrO_2 (LSA) (▲), and Ni/CeO_2 (LSA) (□)).

of carbon formation by TPO. Fig. 5 presents the TPMA results for Ni/Ce-ZrO_2 (LSA), Ni/CeO_2 (HSA), Ni/Ce-ZrO_2 (HSA), and Ni/Al_2O_3, while Fig. 6 presents the TPO results for those catalysts.

As seen in Fig. 5, carbon monoxide and carbon dioxide were also produced together with hydrogen for Ni catalysts on ceria-

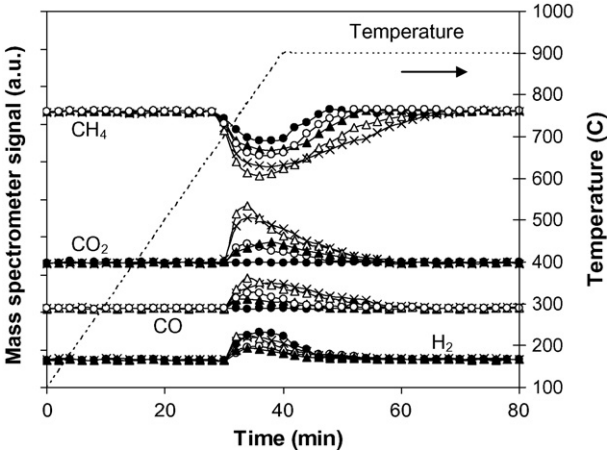

Fig. 5. TPMA over (△) Ni/CeO_2-ZrO_2 (HSA), (×) Ni/CeO_2 (HSA), (◯) Ni/CeO_2-ZrO_2 (LSA), (▲) Ni/CeO_2 (LSA), and (●) Ni/Al_2O_3.

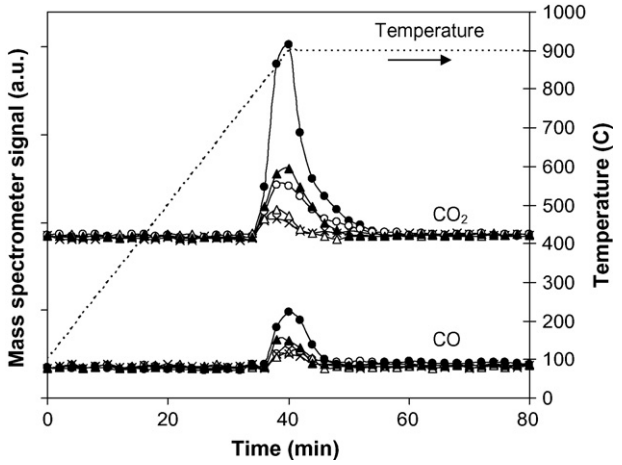

Fig. 6. Temperature programmed oxidation over (△) Ni/CeO_2-ZrO_2 (HSA), (×) Ni/CeO_2 (HSA), (◯) Ni/CeO_2-ZrO_2 (LSA), (▲) Ni/CeO_2 (LSA), and (●) Ni/Al_2O_3 following TPMA to 900 °C.

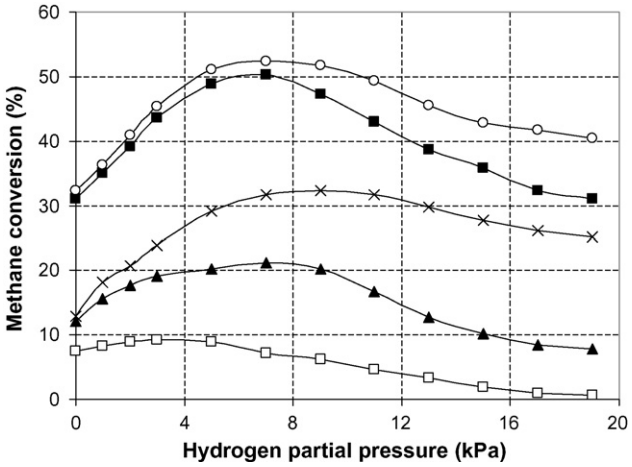

Fig. 7. Effect of hydrogen partial pressure on steam reforming rate over different catalysts at 800 °C (Ni/Ce-ZrO_2 (HSA) (◯), Ni/CeO_2 (HSA) (■), Ni/Al_2O_3 (×), Ni/Ce-ZrO_2 (LSA) (▲), and Ni/CeO_2 (LSA) (□)).

based supports, whereas only hydrogen peak was detected for TPMA over Ni/Al_2O_3. The CO and CO_2 formations from TPMA of Ni catalysts on ceria-based supports comes from the gas–solid reaction of CH_4 with the lattice oxygen (O_x) on ceria surface (Eq. (4)):

$$CH_4 + O_x = 2H_2 + CO + V_O^{\bullet\bullet} + 2e' \quad (4)$$

$V_O^{\bullet\bullet}$ denotes an oxygen vacancy with an effective charge 2^+, e' is an electron which can either be more or less localized on a cerium ion or delocalized in a conduction band. The quantities of carbon deposited (mmol g_{cat}^{-1}) on the surface of each catalyst, which could be calculated by measuring the CO and CO_2 yields, are presented in Table 4. Clearly, Ni/CeO_2 (HSA) and Ni/Ce-ZrO_2 (HSA) provided higher resistance toward carbon formation than Ni/Al_2O_3, Ni/Ce-ZrO_2 (LSA), and Ni/CeO_2 (LSA).

The influence of adding H_2O along with CH_4 at the feed on the amount of carbon formation was studied by varying the inlet H_2O/CH_4 ratio from 0.0/0.05 to 0.15/0.05. As seen in Table 4, it was observed that the carbon deposition over nickel catalyst on ceria-based supports rapidly decreased with increasing inlet steam partial pressure. Nickel catalyst on low surface area (LSA) Ce-ZrO_2 required inlet H_2O/CH_4 ratio of 3.0 in order to prevent the formation of carbon species on catalyst surface, while nickel catalyst on high surface area (HSA) Ce-ZrO_2 required inlet H_2O/CH_4 ratio as low as 1.0. It should be noted that Ni/Al_2O_3 required much higher H_2O/CH_4 ratio to reduce the carbon formation, and the carbon species remains detectable on the surface of Ni/Al_2O_3 even the inlet H_2O/CH_4 ratio is higher than 3.0.

3.4. Effect of inlet co-reactant compositions

The influences of possible co-reactant compositions, i.e. H_2, H_2O, CO_2, and O_2 on the conversion of CH_4 over these Ni catalysts were investigated. First, various inlet H_2 partial pressures were added along with CH_4 and H_2O to the feed in order to investigate the influence of this component on the CH_4 conversion. The inlet CH_4 and H_2O partial pressures were kept constant at 4.0 and 12.0 kPa, respectively. As shown in Fig. 7, with the presence of low H_2 partial pressure (0–5 kPa), H_2 presented positive effect on the CH_4 conversion. Without inlet hydrogen, the CH_4 conversions for all catalysts were apparently low, suggesting that some hydrogen must be fed together with methane and steam to obtain significant reforming rate. Similar result was earlier reported over Ni/ZrO_2 [1]. Table 5 gives the reaction orders in H_2 for all catalysts in this range of H_2 partial pressure. Compared to Ni/Al_2O_3, the reaction orders in hydrogen for Ni catalyst on ceria-based supports, especially on high surface area (HSA) supports were significantly lower. The CH_4 conversion at higher inlet H_2 partial pressures (>5 kPa) was also measured. When the inlet hydrogen partial pressure was greater than 8–10 kPa, a strong reduction in rate was observed for all catalysts, Fig. 7, as expected.

Fig. 8 shows the effect of steam on the CH_4 conversion. It was found that the conversion increased with increasing inlet H_2O partial pressure at low values but H_2O then presented a negative effect on the reforming rate at higher inlet H_2O/CH_4 ratio. It should be noted that the steam requirement for Ni/CeO_2

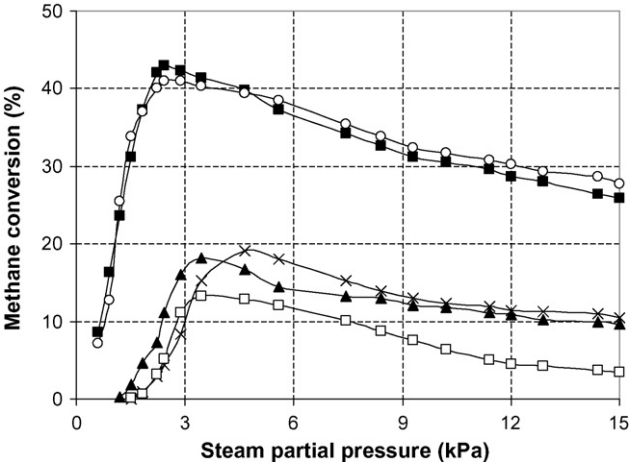

Fig. 8. Effect of steam partial pressure on steam reforming rate over different catalysts at 800 °C (Ni/Ce-ZrO_2 (HSA) (◯), Ni/CeO_2 (HSA) (■), Ni/Al_2O_3 (×), Ni/Ce-ZrO_2 (LSA) (▲), and Ni/CeO_2 (LSA) (□)).

Table 4
Dependence of inlet H_2O/CH_4 ratio on the amount of carbon formation on the catalyst surface (900 °C)

Catalysts	Amount of carbon formation at various H_2O/CH_4 ratios (mmol g_{cat}^{-1})							
	0	0.2	0.4	0.6	0.8	1.0	2.0	3.0
Ni/CeO_2 (HSA)	0.90	0.73	0.59	0.26	0.14	0.09	~0	~0
$Ni/Ce\text{-}ZrO_2$ (HSA)	1.04	0.85	0.54	0.21	0.07	~0	~0	~0
Ni/CeO_2 (LSA)	1.26	1.24	1.09	0.73	0.50	0.34	0.23	0.14
$Ni/Ce\text{-}ZrO_2$ (LSA)	1.30	1.18	0.79	0.56	0.32	0.18	0.09	~0
Ni/Al_2O_3	2.37	2.37	2.25	2.16	2.06	1.99	1.49	1.35

Table 5
Reaction orders in hydrogen from the methane steam reforming reaction at low hydrogen partial pressure (4 kPa CH_4, 12 kPa H_2O, and up to 5 kPa H_2)

Catalysts	Reaction order in hydrogen at different temperatures				
	650 °C	700 °C	750 °C	800 °C	850 °C
Ni/CeO_2 (HSA)	0.16	0.18	0.16	0.16	0.17
$Ni/Ce\text{-}ZrO_2$ (HSA)	0.17	0.18	0.19	0.16	0.17
Ni/CeO_2 (LSA)	0.17	0.18	0.19	0.18	0.17
$Ni/Ce\text{-}ZrO_2$ (LSA)	0.18	0.19	0.18	0.20	0.18
Ni/Al_2O_3	0.34	0.31	0.28	0.30	0.29

(HSA) and $Ni/Ce\text{-}ZrO_2$ (HSA) to achieve the maximum reforming reactivity were lower than the others.

The methane steam reforming in the presence of CO_2 was then investigated by adding different inlet CO_2 partial pressures (1–5 kPa) to the feed gas. Fig. 9 presents the effect of CO_2 on the reforming rate for each catalyst by plotting the relationship between $\ln(\text{Rate}_{\text{with } CO_2}/\text{Rate}_{\text{without } CO_2})$ and $\ln(P_{CO_2})$. As seen from this figure, CO_2 presented a negative effect on the CH_4 conversion for all catalysts; however, in contrast to the influence of H_2, the weaker inhibition effect by CO_2 was observed for Ni on ceria-based supports. According to the reaction order in CO_2 calculation, the reaction order in CO_2 for Ni/Al_2O_3 was approximately −0.12, whereas those over Ni on ceria-based supports were around −0.06 to −0.03, which clearly indicated the weaker inhibitory effect of CO_2 for Ni on ceria-based supports.

Finally, the methane steam reforming in the presence of O_2 (as autothermal reforming) was then carried out by adding different O_2 partial pressures (1–4 kPa) into the feed gas at several operating temperatures. The rate increased with increasing the inlet oxygen partial pressure for all catalysts as shown in Fig. 10. However, H_2 and $CO/(CO + CO_2)$ production selectivity were found to decrease with increasing O_2 concentration as shown in Fig. 11 for Ni/Al_2O_3, $Ni/Ce\text{-}ZrO_2$ (LSA), and Ni/CeO_2 (LSA) and Fig. 12 for $Ni/Ce\text{-}ZrO_2$ (HSA) and Ni/CeO_2 (HSA), respectively. It should be noted that, at the same operating conditions, the $CO/(CO + CO_2)$ production selectivity for Ni/Al_2O_3 was observed to be higher than that over Ni on ceria-based supports. The difference in this production selectivity is due to the reactivity toward the water-gas shift reaction of each support. The water-gas shift reaction (WGS) activities of each support was also carried out in the present work to ensure the influence of this reaction on the $CO/(CO + CO_2)$ selectivity. Fig. 13 shows the activities of all supports toward this reaction at several tem-

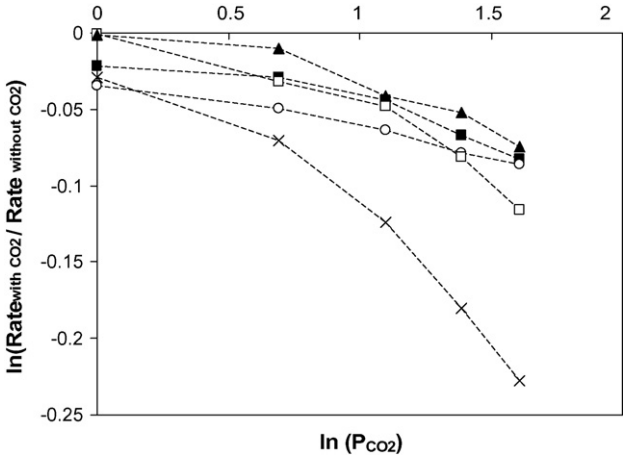

Fig. 9. Effect of carbon dioxide partial pressure on steam reforming rate over different catalysts at 800 °C (Ni/Ce-ZrO_2 (HSA) (◯), Ni/CeO_2 (HSA) (■), Ni/Al_2O_3 (×), Ni/Ce-ZrO_2 (LSA) (▲), and Ni/CeO_2 (LSA) (□)).

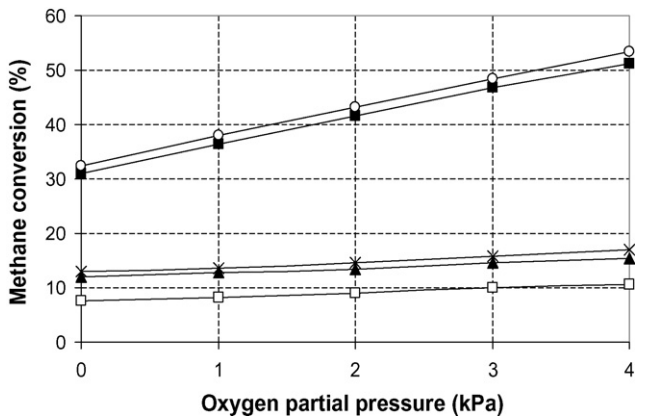

Fig. 10. Effect of oxygen partial pressure on steam reforming rate over different catalysts at 800 °C (Ni/Ce-ZrO_2 (HSA) (◯), Ni/CeO_2 (HSA) (■), Ni/Al_2O_3 (×), Ni/Ce-ZrO_2 (LSA) (▲), and Ni/CeO_2 (LSA) (□)).

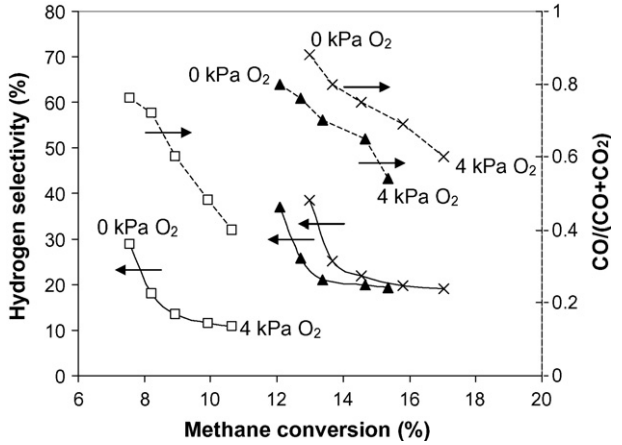

Fig. 11. Effect of oxygen partial pressure on the H_2 selectivity (solid lines) and $CO/(CO+CO_2)$ (dot lines) at isoconversion from steam reforming over Ni/Al_2O_3 (×), $Ni/Ce\text{-}ZrO_2$ (LSA) (▲), and Ni/CeO_2 (LSA) (□) at 800 °C.

peratures. Among the supports, the activity toward this reaction over CeO_2 (HSA) was the highest.

4. Discussion

Improvements of stability and activity toward methane steam reforming were achieved for Ni on high surface area (HSA) ceria-based supports. The high stability is due to the lower sintering rate compared to Ni on low surface area (HSA) ceria-based supports and the higher resistance toward carbon deposition compared to Ni/Al_2O_3, while the high reforming activity is possibly due to the improvement of Ni-dispersion on the high surface area support (Table 2), and also the strong gas–solid redox reaction between methane and the high surface area (HSA) ceria-based supports. It has been reported that the solid–gas reaction between CeO_2 and CH_4 produces synthesis gas with a H_2/CO ratio of two (Eq. (4)), while the reduced ceria can react with CO_2 and H_2O to recover CeO_2 and also produce CO and H_2 (Eqs. (5) and (6)) [39–41]. Importantly, we reported in our previous work that these redox reactions (Eqs. (4)–(6))

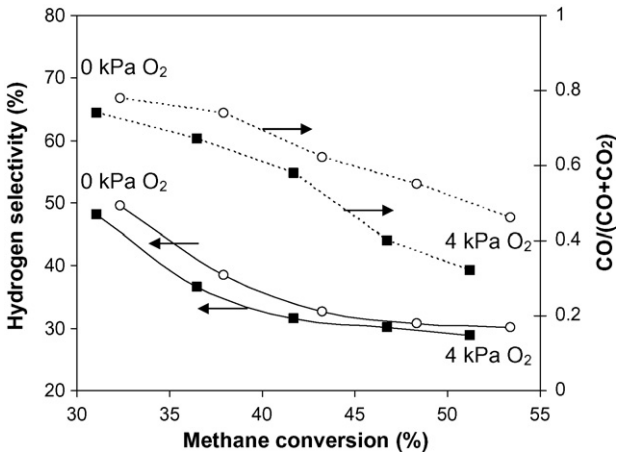

Fig. 12. Effect of oxygen partial pressure on the H_2 selectivity (solid lines) and $CO/(CO+CO_2)$ (dot lines) at isoconversion from steam reforming over $Ni/Ce\text{-}ZrO_2$ (HSA) (◯), and Ni/CeO_2 (HSA) (■) at 800 °C.

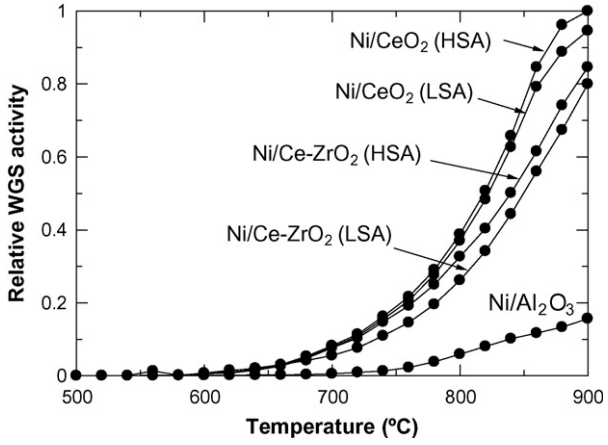

Fig. 13. The activities of each catalyst toward the water-gas shift reaction.

increase with increasing the specific active surface area of CeO_2 [42].

$$V_{O}^{\bullet\bullet} + 2e' + CO_2 = O_x + CO \quad (5)$$

$$V_{O}^{\bullet\bullet} + 2e' + H_2O = O_x + H_2 \quad (6)$$

The addition of suitable ratio of ZrO_2 over ceria, as $Ce\text{-}ZrO_2$, has also been widely reported to improve the oxygen storage capacity, and the redox reactivity of material [22–31]. These benefits were associated with enhanced reducibility of cerium (IV) in $Ce\text{-}ZrO_2$, which is a consequence of high O^{2-} mobility inside the fluorite lattice. The reason for the increasing mobility might be related to the lattice strain, which is generated by the introduction of a smaller isovalent Zr cation into the CeO_2 lattice (Zr^{4+} has a crystal ionic radius of 0.84 Å, which is smaller than 0.97 Å for Ce^{4+} in the same co-ordination environment).

The high resistance toward carbon deposition, which was observed from the catalyst over high surface area ceria-based supports, is also related to the facile redox reaction. During the steam reforming of methane, the following reactions are theoretically the most probable reactions that could lead to surface carbon formation:

$$2CO = CO_2 + C \quad (7)$$

$$CH_4 = 2H_2 + C \quad (8)$$

$$CO + H_2 = H_2O + C \quad (9)$$

$$CO_2 + 2H_2 = 2H_2O + C \quad (10)$$

Reactions (9)–(10) are favorable at low-temperatures, whereas the Boudouard reaction (Eq. (7)) and the decomposition of methane (Eq. (8)) are the major pathways for carbon formation at high-temperatures as they show the largest change in Gibbs energy. According to the range of temperature in this study, carbon formation would be formed via the decomposition of methane and Boudouard reactions. By applying ceria-based supports, the formation of carbon species via both reactions could be inhibited by the redox reactions with the lattice oxygen (O_x) forming H_2 and CO_2, which is thermodynamically unfavored to form carbon species in this range of conditions.

Therefore, significant lower amount of carbon deposition were consequently observed even at low inlet H_2O/CH_4 ratio.

The experiments on the effect of co-reactants yielded non-linear positive hydrogen trend. The positive effect at the low hydrogen appearance could be due to the reduction of oxidized state on the surface active site of nickel, while the inhibitory effect at high hydrogen partial pressure is due to the reverse methane steam reforming methanation, and the reverse water-gas shift reactions [1–3]. In addition, the presence of hydrogen atom on some active sites of nickel particle could also lead to the decrease in methane conversion [1–3]. Regarding the observed reaction order in hydrogen, the inhibitory impact for Ni catalysts on ceria-based supports (both HSA and LSA) is stronger than that for Ni/Al_2O_3 due to the redox property of the ceria-based materials. As described earlier, the gas-solid reaction between the ceria-based materials and CH_4 can generate CO and H_2, while the reduced state can react with steam and CO_2 to produce H_2 and CO, respectively. For $Ni/Ce\text{-}ZrO_2$ and Ni/CeO_2, although hydrogen prevents the oxidized state of nickel, this component can also reduce ceria via the reverse of Eq. (6) and consequently results in the inhibition of methane conversion via Eq. (4). This explanation is in good agreement with the previous studies [43] which investigated kinetics parameters for the methane steam reforming on ceria-based materials and reported the negative effect of hydrogen on methane conversion over these materials due to the change of Ce^{4+} to Ce^{3+}.

The dependence of H_2O on the CH_4 conversion is non-monotonic due to adsorption competition between CH_4 and H_2O on the catalyst active sites. Previous works [4,5] also reported the same results and explanation. The CH_4 conversion increased with increasing the inlet O_2 partial pressure. However, the $CO/(CO + CO_2)$ production selectivity and H_2 production rates strongly decreased with increasing O_2 partial pressure. This could be due to the combustion of H_2 and CO productions and the inhibition of H_2O adsorption on the catalyst surface active sites by O_2.

5. Conclusion

High surface area CeO_2 and $Ce\text{-}ZrO_2$ with Ce/Zr ratio of 3/1 are the good candidates to be used as the support for Ni catalysts for the steam reforming of CH_4 producing H_2 for later utilization in SOFC. The great advantages of Ni on high surface area (HSA) ceria-based supports are the high reforming reactivity, and also the high stability due to their excellent resistance toward carbon formation. Lower inlet H_2O/CH_4 ratio is required for Ni on high surface area (HSA) CeO_2 and $Ce\text{-}ZrO_2$ to prevent the carbon formation.

According to the effect of co-reactants (i.e. H_2O, H_2, CO_2, and O_2), the effects of H_2O on the methane steam reforming over Ni/CeO_2 (HSA) and $Ni/Ce\text{-}ZrO_2$ (HSA) are similar to those for Ni/Al_2O_3 in terms of reaction orders, whereas a stronger negative effect of H_2 was observed over Ni/CeO_2 (HSA) and $Ni/Ce\text{-}ZrO_2$ (HSA) as H_2 inhibits the gas-solid reaction between CeO_2 and CH_4. Additional of CO_2 inhibited the reforming rate, whereas addition of O_2 promoted the CH_4 conversion but reduced both CO and H_2 productions due to the further combustion and/or the inhibition of H_2O adsorption on the catalyst surface active sites. Lastly, the difference between Ni/CeO_2 (HSA) and $Ni/Ce\text{-}ZrO_2$ (HSA) is the $CO/(CO + CO_2)$ production selectivity. This selectivity for $Ni/Ce\text{-}ZrO_2$ is higher than that for Ni/CeO_2 due to the high reactivity toward water-gas shift reaction of CeO_2 compared to $Ce\text{-}ZrO_2$.

Acknowledgement

The financial support from The Thailand Research Fund (TRF) throughout this project is gratefully acknowledged.

References

[1] J. Xu, Ph.D. Thesis, Laboratorium Voor Petrochemische Techniek, Rijkuniversiteit, Gent, Belgium, 1986.
[2] J. Xu, G.F. Froment, AIChE 35 (1989) 88.
[3] J. Xu, G.F. Froment, AIChE 35 (1989) 97.
[4] S.S.E.H. Elnashaie, A.M. Adris, A.S. Al-Ubaid, M.A. Soliman, Chem. Eng. Sci. 45 (1990) 491.
[5] S.S.E.H. Elnashaie, S.S. Elshishini, Modeling, Simulation and Optimization of Industrial Fixed Bed Catalytic Reactors, Gordon and Breach Science Publishers, UK, 1993.
[6] X. Wang, R.J. Gorte, Appl. Catal. A 224 (2002) 209–218.
[7] H.S. Roh, K.W. Jun, W.S. Dong, J.S. Chang, S.E. Park, Y.I. Joe, J. Mol. Catal. A 181 (2002) 137–142.
[8] Q. Miao, G. Xiong, S. Sheng, W. Cui, L. Xu, L.X. Guo, Appl. Catal. A 154 (1987) 17–27.
[9] A.A. Lemonidou, M.A. Goula, I.A. Vasalos, Catal. Today 46 (1987) 175–183.
[10] W.S. Dong, H.S. Roh, K.W. Jun, S.E. Park, Y.S. Oh, Appl. Catal. A 226 (2002) 63–72.
[11] M. Mamak, N. Coombs, G. Ozin, Adv. Mater. 12 (2000) 198–202.
[12] M. Mamak, N. Coombs, G. Ozin, J. Am. Chem. Soc. 122 (2000) 8932.
[13] M. Mamak, N. Coombs, G.A. Ozin, Chem. Mater. 13 (2001) 3564.
[14] P. Bera, S. Mitra, S. Sampath, M.S. Hegde, Chem. Commun. (2001) 927.
[15] A. Martinez-Arias, J.M. Coronado, R. Cataluna, J.C. Conesa, J.C. Soria, J. Phys. Chem. B 102 (1998) 4357.
[16] D. Skarmoutsos, F. Tietz, P. Nikolopoulos, Fuel Cells 1 (2001) 243.
[17] T. Takeguchi, S.N. Furukawa, M. Inoue, J. Catal. 202 (2001) 14.
[18] J. Sfeir, P.A. Philippe, P. Moseki, N. Xanthopoulos, R. Vasquez, J.M. Hans, V.H. Jan, K.R. Thampi, J. Catal. 202 (2001) 229.
[19] N. Kiratzis, P. Holtappels, C.E. Hatchwell, M. Mogensen, J.T.S. Irvine, Fuel Cells 1 (2001) 211.
[20] H.S. Roh, W.S. Dong, K.W. Jun, S.E. Park, Chem. Lett. 88 (2001).
[21] P. Aguiar, E. Ramírez-Cabrera, N. Laosiripojana, A. Atkinson, L.S. Kershenbaum, D. Chadwick, Stud. Surf. Sci. Catal. 145 (2002) 387–390.
[22] M. Ozawa, M. Kimura, A. Isogai, J. Alloys Comp. 193 (1993) 73.
[23] G. Balducci, J. Kaspar, P. Fornasiero, M. Graziani, M.S. Islam, J. Phys. Chem. B 102 (1998) 557.
[24] G. Vlaic, P. Fornasiero, S. Geremia, J. Kaspar, M. Graziani, J. Catal. 168 (1997) 386.
[25] G.R. Rao, J. Kaspar, S. Meriani, R. Dimonte, M. Graziani, Catal. Lett. 24 (1994) 107.
[26] P. Fornasiero, R. Dimonte, G.R. Rao, J. Kaspar, S. Meriani, A. Trovarelli, M. Graziani, J. Catal. 151 (1995) 168.
[27] M. Haneda, K. Miki, N. Kakuta, A. Ueno, S. Tani, S. Matsura, M. Sato, Nihon Kagaku Kaishi (1990) 820.
[28] T. Ohata, Rare Earths 17 (1990) 37.
[29] J.G. Nunan, W.B. Williamson, H.J. Robota, SAE Paper 960768 (1996).
[30] S. Otsuka-Yao, H. Morikawa, N. Izu, K. Okuda, J. Jpn. Inst. Metals 59 (1995) 1237.
[31] M.H. Yao, T.E. Hoost, R.J. Baird, F.W. Kunz, J. Catal. 166 (1997) 67.
[32] C.T. Kresge, M.E. Leonowicz, W.J. Roth, J.C. Vartuli, J.S. Beck, Nature 359 (1992) 710.

[33] Q. Huo, D.I. Margolese, U. Ciesla, P. Feng, T.E. Gier, P. Sieger, R. Leon, P.M. Petroff, B. Schüth, G.D. Stucky, Nature 368 (1994) 317.
[34] P.T. Tanev, T.J. Pinnavaia, Science 267 (1995) 865.
[35] U. Ciesla, S. Schacht, G.D. Stucky, K.K. Unger, F. Schüth, Angew. Chem. Int. Ed. Engl. 35 (1996) 541.
[36] D.M. Antonelli, J.Y. Ying, Angew. Chem. Int. Ed. Engl. 35 (1996) 426.
[37] Q. Huo, D.I. Margolese, U. Ciesla, D.G. Demuth, P. Feng, T.E. Gier, P. Sieger, A. Firouzi, B.F. Chmelka, B. Schüth, G.D. Stucky, Chem. Mater. 6 (1994) 1176.
[38] Daniela Terribile, Alessandro Trovarelli, Jordi Llorca, Carla de Leitenburg and Giuliano Dolcetti, Catal. Today 43 (1998) 79–88.
[39] K. Otsuka, T. Ushiyama, I. Yamanaka, Chem. Lett. (1993) 1517.
[40] K. Otsuka, M. Hatano, A. Morikawa, J. Catal. 79 (1983) 493.
[41] K. Otsuka, M. Hatano, A. Morikawa, Inorg. Chim. Acta 109 (1985) 193.
[42] N. Laosiripojana, S. Assabumrungrat, Appl. Catal. B: Environ. 60 (2005) 107.
[43] E. Ramirez, A. Atkinson, D. Chadwick, Appl. Catal. B 36 (2002) 193–206.

Korean J. Chem. Eng., **25**(2), 223-230 (2008)

High temperature desulfurization over nano-scale high surface area ceria for application in SOFC

Rajesh Shivanahalli Kempegowda, Navadol Laosiripojana† and Suttichai Assabumrungrat*

The Joint Graduate School of Energy and Environment, King Mongkut's University of Technology Thonburi, Bangkok 10140, Thailand
*Center of Excellence in Catalysis and Catalytic Reaction Engineering, Department of Chemical Engineering, Faculty of Engineering, Chulalongkorn University, Bangkok 10330, Thailand
(*Received 13 February 2007 • accepted 27 July 2007*)

Abstract−In the present work, suitable absorbent material for high temperature desulfurization was investigated in order to apply internally in solid oxide fuel cells (SOFC). It was found that nano-scale high surface area CeO_2 has useful desulfurization activity and enables efficient removal of H_2S from feed gas between 500 to 850 °C. In this range of temperature, compared to the conventional low surface area CeO_2, 80-85% of H_2S was removed by nano-scale high surface area CeO_2, whereas only 30-32% of H_2S was removed by conventional low surface area CeO_2. According to the XRD studies, the product formed after desulfurization over nano-scale high surface area CeO_2 was Ce_2O_2S. EDS mapping also suggested the uniform distribution of sulfur on the surface of CeO_2. Regeneration experiments were then conducted by temperature programmed oxidation (TPO) experiment. Ce_2O_2S can be recovered to CeO_2 after exposure in the oxidation condition at temperature above 600 °C. It should be noted that SO_2 is the product from this regeneration process. According to the SEM/EDS and XRD measurements, all Ce_2O_2S forming is converted to CeO_2 after oxidative regeneration. As the final step, a deactivation model considering the concentration and temperature dependencies on the desulfurization activity of CeO_2 was applied and the experimental results were fitted in this model for later application in the SOFC model.

Key words: Desulfurization, SOFC, CeO_2, Deactivation Model

INTRODUCTION

Due to the present oil crisis and global warming, numerous efforts have been focused on the use of alternative and renewable energy sources. Biogas is one important energy source due to its closed cycle operation and producibility from biodegradable solid wastes such as cattle dung (diary wastes), piggery wastes, municipal solid wastes, and industrial effluents. Currently, there are numerous attempts to use biogas as a primary fuel for electrical generation by using several energy devices, i.e., internal combustion engines and fuel cells. As biogas always contains high concentration of hydrogen sulfide (H_2S) (approximately 1,000-2,000 ppm depending on its source), it cannot be utilized directly to the energy devices. Biogas must be initially purified in order to remove H_2S which easily poisons the process reactor. In addition, the removal of H_2S would also help in preventing odors, safety hazards, and corrosion of the biogas transport equipment.

The appropriate technologies of desulfurization depend on the final applications as well as the operating conditions. Several researchers have studied desulfurization by selective oxidation of H_2S over solid absorbents at low temperature (200-300 °C). Park et al. [1] investigated this reaction over $Bi_4V_{2-x}Sb_xO_{11-y}$ material and reported good H_2S conversion with less than 2% of SO_2 selectivity in the temperature range of 220-260 °C. Lee et al. [2] also studied this desulfurization reaction on zeolite-NaX and zeolite-KX. They found that Zeolite-KX was superior to the zeolite-NaX in terms of selectivity to elemental sulfur and resistance to deactivation. In detail, elemental sulfur yield over zeolite-NaX was achieved at about 90% at 225 °C for the first 4 hours, but gradually decreased to 55% after 40 hours, whereas the yield of elemental sulfur on zeolite-KX was obtained within the range of 86% at 250 °C after 40 hours.

It should be noted that selective oxidation may not suitable for high temperature applications such as coal or residual oil gasification, and fuel cell applications, which operate in the temperature range of 400-1,200 °C, due to the large temperature differences in the process. Several high temperature desulfurization techniques are, therefore, desired for use in such applications [3]. Previously, the high temperature removal of hydrogen sulfide from simulated gas was carried out in batch type fluidized-bed reactor by using natural manganese ore consisting of several metal oxides (MnO_x: 51.85%, FeO_y: 3.86%, CaO: 0.11%) [4]. It was found that H_2S removal efficiency increased with increasing temperature but decreased with increasing excess gas velocity. In addition, the breakthrough time for H_2S decreased as the gas velocity increased.

As another example of the high temperature application, fuel cell has drawn a great interest from many researchers as it can generate electricity at high efficiency. Various types of fuel cells are available, in that the solid oxide fuel cell (SOFC) has garnered much attention because of its large electricity production capacity. To establish these highly efficient processes, it is necessary to develop a high temperature treatment process for the various feed stocks, i.e., biogas and natural gas, which consist of a significant amount of H_2S. To date, fuel cell systems rely mainly on batch operation of sorbent

†To whom correspondence should be addressed.
E-mail: navadol_l@jgsee.kmutt.ac.th

technology for sulfur removal. Although this technology possesses the necessary removal efficiency, the low capacity associated with the batchwise operation and the potential utilization of high sulfur hydrocarbon feed stocks greatly affect the fuel cell processor foot print, types of sorbent and sorbent maintenance interval [5]. A widely established metal oxide, ZnO, has been used as a high temperature desulfurization sorbent. ZnO has the most favorable thermodynamics for H_2S removal among sorbents that have been investigated. However, despite its attractive thermodynamic properties, the reduction of ZnO and subsequent vaporization of elemental zinc create a serious problem over many cycles of sulfidation/regeneration at high temperatures [6,7]. As a result, alternate absorbents to minimize ZnO problems at high temperature ranges are needed.

Meng et al. [8] and Kay et al. [9] first described the use of cerium oxide (or ceria) sorbents for high-temperature desulfurization. It is well established that ceria and metal oxide (e.g., Gd, Nb, and Zr) doped cerias provide high oxygen storage capacity, which is beneficial in oxidation processes. Several researchers have also reported the benefit of adding or doping this material on the reforming and partial oxidation catalysts in terms of catalyst stability and the resistance toward carbon deposition [10,11]. Focusing on the use of ceria as the sorbent for desulfurization, in laboratory-scaled fixed-bed reactor tests, the H_2S concentration was reduced from 1.2 v% to 3 ppmv at 872 °C and 1 atm by using reduced ceria, CeO_n ($n<2$). However, only a few data were reported particularly on the material characterization and the mechanism of desulfurization. Abbasian et al. [12] and Li et al. [13] studied mixed-oxide sorbents containing cerium and copper oxides. Although some evidence of cerium sulfidation was reported, the primary function of the ceria was considered to be for maintaining the active copper in a highly dispersed form. Zeng et al. [14] studied the H_2S removal in presence of hydrogen on CeO_2 sorbent. They reported complete conversion of CeO_2 to CeO_2S during sulfidation in the temperature range of 500-700 °C and regeneration of Ce_2O_2S to CeO_2 by using SO_2. According to phase diagrams, relevant reactions were reported by Kay et al. [9] as:

Sulfidation

$$2CeO_2+H_2S+H_2 \leftrightarrow Ce_2O_2S+2H_2O \quad (1)$$

Regeneration

$$Ce_2O_2S+SO_2 \leftrightarrow 2CeO_2+S_2 \quad (2)$$

It should be noted that the major limitations to apply CeO_2 in the high temperature process are its low specific surface and high surface area reduction percentage due to the high surface sintering. It was observed from our previous work that the surface area reduction of CeO_2 after exposure in the reaction conditions at 900 °C was 23% and 28%, respectively. The corresponding post-reaction specific surface areas were only 1.9 and 8.7 $m^2\ g^{-1}$, respectively [15]. The use of high surface area CeO_2 would be a good alternative procedure to improve the performance of H_2S removal at high temperature. In this paper, nano-scale high surface area CeO_2 (from nano-Arc Company, US) was used as a sorbent for the desulfurization process. The reactions during sulfidation and oxidative regeneration were investigated. Some analytical techniques were employed to characterize the sorbents at different stages of operation. In addition, the deactivation model considering the concentration dependency of the activity was developed and fitted with the experimental results to determine the kinetic parameters for the later application in SOFC model fueled by conventional fuel: biogas and natural gas. Regarding the selection of the suitable model, it should be noted that the formation of a dense product layer over the solid reactant results in an additional diffusion resistance and is expected to cause a drop in the reaction rate. One would also expect it to cause significant changes in the pore structure, active surface area, and activity per unit area of solid reactant with reaction extent. These changes cause a decrease of the solid reactant activity with time. As reported in the literature, the deactivation model works well for such gas-solid reactions [16]. In this model, the effects of these factors on the diminishing rate of sulfur fixation were combined in a deactivation rate term [17].

EXPERIMENTAL

1. Fixed Bed Reactor Setup

A laboratory-scaled fixed bed quartz reactor of 30 cm height and 0.635 cm internal diameter was installed vertically in an electric furnace with a programmable temperature controller. Nano-scale CeO_2 (from nano-Arc Company, US) was first calcined at 900 °C before packing between two layers of quartz wool. The physical and chemical properties of CeO_2 are provided in Table 1. A type K thermocouple was located externally at the center of the catalyst to monitor the temperature of the reactor. Swagelok fittings and tubing were used to connect the reactor to the gas supply and gas sampling systems. Details of the reactor setup were shown in Fig. 1.

2. Analytical Methods

Pure CeO_2 and spent CeO_2 were characterized by using X-ray diffractometer (XRD) employing Cu 30 kW and 15 mA to determine the sulfur deposition on the sorbent. SEM and EDS analysis was also carried out to investigate the changes in morphology and sulfur distribution by elemental mapping. The conditions used were 40 kV and resolution of 4000.

Table 1. Physical and chemical properties of CeO_2

Surface area (m^2g^{-1})	42.819
Bulk density	9.102
Pore volume	9.7443×10^{-2}

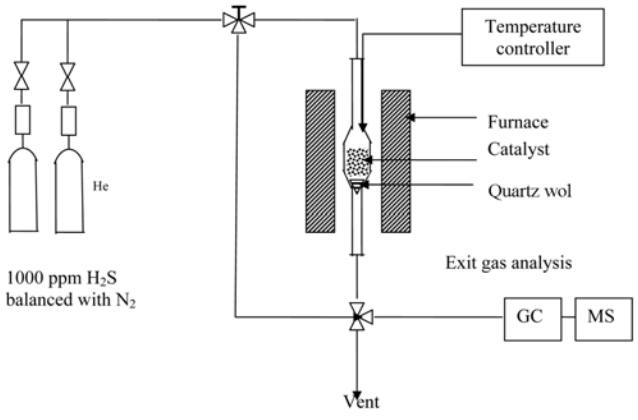

Fig. 1. Schematic diagram of experimental setup.

Table 2. Operating conditions of GC

Detector	TCD
Detector temperature (°C)	150
Column	Porapak-Q
Oven temperature (°C)	Linear programming @ 20 °C min^{-1}
Current (mA)	150

3. Gas Analysis

Gas analysis was carried out by using Shimadzu gas chromatography (GC-14B) equipped with a Porapak-Q column and a TCD detector. The H_2S peak was obtained by using a linear temperature programming in the column oven. The temperature was increased from 40 to 200 °C at a ramp rate of 20 °C min^{-1}. The operating conditions of the GC are summarized in Table 2. It should be noted that the TCD calibration was carried out by mixing pure H_2S and N_2 at various ratios. Mixture of 0.01% (molar) H_2S balanced with nitrogen was used to calibrate the concentration by diluting with helium gas.

4. Procedures for Sulfidation Experiments

The sulfidation experiments were carried out in a fixed bed reactor. The experimental procedures were divided into the study of optimum temperature and the establishment of breakthrough curves for the adsorption of H_2S on CeO_2 sorbent.

Regarding the study of optimum temperature, a set of experiments was carried out to test the desulfurization activity of CeO_2 sorbent at various temperatures: 400, 500, 600, 700, 800 and 850 °C. The amount of CeO_2 was kept at 500 mg, while the total flow rate was 100 cm^3 min^{-1}. The temperature was increased linearly at a rate of 10 °C min^{-1} until reaching a desired temperature. The reactor was then kept under isothermal condition for 30 min. The exit gases from the reactor were connected to the gas chromatography (GC) equipped with TCD detector to detect the H_2S level after adsorption at each temperature level. The breakthrough curve experiments were then carried out at the suitable temperatures for the desulfurization. The reactor was operated by using a feed gas (100 cm^3 min^{-1}) with H_2S concentration of 1,000 ppm. The reactor was heated to a desired temperature at a heating rate of 10 °C min^{-1}. The system was operated under isothermal until breakthrough of H_2S appeared at the exit of the bed.

5. Oxidative Regeneration of Sulfided CeO_2 by Temperature Programmed Reaction Study

The characteristics of the regeneration of the sulfided CeO_2 were examined with a temperature programmed oxidation (TPO) apparatus equipped with quadrupole mass spectrometer. In the TPO examination, 10% oxygen balanced in helium or nitrogen was fed into the microreactor in the TPO apparatus at a flow rate of 100 cm^3 min^{-1}. A sample of 50 mg was packed into the micro reactor of ¼" size. The sample was heated to 900 °C at a constant heating rate of 10 °C min^{-1}. The exit gases were monitored continuously with the mass spectrometer.

RESULTS AND DISCUSSION

1. Sulfidation Results

First, the effect of temperature on the desulfurization activity of nano-scale CeO_2 sorbent was studied in the range of 400 to 850 °C.

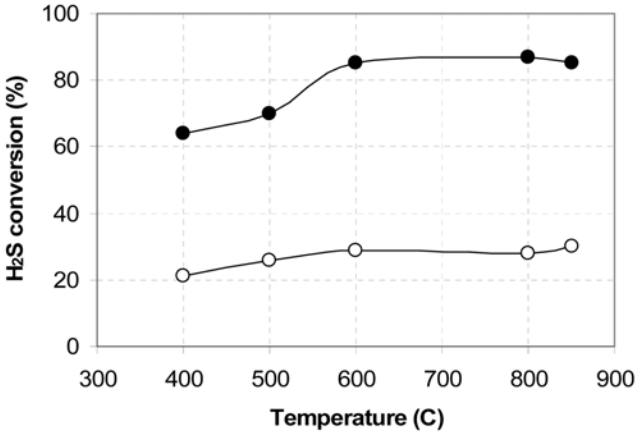

Fig. 2. Conversions of H_2S at different temperatures (nano-scale high surface area CeO_2 (●), and conventional low surface area CeO_2 (○)).

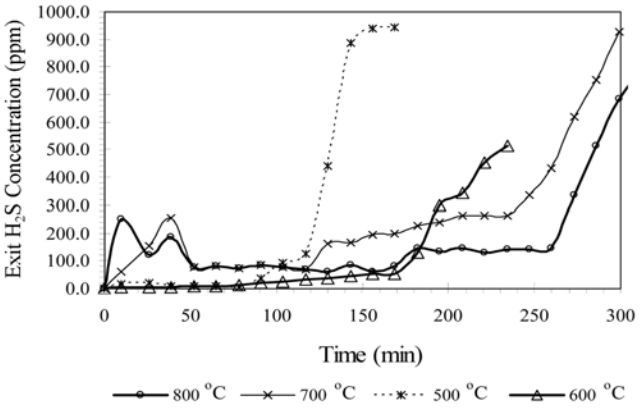

Fig. 3. Sulfidation break through curves of CeO_2.

The conversion of H_2S (X) defined in Eq. (3) was plotted with temperature as shown in Fig. 2. It should be noted that the desulfurization activity of conventional low surface area CeO_2 (synthesized by the precipitation method with the specific surface area of 3.1 m^2 g^{-1}) was also performed for comparison.

$$X = \frac{Conc_{Initial} - Conc_{Exit}}{Conc_{Initial}} \times 100 \quad (3)$$

It was found that the H_2S conversion from the desulfurization over nano-scale CeO_2 was almost 3 times higher than that over conventional low surface area CeO_2. The conversion increased readily with increasing temperature and then became constant at above 600 °C. The breakthrough results for nano-scale CeO_2, which refers to a predetermined H_2S outlet condition when a certain concentration of H_2S cannot be removed by the catalyst bed [18], at several temperatures are presented in Fig. 3. As seen from the figure, the breakthrough period increased with increasing temperature. It should be noted that a few bumps (higher H_2S concentration regions) appeared in some early part of the pre-breakthrough curves. These early bumps could be associated with incomplete reduction of ceria at the early state. Without pre-reduction, the reduction and sulfidation occurred simultaneously on the surface of ceria, as explained by Zeng et al.

[14]. According to the gas product detected from gas chromatography during the sulfidation testing, small amounts of hydrogen and oxygen were also detected along with steam, which could have been formed by the combustion of hydrogen and oxygen.

2. Regeneration of Sulfided CeO_2

Regeneration of sulfided CeO_2 was conducted by using 10% oxygen as a regeneration agent for two different samples sulfided at 700 and 800 °C. A sample was packed and heated in a micro tube reactor installed in the furnace at a constant heating rate of 10 °C min^{-1}. The amount of O_2 and SO_2 evolved at each temperature level was monitored by mass spectrometer. Figs. 4 and 5 show the results of the samples sulfided at 700 and 800 °C, respectively. Both figures indicate the consumption of O_2 and evolution of SO_2 during the temperature range of 600 and 800 °C. The evolution temperature observed in the present work is in good agreement with several previous works in the literature [19-21], which investigated the oxidation of Ce_2O_2S in the range of operating temperature between 600-800 °C by TPO technique and observed the evolution of SO_2 around 800 °C. According to the calculation of area under peaks from Figs. 4 and 5, the amount of SO_2 evolved was approximately 1.25 mol% from the sulfided sample at 700 °C by consuming oxygen of 2% whereas the amount of SO_2 evolved from the sulfided sample at 800 °C was about 3 mol% with the oxygen consuming of 4%. The difference in the amount of SO_2 evolution from the sulfidation at different temperatures, which was also observed by several researchers, could be mainly due to the increase of oxygen mobility on the

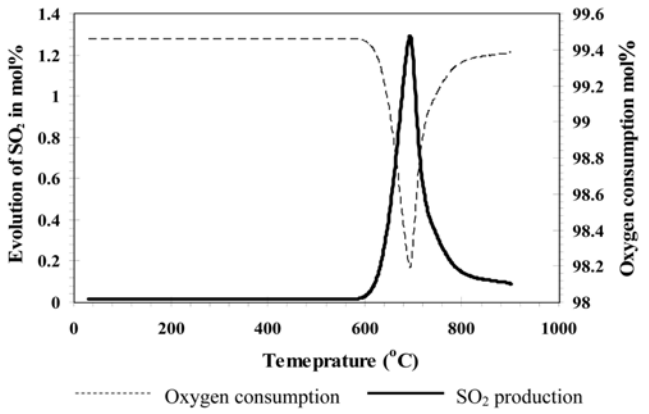

Fig. 4. Oxidative regeneration of CeO_2 sulfided at 700 °C.

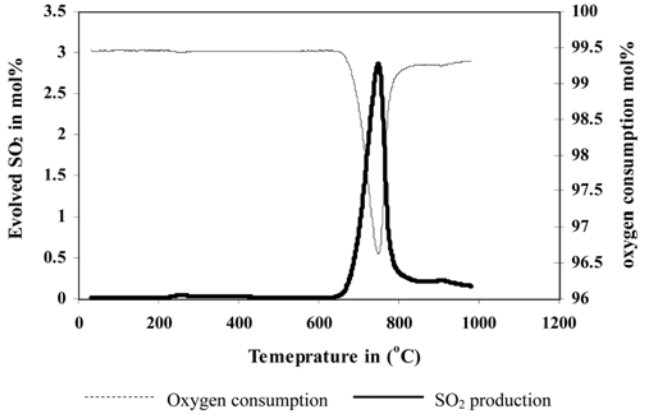

Fig. 5. Oxidative regeneration of CeO_2 sulfided at 800 °C.

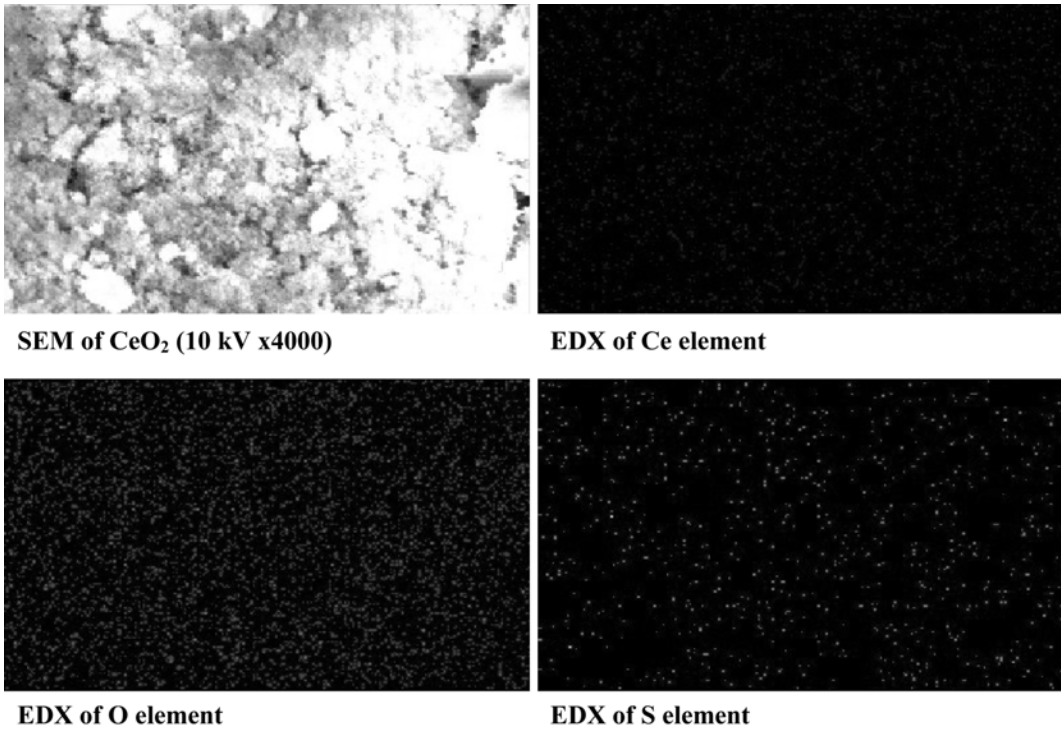

(a) SEM and elemental mapping of CeO_2 sulfided at 700°C

Fig. 6. Mapping of sulfur, oxygen and cerium distribution on the sulfided CeO_2.

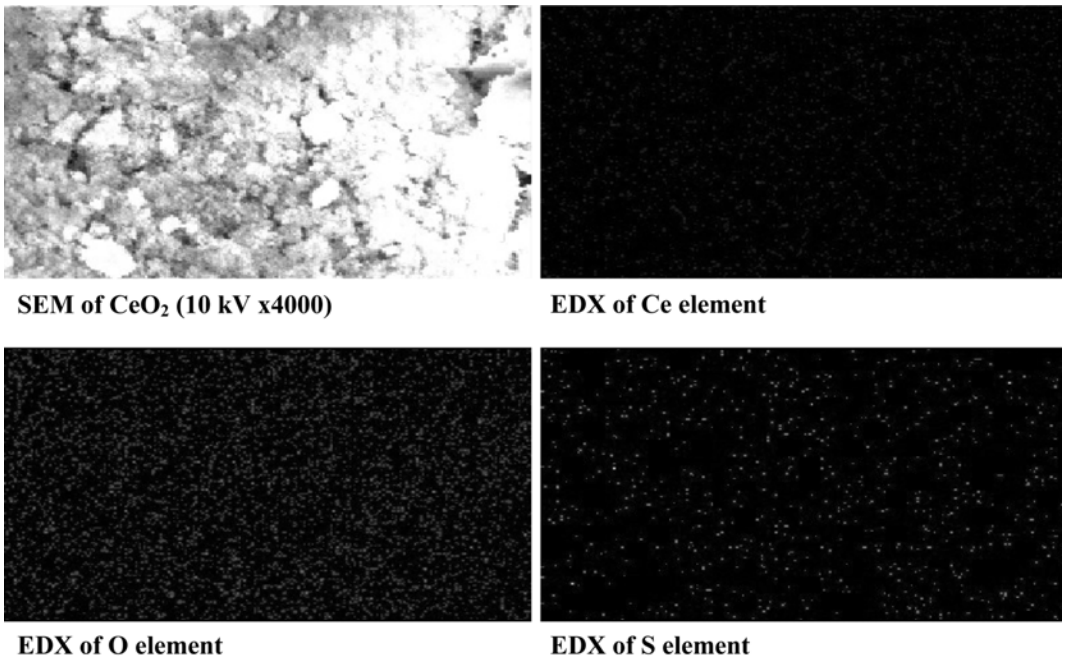

(b) SEM and elemental mapping of CeO_2 sulfided at 800°C

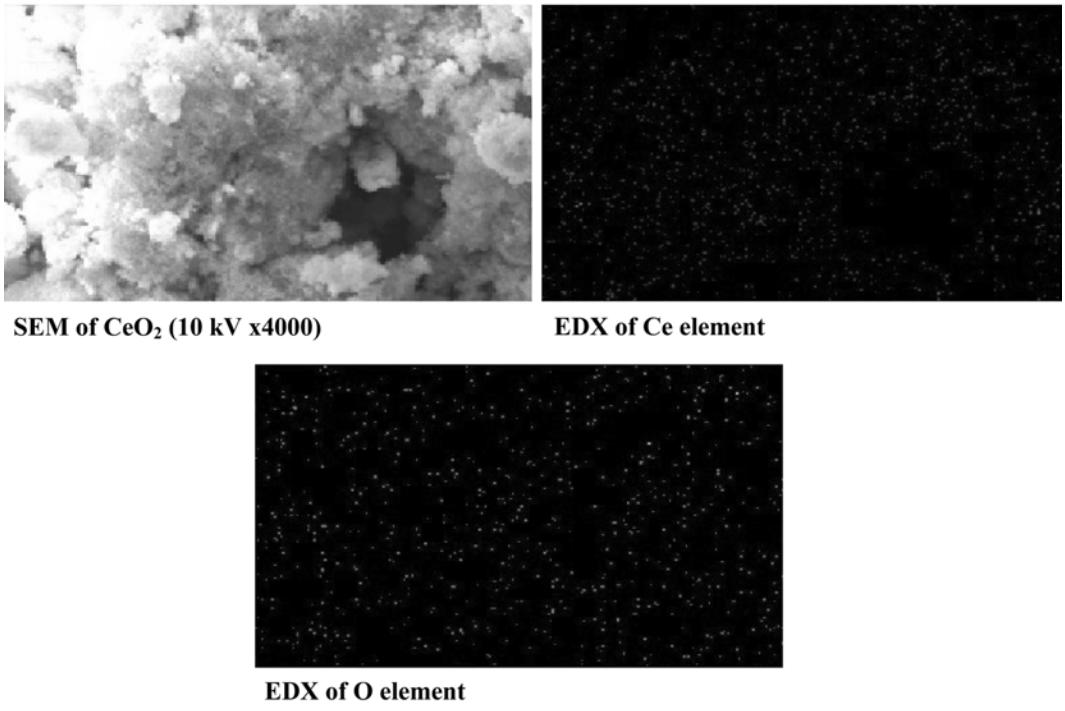

(c) SEM and elemental mapping of regenerated CeO_2

Fig. 6. Continued.

surface of CeO_2 by increasing temperature. It is well established that ceria-based material contains a high concentration of highly mobile oxygen vacancies, which act as local sources or sinks for oxygen involved in reactions taking place on its surface. That high oxygen mobility, high oxygen storage capacity, and its modifiable ability render the ceria-based material very interesting for a wide range of catalytic applications. At higher temperature, the gas-solid reaction between the inlet sulfur compound and the bulk lattice oxygen on the surface of CeO_2 occurred easily, and consequently resulted in a high sulfidation reaction [22]. Previous work from Zeng et al. [14] also reported that the degree of sulfidation increases with increasing temperature.

3. Characterization of Absorbent

Sulfided CeO_2 was subjected to its surface analysis by SEM/EDS and XRD measurements to determine the distribution of sulfur and the type of product formation on the surface of the CeO_2. From the SEM & EDS mapping as shown in Fig. 6, sulfur distribution on the surface of the catalyst was detected. According to the sulfur distribution at 700 and 800 °C, as shown in Figs. 6(a) and 6(b), respectively, the sulfur concentrations at 800 °C are higher than those at 700°C, which is in good agreement with the observed SO_2 peaks shown in Figs. 4 and 5. In addition, from the sulfur mapping observed by the EDS, it was found that the sulfur element was uniformly distributed over the surface of CeO_2. Larger particles in the figure are due to aggregation of smaller particles and the change in the porous structure. As CeO_2 consists of high surface oxygen ions, these ions make it become easily exchanged to sulfur upon H_2S adsorption [23].

In addition to the SEM/EDS measurement, sulfided CeO_2 was subjected to XRD studies to determine the type product formed. From the XRD analysis as shown in Fig. 8, major phases of the sulfided CeO_2 are Ce_2O_2S (Pattern 26-1085). The pattern was compared with that of pure CeO_2 (pattern 34-0394) as shown in Fig. 7. The XRD patterns of spent CeO_2 indicate that the cerium oxide sulfide (Ce_2O_2S) was formed from the reaction of CeO_2 with H_2S. Peaks of spent CeO_2 were decreased and peak broadening occurred at the

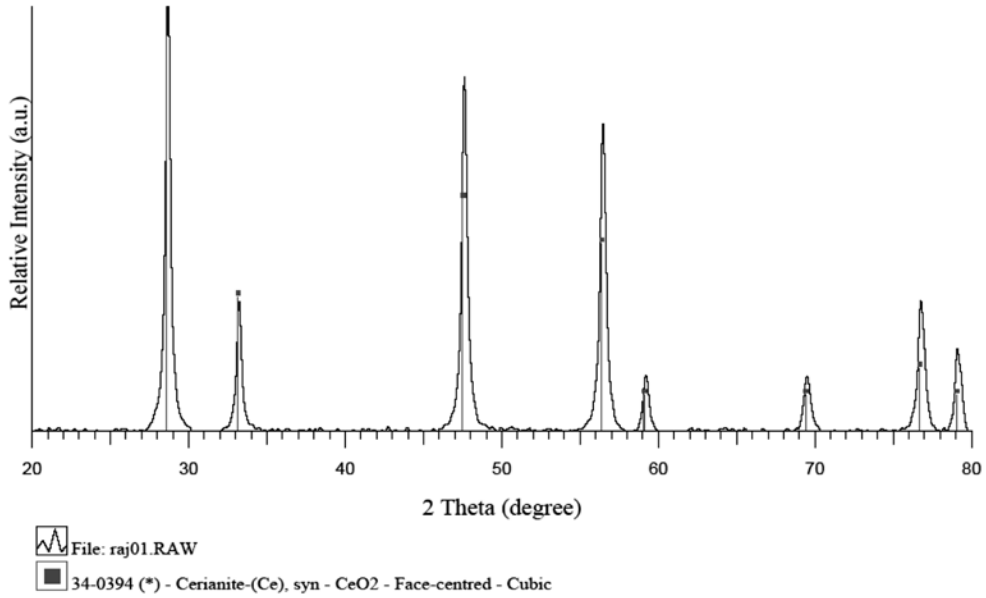

Fig. 7. XRD pattern of pure CeO_2.

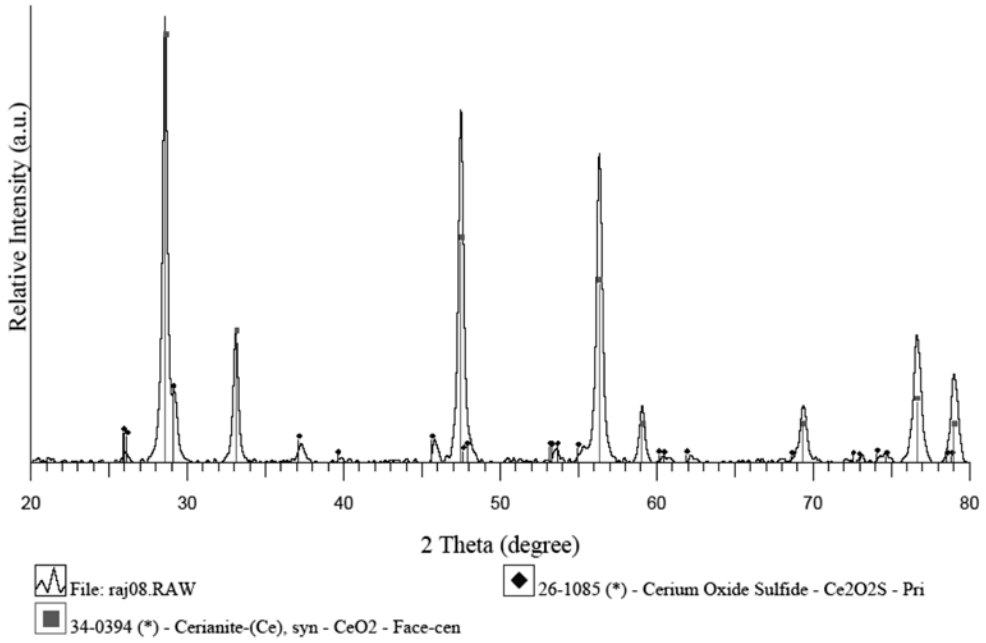

Fig. 8. XRD pattern of CeO_2 sulfided at 800 °C (JCPDS-ICDD).

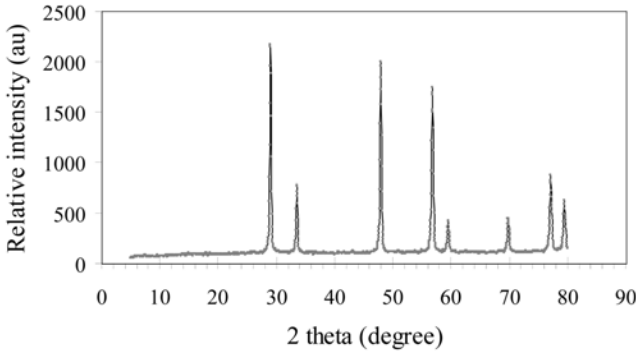

Fig. 9. XRD pattern of regenerated sulfided CeO_2 (JCPDS-ICDD).

CeO_2 peaks due to the formation of Ce_2O_2S. Sulfided CeO_2 was subjected to oxidative regeneration at a constant heating rate of 10 °C min^{-1} until 900 °C. The sample after regeneration was analyzed by XRD to determine its potential reuse as a CeO_2. It was found that the regenerated CeO_2 showed peaks at the same two theta angles as those of pure CeO_2 as shown in Fig. 9. This ensures the possible regeneration of sulfided CeO_2.

From the evidence of sulfidation, regeneration, and catalyst characterization, a sequence of reactions that occurred during these processes can be proposed. The possible reaction mechanism of the sulfidation and regeneration can be predicted as follows:

$$2CeO_2+H_2S \rightarrow Ce_2O_2S+H_2O+0.5O_2 \quad (4)$$

$$Ce_2O_2S+2O_2 \rightarrow SO_2+2CeO_2 \quad (5)$$

It should be noted that the detectable of steam from the desulfurization experiments and the observation of Ce_2O_2S phase from the XRD studies support this proposed sulfidation reaction mechanism: TPO and XRD analysis. The first experiment observed the formation of SO_2 from the regeneration process, while the second one confirmed that CeO_2 can be regenerated.

4. Deactivation Model for CeO_2 Absorbent

Deactivation models proposed in the literature [24] for gas-solid reactions with significant changes of activity of the solid due to textural changes, as well as product layer diffusion resistance during reaction, were reported to be quite successful in predicting conversion-time data. In the early work of Orbey et al. [16] and in the recent work of Suyadal et al. [25], deactivation models were used for the prediction of breakthrough curves in packed adsorption columns. In the present work, a deactivation model is proposed with the following assumptions: isothermal condition, pseudo-steady-state condition, first-order deactivation of the absorbent with respect to the solid surface which can be described in terms of an exponential decrease with time in its available surface, and constant activity throughout the surface of absorbent. The combined equation of mole balance and rate law for the packed bed reactor is given below:

$$Vo \cdot t\frac{dC_{H_2S}}{dt} = -k_o \cdot a(t)C_{H_2S} \quad (6)$$

The boundary conditions at inlet concentrations are

At $t=0$, $C_{H_2S}=C_{H_2Sin}$
At $t=t$, $C_{H_2S}=C_{H_2Sout}$

Therefore,

$$a(t)=\frac{Vo}{Wk}Ln\left(\frac{C_{H_2Sin}}{C_{H_2Sout}}\right) \quad (7)$$

The first order exponential decay is $a(t)=e^{-k_d t}$, substituting Eq. (6) to Eq. (8):

$$-k_d \cdot t = \ln\frac{Vo}{Wk_o} + \ln\ln\left(\frac{C_{H_2Sin}}{C_{H_2Sout}}\right) \quad (8)$$

This equation is equivalent to the breakthrough [25]. Thus, when $\ln\ln(C_{H_2Sin}/C_{H_2Sout})$ is plotted versus operating time (t), a straight line should be obtained with a slope equal to $-k_d$ and intercept equal to $\ln(Vo/Wk_o)$ as shown in Fig. 10. Table 3 summarizes the model parameters determined at different temperatures. The fluctuation of 10 to 15% in correlation coefficient may be due to initial bumps.

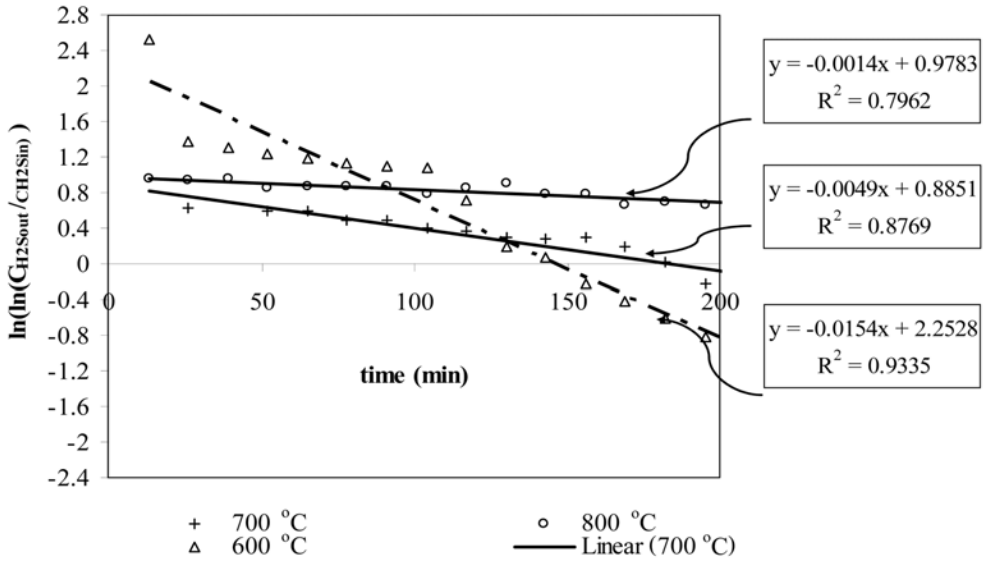

Fig. 10. Test of deactivation model equation.

Table 3. Summary of deactivation model parameters

Temperature (°C)	Vo/Wk$_o$ (-)	k$_o$ (cm^3 min^{-1} g^{-1})	k$_d$ (min^{-1})	R^2 (-)
600	2.55	3.566	0.0144	0.79
700	2.40	1.66	0.0049	0.89
800	2.66	1.503	0.0014	0.9351

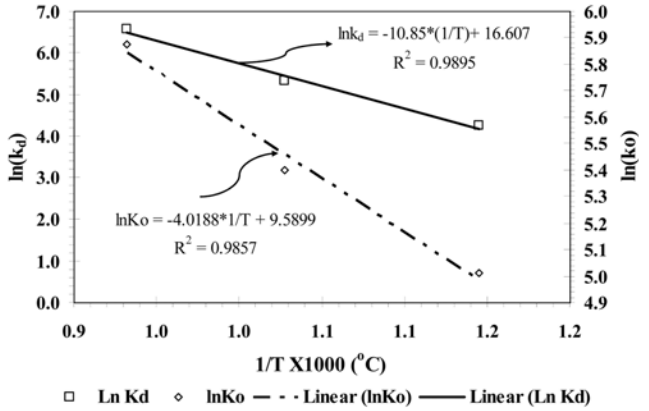

Fig. 11. Arrhenius plots of sorption rate constants and deactivation rate constants.

The advantage of the deactivation model is the presence of only two adjustable parameters such as initial sorption rate constant K_o and the deactivation rate constant K_d. Both parameters showed an increasing trend with respect to an increase in the temperature. Sorption rate constant K_o and the deactivation rate constant K_d were correlated as a function of temperature using by Arrhenius equations (Eqs. (9) and (10)).

$$K_o = k_o e^{-e/RT} \quad (9)$$

$$K_d = k_o e^{-e/RT} \quad (10)$$

The temeprature dependency was illustrated as shown in Fig. 11. The activation energies of k_o and k_d were found to be 33.4 and 90 kJ mol^{-1}. These high values of the activation energies indicate that the H_2S sorption on CeO_2 is chemical adsorption.

CONCLUSION

Nano-scale high surface area CeO_2 has useful desulfurization activity between 500 and 850 °C. Compared to the conventional low surface area CeO_2, 80-85% of H_2S was removed by nano-scale high surface area CeO_2, whereas 30-32% of H_2S was removed by conventional low surface area CeO_2. According to the XRD and EDS mapping, uniform Ce_2O_2S was formed after desulfurization. According to the TPO experiment, this component (Ce_2O_2S) can be recovered to CeO_2 after exposure in the oxidation condition at temperature above 600 °C. Furthermore, regarding the SEM/EDS and XRD measurements, all Ce_2O_2S forming is converted to CeO_2 after this oxidative regeneration.

As the final step, a deactivation model considering the concentration and temperature dependencies of the desulfurization activity was proposed for later application in the SOFC model.

ACKNOWLEDGMENT

The financial support from the Thailand Research Fund (TRF) and the Joint Graduate School of Energy and Environment (JGSEE) throughout this project is gratefully acknowledged. The authors are also thankful to Dr.Nakorn Srisukhumbowornchai for his valuable suggestions on XRD patterns.

REFERENCES

1. D. W. Park, B. H. Hwang, W. D. Ju, M. I. Kim, K. H. Kim and H. C. Woo, *Korean J. Chem. Eng.*, **22**, 190 (2005).
2. J. D. Lee, J. H. Jun, N. K. Park, S. O. Ryu and T. J. Lee, *Korean J. Chem. Eng.*, **22**, 36 (2005).
3. P. R. Westmoreland and D. P. Harrison, *Environ. Sci. Technol.*, **10**, 559 (1976).
4. H. T. Jang, S. B. Kim and D. S. Doh, *Korean J. Chem. Eng.*, **20**, 116 (2003).
5. T. H. Gardener, *Fuel*, **81**, 2157 (2002).
6. J. H. Swisher and K. Schwerdtfeger, *J. Mater. Eng. Perform.*, **1**, 399 (1992).
7. V. Patrick and G. R. Gavalas, *Ind. Eng. Chem. Res.*, **28**, 931 (1989).
8. V. V. Meng and D. A. R. Kay, *High technology ceramics*, Elsevier, Amsterdam, 2247 (1987).
9. D. A. R. Kay, W. G. Wilson and V. Jalan, *J. Alloys and Compounds*, **192**, 11 (1993).
10. K. H. Kim, S. Y. Lee and K. J. Yoon, *Korean J. Chem. Eng.*, **23**, 356 (2006).
11. K. H. Kim, S. Y. Lee, S. W. Nam, T. H. Lim, S. A. Hong and K. J. Yoon, *Korean J. Chem. Eng.*, **23**, 17 (2006).
12. J. Abbasian, A. H. Hill, M. Flytzani-Stephanopoulos and Z. Li, Final Report, DE-FC22-92PC92521 (1994).
13. Z. Li and M. Flytzani-Stephanopoulos, *Ind. Eng. Chem. Res.*, **36**, 187 (1997).
14. Y. Zeng, S. Zhang, F. R. Groves and D. P. Harrison, *Chem. Eng. Sci.*, **54**, 3007 (1999).
15. N. Laosiripojana and S. Assabumrungrat, *Applied Catal. B*, **60**, 107 (2005).
16. N. Orbey, G. Dogu and T. Dogu, *Can. J. Chem. Eng.*, **60**, 314 (1982).
17. H. S. Fogler, *Elements of chemical reaction engineering*, Prentice-Hall Inc, Englewood Cliffs, New Jersey 07632, ISBN 0-13-263476-7 (1986).
18. M. P. Cal, B. W. Strickler and A. A. Lizzio, *Carbon*, **38**, 1757 (2000).
19. R. M. Ferriz, R. J. Gorte and J. M. Vohs, *Applied Catal. B*, **43**, 273 (2003).
20. Z. Wang and M. Flytzani-Stephanopoulos, *Energy & Fuels*, **19**, 2093 (2005).
21. M. Flytzani-Stephanopoulos, Angela D. Surgenor, Report, NASA/TM-2007-214686.
22. S. Yasyerli, G. Dogu and T. Dogu, *Catal. Today*, **117**, 271 (2006).
23. M. Ziolek, *J. Molecular Catalysis A*, **97**, 49 (1995).
24. T. Dogu, *Chem. Eng. J.*, **21**, 213 (1981).
25. Y. Suyadal, M. Erol and H. Oguz, *Ind. Eng. Chem. Res.*, **39**, 724 (2000).

Available online at www.sciencedirect.com
ScienceDirect
Applied Catalysis B: Environmental 82 (2008) 103–113
APPLIED CATALYSIS B: ENVIRONMENTAL
www.elsevier.com/locate/apcatb

Kinetic dependencies and reaction pathways in hydrocarbon and oxyhydrocarbon conversions catalyzed by ceria-based materials

N. Laosiripojana [a,*], S. Assabumrungrat [b]

[a] *The Joint Graduate School of Energy and Environment, King Mongkut's University of Technology Thonburi, Bangkok 10140, Thailand*
[b] *Center of Excellence on Catalysis and Catalytic Reaction Engineering, Department of Chemical Engineering, Chulalongkorn University, Bangkok 10330 Thailand*

Received 8 February 2007; received in revised form 8 January 2008; accepted 16 January 2008
Available online 20 January 2008

Abstract

Hydrocarbons (i.e. CH_4, C_2H_4, C_2H_6, and C_3H_8) and oxyhydrocarbon (i.e. CH_3OH) conversions with and without co-reactants (H_2O and CO_2) were studied over ceria-based materials prepared by precipitation and cationic surfactant-assisted methods with/without Zr doping with an aim to understand their influences on material specific surface area, oxygen storage capacity (OSC), hydrocarbon reaction rate, resistance toward carbon deposition, and rigorous kinetic dependencies.

High surface area CeO_2 and Ce-ZrO_2 from the cationic surfactant-assisted method provided a higher degree of oxygen storage capacity (OSC) and reaction rates with greater resistance toward carbon deposition than those from the precipitation method. The reaction rates (mol g_{cat}^{-1} s^{-1}) per degree of OSC (mol_{Oxygen} g_{cat}^{-1}) were identical for all materials, indicating the linear influence of OSC on the rates. Nevertheless, the kinetic dependencies were unaffected by specific surface area, doping element, degree of OSC and reactions (i.e. H_2O reforming, CO_2 reforming and cracking). The rates were proportional to hydrocarbon partial pressures with positive fraction reaction orders; independent of co-reactant partial pressures; but inhibited by CO and H_2. These kinetic dependencies were explained by a set of redox mechanistic proposal, in which the relevant elementary step is the reaction of intermediate surface hydrocarbon with lattice oxygen (O_O^x), and that lattice oxygen is efficiently replenished by rapid surface reactions with oxygen source from either CO_2, H_2O, or even CH_3OH.

Keywords: Ceria; Oxygen storage capacity; Reforming; Redox mechanistic; Kinetic

1. Introduction

Cerium oxide (or ceria) based material contains a high concentration of mobile oxygen vacancies, which act as local sources or sinks for oxygen involved in reactions taking place on its surface. The high oxygen mobility and oxygen storage capacity render this material very interesting for a wide range of catalytic applications involving oxidation and reforming of hydrocarbons [1–8]. Recently, one of the great potential applications of ceria-based materials is in an Indirect Internal Reforming-Solid Oxide Fuel Cell (IIR-SOFC) as an in-stack reforming catalyst [9,10]. In addition, it is also successfully applied in a direct internal reforming (DIR-SOFC), in which hydrocarbon and oxyhydrocarbon compounds (i.e. C_4H_{10} and CH_3OH) were efficiently reformed at ceria-based anodes (i.e. Cu-CeO_2 and Cu-CeO_2-YSZ) [11–16].

It has been well established that the gas–solid reaction between hydrocarbons and the lattice oxygen (O_x^o) on ceria surface can generate CO and H_2 at high temperature; in addition, the reactions of reduced ceria with oxygen-containing reactants, i.e. CO_2 and H_2O can regenerate the lattice oxygen (O_x^o) on CeO_2 surface [10,17–19]. The great benefit of ceria-based catalysts for reforming reactions is their high resistance toward carbon deposition compared to conventional metal catalysts [9,10]; however, the weaknesses are their low specific surface area and high deactivation due to the thermal sintering particularly when operated at such a high temperature [20]. The use of high surface area ceria (CeO_2 (HSA)) with high resistance toward the sintering was proposed to be a good approach to improve its catalytic reactivity [20]. Several techniques have been described for the preparation of CeO_2 (HSA) solid solution, i.e. homogeneous precipitation techni-

* Corresponding author. Tel.: +66 2 8729014; fax: +66 2 8726736.
E-mail address: navadol_l@jgsee.kmutt.ac.th (N. Laosiripojana).

0926-3373/$ – see front matter © 2008 Elsevier B.V. All rights reserved.
doi:10.1016/j.apcatb.2008.01.009

ques with precipitating agents and additives [21–24], hydrothermal synthesis [25], spray pyrolysis methods [26], inert gas condensation of Ce followed by oxidation [27], thermal decomposition of carbonates [28], microemulsion [29], and electrochemical methods [30]. However, a few of these composites showed regular pore structure after calcination at moderate temperatures and a severe loss of surface area occurs during the thermal treatment [31]. Recently, Terribile et al. [32] synthesized CeO_2 (HSA) with improved textural, structural and chemical properties by using a novel cationic surfactant-assisted approach. They reported that CeO_2 with surface area of 40 $m^2\ g^{-1}$ was achieved after calcination at 1173 K. Compared to conventional CeO_2 (CeO_2 (LSA)) prepared by precipitation technique with surface area less than 10 $m^2\ g^{-1}$ after calcination at 1173 K [10], this highlights the great potential of CeO_2 prepared by surfactant-assisted technique for application as a catalyst under high reaction temperature. It should be noted that, apart from the investigation on preparation method, the addition of zirconium oxide (ZrO_2) has also been widely reported to improve surface area, oxygen storage capacity, redox property, thermal stability and catalytic activity of ceria [33–39].

Focusing on the reforming reactions of hydrocarbon compounds over ceria-based materials, until now, the reaction pathways and kinetic dependencies remains unclear. Here, we thereby probe the kinetic dependencies of hydrocarbons (i.e. CH_4, C_2H_4, C_2H_6, and C_3H_8) and also oxyhydrocarbon (i.e. CH_3OH) conversion with and without co-reactants over ceria-based materials prepared by precipitation and cationic surfactant-assisted methods and with/without Zr doping. The relation between the material specific surface area, doping element, oxygen storage capacity (OSC), reaction rate, resistance toward carbon deposition, and kinetic dependence were identified. A rigorous kinetic, reaction pathways and rate expressions were then established.

2. Experimental methods

2.1. Material synthesis and characterization

CeO_2 was synthesized by precipitation (CeO_2 (LSA)) and cationic surfactant-assisted (CeO_2 (HSA)) methods. These preparation methods were described elsewhere in our previous publication [40]. The materials were dried overnight in ambient air at 383 K, and then calcined in a flow of dry air by increasing the temperature to 1173 K with a rate of 0.167 K s^{-1} and holding at 1173 K for 6 h. After calcined, fluorite-structured CeO_2 with good homogeneity were obtained.

$Ce_{1-x}Zr_xO_2$ (or Ce-ZrO_2) with different Ce/Zr molar ratios were prepared by either co-precipitation or surfactant-assisted method of cerium nitrate ($Ce(NO_3)_3{\cdot}H_2O$), and zirconium oxychloride ($ZrOCl_2{\cdot}H_2O$) (from Aldrich). The ratio between each metal salt was altered to achieve nominal Ce/Zr molar ratios: $Ce_{1-x}Zr_xO_2$, where x = 0.25, 0.50, and 0.75 respectively. After treatment, the specific surface areas of all CeO_2 and Ce-ZrO_2 were achieved from BET measurement. As presented in Table 1, after drying in the oven, surface areas of 105 and 55 $m^2\ g^{-1}$ were observed for CeO_2 (HSA) and CeO_2 (LSA), respectively and, as expected, the surface area decreased at high calcination temperatures. However, the value for CeO_2 (HSA) is still appreciable after calcination at 1173 K. It can also be seen that the introduction of ZrO_2 stabilizes the surface area of ceria, which is in good agreement with several previous reports [41–43]. After treatment, the degree of OSC and redox reversibilities of all CeO_2 and Ce-ZrO_2 were determined by the temperature programmed reduction (TPR-1) and temperature programmed oxidation (TPO) following with second time temperature programmed reduction (TPR-2), respectively, at the same conditions. Details of these measurements are given in Section 3.1.

Table 1
Specific surface areas of ceria-based materials before and after calcination at 1173 K

Catalysts	Surface area after drying ($m^2\ g^{-1}$)	Surface area after calcinations ($m^2\ g^{-1}$)
CeO_2 (HSA)	105	29
Ce-ZrO_2 (HSA) (Ce/Zr = 1/3)	135	49
Ce-ZrO_2 (HSA) (Ce/Zr = 1/1)	120	47
Ce-ZrO_2 (HSA) (Ce/Zr = 3/1)	115	46.5
CeO_2 (LSA)	55	11
Ce-ZrO_2 (LSA) (Ce/Zr = 1/3)	82	22
Ce-ZrO_2 (LSA) (Ce/Zr = 1/1)	74	20.5
Ce-ZrO_2 (LSA) (Ce/Zr = 3/1)	70	20

2.2. Catalytic H_2O and CO_2 reforming and cracking of hydrocarbons

To undergo the catalytic testing, an experimental reactor system was constructed as shown elsewhere [40]. The feed gases including the components of interest, i.e. CH_4, C_2H_4, C_2H_6, C_3H_8, CH_3OH, deionized H_2O (introduced via a syringe pump pass through an evaporator), CO_2, CO, and H_2 were introduced to a 10-mm diameter quartz reactor, which was mounted vertically inside tubular furnace. The catalysts (50 mg of ceria-based catalysts) were diluted with SiC (to obtain the total weight of 500 mg) in order to avoid temperature gradients and loaded in the quartz reactor. Preliminary experiments were carried out to find suitable conditions in which internal and external mass transfer effects are not predominant. Considering the effect of external mass transfer, the total flow rate was kept constant at 100 $cm^3\ min^{-1}$ under a constant residence time of 5×10^{-3} g min cm^{-3} in all testing. The suitable average sizes of catalysts were also verified in order to confirm that the experiments were carried out within the region of isothermal kinetics. In our system, a Type-K thermocouple was placed into the annular space between the reactor and furnace. This thermocouple was mounted in close contact with the catalyst bed to minimize the temperature difference. Another Type-K thermocouple, covering by closed-end quartz tube, was inserted in the middle of the quartz reactor in order to re-check the possible temperature gradient.

Table 2
Results of TPR-1, TPO, TPR-2 analyses of ceria-based materials after calcination

Catalyst	Total H_2 uptake from TPR-1 ($\mu mol/g_{cat}$)	Total O_2 uptake from TPO ($\mu mol/g_{cat}$)	Total H_2 uptake from TPR-2 ($\mu mol/g_{cat}$)
CeO_2 (HSA)	4105	2067	4109
Ce-ZrO_2 (HSA) (Ce/Zr = 1/3)	2899	1475	2876
Ce-ZrO_2 (HSA) (Ce/Zr = 1/1)	3701	1862	3694
Ce-ZrO_2 (HSA) (Ce/Zr = 3/1)	5247	2640	5250
CeO_2 (LSA)	1794	898	1788
Ce-ZrO_2 (LSA) (Ce/Zr = 1/3)	1097	553	1085
Ce-ZrO_2 (LSA) (Ce/Zr = 1/1)	1745	744	1746
Ce-ZrO_2 (LSA) (Ce/Zr = 3/1)	2649	1328	2643

After the reactions, the exit gas mixture was transferred via trace-heated lines (373 K) to the analysis section, which consists of an online Porapak Q column Shimadzu 14B gas chromatograph (GC) with TCD and FID detectors and a mass spectrometer (MS). The GC was applied for the steady state kinetic studies, whereas the MS in which the sampling of the exit gas was done by a quartz capillary and differential pumping was used for the transient experiments. Kinetic effects were studied over wide ranges of temperature and reactant partial pressures.

2.3. Measurement of carbon formation

The temperature programmed oxidation (TPO) was applied to investigate the amount of carbon formed on catalyst surface by introducing 10% O_2 in He into the system, after purging with helium. The operating temperature increased from room temperature to 1273 K by a rate of 10 K min^{-1}. The amount of carbon formation on the surface of catalysts was determined by measuring the CO and CO_2 yields from the TPO results. In addition to the TPO method, the amount of carbon deposition was reconfirmed by the calculation of carbon balance in the system, which theoretically equals to the difference between inlet and outlet carbon containing components.

3. Results and discussion

3.1. Redox properties and redox reversibility

After treatment, the degree of OSC for fresh ceria-based materials were investigated using TPR-1, which was performed by heating the catalysts up to 1273 K in 5%H_2 in He. The amount of H_2 uptake was correlated to the amount of oxygen stored in the catalysts. As presented in Table 2, the amount of H_2 uptakes over Ce-ZrO_2 and CeO_2 (HSA) are significantly higher than those over the low surface area cerias, suggesting the increasing of OSC with the doping of Zr and the increasing of material specific surface area. The benefit of OSC on the reforming reaction will be later presented in Section 3.3.

After purging with He, the redox reversibilities were then determined by applying TPO following with TPR-2. The TPO was carried out by heating the catalyst up to 1273 K in 10%O_2 in He; the amounts of O_2 chemisorbed were then measured, Table 2. Regarding the TPR-2 results as also shown in Table 2, the amount of hydrogen uptakes for all materials were approximately similar to those from the TPR-1, indicating the reversibility of OSC for these synthesized ceria-based materials.

3.2. Reactivity toward the (H_2O and CO_2) reforming and cracking of CH_4

The H_2O reforming, CO_2 reforming and cracking of CH_4 were tested at 1123 K by introducing CH_4 along with co-reactant (for H_2O and CO_2 reforming). It should be noted that the reactions over Ce-ZrO_2 catalysts with different Ce/Zr ratios (1/3, 1/1, and 3/1) were firstly tested. The results revealed that Ce-ZrO_2 with Ce/Zr ratio of 3/1 shows the best performance in terms of stability and activity. Therefore, we report here detailed reactivity and kinetic data of Ce-ZrO_2 only with Ce/Zr ratio of 3/1.

Fig. 1 shows the variations in CH_4 reforming rate ($mol_{CH_4}\, g_{cat}^{-1}\, s^{-1}$) with time at the initial state (10 min; using MS) over Ce-ZrO_2 (HSA) by varying inlet co-reactant/CH_4 ratios from 0.0 (cracking reaction) to 0.3, 0.5, 0.7, 1.0, and 2.0, while Fig. 2 shows the stability and activity (under the period of 10 h; using GC-TCD) of H_2O and CO_2 reforming of CH_4 over several catalysts. The reforming rates expressed in the figures are obtained from the relation between the measured net reaction rate (r_m; $mol_{CH_4}\, g_{cat}^{-1}\, s^{-1}$) and the approach to equilibrium condition (η) using the following equation [44]:

$$r_t = r_m(1-\eta)^{-1} \tag{1}$$

where η is either the approach to equilibrium for H_2O reforming (η_s) or for CO_2 reforming (η_d). Both parameters are determined from the following equation:

$$\eta_s = \frac{[P_{CO}][P_{H_2}]^3}{[P_{CH_4}][P_{H_2O}]}\frac{1}{K_s} \tag{2}$$

$$\eta_d = \frac{[P_{CO}]^2[P_{H_2}]^2}{[P_{CH_4}][P_{CO_2}]}\frac{1}{K_d} \tag{3}$$

where P_i is partial pressure of component i (atm); K_s and K_d are the equilibrium constants for H_2O and CO_2 reforming of CH_4 at a given temperature. It should be noted that, in the present work, the values of η were always kept below 0.2 in all experiments.

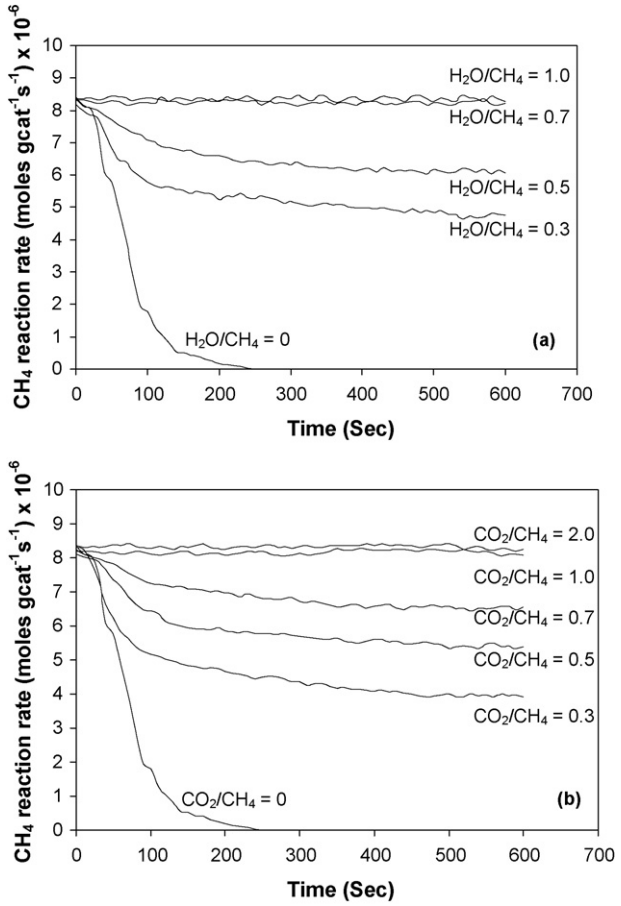

Fig. 1. CH_4 reaction rate at initial state (10 min) for H_2O reforming of CH_4 (a) and CO_2 reforming of CH_4 (b) over Ce-ZrO_2 (HSA) (1123 K with 3 kPa CH_4 in He).

The main products from the reactions over these catalysts were H_2 and CO with some CO_2, indicating a contribution from the water–gas shift at this high temperature. Based on the measured concentrations of reactants and products during CH_4 reforming, the approach to water-gas shift equilibrium condition (η_{WGS}) in the range of temperature studied (1023–1123 K) are always close to 1.0 in all type of catalysts, indicating that water–gas shift (WGS) reaction is at equilibrium. Fig. 1 indicates that the initial CH_4 reforming rate is unaffected by the concentration and type of co-reactants. Nevertheless, significant deactivation was observed for the cracking of CH_4 due to the loss of lattice oxygen (O_O^x) on the surface of ceria-based materials without the replacement by external oxygen containing sources (i.e. H_2O and CO_2). The rate of deactivation rapidly reduced when small content of H_2O or CO_2 was added.

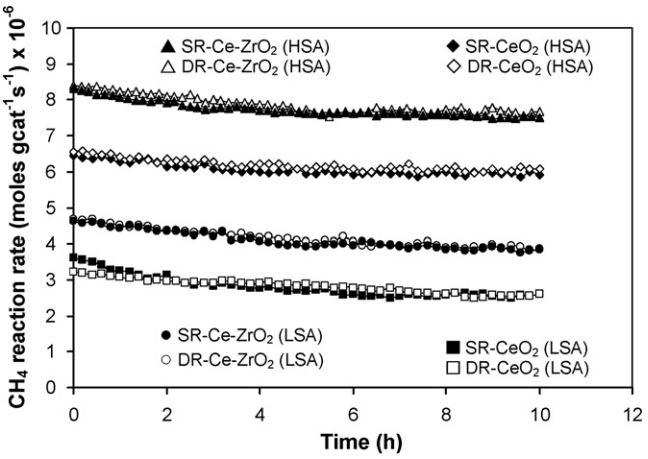

Fig. 2. Stability and activity testing of H_2O reforming (SR) and CO_2 reforming (DR) of CH_4 over several catalysts (at 1123 K with 3 kPa CH_4 and 3 kPa co-reactants).

Fig. 2 indicates that, at steady state, the high surface area materials showed much higher reactivity toward the CH_4 reforming than the low surface area one. Nevertheless, it should be noted that the CH_4 reaction rates ($mol_{CH_4}\ g_{cat}^{-1}\ s^{-1}$) per surface area ($m^2\ g^{-1}$) (in Table 1) for each type of catalyst with different surface areas are in the same range, e.g. $2.0-2.2 \times 10^{-7}\ mol_{CH_4}\ (m^2\ s)^{-1}$ for CeO_2, $1.0-1.1 \times 10^{-7}\ mol_{CH_4}\ (m^2\ s)^{-1}$ for Ce-ZrO_2 (Ce/Zr = 1/1), and $1.6-1.8 \times 10^{-7}\ mol_{CH_4}\ (m^2\ s)^{-1}$ for Ce-ZrO_2 (Ce/Zr = 3/1) (with the operating conditions of 3 kPa CH_4 at 1123 K) indicating the great impact of catalyst specific surface area on the rate. In addition, importantly, at the same reaction conditions, the CH_4 reaction rates ($mol_{CH_4}\ g_{cat}^{-1}\ s^{-1}$) per degree of OSC ($mol_{Oxygen}\ g_{cat}^{-1}$) (in Table 2) for all catalyst are approximately identical ($2.8 \times 10^{-3}\ mol_{CH_4}\ mol_{oxygen}^{-1}\ s^{-1}$ for the inlet CH_4 of 3 kPa at 1123 K) indicating the linear influence of OSC on the reforming reactivity.

After purging in helium, the TPO detected small amount of carbon on the surface of materials from CH_4 cracking reaction (between 0.09 and 0.15 mmol g_{cat}^{-1} for high surface area materials and between 0.18 and 0.21 mmol g_{cat}^{-1} for low surface area one). These amounts of carbon deposited were ensured by the calculation of carbon balance. Regarding the calculation, the moles of carbon remaining in the system were 0.07–0.14 mmol g_{cat}^{-1} for high surface area materials and were 0.20 ± 0.01 mmol g_{cat}^{-1} for low surface area materials, which are in good agreement with the values observed from the TPO. No carbon formation was observed on high surface area materials when the inlet H_2O/CH_4 and CO_2/CH_4 ratios were higher than 0.7 and 1.0, whereas low surface area materials required inlet H_2O/CH_4 and CO_2/CH_4 ratios higher than 1.0 and 2.0 to operate without detectable carbon. The good resistance toward carbon deposition for ceria-based materials, which has been widely reported by previous researchers [9–10], is mainly due to their sufficient oxygen storage capacity (OSC). It should be noted that we observed high amount of carbon formation on the surface of Ni catalysts after exposure in the same reforming conditions as ceria-based materials [45,46]. Regarding the possible carbon formation during the reforming processes, the following reactions are theoretically the most probable reactions that could lead to carbon formation:

$$2CO \Leftrightarrow CO_2 + C \quad (4)$$

$$CH_4 \Leftrightarrow 2H_2 + C \quad (5)$$

$$CO + H_2 \Leftrightarrow H_2O + C \quad (6)$$

$$CO_2 + 2H_2 \Leftrightarrow 2H_2O + C \quad (7)$$

At low temperature, reactions (6) and (7) are favorable, while reactions (4) and (5) are thermodynamically unflavored [47]. The Boudouard reaction (Eq. (4)) and the decomposition of CH_4 (Eq. (5)) are the major pathways for carbon formation at such a high temperature as they show the largest changes in Gibbs energy [48]. According to the range of temperature in this study, carbon formation would be formed via the decomposition of CH_4 and Boudouard reactions especially at high inlet CH_4/co-reactant ratio. By applying CeO_2, both reactions (Eqs. (4) and (5)) could be inhibited by the redox reaction between the surface carbon (C) forming via the adsorptions of CH_4 and CO (produced during the reforming process) with the lattice oxygen (O_O^x) at CeO_2 surface (Eq. (8)).

$$C + O_O^x \rightarrow CO + V_O^{\bullet\bullet} + 2e' \quad (8)$$

Using the Kroger–Vink notation, $V_O^{\bullet\bullet}$ denotes as an oxygen vacancy with an effective charge 2^+, and e' is an electron which can either be more or less localized on a cerium ion or delocalized in a conduction band. The greater resistance toward carbon deposition for high surface area ceria-based catalyst particularly Ce-ZrO_2 (HSA) is due to the significant higher amount of lattice oxygen (O_O^x) on their surfaces, according to the results in Section 3.1.

3.3. Kinetic dependencies of forward CH_4 reforming rate on partial pressures of reactants (i.e. CH_4 and H_2O or CO_2) and products (CO and H_2)

The kinetic dependencies of CH_4 reforming rates on the partial pressures of CH_4, H_2O, CO_2, CO, and H_2 for all ceria-based materials were studied in the temperature range of 1023–1123 K. All measurements were carried out under the operating conditions without detectable carbon formation by controlling H_2O/CH_4 and CO_2/CH_4 inlet ratios according to the results from Section 3.2.

Fig. 3 shows the effect of CH_4 partial pressure on the rate ($mol_{CH_4}\ mol_{oxygen}^{-1}\ s^{-1}$) over Ce-$ZrO_2$ (HSA) at several reaction temperatures, while Fig. 4 shows the effect of CH_4 partial pressure on the rate (per degree of OSC) over different catalysts

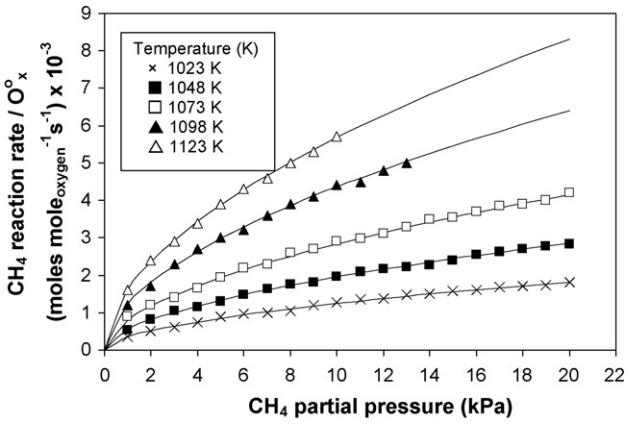

Fig. 3. Effect of temperature on CH_4 steam reforming over Ce-ZrO_2 (HSA) (with inlet CH_4/H_2O of 1.0).

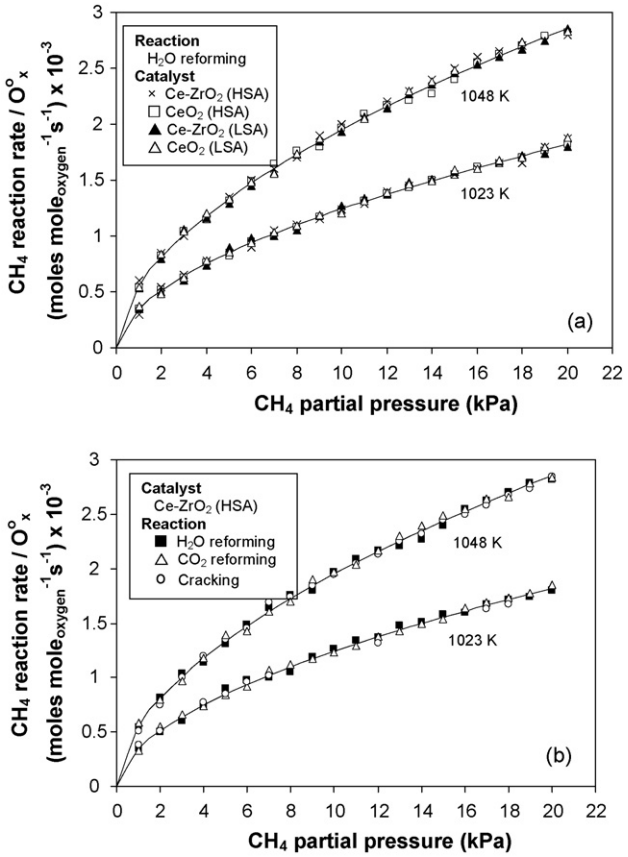

Fig. 4. Effect of CH_4 partial pressure on CH_4 reaction rate (per moles of oxygen stored) over different catalysts (a) and different reactions (b).

(Fig. 4a) and different reactions (i.e. H_2O reforming, CO_2 reforming and cracking (initial rates) of CH_4) (Fig. 4b). The rate increased with increasing CH_4 partial pressures and operating temperature for all catalysts and reactions. The reaction order in CH_4 was determined by plotting $\ln(r_t)$ versus $\ln \ln P_{CH_4}$ (the effects of product concentrations are taken into account via the term equilibrium condition (η)). The reaction orders in other components (CO_2, H_2O, H_2, and CO) were achieved using the same approach. The reaction order in CH_4 was observed to be positive fraction values approximately 0.52 ($\pm$0.03) for all catalysts and reactions, and seemed to be independent of temperature and co-reactant (CO_2 and H_2O) partial pressures in the range of conditions studied.

Several inlet CO_2 or H_2O partial pressures were then introduced to the feed with constant CH_4 partial pressure in order to investigate the influence of these co-reactant partial pressures on the rate. Fig. 5 shows the effects of co-reactant on CH_4 reaction rate with several inlet CH_4 partial pressures over different reactions (Fig. 5a) and over different catalysts (Fig. 5b). It is clear that the rates were not influenced by H_2O and CO_2 partial pressures; thus, the reaction orders in both components would be zero. The reforming in the presences of CO and H_2 were also investigated by adding either CO or H_2 to the feed gas at several operating temperatures. The results in Figs. 6 and 7 showed that the rates are dependent on both CO and H_2 concentrations. Unlike CH_4, both components inhibited the rate. The reaction order in CO was in the range of -0.15 to

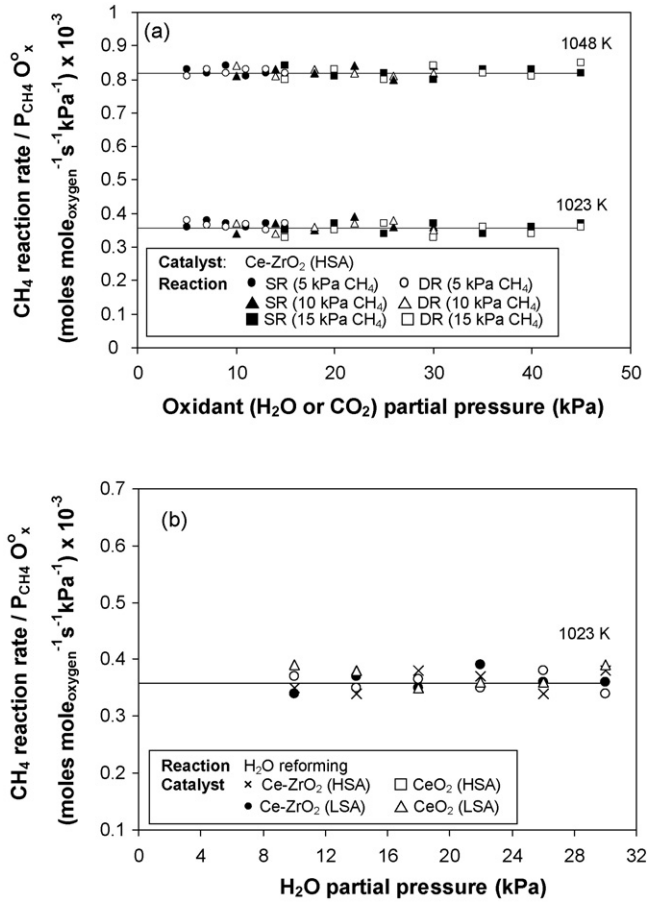

Fig. 5. Effect of co-reactant on CH_4 reaction rate (per moles of oxygen stored and inlet CH_4 partial pressure) over different reactions (with several inlet CH_4 partial pressures) (a) and different catalysts (b).

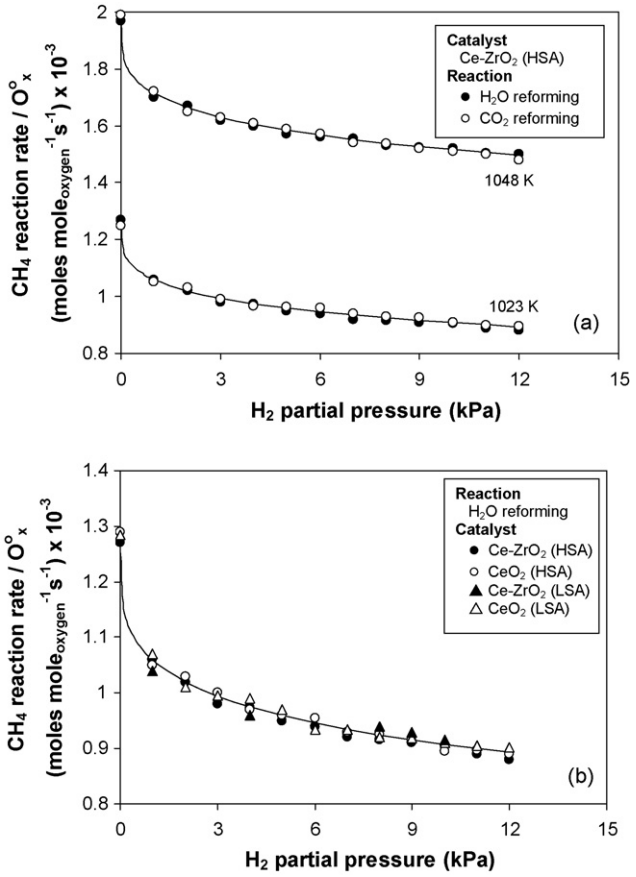

Fig. 6. Effect of H_2 on CH_4 reaction rate (per moles of oxygen stored) over different reactions (a) and different catalysts (b).

-0.12, while the reaction order in H_2 was between -0.31 and -0.28 for all catalysts. Similar reaction orders and kinetic constants for all ceria-based materials indicate that the kinetic dependencies are not affected by the specific surface area (or degree of OSC) and the doping of Zr.

Some previous researchers have proposed the redox mechanism to explain the reforming behavior of ceria-based catalysts [9,10]. They indicated that the reforming reaction mechanism involves the reaction between methane, or an intermediate surface hydrocarbon species, and lattice oxygen at the ceria-based material surface [9]. During reforming reaction, the isothermal reaction rate reaches steady state where the co-reactant, i.e. steam, provides a continuous source of oxygen. They also proposed that the controlling step is the reaction of methane with ceria, and that oxygen is replenished by a significantly more facile surface reaction of the ceria with steam [9]. Therefore, we suggested here that the CH_4 reaction pathway for ceria-based materials involves the reaction between absorbed CH_4 (forming intermediate surface hydrocarbon species) with the lattice oxygen (O_O^x) at CeO_2 surface, as illustrated schematically below.

CH_4 adsorption

$$CH_4 + 2* \rightarrow CH_3* + H* \quad (9)$$

$$CH_3* + * \rightarrow CH_2* + H* \quad (10)$$

$$CH_2* + * \rightarrow CH* + H* \quad (11)$$

$$CH* + * \rightarrow C* + H* \quad (12)$$

Co-reactant (H_2O and CO_2) adsorption

$$H_2O + 2* \Leftrightarrow OH* + H* \quad (13)$$

$$OH* + * \Leftrightarrow H* + O* \quad (14)$$

$$CO_2 + 2* \Leftrightarrow CO* + O* \quad (15)$$

Redox reactions of lattice oxygen (O_O^x) with C* and O*

$$C* + O_O^x \rightarrow CO* + V_O^{\bullet\bullet} + 2e' \quad (16)$$

$$V_O^{\bullet\bullet} + 2e' + O* \Leftrightarrow O_O^x + * \quad (17)$$

Inhibitory effects of CO and H_2

$$H_2 + 2* \Leftrightarrow H* + H* \quad (18)$$

$$H* + O_O^x \Leftrightarrow OH* + V_O^{\bullet\bullet} + 2e' \quad (19)$$

$$CO + * \Leftrightarrow CO* \quad (20)$$

$$CO* + O_O^x \Leftrightarrow CO_2* + V_O^{\bullet\bullet} + 2e' \quad (21)$$

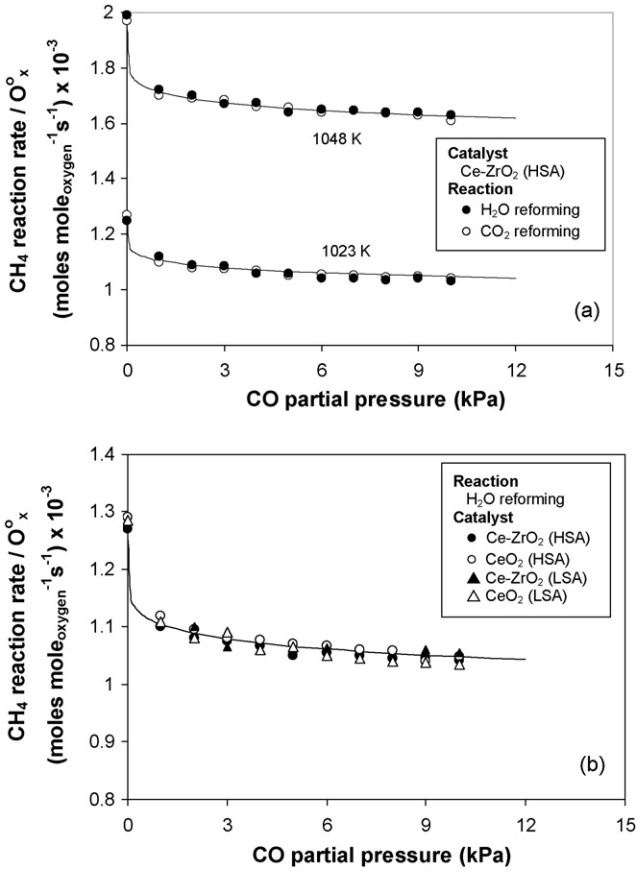

Fig. 7. Effect of CO on CH_4 reaction rate (per moles of oxygen stored) over different reactions (a) and different catalysts (b).

where * is the surface active site of ceria-based materials. During the reactions, CH_4 adsorbed on * forming intermediate surface hydrocarbon species (CH^*_x) (Eqs. (9–12)) and later reacted with the lattice oxygen (O_O^x) (Eq. (16)). The steady-state reforming rate is due to the continuous supply of the oxygen source by either CO_2 or H_2O (Eqs. (13–15)) that reacted with the reduced-state catalyst to recover lattice oxygen (O_O^x) (Eq. (17)). The identical rate for the H_2O and CO_2 reforming at similar CH_4 partial pressures, as well as the stronger linear dependence of the reforming rate on CH_4 partial pressure with the positive fraction value of reaction order in this component, and the independent effects of CO_2 and H_2O provide the evidence that the sole kinetically relevant elementary step is the reaction of intermediate surface hydrocarbon species with the lattice oxygen (O_O^x), and that oxygen is replenished by a significantly rapid surface reaction of the reduced state with the oxygen source from either CO_2 or H_2O; this fast step maintains the lattice oxygen (O_O^x) essentially unreduced by adsorbed intermediate surface hydrocarbon. The unchanged state of lattice oxygen was confirmed by the calculation of oxygen balance during reactions and TPO after reactions. We have used these methods to probe the state of lattice oxygen, because characterizations of used catalysts are not practical due to the low catalyst amounts used and its mixing with SiC. According to the oxygen balance calculation, the mole of oxygen (from co-reactant) fed into the system was almost similar to that in the products for all reactions and testing times indicating the unchanged state of CeO_2 (to CeO_{2-x}) during the experiments. Furthermore, the TPO results after reactions also proved the unchanged state of material, as no oxygen uptakes were detected.

The negative effects of CO and H_2 are due to the reactions between these adsorbed components (CO* and H*) with the lattice oxygen (O_O^x) (Eqs. (18–21)), which consequently result in the inhibition of CH_4 conversion. From all observation, a simple CH_4 reaction rate expression for H_2O reforming, CO_2 reforming and cracking (initial rate) can be written as following:

$$\text{Rate} = \frac{k[P_{CH_4}]^{0.5}}{1 + K_H[P_{H_2}]^{0.3} + K_{CO}[P_{CO}]^{0.15}} \quad (22)$$

where P_i is the partial pressure of chemical component i, k is the rate constant, and K_{CO} and K_H are adsorption parameters, obtained from Van't Hoff equation. The rate constants (k) and the activation energies measured from the H_2O reforming, CO_2 reforming and cracking (initial rate) of CH_4 are identical

Table 3
CH_4 reaction rate, rate constant and activation energies for CH_4 reactions on ceria-based materials (1048 K, 10 kPa CH_4 balance in He)

Catalysts	Reaction	CH_4 reaction rate/O_O^x (moles mole$_{oxygen}^{-1}$ s^{-1}) × 10^{-3}	Rate constant (s^{-1} kPa^{-1}) × 10^{-3}	Activation energy (kJ mol^{-1})
CeO_2 (HSA)	H_2O reforming	1.96	0.53	154.2
	CO_2 reforming	1.98	0.55	155.0
	Cracking	1.95[a]	0.53	151.8
Ce-ZrO_2 (HSA)	H_2O reforming	1.97	0.54	154.2
	CO_2 reforming	1.95	0.52	153.4
	Cracking	1.94	0.55	150.9
CeO_2 (LSA)	H_2O reforming	1.96	0.56	154.9
	CO_2 reforming	1.95	0.54	152.1
	Cracking	1.96	0.57	154.3
Ce-ZrO_2 (LSA)	H_2O reforming	1.95	0.56	155.2
	CO_2 reforming	1.94	0.55	154.4
	Cracking	1.97	0.55	153.2

[a] Initial CH_4 reaction rate.

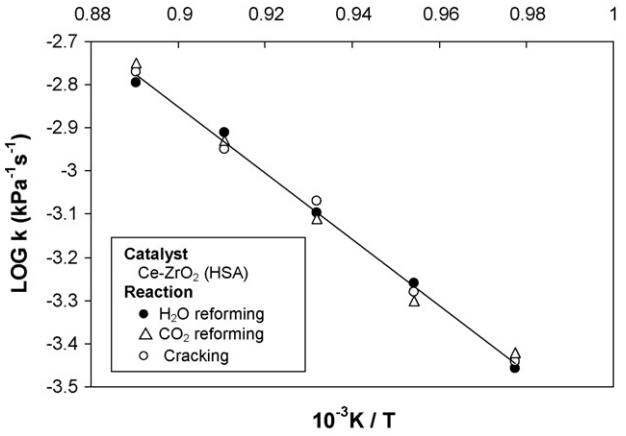

Fig. 8. Arrhenius plots for H_2O reforming, CO_2 reforming and cracking of CH_4 over Ce-ZrO_2 (HSA).

at each reaction temperature, Table 3. The activation energies for these three reactions, achieved by the Arrhenius plots as shown in Fig. 8, were between 150 and 155 kJ mol^{-1}, which are in good agreement with the values previously reported [9–10]. Due to the identical CH_4 reaction rates, the reaction order in CH_4, the rate constants, and the activation energies for all H_2O reforming, CO_2 reforming and cracking of CH_4, it could be concluded that all three reactions over ceria-based materials have similar reaction pathways in CH_4 activity.

3.4. Reactivity toward reforming and decomposition of oxyhydrocarbon

The decompositions of CH_3OH with and without co-reactant elements (i.e. H_2O and CO_2) were studied to confirm the above redox mechanism. The feed condition was co-reactant/CH_3OH in helium with the several molar ratios in the temperature range of 873–1073 K (to prevent the influence of homogeneous non-catalytic reaction). It should be noted according to our experimental results that, similar to CH_4 reforming, the reaction rate (per degree of OSC) and the kinetic dependencies of CH_3OH reaction rates were identical for all ceria-based materials, except the requirement of inlet co-reactant partial pressure to operate without detectable carbon formation. We thereby report here detailed reactivity and kinetic data only on Ce-ZrO_2 (HSA) sample.

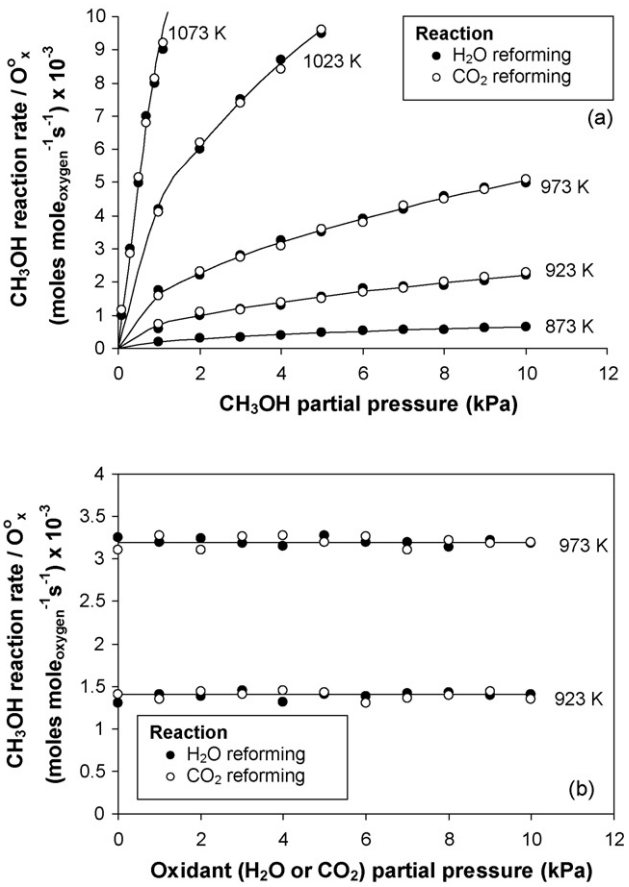

Fig. 9. Effects of CH_3OH partial pressure (a) and co-reactant partial pressure (b) on CH_3OH reaction rate (per moles of oxygen stored) over Ce-ZrO_2 (HSA).

After operation for 10 h, the main products from the reaction were H_2, CO, and CO_2, with small amount of CH_4 depending on the operating conditions, Table 4. According to the TPO, no carbon formation was observed in all studies. The effects of CH_3OH, H_2O, CO_2, CO and H_2 partial pressures on the rate was then studied by varying inlet CH_3OH partial pressure from 1 to 10 kPa (Fig. 9a) and changing the inlet co-reactant (H_2O or CO_2) partial pressure from 0 to 10 kPa (while keeping CH_3OH partial pressure constant at 4 kPa) (Fig. 9b). The results show that the reaction rate was proportional to CH_3OH concentration with the reaction order of 0.50 (±0.04). The rate was unaffected by H_2O and CO_2 partial pressures, in contrast, it was inhibited by the presence of H_2 and CO in the feed. The reaction orders in

Table 4
Reaction rate and fraction of by-products from the H_2O reforming of CH_3OH on Ce-ZrO_2 (HSA) at several temperature and various inlet H_2O/CH_3OH ratios (3 kPa CH_3OH balance in He)

Temperature (K)	H_2O/CH_3OH ratio	CH_3OH reaction rate/O_O^x (moles $mole_{oxygen}^{-1}$ s^{-1}) × 10^{-3}	Yield of H_2 production (%)	Fraction of by-products (%)		
				CO	CO_2	CH_4
923	0.0	1.21	24.5	46.6	17.5	35.9
973	0.0	2.77	34.9	68.1	16.7	15.2
1023	0.0	7.45	42.8	85.1	14.9	0
1023	1.0	7.44	44.1	77.2	22.8	0
1023	2.0	7.46	45.9	70.3	29.7	0
1023	3.0	7.42	47.7	64.2	35.8	0

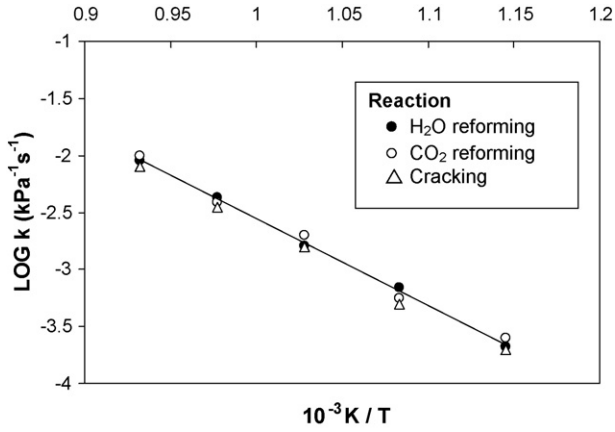

Fig. 10. Arrhenius plots for H_2O reforming, CO_2 reforming and cracking of CH_3OH over Ce-ZrO_2 (HSA).

H_2 and CO were between −0.28 (±0.01) and −0.13 (±0.02), respectively. The activation energies for H_2O reforming, CO_2 reforming and cracking of CH_3OH, achieved by the Arrhenius plots (Fig. 10), were 150–155 kJ/mol, which are closed to those observed from the CH_4 reactions. Therefore, based on the redox mechanistic proposal for CH_4 reaction, we suggested that the CH_3OH reaction mechanism over ceria-based materials could be written as followings:

$$CH_3OH + 2* \rightarrow CH_3* + OH* \quad (23)$$

$$CH_3* + 3* \rightarrow C* + 3H* \quad (24)$$

$$C* + O_O{}^x \rightarrow CO* + V_O{}^{\bullet\bullet} + 2e' \quad (25)$$

$$OH* + * \Leftrightarrow H* + O* \quad (26)$$

$$V_O{}^{\bullet\bullet} + 2e' + O* \Leftrightarrow O_O{}^x + * \quad (27)$$

CH_3OH first adsorbed on * forming intermediate surface hydrocarbon species (CH_x*) and OH* (Eq. (23)). Similar to CH_4 reforming, the intermediate surface hydrocarbons then adsorbed on the active surface site and reacted with the lattice oxygen ($O_O{}^x$) (Eqs. (24) and (25)). The steady-state reforming rate is due to the continuous supply of the oxygen containing compounds present in the system (i.e. H_2O, CO_2 and also CH_3OH) to regenerate the lattice oxygen ($O_O{}^x$). The dependence of the CH_3OH decomposition rate on CH_3OH partial pressure without the co-reactant requirement and its independence of the co-reactant partial pressures indicate that the lattice oxygen ($O_O{}^x$) is replenished by a sufficiently rapid reaction of the partially reduced state with the oxygen containing molecules in CH_3OH. The unchanged state of material was also confirmed by the calculation of oxygen balance during reactions and TPO after reactions.

The capability to decompose CH_3OH without requirement of steam is the great advantage of ceria-based materials for applying in SOFC system. Without the presence of steam being required, the consideration of water management in SOFC system is negligible and it is expected to simplify the overall SOFC system design, making SOFC more attractive to be used commercially.

3.5. Reactivity toward the high hydrocarbons (C_2H_4, C_2H_6, and C_3H_8) reforming

We again report here details only on Ce-ZrO_2 (HSA) sample, as the kinetic dependencies for these hydrocarbons were identical for all ceria-based materials. The feed was hydrocarbon (either C_2H_4, C_2H_6, or C_3H_8) and co-reactant (either H_2O or CO_2) in He. Catalyst reactivity and the product selectivities are given in Table 5. At 923 K, the main products from the reforming reactions were CH_4, H_2 CO, and CO_2. The formation of C_2H_4 was also observed toward the reforming of C_3H_8 and C_2H_6. From the studies, H_2 and CO selectivities increased with increasing temperature, whereas CO_2 and C_2H_4 selectivities decreased. The dependence of CH_4 selectivity on the operating temperature was non-monotonic; maximum CH_4 production occurred at approximately 1073 K (43.8%, 30.6% and 23.5% from steam reforming of C_2H_4, C_2H_6, and C_3H_8, respectively). These observations are in good agreement with our previous work, which studied the effect of temperature on the steam reforming of ethanol, ethane and ethylene over CeO_2 [49]. The decreases in CH_4 and C_2H_4 selectivities at higher temperature could be due to the further reforming to generate more CO and H_2. From the TPO testing, the amount of carbon deposited decreased with increasing inlet co-reactant concentration. At H_2O/hydrocarbons molar ratio higher than 3.0 and CO_2/hydrocarbons molar ratio higher than 5.0, no carbon formation was detected on the surface of Ce-ZrO_2 (HSA).

The influences of inlet component partial pressures on the reaction rate were then studied under the operating conditions without detectable carbon formation by changing the inlet

Table 5
Reaction rate and fraction of by-products from the H_2O and CO_2 reforming of C_nH_m on Ce-ZrO_2 (HSA) (923 K, 3 kPa C_nH_m and 15 kPa co-reactant, balance in He)

Reactant	Co-reactant	C_nH_m reaction rate/$O_O{}^x$	Yield of H_2 production (%)	Fraction of by-products (%)				Activation energy (kJ mol^{-1})
				C_2H_4	CH_4	CO	CO_2	
C_2H_4	H_2O	2.04[a]	26.7	–	40	48.2	11.8	150.4
	CO_2	2.10	15.5					151.9
C_2H_6	H_2O	2.85	29.9	9.3	28.6	49.2	12.9	148.6
	CO_2	2.78	18.4					147.5
C_3H_8	H_2O	5.39	34.3	18.6	20.3	48.5	12.6	145.0
	CO_2	5.44	22.1					149.7

[a] (moles $mole^{-1}_{oxygen}$ s^{-1}) × 10^{-3}.

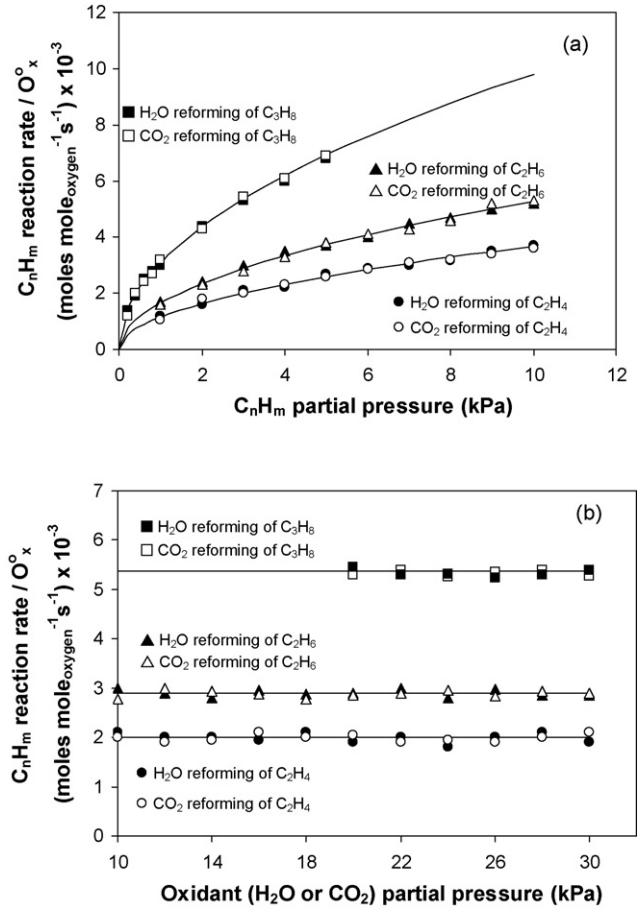

Fig. 11. Effects of C_nH_m partial pressures (a) and co-reactant partial pressure (b) on C_nH_m reaction rate (per moles of oxygen stored) over Ce-ZrO_2 (HSA) at 923 K.

hydrocarbon and co-reactant partial pressures as represented in Fig. 11a and b. Similar trends as CH_4 and CH_3OH reforming were observed. The reforming rate was proportional to the hydrocarbons concentration with the reaction orders in all hydrocarbons between 0.53 and 0.55. The rate was independent of inlet H_2O and CO_2 partial pressures, but it was inhibited by the presence of H_2 and CO in the feed. Fig. 12 shows the

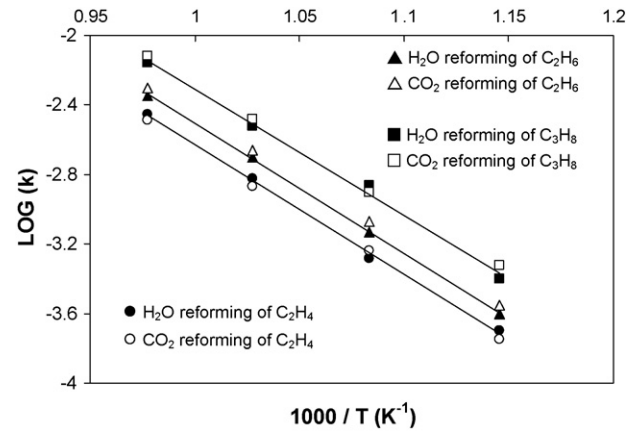

Fig. 12. Arrhenius plots for H_2O and CO_2 reforming of C_nH_m over Ce-ZrO_2 (HSA).

Arrhenius plots for both H_2O and CO_2 reforming of C_nH_m over Ce-ZrO_2 (HSA). The observed activation energies for these C_nH_m reactions were in the same range as achieved from the CH_4 and CH_3OH reactions (145–152 kJ mol^{-1}). Therefore, it can also be summarized that the mechanisms for H_2O and CO_2 reforming of high hydrocarbon are almost similar to those of CH_4 except that the adsorptions of these hydrocarbon elements (Eqs. (28–30)) are applied instead of the CH_4 adsorption. In addition, the reforming of high hydrocarbons requires considerably higher content of co-reactant at the feed in order to operate properly without the problem of carbon deposition.

$$C_3H_8 + 3* \rightarrow 2(CH_3*) + CH_2* \quad (28)$$

$$C_2H_6 + 2* \rightarrow 2CH_3* \quad (29)$$

$$C_2H_4 + 2* \rightarrow 7CH_2* \quad (30)$$

The capability to reform high hydrocarbon compounds with excellent resistance toward carbon deposition is another great benefit of ceria-based catalysts. Currently, natural gas and liquid petroleum gas (LPG) are the most promising primary fuels for the production of H_2 via reforming process. In order to reform these fuels, either an external pre-reforming unit or expensive noble metal catalysts (i.e. Rh) is normally required. By applying high surface area ceria-based materials as the reforming catalyst, all hydrocarbon elements can be reformed properly without the problem of carbon deposition eliminating the requirements of these costly processes.

4. Conclusion

High surface area CeO_2 and Ce-ZrO_2 provided higher CH_4, C_2H_4, C_2H_6, C_3H_8 and CH_3OH reforming rates with greater resistance toward carbon deposition than conventional Ce-ZrO_2 and CeO_2. The rates per amount of oxygen stored (moles $mol_{Oxygen}^{-1} s^{-1}$) on the surface of all ceria sample were in the same range, indicating the linear influence of OSC on the reaction rates. The kinetic dependencies of hydrocarbon conversions and the activation energies over these ceria-based materials were unaffected by the material specific surface area, doping element, degree of OSC and reactions. The rates were proportional to hydrocarbon partial pressures with positive fraction reaction order; independent of co-reactant partial pressures; but inhibited by CO and H_2. A set of unifying redox mechanistic proposal, in which the sole relevant elementary step is the reaction of intermediate surface hydrocarbon species with the lattice oxygen (O_O^x) and that oxygen is efficiently replenished by a rapid surface reaction with oxygen source in the system, was applied to explain these observed kinetic dependencies.

The capabilities to decompose oxyhydrocarbons without the requirement of steam and reform high hydrocarbon compounds with excellent resistance toward carbon deposition are the great benefit of ceria-based catalysts particularly for applying in SOFC system. Without the presence of steam being required, the consideration of water management in SOFC system is negligible, while the capability to reform high hydrocarbon

compounds with excellent resistance toward carbon deposition eliminates the requirement of expensive noble metal catalysts or the installation of external pre-reformer. These benefits simplify the overall SOFC system design, making SOFC more attractive for commercial uses.

Acknowledgements

The financial support from The Thailand Research Fund (TRF) throughout this project is gratefully acknowledged.

References

[1] A. Trovarelli, Catal. Rev. -Sci. Eng. 38 (1996) 439.
[2] P. Fornasiero, G. Balducci, R.D. Monte, J. Kaspar, V. Sergo, G. Gubitosa, A. Ferrero, M. Graziani, J. Catal. 164 (1996) 173.
[3] T. Miki, T. Ogawa, M. Haneda, N. Kakuta, A. Ueno, S. Tateishi, S. Matsuura, M. Sato, J. Phys. Chem. 94 (1990) 339.
[4] C. Padeste, N.W. Cant, D.L. Trimm, Catal. Lett. 18 (1993) 305.
[5] S. Kacimi, J. Barbier Jr., R. Taha, D. Duprez, Catal. Lett. 22 (1993) 343.
[6] G.S. Zafiris, R.J. Gorte, J. Catal. 143 (1993) 86.
[7] G.S. Zafiris, R.J. Gorte, J. Catal. 139 (1993) 561.
[8] S. Imamura, M. Shono, N. Okamoto, R. Hamada, S. Ishida, Appl. Catal. A 142 (1996) 279.
[9] E. Ramírez-Cabrera, A. Atkinson, D. Chadwick, Appl. Catal. B 47 (2004) 127.
[10] E. Ramírez-Cabrera, N. Laosiripojana, A. Atkinson, D. Chadwick, Catal. Today 78 (2003) 433.
[11] R.J. Gorte, J.M. Vohs, S. McIntosh, Solid State Ionics 175 (2004) 1.
[12] S. Jung, C. Lu, H. He, K. Ahn, R.J. Gorte, J.M. Vohs, J. Power Sources 154 (1) (2006) 42.
[13] T. Kim, G. Liu, M. Boaro, S.-I. Lee, J.M. Vohs, R.J. Gorte, O.H. Al-Madhi, B.O. Dabbousi, J. Power Sources 155 (2) (2006) 231.
[14] O. Costa-Nunes, R.J. Gorte, J.M. Vohs, J. Power Sources 141 (2005) 241.
[15] S. An, C. Lu, W.L. Worrell, R.J. Gorte, J.M. Vohs, Solid State Ionics 175 (2004) 135.
[16] D.J.L. Brett, A. Atkinson, D. Cumming, E. Ramírez-Cabrera, R. Rudkin, N.P. Brandon, Chem. Eng. Sci. 60 (2005) 5649.
[17] K. Otsuka, M. Hatano, A. Morikawa, J. Catal. 79 (1983) 493.
[18] K. Otsuka, M. Hatano, A. Morikawa, Inorg. Chim. Acta 109 (1985) 193.
[19] P.J. Gellings, H.J.M. Bouwmeester, Catal. Today 58 (2000) 1.
[20] D. Terribile, A. Trovarelli, J. Llorca, C. Leitenburg, G. Dolcetti, J. Catal. 178 (1998) 299.
[21] E. Abi-aad, R. Bechara, J. Grimblot, A. Aboukaïs, Chem. Mater. 5 (1993) 793.
[22] L.A. Bruce, M. Hoang, A.E. Hughes, T.W. Turney, Appl. Catal. A 134 (1996) 351.
[23] P.L. Chen, I.W. Chen, J. Am. Ceram. Soc. 76 (1993) 1577.
[24] H.K. Varma, P. Mukundam, K.G.K. Warrier, A.D. Damodaran, J. Mater. Sci. Lett. 10 (1991) 666.
[25] M. Hirano, E. Kato, J. Am. Ceram. Soc. 79 (1996) 777.
[26] M. Vallet-Regi, F. Conde, S. Nicolopoulos, C.V. Ragel, J.M. Gonzales-Calbet, Mater. Sci. Forum 235–238 (1997) 291.
[27] A. Tschöpe, J.Y. Ying, NanoStruct. Mater. 4 (1994) 617.
[28] M. Pijolat, J.P. Viricelle, M. Soustelle, Stud. Surf. Sci. Catal. 91 (1995) 885.
[29] T. Masui, K. Fujiwara, K. Machida, G. Adachi, T. Sakata, H. Mori, Chem. Mater. 9 (1997) 2197.
[30] Y. Zhou, R.J. Phillips, J.A. Switzer, J. Am. Ceram. Soc. 78 (1995) 981.
[31] V. Perrichon, A. Laachir, S. Abouarnadasse, O. Touret, G. Blanchard, Appl. Catal. A 129 (1995) 69.
[32] D. Terribile, A. Trovarelli, J. Llorca, C. Leitenburg, G. Dolcetti, Catal. Today 43 (1998) 79.
[33] M. Ozawa, M. Kimura, A. Isogai, J. Alloys Comp. 193 (1993) 73.
[34] G. Balducci, J. Kaspar, P. Fornasiero, M. Graziani, M.S. Islam, J. Phys. Chem. B 102 (1998) 557.
[35] G. Vlaic, P. Fornasiero, S. Geremia, J. Kaspar, M. Graziani, J. Catal. 168 (1997) 386.
[36] G.R. Rao, J. Kaspar, S. Meriani, R. Dimonte, M. Graziani, Catal. Lett. 24 (1994) 107.
[37] P. Fornasiero, R. Dimonte, G.R. Rao, J. Kaspar, S. Meriani, A. Trovarelli, M. Graziani, J. Catal. 151 (1995) 168.
[38] M.H. Yao, T.E. Hoost, R.J. Baird, F.W. Kunz, J. Catal. 166 (1997) 67.
[39] D. Kim, J. Am. Ceram. Soc. 72 (1989) 1415.
[40] N. Laosiripojana, W. Sutthisripok, S. Assabumrungrat, Chem. Eng. J. 127 (13) (2007) 36.
[41] N. Kruse, A. Frennet, J.M. Bastin (Eds.), Catalysis and Automotive Pollution Control IV, Elsevier, Amsterdam, 1998.
[42] J. Kaspar, P. Fornasiero, M. Graziani, Catal. Today 50 (1999) 285.
[43] H.S. Roh, H.S. Potdar, K.W. Jun, Catal. Today 93–95 (2004) 39.
[44] J. Wei, E. Iglesia, J. Catal. 225 (2004) 116.
[45] N. Laosiripojana, S. Assabumrungrat, Appl. Catal. A 290 (2005) 200.
[46] N. Laosiripojana, S. Assabumrungrat, Appl. Catal. B 60 (2005) 107.
[47] Y. Lwin, W.R.W. Daud, A.B. Mohamad, Z. Yaakob, Int. J. Hydrogen Energy 25 (2000) 47.
[48] J.N. Amor, Appl. Catal. A 176 (1999) 159.
[49] N. Laosiripojana, S. Assabumrungrat, Appl. Catal. B 66 (2006) 29.

Chemical Engineering Science 64 (2009) 459 – 466

Contents lists available at ScienceDirect

Chemical Engineering Science

journal homepage: www.elsevier.com/locate/ces

Reactivity of CeO_2 and $Ce–ZrO_2$ toward steam reforming of palm fatty acid distilled (PFAD) with co-fed oxygen and hydrogen

A. Shotipruk[a], S. Assabumrungrat[a], P. Pavasant[a,c], N. Laosiripojana[b,*]

[a]Department of Chemical Engineering, Faculty of Engineering, Chulalongkorn University, Bangkok, Thailand
[b]The Joint Graduate School of Energy and Environment, King Mongkut's University of Technology Thonburi, Bangkok 10140, Thailand
[c]National Center of Excellence for Environmental and Hazardous Waste Management, Chulalongkorn University, Bangkok 10330, Thailand

ARTICLE INFO

Article history:
Received 14 June 2008
Received in revised form 30 August 2008
Accepted 3 September 2008
Available online 4 October 2008

Keywords:
Ceria
Hydrogen
Oxygen storage capacity
Steam reforming
Autothermal reforming
Palm fatty acid distillate

ABSTRACT

Steam reforming of three types free fatty acids (i.e. palmitic, oleic and linoleic acids) and palm fatty acid distilled (PFAD) were studied over ceria-based materials prepared by precipitation and cationic surfactant-assisted methods with/without Zr doping with an aim to develop good reforming catalyst for converting PFAD to hydrogen with high reforming reactivity and low carbon deposition. Among all catalysts, high surface area (HSA) $Ce–ZrO_2$ (with Ce/Zr ratio of 3/1) prepared by cationic surfactant-assisted method provided the highest steam reforming reactivity with greatest resistance toward carbon deposition; due to the high oxygen storage capacity (OSC) of this material. During steam reforming, the redox reactions between absorbed hydrocarbons (forming intermediate surface hydrocarbon species) with lattice oxygen (O_O^x) at $Ce–ZrO_2$ surface take place. The rapid redox reactions between surface carbon (C^*) forming via the adsorptions of hydrocarbon with lattice oxygen (O_O^x) prevents the formation of carbon species from decomposition of hydrocarbons. At 1173 K, the main products from the steam reforming of PFAD over this catalyst are H_2, CO, and CO_2 with some amounts of CH_4 and C_2H_4 generated; the formations of these high hydrocarbons can be eliminated by increasing temperature up to 1273 K.

The addition of either oxygen or hydrogen together with PFAD and steam considerably reduced the degree of carbon deposition. The presence of oxygen also reduced the formations of hydrocarbons, on the other hand, these formations increased when hydrogen was introduced at the feed. The negative effect of hydrogen is due to hydrogenation reaction as well as the reduction of lattice oxygen by hydrogen, which consequently inhibits the reaction of lattice oxygen with surface hydrocarbon species.

1. Introduction

According to the current oil crisis and the shortage of fossil fuels, the development of the biomass-based fuels (or biofuel) attracts much attention. Nowadays, one of the most practical biofuels is biodiesel, which are produced from palm oil. It should be noted that, recently, there are also several attempts to convert lignocellulosic biomass to biofuels (i.e. BTL); this conversion will reduce the competition of fuel with food market, which results in the food shortage and the rising of food price. Nevertheless, this technology remains need further development to achieve high efficiency.

Focusing on palm oil, over the past 10 years, this compound has become one of the attractive resources for biodiesel production since it constitutes a renewable and sustainable source of energy. Importantly, palm oil always contain high amount of free fatty acid (FFA) and the presence of too high FFA easily results in high amounts of soap produced simultaneously with the transesterification reaction. Therefore, to avoid this reaction, most of FFA in palm oil must be firstly processed or removed (as called palm fatty acid distilled or PFAD). The conversion of this removed PFAD to valuable products or fuels (e.g. fatty acid methyl esters via esterification or even hydrogen) is an alternative way to reduce the cost for biodiesel production and consequently make biodiesel enable to compete economically with conventional petroleum diesel fuels. Among the prospective fuels, hydrogen is expected to be one of the most promising fuels in the near future. It is known as the zero-emission fuel and could be produced efficiently from the catalytic reforming of several hydrocarbon sources such as methane, methanol, bio-ethanol, gasoline and other oil derivatives. On this basis, the production of hydrogen from PFAD will provide the great benefit in terms of energy, environmental, and economical aspects.

Focusing on catalytic reforming process, steam reforming of several oxygenated hydrocarbons, e.g. methanol, acetic acid, ethanol, acetone, phenol or cresol as model compounds of bio-oils has widely

* Corresponding author. Tel.: +66 2 8729014; fax: +66 2 8726736.
E-mail address: navadol_l@jgsee.kmutt.ac.th (N. Laosiripojana).

0009-2509/$ - see front matter © 2008 Elsevier Ltd. All rights reserved.
doi:10.1016/j.ces.2008.09.013

been investigated (Basagiannis and Verykios, 2006; Galdámez et al., 2005; Czernik et al., 2004; Wang et al., 1997, 1996; Polychronopoulou et al., 2004; Takanabe et al., 2004; Fatsikostas et al., 2002; Liguras et al., 2003). Recently, many researchers have also investigated the addition of oxygen together with steam in a single process, calling an autothermal reforming, in order to reduce the degree of carbon formation as well as provide the thermal self-sustaining process. Until now, no literature work has reported the conversion fatty acids or PFAD to hydrogen by the catalytic reforming process; only few works have presented the catalytic reforming or cracking of acetic acid to hydrogen (Basagiannis and Verykios, 2007, in press; Davidian et al., 2008). PFAD normally consists mainly of palmitic acid ($C_{16}H_{32}O_2$; $CH_3(CH_2)_{14}COOH$), oleic acid ($C_{18}H_{34}O_2$; $CH_3(CH_2)_7CH=CH(CH_2)_7COOH$) and linoleic acid ($C_{18}H_{32}O_2$; $CH_3(CH_2)_4CH=CHCH_2CH=CH(CH_2)_7CO_2H$) with various ratios depending on the source of palm oils. The major difficulty to reform high hydrocarbon compounds like PFAD is the possible deactivation of the reforming catalyst due to the carbon deposition, as fatty acids can decompose homogenously and form carbon species on the surface of catalyst. In addition, from its thermal decomposition, several gaseous hydrocarbon elements, which act as very strong promoters for carbon formation, can be formed. Worldwide efforts are in progress to explore a novel catalyst with high activity and stability for the reforming of heavy hydrocarbon compounds.

Recently, it is established that ceria and metal oxide (e.g. Gd, Nb, and Zr) doped cerias provide high oxygen storage capacity (OSC), which is beneficial in oxidation and reforming processes (Ramirez et al., 2002). The great benefit of ceria-based catalysts for the reforming reaction is their high resistance toward carbon deposition compared to the conventional metal catalysts i.e. Ni (Ramírez-Cabrera et al., 2003; Terribile et al., 1998a); however, the main weaknesses of the materials are their low specific surface area and high deactivation due to the thermal sintering particularly when operated at such a high temperature (Terribile et al., 1998a). The preparation and use of high surface area (HSA) ceria (CeO_2, HSA) with high resistance toward the sintering would be a good alternative method to improve the catalytic reactivity (Terribile et al., 1998a). Recently, Terribile et al. (1998b) synthesized CeO_2 (HSA) with improved textural, structural and chemical properties for environmental applications by using a novel cationic surfactant-assisted approach. They reported that the reaction of cerium salts under basic conditions with ammonia in the presence of a cationic surfactant results in the precipitation of a gelatinous hydrous cerium oxide/surfactant mixture, which after calcination gives HSA, fluorite-structured CeO_2 with good homogeneity and stability. They suggested that the cationic surfactant acts as a surface area enhancer by incorporation into the hydrous oxide and lowering of the surface tension of water in the pores during drying.

In addition to the investigation on preparation method, the addition of zirconium oxide (ZrO_2) has also been reported to improve the specific surface area, OSC, redox property, thermal stability and catalytic activity of ceria (Ozawa et al., 1993; Balducci et al., 1998; Vlaic et al., 1997; Rao et al., 1994; Fornasiero et al., 1995; Yao et al., 1997). These benefits were associated with enhanced reducibility of cerium (IV) in Ce–ZrO_2, which is a consequence of high O^{2-} mobility inside the fluorite lattice. The reason for the increasing mobility might be related to the lattice strain, which is generated by the introduction of a smaller isovalent Zr cation into the CeO_2 lattice (Zr^{4+} has a crystal ionic radius of 0.84 å, which is smaller than 0.97 å for Ce^{4+} in the same co-ordination environment) (Kim, 1989).

In the present work, it is aimed to develop the reforming catalysts that can convert PFAD to hydrogen with high reforming activity and great resistance toward carbon formation. CeO_2 and Ce– ZrO_2 prepared by two different methods i.e. typical (co-) precipitation and cationic surfactant-assisted methods were selected as the catalyst in the present work. The steam reforming of palmitic acid, oleic acid and linoleic acid (as main components in PFAD) over these catalysts were firstly studied and compared to conventional Ni/Al_2O_3. The steam reforming of PFAD over selected catalyst was then carried out. The effects of temperature, oxygen adding and hydrogen adding on the reforming reactivity were also investigated. Lastly, the possible mechanism for steam reforming of PFAD over ceria-based catalysts was discussed.

2. Experimental methods

2.1. Raw material and chemicals

In the present work, palm fatty acid distillate (PFAD) was obtained from Chumporn Palm Oil Industry Public Company Limited., Thailand. It consists of 93 wt% FFA (mainly contains 46% palmitic acid, 34% oleic acid and 8% linoleic acid with small amount of other fatty acids i.e. stearic, myristic, tetracosenoic, linolenic, ecosanoic, ecosenoic, and palmitoleic acid). The rest elements are triglycerides, diglycerides (DG), monoglycerides (MG) and traces of impurities. The lab grade palmitic acid, oleic acid, and linoleic acid were supplied from Aldrich.

2.2. Material synthesis and characterization

In the present work, CeO_2 was synthesized by precipitation (CeO_2 (LSA)) and cationic surfactant-assisted (CeO_2 (HSA)) methods. CeO_2 (LSA) was prepared by the precipitation of cerium nitrate ($Ce(NO_3)_3 \cdot H_2O$) from Aldrich. The starting solution was prepared by slowly adding of 0.4 M ammonia (with flow rate of 0.254 $cm^3\,h^{-1}$) to 0.1 M of cerium nitrate solution until reaching volumetric ratio of 2:1. This solution was stirred by magnetic stirring (100 rpm) for 3 h, then sealed and placed in a thermostatic bath maintained at 363 K for 3 days to prevent an agglomeration of the particles. The precipitate was filtered and washed with deionized water and acetone to remove the free surfactant. It was dried overnight in an oven at 383 K, and then calcined at 1173 K for 6 h. Following to the work from Terribile et al. (1998b), CeO_2 (HSA) were prepared by adding an aqueous solution of the appropriate cationic surfactant, 0.1 M cetyltrimethylammonium bromide solution from Aldrich, to a 0.1 M cerium nitrate. The molar ratio of ([Ce])/[cetyltrimethylammonium bromide] was kept constant at 0.8. The mixture was stirred and then aqueous ammonia was slowly added with vigorous stirring until the pH was 11.5 (Terribile et al., 1998b). After treatment with the same procedure as CeO_2 (LSA), fluorite-structured CeO_2 with good homogeneity were obtained.

$Ce_{1-x}Zr_xO_2$ (or Ce–ZrO_2) with different Ce/Zr molar ratios were also prepared by either co-precipitation or surfactant-assisted method of cerium nitrate ($Ce(NO0_3)_3 \cdot H_2O$), and zirconium oxychloride ($ZrOCl_2 \cdot H_2O$) (from Aldrich). The ratio between each metal salt was altered to achieve nominal Ce/Zr molar ratios: $Ce_{1-x}Zr_xO_2$, where $x = 0.25$, 0.50, and 0.75, respectively. After treatment, the specific surface areas of all CeO_2 and Ce–ZrO_2 were achieved from BET measurement. As presented in Table 1, after drying in the oven,

Table 1
Specific surface area of CeO_2 and Ce–ZrO_2 before and after calcination at 1173 K

Catalysts	Surface area after drying ($m^2\,g^{-1}$)	Surface area after calcination ($m^2\,g^{-1}$)
CeO_2 (HSA)	105	29
Ce–ZrO_2 (HSA) (Ce/Zr = 1/3)	135	49
Ce–ZrO_2 (HSA) (Ce/Zr = 1/1)	120	47
Ce–ZrO_2 (HSA) (Ce/Zr = 3/1)	115	46.5
CeO_2 (LSA)	55	11
Ce–ZrO_2 (LSA) (Ce/Zr = 1/3)	82	22
Ce–ZrO_2 (LSA) (Ce/Zr = 1/1)	74	20.5
Ce–ZrO_2 (LSA) (Ce/Zr = 3/1)	70	20

Table 2
Physicochemical properties of Ni/Al_2O_3 after reduction

Catalyst	Metal-load[a] (wt%)	BET surface area ($m^2\,g^{-1}$)	Metal-reducibility[b] (%)	Metal-dispersion[c] (%)
Ni/Al_2O_3	4.9	40	92.1	4.87

[a]Measured from X-ray fluorescence analysis.

[b]Measured from temperature-programmed reduction (TPR) with 5% hydrogen.

[c]Measured from temperature-programmed desorption (TPD) of hydrogen after TPR measurement.

surface areas of 105 and 55 $m^2\,g^{-1}$ were observed for CeO_2 (HSA) and CeO_2(LSA), respectively, and, as expected, the surface area decreased at high calcination temperatures. However, the value for CeO_2 (HSA) is still appreciable after calcination at 1173 K. The achievement of HSA material by surfactant-assisted procedure is due to the interaction of hydrous oxide with cationic surfactants under basic conditions during the preparation (Terribile et al., 1998b). At high pH value, conducting the precipitation of hydrous oxide in the presence of cationic surfactant allows cation exchange process between H^+ and the surfactant, resulting in a developed pore structure with an increase in surface area (Terribile et al., 1998b). It can also be seen that the introduction of ZrO_2 stabilizes the surface area of ceria, which is in good agreement with several previous reports (Kruse et al., 1998; Kaspar et al., 1999; Roh et al., 2004).

For comparison, Ni/Al_2O_3 (5 wt% Ni) was also prepared by impregnating γ-Al_2O_3 (from Aldrich) with $Ni(NO_3)_2$ solution (from Aldrich). After stirring, the solution was dried and calcined at 1173 K for 6 h. The catalyst powder was reduced with 10% H_2/Ar at 773 K for 6 h before use. After reduction, Ni/Al_2O_3 was characterized by several physicochemical methods. The weight contents of Ni were determined by X-ray fluorescence (XRF) analysis. The reducibility percentage of nickel was measured and calculated from the degree of H_2 uptakes from temperature-programmed reduction (TPR) test using 5% H_2 with the total flow rate of 100 $cm^3\,min^{-1}$ and temperature from room temperature to 773 K, while the dispersion percentage of nickel was identified from temperature-programmed desorption (TPD) by measuring the volumetric H_2 chemisorbed. All physicochemical properties of the synthesized catalysts are presented in Table 2.

2.3. Apparatus and procedures

To undergoing the catalytic testing, an experimental reactor system was constructed. The feed including palmitic acid, oleic acid and linoleic acid, PFAD and deionized H_2O was introduced via a heated syringe pump passing through our design quartz vaporizer-mixer system, where the inlet fatty acids are injected as droplet before vaporized and mixed with steam/carrier gas. All inlet components were introduced to a 10-mm diameter quartz reactor, which is mounted vertically inside tubular furnace. The catalyst (100 mg) was loaded in the quartz reactor, which was packed with a small amount of quartz wool to prevent the catalyst from moving. Preliminary experiments were carried out to find suitable conditions in which internal and external mass transfer effects are not predominant. Considering the effect of external mass transfer, the total gas flow rate was varied between 10 and 150 $cm^3\,min^{-1}$ under a constant residence time of 10^{-3} g min cm^{-3}. It was found that the reforming rate was independent of gas velocity when the gas flow rate was higher than 70 $cm^3\,min^{-1}$, indicating the absence of external mass transfer effects at this high velocity. Furthermore, the reactions on different average sizes of catalysts (up to 500 μm) were carried out to confirm that the experiments were in the region of intrinsic kinetics. It was observed that the catalysts with the particle size less than 200 μm showed no intraparticle diffusion limitation in the range of conditions studied. Therefore, the total flow rate was kept constant at 100 $cm^3\,min^{-1}$ whereas catalyst diameter was between 100 and 200 μm in all experiments.

In our system, a Type-K thermocouple was placed into the annular space between the reactor and the furnace. This thermocouple was mounted on the tubular reactor in close contact with the catalyst bed to minimize the temperature difference between the catalyst bed and the thermocouple. Another Type-K thermocouple was inserted in the middle of the quartz tube in order to re-check the possible temperature gradient. It is noted that the inner-system thermocouple is covered with small closed-end quartz rod to prevent the catalytic reactivity of thermocouple during reaction. After the reactions, the exit gas mixture was transferred via trace-heated lines to the analysis section, which consists of a Porapak Q column Shimadzu 14B gas chromatograph (GC) and a mass spectrometer (MS). The MS in which the sampling of the exit gas was done by a quartz capillery and differential pumping was used for the transient and carbon formation experiments, whereas the GC was applied in order to investigate the steady-state condition experiments and to recheck the results from MS. In the present work the reactivity of catalyst toward the reaction was defined in terms of hydrogen and other gaseous hydrocarbon by-product selectivities (based on carbon balance).

2.4. Measurement of carbon formation

In order to investigate the amount of carbon formed on catalyst surface, the oxidation reaction was applied by introducing 10% O_2 in helium into the system at isothermal condition (1173 K), after purging the system with helium. The amount of carbon formation on the surface of catalysts was determined by measuring the areas under peak of CO and CO_2 from the test compared with those from the calibrations of these components. It is noted that the calibrations of CO and CO_2 were performed by injecting a known amount of these calibration gases from a loop, in an injection valve in the bypass line.

3. Results and discussion

3.1. Redox properties and redox reversibility

After treatment, the degrees of OSC for fresh ceria-based materials were investigated using reduction measurement (R-1), which was performed by purging the catalysts with 5% H_2 in helium at 1173 K. The amount of H_2 uptake is correlated to the amount of oxygen stored in the catalysts. As presented in Table 3, the amount of H_2 uptakes over HSA Ce–ZrO_2 and CeO_2 are significantly higher than those over the low surface area cerias, suggesting the increasing of OSC with the doping of Zr and the increasing of material specific surface area. The benefit of OSC on the reforming reaction will be later presented in Section 4. After purged with helium, the redox

Table 3
R-1, Ox-1, R-2 analyses of ceria-based materials after calcination

Catalyst	Total H_2 uptake from R-1 ($\mu mol/g_{cat}$)[a]	Total O_2 uptake from Ox-1 ($\mu mol/g_{cat}$)[a]	Total H_2 uptake from R-2 ($\mu mol/g_{cat}$)[a]
CeO_2 (HSA)	4087	2012	4077
Ce–ZrO_2 (HSA) (Ce/Zr = 1/3)	2883	1423	2879
Ce–ZrO_2 (HSA) (Ce/Zr = 1/1)	3692	1848	3687
Ce–ZrO_2 (HSA) (Ce/Zr = 3/1)	5221	2620	5213
CeO_2 (LSA)	1789	884	1780
Ce–ZrO_2 (LSA) (Ce/Zr = 1/3)	1087	551	1075
Ce–ZrO_2 (LSA) (Ce/Zr = 1/1)	1701	709	1694
Ce–ZrO_2 (LSA) (Ce/Zr = 3/1)	2625	1305	2621

[a]Deviation = ±3%

Table 4
Hydrogen selectivity and distribution of other gaseous by-products from the steam reforming of fatty acids over several catalysts at 1173 K

Fuel	Catalyst	Hydrogen selectivity (%)	Distribution of the by-products (%)					
			CO	CO_2	CH_4	C_2H_6	C_2H_4	C_3H_6
Palmitic acid	Ce– ZrO_2 (HSA)	71.8	24.1	44.7	25.4	1.9	3.7	0.2
	CeO_2 (HSA)	68.3	21.4	39.1	30.7	2.5	5.8	0.5
	Ce–ZrO_2 (LSA)	62.7	19.2	38.6	31.7	3.3	6.3	0.9
	CeO_2 (LSA)	54.9	18.1	35.5	34.8	3.5	7.1	1.0
Oleic acid	Ce– ZrO_2 (HSA)	69.2	22.2	40.9	28.3	2.5	5.3	0.8
	CeO_2 (HSA)	61.9	19.1	38.2	33.8	2.6	5.4	0.9
	Ce–ZrO_2 (LSA)	60.4	18.9	37.6	33.3	2.9	6.7	0.6
	CeO_2 (LSA)	52.3	17.4	32.2	36.4	3.9	8.9	1.2
Linoleic acid	Ce– ZrO_2 (HSA)	67.4	21.8	39.5	27.6	3.8	5.9	1.4
	CeO_2 (HSA)	63.8	20.1	37.5	29.0	3.7	8.5	1.2
	Ce–ZrO_2 (LSA)	57.8	19.7	36.1	30.2	3.9	8.7	1.4
	CeO_2 (LSA)	51.5	18.7	32.0	35.1	3.7	9.2	1.3
Palmitic acid	Ni/Al_2O_3	65.5	29.8	40.1	22.2	3.9	9.8	1.4

reversibilities were then determined by applying oxidation measurement (Ox-1) following with second time reduction measurement (R-2). The amounts of O_2 chemisorbed and H_2 uptake are presented in Table 3. Regarding the results as also shown in Table 3, the amount of hydrogen uptakes for all materials were approximately identical to those from the R-1, indicating the reversibility of OSC for these synthesized ceria-based materials.

3.2. Reactivity toward the steam reforming of fatty acids

Before undergoing the tests on PFAD, the steam reforming of palmitic acid, oleic acid and linoleic acid were firstly investigated as these three hydrocarbons are the main components in PFAD. The experiments were carried out at 1173 K by introducing each fatty acid along with steam as co-reactant. It should be noted that the reactions for Ce–ZrO_2 with different Ce/Zr ratios (1/3, 1/1, and 3/1) were preliminary done over palmitic acid and the results revealed that Ce–ZrO_2 with Ce/Zr ratio of 3/1 synthesized from both techniques shows the best performance in terms of stability, activity and product selectivities. Therefore, we report here detailed reactivity of Ce– ZrO_2 only with Ce/Zr ratio of 3/1.

Table 4 presents the summarize of gaseous product distribution from the steam reforming of palmitic acid, oleic acid and linoleic acid over CeO_2 and Ce–ZrO_2 prepared by two techniques, while Fig. 1 shows the variations in hydrogen selectivity (%) with time (under the period of 48 h) from the steam reforming of palmitic acid over these catalysts. It is noted that the product distribution in the present work is reported in term of selectivity, as the conversion of fatty acids is always 100% in the range of conditions studied. It can be seen from Fig. 1 that no significant deactivation was detected from these four catalysts indicating their good stability toward the reactions. From Table 4, apart from H_2, CO, and CO_2 productions, significant amount of CH_4, C_2H_4, C_2H_6, and C_3H_6 were also detected from the reactions. The production of CO_2 indicates the contribution of the water–gas shift at this high temperature, while the presenting of gaseous hydrocarbons (i.e. CH_4, C_2H_4, C_2H_6, and C_3H_6) comes from the decomposition of these fatty acids Eq. (1) in the Discussion section). Between these three fatty acids, palmitic acid provides highest hydrogen production, whereas hydrogen production from oleic acid is slightly higher than that from linoleic acid. Furthermore, compared between four catalysts (CeO_2 (HSA), CeO_2 (LSA), Ce– ZrO_2 (HSA), and Ce–ZrO_2 (LSA)), Ce–ZrO_2 (HSA) presents the highest hydrogen production with considerably lower formations of CH_4, C_2H_4, C_2H_6, and C_3H_6. It should be noted that, for comparison, the steam reforming of palmitic acid over conventional Ni/Al_2O_3 was tested at 1173 K. As

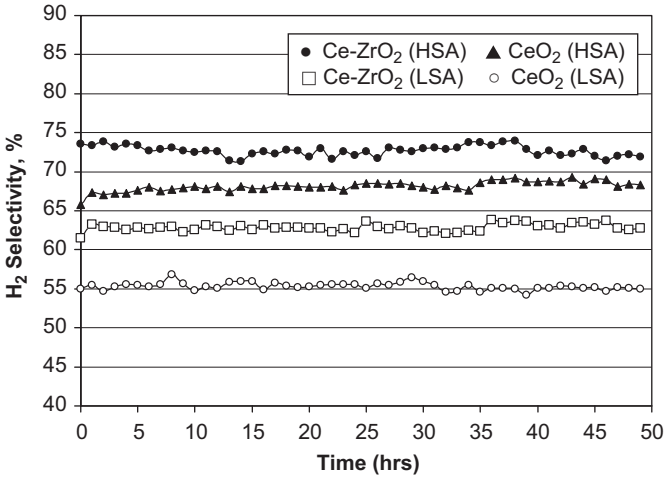

Fig. 1. Variation in hydrogen selectivities with time from steam reforming of palmitic acid at 1173 K over several catalysts.

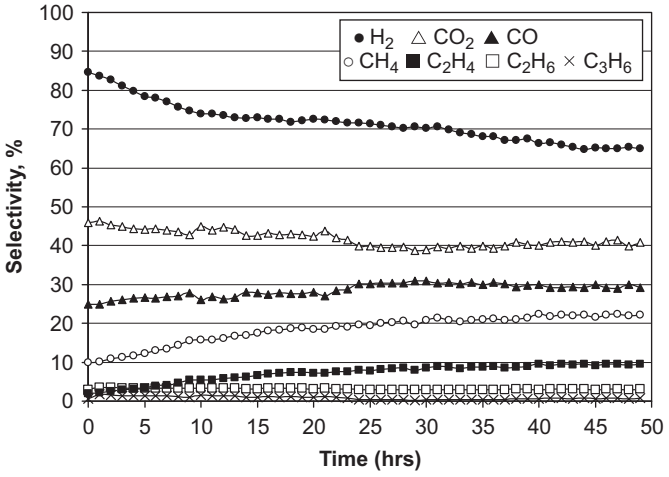

Fig. 2. Variations in hydrogen and other gaseous product selectivities with time from steam reforming of palmitic acid at 1173 K over Ni/Al_2O_3.

seen in Fig. 2, unstable profiles of hydrogen production yield, which related to the formation of carbon species on the surface of catalyst, were observed.

Table 5
Amount of carbon deposition on the surface of each catalyst after exposure in the steam reforming of fatty acids at 1173 K for 48 h

Fuel	Catalyst	Carbon formation (mmol g_{cat}^{-1})
Palmitic acid	Ce– ZrO_2 (HSA)	5.0
	CeO_2 (HSA)	5.3
	Ce–ZrO_2 (LSA)	5.9
	CeO_2 (LSA)	6.4
Oleic acid	Ce– ZrO_2 (HSA)	5.1
	CeO_2 (HSA)	5.5
	Ce–ZrO_2 (LSA)	6.4
	CeO_2 (LSA)	6.9
Linoleic acid	Ce– ZrO_2 (HSA)	5.4
	CeO_2 (HSA)	5.5
	Ce–ZrO_2 (LSA)	6.6
	CeO_2 (LSA)	7.0
Palmitic acid	Ni/Al_2O_3	9.5

After purging in helium, the post-reaction oxidation experiments were carried out by introducing of 10% oxygen in helium to determine the amount of carbon formation occurred in the system. The oxidation measurement detected some amount of carbon on the surface of ceria-based catalysts (between 5.0 and 5.5 mmol g_{cat}^{-1} for HSA materials and between 5.9 and 7.0 mmol g_{cat}^{-1} for low surface area one), whereas significantly higher amount of carbon was found over Ni/Al_2O_3, Table 5, indicating the greater resistance toward carbon deposition of ceria-based catalysts. The explanation for the steam reforming reactivity of ceria-based catalysts with high resistance toward carbon deposition will be given in the Discussion section.

3.3. Reactivity toward the steam reforming of PFAD

From the results in Section 3.1, among all ceria-based catalysts, Ce– ZrO_2 (HSA) with Ce/Zr ratios of 3/1 showed the greatest reactivities toward the steam reforming of palmitic acid, oleic acid and linoleic acid. Therefore, it was chosen for the further study to investigate the reactivity toward the steam reforming of PFAD. Instead of individual fatty acid, the feed was PFAD/H_2O in helium with the steam/carbon ratio of 3.0. It is noted that, before studying the catalyst performance, homogeneous (non-catalytic) steam reforming of PFAD (with above steam/carbon ratio) was also investigated at 1123 K. It was found that at this temperature PFAD were all homogeneously converted to $CH_4, C_2H_6, C_2H_4, C_3H_6$, CO, CO_2 and H_2 (with H_2 selectivity of 41.3% and $CH_4, C_2H_6, C_2H_4, C_3H_6$, CO, CO_2 selectivities of 22.3, 10.3, 16.8, 5.0, 16.4, 29.2%, respectively). It should also be noted that significant amount of carbon was also detected in the blank reactor after exposure for 10 h.

As for the catalyst testing, the variations in hydrogen production and gaseous by-product selectivities with time from the steam reforming of PFAD over Ce– ZrO_2 at 1123 K are shown in Fig. 3. Similar trend as all three fatty acids was observed; the main products are H_2, CO, and CO_2 with some amounts of CH_4, C_2H_4, C_2H_6, and C_3H_6. The post-reaction oxidation measurement indicated that the amount of carbon deposition on the surface of Ce–ZrO_2 after exposure in reforming condition for 48 h is 5.1 mmol g_{cat}^{-1}. As the next step, the effects of inlet steam/carbon ratio and temperature on the reforming reactivity were then studied by varying the inlet steam/carbon ratio from 3.0 to 5.0, 7.0, 9.0 and 11.0, and increasing the operating temperature from 1173 to 1198, 1223, 1248 and 1273 K. Fig. 4 presents the effect of inlet steam/carbon ratio on the hydrogen production and other by-product selectivities (after held the system for 10 h at each condition to ensure that the reaction reactivity is stable), whereas Table 6 presents the degree of carbon deposition observed from the post-reaction oxidation measurement.

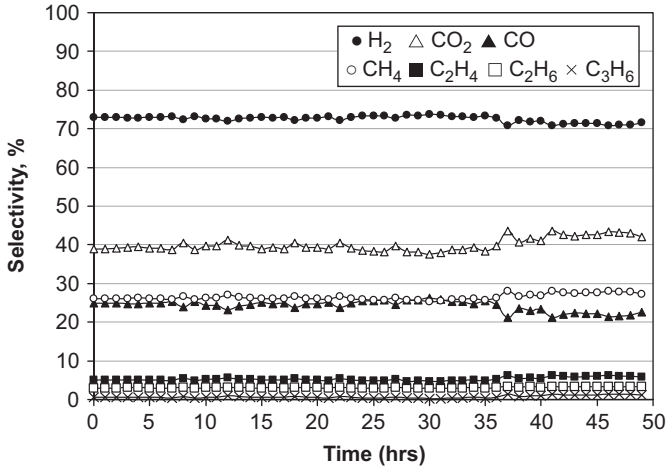

Fig. 3. Variations in hydrogen and other gaseous product selectivities with time from steam reforming of PFAD at 1173 K over Ce–ZrO_2 with Ce/Zr ratio of 3/1.

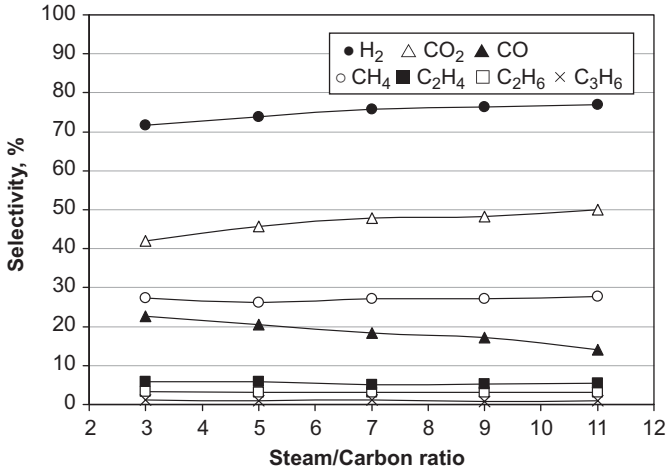

Fig. 4. Effect of inlet steam/carbon molar ratio on gaseous product selectivities from steam reforming of PFAD at 1173 K over Ce–ZrO_2 with Ce/Zr ratio of 3/1.

Table 6
Effects of inlet steam/carbon molar ratio and temperature on the degree of carbon formation after exposure in steam reforming of PFAD for 10 h

Catalyst	Steam/carbon molar ratio	Temperature (K)	Carbon formation (mmol g_{cat}^{-1})
Ce–ZrO_2 (Ce/Zr = 3/1)	3.0	1173	5.1
	5.0	1173	5.0
	7.0	1173	5.2
	9.0	1173	5.1
	11.0	1173	5.0
	3.0	1198	4.7
	3.0	1223	4.3
	3.0	1248	3.9
	3.0	1273	3.5

It can be seen that hydrogen and carbon dioxide increase with increasing steam content, whereas carbon monoxide decreases; this could be mainly due to the contribution of the water gas shift reaction. Nevertheless, all hydrocarbon (CH_4, C_2H_4, and C_2H_6) selectivities remain unchanged with increasing steam content and the amount of carbon deposition was relatively unaffected by the increasing of steam. Fig. 5 illustrates the influence of temperature

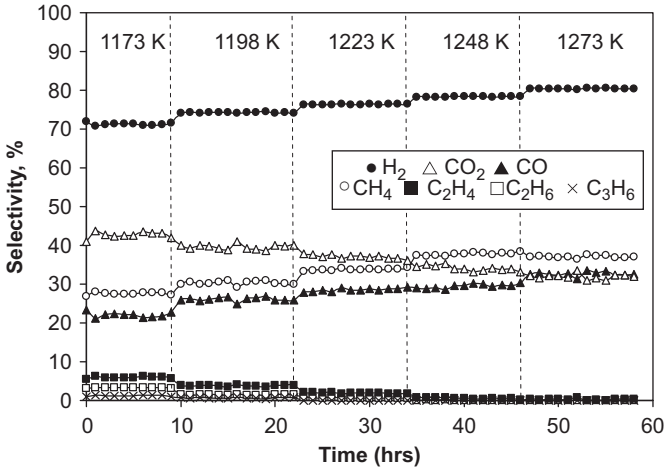

Fig. 5. Effect of temperature on hydrogen and other gaseous product selectivities with time from steam reforming of PFAD over Ce–ZrO_2 with Ce/Zr ratio of 3/1.

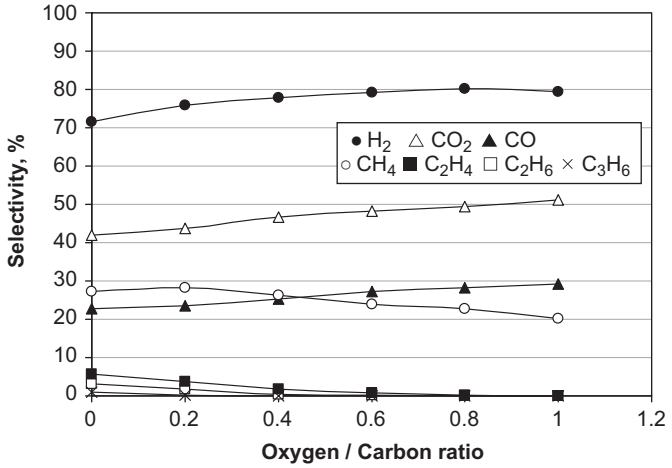

Fig. 6. Effect of inlet oxygen/carbon molar ratio on gaseous product selectivities from steam reforming of PFAD at 1173 K over Ce–ZrO_2 with Ce/Zr ratio of 3/1.

on the hydrogen yield and gaseous product selectivities. Clearly, the activities of catalyst increased with increasing temperature. At 1273 K, the main products from the steam reforming of PFAD over Ce–ZrO_2 were H_2, CO, CO_2, and CH_4, with insignificant amounts of C_2H_4, C_2H_6, and C_3H_6. Table 6 also presents the effect of temperature on the degree of carbon deposition; it can be seen that the amount of carbon formation on Ce–ZrO_2 surface decreased with increasing temperature.

3.4. Reactivity towards reforming of PFAD with co-fed oxygen

According to the results in Section 3.3, Ce–ZrO_2 can reform PFAD efficiently with high resistance toward carbon formation compared to conventional Ni/Al_2O_3. Nevertheless, the major consideration for ceria-based catalyst is its relatively low reforming reactivity, which results in the remains of high hydrocarbons in the product due to the incomplete reforming reaction particularly at low operating temperature (1173–1198 K). These formations could be minimized by increasing the temperature to 1273 K, which means significantly high energy input is required for the system. As an alternative procedure to reduce the formations of these hydrocarbons, oxygen was added in the feed together with PFAD and steam as autothermal reforming operation. In the present work, the inlet steam/carbon molar ratio was kept constant at 3.0, while the inlet O_2/carbon molar ratios were varied from 0.2, 0.4, 0.6, 0.8, to 1.0. The effect of oxygen concentration on product selectivities at 1173 K (after held the system for 10 h at each condition to ensure that the reaction reactivity is stable) is shown in Fig. 6.

It can be seen that hydrogen selectivity increased with increasing O_2/carbon molar ratio until the ratio reached 0.8, then oxygen showed no effect on the hydrogen production at higher inlet O_2/carbon molar ratio values. It should be noted that the conversion of O_2 was always closed to 100% in all testing. Fig. 6 also indicates that the dependence of oxygen on CH_4 production is non-monotonic. At suitable O_2/carbon molar ratio, higher H_2, CO, and CO_2 were observed from the autothermal reforming of PFAD, whereas no formation of C_2H_6, C_2H_4, and C_3H_6 was found compared to the steam reforming at the same operating conditions. The post-reaction oxidation measurement was then carried out to determine the degree of carbon formation on catalyst surface. From the oxidation measurement results shown in Table 7, significantly less quantities of carbon deposited were observed at high O_2/carbon molar ratio.

Table 7
Effects of inlet oxygen/carbon and hydrogen/carbon molar ratio on the degree of carbon formation after exposure in steam reforming of PFAD at 1023 K for 10 h

Catalyst	Oxygen/carbon molar ratio	Hydrogen/carbon molar ratio	Carbon formation (mmol g_{cat}^{-1})
Ce–ZrO_2 (Ce/Zr = 3/1)	0.2	–	4.7
	0.4	–	4.1
	0.6	–	3.6
	0.8	–	3.2
	1.0	–	3.0
	–	0.5	4.8
	–	1.0	4.5
	–	1.5	4.4
	–	2.0	4.2
	–	2.5	4.1
	–	3.0	3.9
	–	3.5	3.9
	–	4.0	3.8
	–	4.5	3.9
	–	5.0	3.8

3.5. Reactivity towards reforming of PFAD with co-fed hydrogen

Previously, we reported that the addition of hydrogen as co-feeding along with oxyhydrocarbon (i.e. ethanol) and steam over Ni catalysts could reduce the degree of carbon formation in the system as well as minimize the presences of intermediate hydrocarbon i.e. C_2H_4 and C_2H_6 occurring form the decomposition of ethanol during reaction (Laosiripojana et al., 2007). Here, we thereby investigated the reactivity of Ce–ZrO_2 towards reforming of PFAD with co-fed hydrogen. The inlet steam/carbon molar ratio was kept constant at 3.0, while the inlet H_2/carbon molar ratios were varied from 0.5 to 5.0. As hydrogen was used as the feed, the effect of this component on the catalyst performance was investigated in term of gaseous hydrocarbon (i.e. CH_4, C_2H_6, C_2H_4, and C_3H_6) distribution instead of hydrogen production selectivity. Fig. 7 presents all product distribution from the steam reforming of PFAD in the presence of hydrogen over Ce–ZrO_2 (after held the system for 10 h at each condition to ensure that the reaction reactivity is stable), while Table 7 also reports the effect of hydrogen adding on the amount of carbon formation.

It was found that, with the presence of hydrogen, less amount of carbon deposited were observed on the surface of Ce–ZrO_2. However, the formations of hydrocarbon particularly CH_4 in the product increased with increasing H_2 content. Thus, the adding of hydrogen

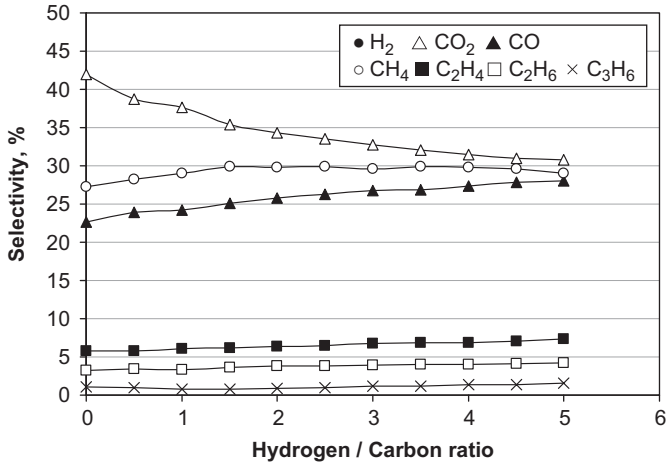

Fig. 7. Effect of inlet hydrogen/carbon molar ratio on gaseous product selectivities from steam reforming of PFAD at 1173 K over Ce–ZrO_2 with Ce/Zr ratio of 3/1.

as co-fed is not the suitable procedure for improving the steam reforming performance of PFAD over Ce–ZrO_2.

4. Discussion

Ce–ZrO_2 (HSA) was found in this study to have good reactivity toward the steam reforming of PFAD with excellent resistance towards carbon deposition compared to conventional Ni/Al_2O_3. Although Ni/Al_2O_3 provided higher initial H_2 yield, the reactivity decreases rapidly with time due to the significant carbon formation on its surface resulting in the low H_2 yield at steady-state condition (Fig. 2, Tables 4 and 5). It is noted that Ce–ZrO_2 (HSA) also presented good reactivity toward steam reforming of palmitic, oleic, and linoleic acids. Among these three fatty acids, the steam reforming of palmitic acid provided highest hydrogen production with lowest presence of hydrocarbons (i.e. CH_4, C_2H_6, C_2H_4, and C_3H_6) in the product; this could be due to the lighter carbon molecule of palmitic acid (C_{16}) compared to oleic and linoleic acids (C_{18}). Nevertheless, the differences are not much significant. At the temperature of 1173 K, the main products from the reforming of PFAD over Ce–ZrO_2 (HSA) were H_2, CO, CO_2, and CH_4 with some amounts of C_2H_6, C_2H_4, and C_3H_6. According to the mechanistic viewpoint, the overall reactions involved in the steam reforming of PFAD are very complex. At such a high operating temperature in the present work, the thermal decomposition of PFAD can take place producing several gaseous products (i.e. hydrogen, carbon monoxide, carbon dioxide, light hydrocarbons (C_nH_m) and oxygenates ($C_nH_mO_x$)) as well as carbon species forming on the surface of catalyst. By feeding steam, the steam reforming of hydrocarbons and oxygenates can then occur along with some side-reactions (e.g. water gas shift reaction and methanation).

$$C_nH_m + nH_2O \rightarrow nCO + (n + 0.5m)H_2 \quad (1)$$

$$C_nH_mO_x + (n - x)H_2O \rightarrow nCO + (n - x + 0.5m)H_2 \quad (2)$$

$$nCO + nH_2O \rightarrow nCO_2 + nH_2 \quad (3)$$

$$nCO + 3nH_2 \rightarrow nCH_4 + nH_2O \quad (4)$$

$$nCO_2 + 4nH_2 \rightarrow nCH_4 + 2nH_2O \quad (5)$$

Previously, we have proposed the redox mechanism to explain the reforming behavior of ceria-based catalysts by indicating that the reforming reaction mechanism involves the reaction between methane, or an intermediate surface hydrocarbon species, and lattice oxygen at the ceria-based material surface (Laosiripojana and Assabumrungrat, 2005). During reforming reaction, the isothermal reaction rate reaches steady-state where co-reactant i.e. steam provides a continuing source of oxygen. We also proposed that the controlling step is the reaction of methane with ceria, and that oxygen is replenished by a significantly more facile surface reaction of the ceria with steam (Laosiripojana and Assabumrungrat, 2005). Therefore, we suggested here that the reaction pathway for steam reforming of PFAD over ceria-based materials involves the reaction between absorbed hydrocarbons (forming intermediate surface hydrocarbon species) with the lattice oxygen (O_O^x) at CeO_2 surface, as illustrated schematically below.

C_nH_m *adsorption*:

$$C_nH_m + (n + m)^* \rightarrow (CH_x^*) + (H^*) \rightarrow n(C^*) + m(H^*) \quad (6)$$

Co-reactant (H_2O) *adsorption*:

$$H_2O + 2^* \Leftrightarrow OH^* + H^* \quad (7)$$

$$OH^* + ^* \Leftrightarrow H^* + O^* \quad (8)$$

Redox reactions of lattice oxygen (O_O^x) *with* C* *and* O*

$$C^* + O_O^x \rightarrow CO^* + V_O^{\cdot\cdot} + 2e' \quad (9)$$

$$V_O^{\cdot\cdot} + 2e' + O^* \Leftrightarrow O_O^x + ^* \quad (10)$$

Desorption of products (CO and H_2)

$$CO^* \Leftrightarrow CO + ^* \quad (11)$$

$$2(H^*) \Leftrightarrow H_2 + 2^* \quad (12)$$

Using the Kroger–Vink notation, $V_O^{\cdot\cdot}$ denotes as an oxygen vacancy with an effective charge 2^+, and e' is an electron which can either be more or less localized on a cerium ion or delocalized in a conduction band. * is the surface active site of ceria-based materials, there are two possibilities for this scheme depending on what is assumed for the catalyst active site. It can be a unique site, or can also be considered to be the same site as the catalyst oxidized site (O_x) (Laosiripojana and Assabumrungrat, 2005). During the reactions, hydrocarbons adsorbed on * forming intermediate surface hydrocarbon species (CH_x^*) (Eq. (6)) and later reacted with the lattice oxygen (O_O^x) (Eq. (9)). The steady-state reforming rate is due to the continuous supply of the oxygen source by H_2O (Eqs. (7) and (8)) that reacted with the reduced-state catalyst to recover lattice oxygen (O_O^x) (Eq. (10)).

The high resistance towards carbon deposition for ceria-based catalysts particularly Ce–ZrO_2 (HSA) is mainly due to the high OSC of material. Previously, we reported the excellent resistance towards carbon deposition for CeO_2 especially for HSA CeO_2 (Laosiripojana and Assabumrungrat, 2005). CeO_2 contains a high concentration of highly mobile oxygen vacancies and thus acts as a local source or sink for oxygen on its surface. It has been reported that at high temperature the lattice oxygen (O_O^x) at the CeO_2 surface can oxidize gaseous hydrocarbons (methane Laosiripojana and Assabumrungrat, 2005, propane and butane Laosiripojana and Assabumrungrat, 2006). Although conventional CeO_2(CeO_2 (LSA)) has also been reported to provide high resistance towards carbon formation, the major weaknesses of CeO_2 (LSA) are its low specific surface area and also high size reduction due to the thermal sintering impact, resulting in its significant lower redox properties than CeO_2 (HSA). These disadvantages result in the low steam reforming reactivity for CeO_2 (LSA). It was also concluded here that the addition of ZrO_2 on CeO_2 promoted the reforming reactivity, which is in good agreement with the literatures.

According to our interested reaction (steam reforming of PFAD), carbon formation could occur from the decompositions of fatty acids

and gaseous hydrocarbon products. Theoretically, it can also occur from the Boudouard reaction especially at low inlet steam/carbon molar ratio:

$$2CO \Leftrightarrow CO_2 + C \quad (13)$$

These reactions could be inhibited by the redox reaction between the surface carbon (C) with the lattice oxygen (O_O^x) at CeO_2 surface:

$$C + O_O^x \rightarrow CO + V_O^{\cdot\cdot} + 2e' \quad (14)$$

The greater resistance toward carbon deposition for HSA ceria-based catalyst particularly Ce–ZrO_2 (HSA) is due to the significant higher amount of lattice oxygen (O_O^x) on their surfaces, according to the results in Section 3.1.

It was also observed from the study that the addition of either oxygen or hydrogen together with PFAD and steam reduced the degree of carbon deposition. By addition of oxygen along with PFAD and steam as autothermal reforming, the partial oxidation of fatty acids takes place and fatty acids could possibly oxidize to methane and carbon monoxide; thus, the rate of fatty acid decomposition reduces and less C_2H_6, C_2H_4, and C_3H_6 are generated, which consequently results in the lower degree of carbon deposition on the surface of catalyst. In addition, oxygen also prevents the formation of carbon species via the hydrocarbon depositions by oxidizing these hydrocarbons to gaseous elements that are unfavored to form carbon species. Importantly, the presence of oxygen also helps steam to regenerate the lattice oxygen (O_O^x) on CeO_2 surface ($0.5O_2 + V_{O^{\cdot\cdot}} + 2e' \rightarrow O_O^x$), which eventually help promoting the reforming reactivity of ceria. It is noted that the major consideration of the autothermal reforming operation is the O_2/carbon ratio. The presence of too high oxygen concentration could oxidize hydrogen produced from the reaction and generate more steam.

By adding hydrogen at the feed, the degree of carbon formation also reduced due to the hydrogenation reaction. Nevertheless, it was found that in the presence of hydrogen at the feed the formations of hydrocarbon particularly CH_4 in the product increased. This negative effect of hydrogen appearance on CH_4, C_2H_4, and C_2H_6 conversions could be due to the hydrogenation of adsorbed CH_x species with this adding hydrogen and also from reduction of lattice oxygen by hydrogen and consequently inhibits the reaction of the lattice oxygen with the surface hydrocarbon species. This explanation is in good agreement with our previous studies (Laosiripojana and Assabumrungrat, 2005) which studied kinetics parameters for the methane steam reforming on ceria-based materials and reported the negative effect of hydrogen on methane conversion.

5. Conclusion

Steam reforming of free fatty acids (i.e. palmitic, oleic and linoleic acids) and palm fatty acid distilled (PFAD) were tested over ceria-based materials prepared by precipitation and cationic surfactant-assisted methods with/without Zr doping. Among all ceria-based catalysts, Ce–ZrO_2 (with Ce/Zr ratio of 3/1) from cationic surfactant-assisted method (Ce–ZrO_2 (HSA)) provided the highest degree of oxygen storage capacity (OSC) and steam reforming reactivity with greatest resistance toward carbon deposition. At 1173 K, the main products from the steam reforming of PFAD over Ce–ZrO_2 (HSA) are H_2, CO, and CO_2 with some amounts of CH_4, C_2H_4, C_2H_6, and C_3H_6; the formations of high hydrocarbon can be eliminated by increasing the operating temperature up to 1273 K.

The addition of either oxygen or hydrogen together with PFAD and steam reduced the degree of carbon deposition. The presence of oxygen also reduced the formations of C_2H_6, C_2H_4, and C_3H_6 due to the possible oxidation of fatty acids, which is eventually converted to methane and carbon monoxide. At suitable O_2H_2O/PFAD ratio, high H_2 selectivity without the formation of C_{2+} hydrocarbon was achieved. On the other hand, in the presence of hydrogen at the feed the formations of hydrocarbon in the product increased. This negative effect of hydrogen appearance on CH_4, C_2H_4, and C_2H_6 conversions is due to hydrogenation reaction and the reduction of lattice oxygen by hydrogen, which consequently inhibits the reaction of the lattice oxygen with the surface hydrocarbon species.

Acknowledgements

The financial support from The Thailand Research Fund (TRF) and National Metal and Materials Technology Center (MTEC) throughout this project is gratefully acknowledged.

References

Balducci, G., Kaspar, J., Fornasiero, P., Graziani, M., Islam, M.S., 1998. Journal of Physical Chemistry B 102, 557.
Basagiannis, A.C., Verykios, X.E., 2006. Applied Catalysis A 308, 182.
Basagiannis, A.C., Verykios, X.E., 2007. International Journal of Hydrogen Energy 32, 3343.
Basagiannis, A.C., Verykios, X.E., 2008. Applied Catalysis B 82, 77.
Czernik, S., French, R.J., Magrini-Bair, K.A., Chornet, E., 2004. Energy Fuels 18, 1738.
Davidian, T., Guilhaume, N., Daniel, C., Mirodatos, C., 2008. Applied Catalysis A 335, 64.
Fatsikostas, A.N., Kondarides, D.I., Verykios, X.E., 2002. Catalysis Today 75, 145.
Fornasiero, P., Dimonte, R., Rao, G.R., Kaspar, J., Meriani, S., Trovarelli, A., Graziani, M., 1995. Journal of Catalysis 151, 168.
Galdámez, J.R., García, L., Bilbao, R., 2005. Energy Fuels 19, 1133.
Kaspar, J., Fornasiero, P., Graziani, M., 1999. Catalysis Today 50, 285.
Kim, D., 1989. Journal of the American Ceramic Society 72, 1415.
Kruse, N., Frennet, A., Bastin, J.M. (Eds.), 1998. Catalysis and Automotive Pollution Control IV. Elsevier, Amsterdam.
Laosiripojana, N., Assabumrungrat, S., 2005. Applied Catalysis B: Environmental 60, 107.
Laosiripojana, N., Assabumrungrat, S., 2006. Journal of Power Sources 158, 1348.
Laosiripojana, N., Assabumrungrat, S., Charojrochkul, S., 2007. Applied Catalysis A 327, 180.
Liguras, D.K., Kondarides, D.I., Verykios, X.E., 2003. Applied Catalysis B: Environmental 43, 345.
Ozawa, M., Kimura, M., Isogai, A., 1993. Journal of Alloys and Compounds 193, 73.
Polychronopoulou, K., Costa, C.N., Efstathiou, A.M., 2004. Applied Catalysis A 272, 37.
Ramirez, E., Atkinson, A., Chadwick, D., 2002. Applied Catalysis B 36, 193.
Ramírez-Cabrera, E., Laosiripojana, N., Atkinson, A., Chadwick, D., 2003. Catalysis Today 78, 433.
Rao, G.R., Kaspar, J., Meriani, S., Dimonte, R., Graziani, M., 1994. Catalysis Letters 24, 107.
Roh, H.S., Potdar, H.S., Jun, K.W., 2004. Catalysis Today 93–95, 39.
Takanabe, K., Aika, K., Seshan, K., Lefferts, L., 2004. Journal of Catalysis 227, 101.
Terribile, D., Trovarelli, A., Llorca, J., Leitenburg, C., Dolcetti, G., 1998a. Journal of Catalysis 178, 299.
Terribile, D., Trovarelli, A., Llorca, J., Leitenburg, C., Dolcetti, G., 1998b. Catalysis Today 43, 79–88.
Vlaic, G., Fornasiero, P., Geremia, S., Kaspar, J., Graziani, M., 1997. Journal of Catalysis 168, 386.
Wang, D., Montané, D., Chornet, E., 1996. Applied Catalysis A 143, 245.
Wang, D., Czernik, S., Montané, D., Mann, M., Chornet, E., 1997. Industrial and Engineering Chemistry Research 36, 1507.
Yao, M.H., Hoost, T.E., Baird, R.J., Kunz, F.W., 1997. Journal of Catalysis 166, 67.